OUKA
The University of Osaka
Institutional Knowledge Archive

Title	Titanium-Based Organic/Inorganic Semiconductors for Efficient Photocatalytic Hydrogen Peroxide Production Under Two-Phase Reaction System
Author(s)	Zhao, Yifan
Citation	大阪大学, 2025, 博士論文
Version Type	VoR
URL	https://doi.org/10.18910/103215
rights	
Note	

The University of Osaka Institutional Knowledge Archive : OUKA

https://ir.library.osaka-u.ac.jp/

The University of Osaka

博士学位論文

Titanium-Based Organic/Inorganic Semiconductors for Efficient Photocatalytic Hydrogen Peroxide Production Under Two-Phase Reaction System

二相反応系における高効率光触媒的過酸化水素生成のための
チタン系有機／無機半導体

ZHAO Yifan

赵 一凡

2025 年 7 月

Division of Materials and Manufacturing Science

Graduate School of Engineering

The University of Osaka

大阪大学

大学院工学研究科

マテリアル生産科学専攻

Contents

Chapter I

General Introduction

1.1 Background

1.1.1 Fundamentals of photocatalytic H_2O_2 production

Hydrogen peroxide (H_2O_2), one of the 100 most valuable chemicals in the world,[1] is widely used for various purposes due to its oxidizing and disinfectant properties. H_2O_2 usually acts as an oxidizing agent in some chemical organic synthesis processes, due to its ability to readily donate oxygen atoms.[2] Especially, H_2O_2 is often considered environmentally friendly because of its decomposition into water and oxygen, leaving behind only harmless byproducts, which entitles it to broad applications in wastewater treatment, disinfection,[3] and bleaching[4] fields. Recently, H_2O_2 has been employed as an energy carrier in a kind of novel single-compartment fuel cell, with a theoretical output potential similar to that of the traditional hydrogen fuel cell.[5]

According to the report,[6] the global market size of H_2O_2 in 2022 was USD 3.07 billion, which grew to USD 3.24 billion in 2023 at a compound annual growth rate (CAGR) of 5.4 %. It is expected to increase to USD 4.05 billion in 2027 with a CAGR of 5.7 %. In order to meet such growing market demands, some efficient methods have been researched and developed for H_2O_2 production.

At present, the oxidation of anthraquinone (AQ) has been a well-established method for H_2O_2 synthesis due to its efficiency and ability to generate H_2O_2 on a large scale.[1,7] However, process complexity and waste by-products of AQ oxidation method not only result in substantial energy input but also greatly exacerbate the burden on the natural environment and ecosystems.[8] Therefore, subsequent efforts have been committed to exploring some novel methods for H_2O_2 production under more benign conditions and without producing wastes. One alternative method is the direct synthesis of hydrogen (H_2) and oxygen (O_2) for H_2O_2 production, which has a potential to simplify the production process and reduce resource consumption.[9] However, this method requires precise control of reaction conditions, such as a reaction temperature of nearly 0 ^oC, specific noble metal catalysts, and the ratio of H_2/O_2 mixture reaction gas. Despite adding some diluent gases such as carbon dioxide (CO_2) and inert gas, the explosion risk of the H_2/O_2 mixture gas limits industrial applications of this reaction

process. As a result, there is an urgent need for an ecologically responsible and operationally safe method to generate H_2O_2.

Currently, artificial photosynthesis to produce H_2O_2 offers a sustainable and direct approach, utilizing renewable solar energy to convert water and oxygen into H_2O_2 with high selectivity and minimal resource consumption.[10]

1.1.2 Reaction principles on photocatalytic ORR

As illustrated in **Figure 1a**, the mechanism of photocatalytic H_2O_2 synthesis via the oxygen reduction reaction (ORR) on semiconductor substrates typically encompasses three substantial processes, including light absorption, charge separation, and surface redox reaction.[11] In the first step, the semiconductor irradiated by a light source absorbs photons with greater energy values than the bandgap (E_g) of the semiconductor, which activate electrons to transfer from the valence band (VB) to the conduction band (CB). The transition of electrons leaves behind holes with positive charge, which forms electron-hole pairs known as photogenerated charges. Subsequently, photogenerated charges separate and only a minority of them can migrate to the surface of semiconductors whereas most will recombine. Finally, the photoinduced electrons and holes, with their respective reducing and oxidizing capabilities, have the potential to propel the redox chemical reactions as shown in **Figure 1b**, provided they can surpass the necessary overpotentials for each electron transfer step.[12,13]

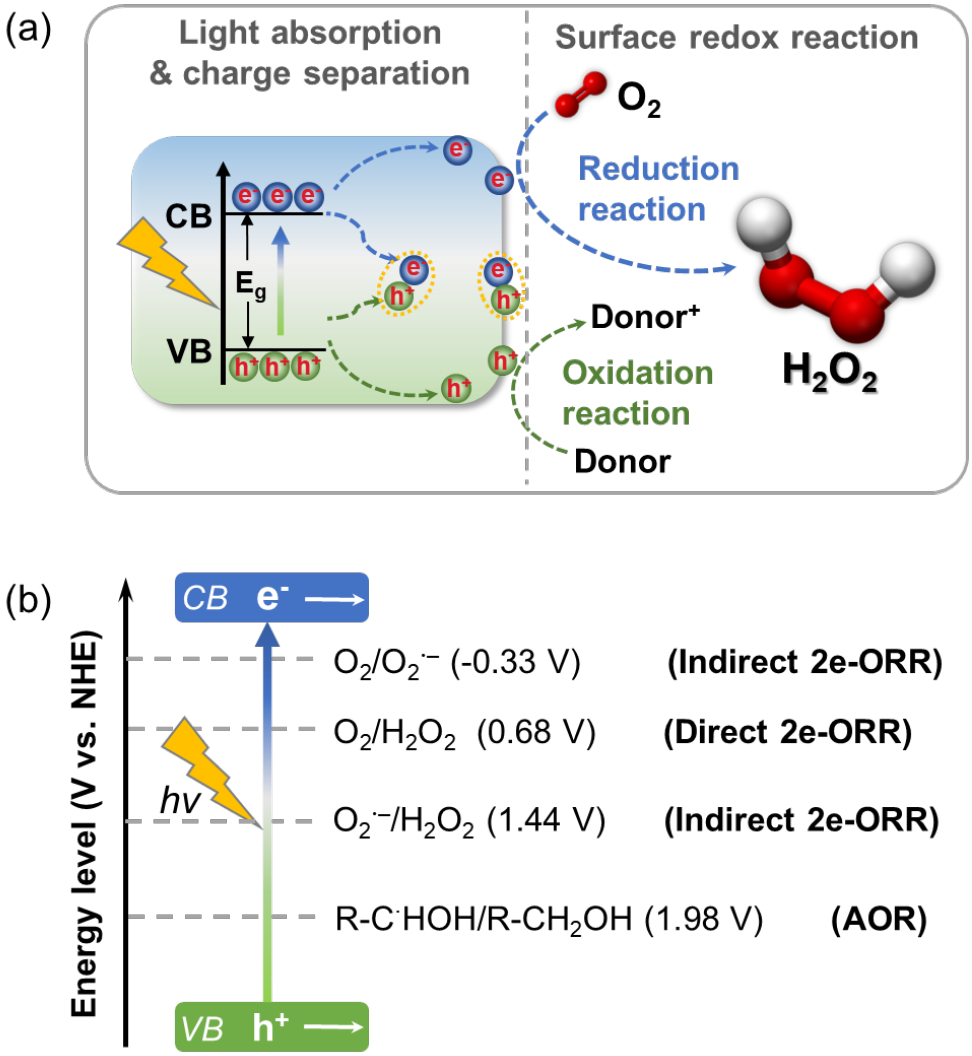

Figure 1. (a) Schematic illustration of the photocatalytic processes for H_2O_2 production; (b) Energy level diagram of photocatalytic H_2O_2 production via ORR and alcohol oxidation routes using a semiconductor.

Traditionally, the photocatalytic ORR process is conducted in single-phase batch reactors, where the catalyst and H_2O_2 product exist in the same solvent (left diagram in **Figure 2**). In a typical monophasic photocatalytic ORR system, the photogenerated electrons engage in the formation of H_2O_2 through two possible pathways: an indirect, stepwise two-electron process (Indirect 2e-ORR, **Equations 1 and 2**) or a direct two-electron transfer in a single step (Direct 2e-ORR, **Equation 3**). As illustrated in the energy diagram (**Figure 1b**), the indirect pathway requires the CB potential of the photocatalyst to be more negative than -0.33 V versus normal hydrogen electrode (vs. NHE) to proceed, as it involves superoxide radicals ($O_2^{\bullet-}$) as

intermediates. Therefore, the direct 2e-ORR pathway (0.68 V vs. NHE) is thermodynamically more favorable than the indirect route (-0.33 V vs. NHE).[14] On the contrary, the indirect 2e-ORR pathway is more kinetically preferred, as it proceeds through successive single-electron transfers, which typically occur more readily.[15,16] Despite this advantage in kinetics, the high reactivity of $O_2^{\bullet-}$, as evidenced by properties of over-reduction and electronic counter-transmission to photocatalysts, could readily result in the decomposition and limited production of H_2O_2.[17,18] Therefore, mitigating this high reactivity of $O_2^{\bullet-}$ would be advantageous to inhibit the H_2O_2 decomposition and enhance the effective generation of H_2O_2 through the indirect ORR route.

To enhance the productivity of photocatalytic H_2O_2 production, various alcohols such as methanol, ethanol,[19] isopropanol, benzyl alcohol (BA),[20] etc. are often introduced into the photoreaction system as sacrificial agents to drive alcohol oxidation reactions (AOR). They are used to quench photogenerated holes, thus donating more electrons to the ORR process. Shiraishi et al.[21] demonstrated that BA outperforms aliphatic alcohols as an electron donor in H_2O_2 formation, owing to its ability to efficiently form peroxo species that readily convert into H_2O_2. Therefore, the synthesis of H_2O_2 is followed by the BA oxidation reaction process to produce another high-value compound, benzaldehyde (BAL), showing a redox potential of 1.98 V vs. NHE (**Equation 4**), where R represents the benzene ring. However, in single-phase systems, H_2O_2 decomposition is difficult to avoid due to the over-reduction of $O_2^{\bullet-}$ and the direct contact between the formed H_2O_2 and semiconductors, ultimately hampering its overall productivity. Besides, the separation of H_2O_2 and BAL products in a single phase requires significant energy consumption and additional economic expenses.

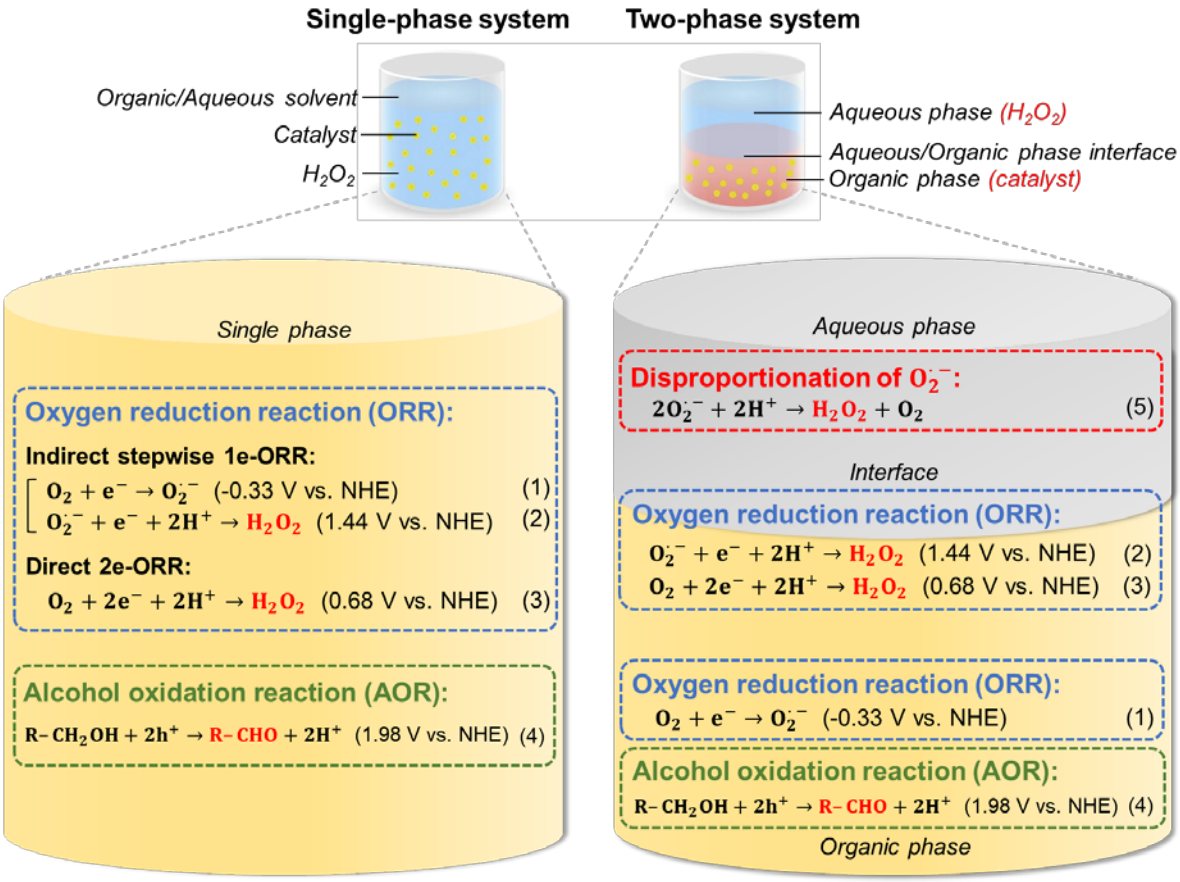

Figure 2. Reaction mechanism diagram of photocatalytic ORR for H_2O_2 production under the single-phase (left) and two-phase (right) systems.

1.1.3 Organic/inorganic semiconductors photocatalysts

Transitioning from conventional single-phase to biphasic reaction systems allows for the spontaneous separation of H_2O_2 from the photocatalyst, thereby improving production efficiency from a kinetic standpoint. However, to accelerate the industrialization of photocatalytic ORR for H_2O_2 generation, fundamental research on catalyst modification remains highly valuable and essential.

Over the past decade, substantial academic research has been dedicated to the development of efficient photocatalysts for H_2O_2 production. Efforts have primarily focused on both inorganic and organic semiconductor materials, as summarized in **Figures 3 and 4**. Inorganic semiconductors, such as TiO_2,[22–24] $BiVO_4$,[25–27] WO_3,[25,28] and CdS,[29,30] are widely recognized for their resistance to chemical and thermal degradation. Moreover, their inherently

high charge mobility enables efficient separation and transport of photogenerated electrons. However, many inorganic semiconductors possess wide bandgaps, for instance, TiO_2 has a bandgap of 3.2 eV, confining its light absorption to the ultraviolet region (approximately 5% of the solar spectrum), which significantly limits its efficiency in solar energy conversion.[31]

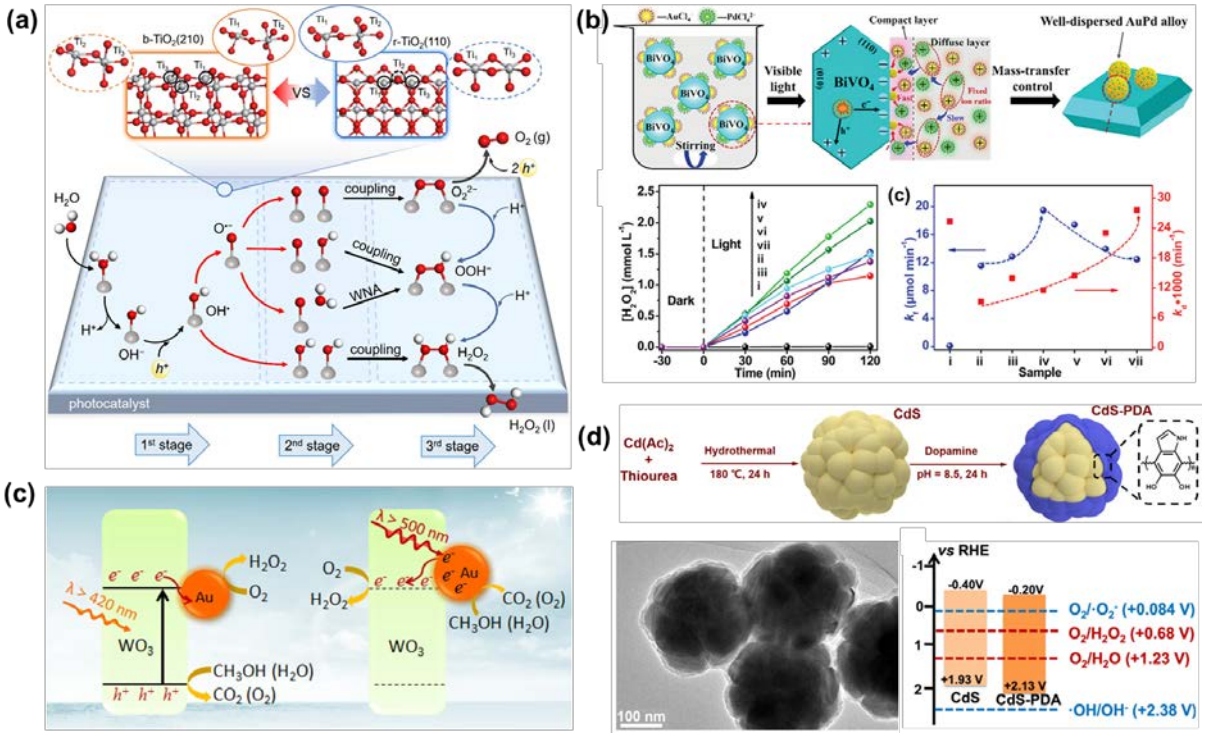

Figure 3. Utilization of inorganic semiconductors in photocatalytic H_2O_2 production.

(a) Coordination configurations of brookite-TiO_2(210) and rutile-TiO_2(110) and the mechanism for photocatalytic H_2O_2 production;[32] (b) Utilization of AuPd alloy as the metal cocatalyst for photocatalytic H_2O_2 production on $BiVO_4$;[27] (c) Possible mechanism for ORR to H_2O_2 under different visible light using the Au/WO_3 catalyst;[28] (d) Synthesis process and energy levels of CdS and CdS–PDA.[33]

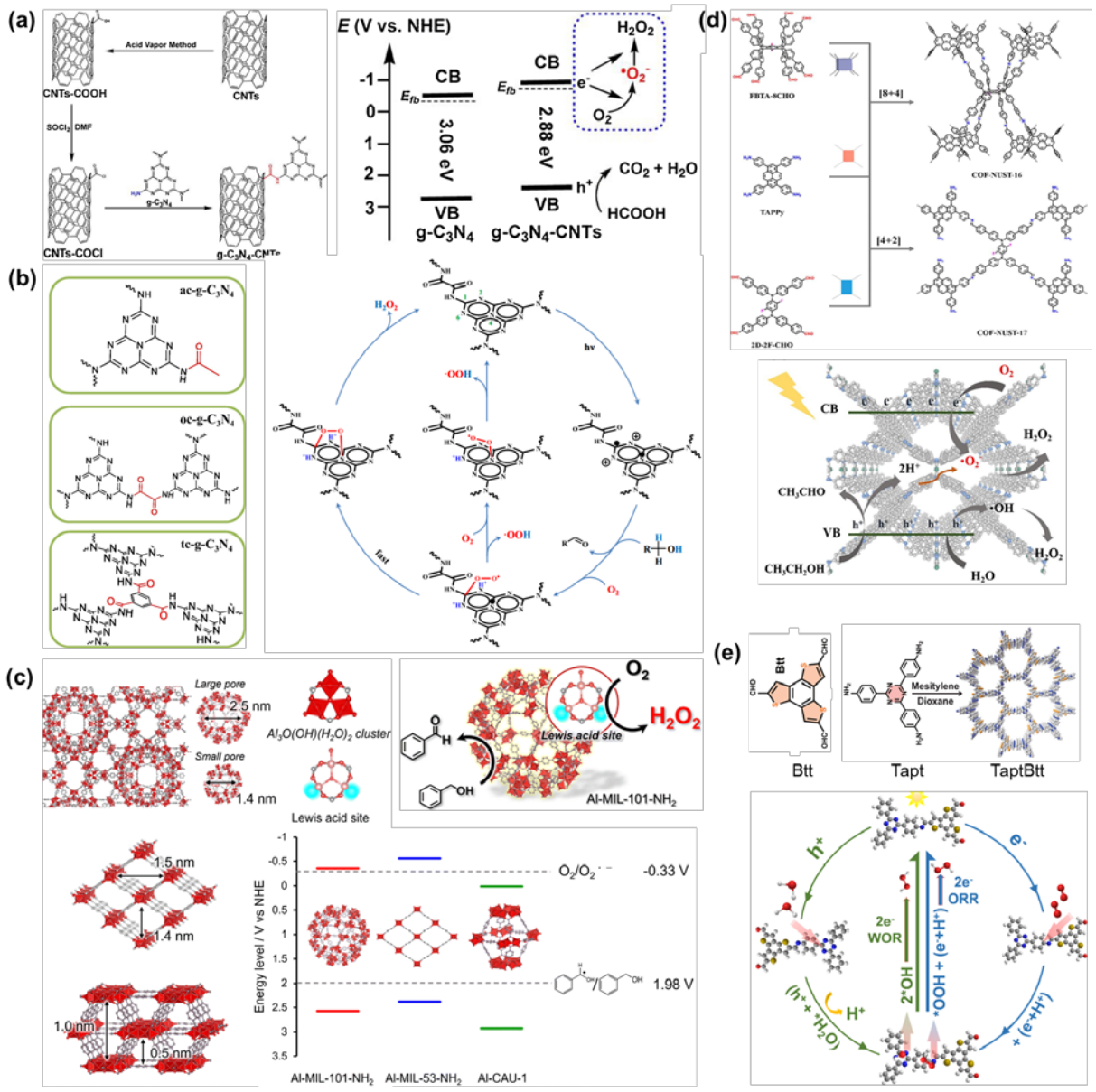

Figure 4. Application of organic semiconductors in photocatalytic H_2O_2 production.

(a) Schematic illustration of the preparation of g-C_3N_4 and g-C_3N_4-CNTs, along with their energy levels and charge transfer pathways;[34] (b) Proposed mechanism of H_2O_2 generation on oc-g-C_3N_4 from alcohol and O_2;[35] (c) Band structures of the Al-MIL-101-NH_2, Al-MIL-53-NH_2, and Al-CAU-1 Al-MOFs;[6] Preparation schematic of (d) COF-NUST-16[36] and (e) TaptBtt COF[37] and their proposed mechanisms of photocatalytic H_2O_2 formation.

In contrast, organic semiconductors with π-conjugated structures, such as g-C_3N_4,[38–41] metal-organic frameworks (MOFs),[42–45] and covalent organic frameworks (COFs),[46,47] demonstrate strong absorption in the visible-light region, making them promising candidates

for solar energy applications. Nevertheless, their chemical stability is generally lower than that of their inorganic counterparts, and they are prone to degradation under high-energy irradiation. Organic materials are typically composed of small organic molecules, metal clusters, or extended conjugated polymer networks arranged in ordered molecular frameworks.[48] These structural characteristics often lead to larger particle sizes, resulting in longer charge transport paths and higher recombination rates of electron-hole pairs.[31]

1.1.4 Functionalization strategies on semiconductor materials

Achieving high H_2O_2 production via photocatalytic ORR fundamentally relies on two interrelated factors: utilization efficiency of solar energy and the quantum yield of the reaction.[49] These are inherently governed by the light-harvesting capability and charge carrier dynamics of the photocatalyst, respectively.

On one hand, strategies such as organic molecule grafting, functional group modification, plasmonic metal incorporation, and facet engineering have been proven effective in boosting the optical absorption of semiconductor materials.[50] First, single-type photocatalysts have been subjected to molecular modification (**Figure 5a**) by incorporating diverse organic units with an abundant π-π stacking system, leading to the formation of novel organic composite materials.[51] For instance, Xia et al.[52] incorporated a two-dimensional NH_2-MIL-53(Al) MOF with tetrakis (4-carboxyphenyl) porphyrin (TCPP) molecules, which improved light absorption and regulated the electronic structure of Al-MOFs. In our previous research, Chen et al.[53] reported that perylenetetracarboxylic diimide (PDI), as one kind of n-type organic semiconductors, could be synthesized onto the MIL-125-NH_2 ligand by substituting its -NH_2 groups. Thanks to its narrow bandgap of 2.5 eV, the obtained MIL-125-PDI exhibited strong visible-light response and excellent charge transportation.

Second, functional groups (e.g., -NH_2, -SO_3H, -C≡N) can be incorporated into the main chain of the catalyst through copolymerization, inducing charge-transfer complexes (**Figure 5b**). Luo et al.[54] introduced sulfonate (-SO_3H) via a post-modification strategy to a conjugated porous polymer (CPP) containing donor-acceptor structures, forming NI-TPA-NI-SO_3H. The

electron-withdrawing -SO_3H groups contribute to the construction of photogenerated electron transfer channels. In addition, Yuan et al.[55] reported that methoxy groups (-OMe), with the electron-donating property, were coordinated with Zr-oxo clusters in UiO-66-NH_2, which contributes to promoted light harvesting and charge separation efficiency.

Third, the localized surface plasmon resonance (LSPR) effect (**Figure 5c**) generated by metal nanoparticles (e.g., Au, Ag, Cu) has been found to boost light absorption and enhance photocatalytic activity by producing hot electrons under LSPR excitation.[56–58] For example, Teranishi et al.[59] found that plasmonic Au-deposition enables TiO_2 visible-light absorption, and that interfacial hot electrons are transferred from smaller to larger Au nanoparticles (NPs) through the CB of TiO_2. Apart from metallic materials, the LSPR effect can also occur in some metal oxides and sulfides with considerable free carrier density.[60] For the first time, Meng et al.[61] found that interfacial charge migration occurs between ZnO and $CuInS_2$ quantum dots (QDs) can transform a near-infrared (NIR) light-active ZnO into a NIR-active composite, attributed to the LSPR effect and the NIR response of $CuInS_2$.

Fourth, by modifying crystal facets, facet engineering significantly influences the catalysts' surface electronic states, light harvesting, and electron mobility. (**Figure 5d**). Cheng et al.[62] reported the precise control over six types of MIL-125-NH_2(Ti) with the exposure of single facet or mixed facets, enabling effective tuning of light absorption properties. Among them, the co-exposure of {111}/{110} facets exhibits the highest photocatalytic activity, benefiting from a surface heterojunction that facilitates efficient interfacial charge migration. In addition, the facet engineering for the host semiconductors can provide a suitable platform for the selective localization of metals and metal oxides on them.[63] For instance, Liu et al.[64] constructed a $BiVO_4$ crystal with {010}/{110} mixed facets exposure, which spatially separate the surface energetics for electron and hole accumulation. This can be achieved by selectively depositing AgPd alloy and CoO_x species on the catalysts to regulate surface reactions.

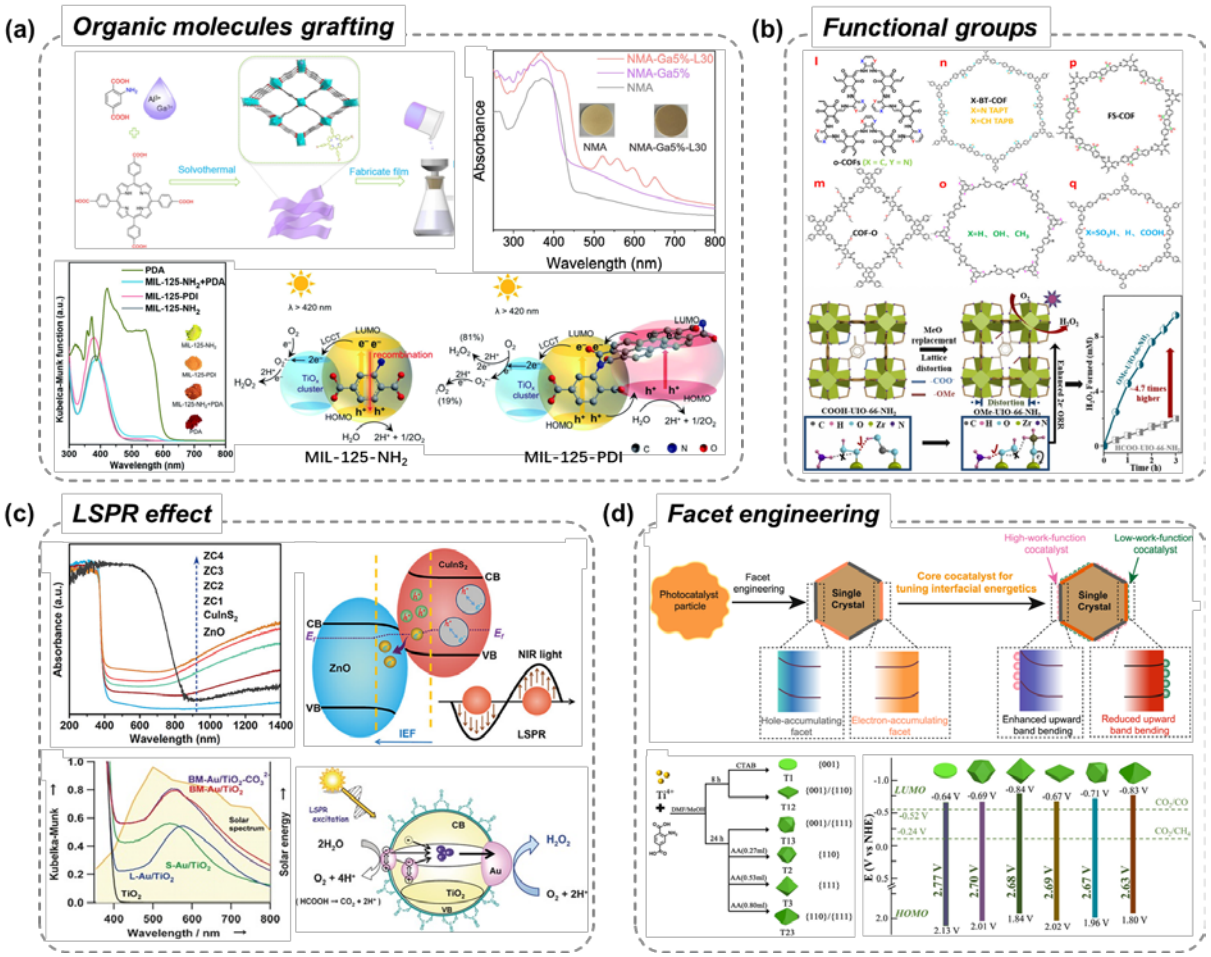

Figure 5. (a) Visible-light responsive MOFs modified by tetrakis (4-carboxyphenyl) porphyrin (TCPP) and perylenetetracarboxylic diimide (PDI);[52,53] (b) Functional groups of COFs and OMe-modified UiO-66-NH_2;[31,55] (c) Photocatalytic H_2O_2 upon the ZnO/$CuInS_2$ heterojunction with LSPR of the NIR light and Au/TiO_2 with LSPR of visible light;[59,61] (d) Approach for interfacial-energetics-tuning on $BiVO_4$ crystal and facet engineering of MIL-125-NH_2.[62,64]

On the other hand, approaches like metal surface modification, heteroatom doping, heterojunctions, and defect engineering are effective strategies to significantly enhance charge separation and transport capabilities on various semiconductor materials (**Figure 6**). First, considerable research has focused on the deposition of metal NPs and their derivatives, like single atoms (SAs), thanks to their enhanced surface properties and high availability of exposed active sites. As shown in **Figure 6a**, Hao et al.[65] designed Ir and Pd SAs-anchored UiO-66-NH_2 with the strong interaction between metal species and the MOF host. The interaction could substantially modulate electronic structures of Ir or Pd species. Besides, our previous work synthesized NiO NPs-deposited MIL-125-NH_2 and applied it for photosynthesis of H_2O_2.[17]

NiO played a bifunctional role, facilitating ORR through its electron-withdrawing characteristics, while also catalyzing water oxidation when water served as the electron donor.

Second, heteroatom doping (**Figure 6b**), such as O, K, Cl, and P, could also facilitate the obvious electronic structure transformation. Zhang et al.[66] incorporated K and Cl atoms in the g-C_3N_4 framework (AKCN), via surface alkalization by KOH and KCl precursors, bridging the interlayers for efficient charge separation. It was observed that charge recombination in AKCN was hindered for prolonging the lifetimes of charge carriers. Moon et al.[67] revealed that polymetric carbon nitride (PCN), modified with multiple earth-abundant heteroatoms such as K, P, and O, achieves remarkably high apparent quantum yield (AQY) in photocatalytic H_2O_2 generation. This multi-element doping strategy facilitates efficient electron transfer to molecular O_2 and inhibits the unwanted decomposition of the H_2O_2 product. Moreover, Liu et al.[68] further observed that O and K co-incorporated PCN accelerates the activation of O_2, facilitating the generation of *OOH intermediate species and lowering the thermodynamic barrier for H_2O_2 formation.

Third, heterojunctions formed between semiconductors (**Figure 6c**), such as type II, S-scheme, and Z-scheme,[69] with staggered band alignments can create internal electric fields (IEF) that drive efficient separation of photogenerated charge carriers and maximize redox power.[70] Ye et al.[71] first developed a Z-scheme heterojunction by coupling zinc polyphthalocyanine (ZnPPc) with modified carbon nitride (NBCN), characterized by well-aligned Fermi levels. This system enables wavelength-dependent control over the electron transfer pathway between type II and Z-scheme mechanisms, providing a new strategy for constructing Z-scheme photocatalysts based on Fermi level alignment. Yang et al.[72] prepared an S-scheme heterojunction composed of TiO_2 and BTTA-COF, which efficiently suppressed electron-hole recombination and boosted the migration of photoexcited electrons with strong redox capacity to surface reactive sites.

Besides the above-proposed strategies, defect engineering (**Figure 6d**) can introduce localized energy states that trap charge carriers, thereby extending their lifetimes and enhancing their likelihood of participating in photocatalytic reactions. Specifically, two-dimensional carbon nitride with a layered structure is an ideal matrix for generating structural vacancies,

like C and N vacancies, attributed to the weak van der Waals forces between layers.[73] Miao et al.[74] designed a g-C_3N_4 with abundant three-coordinate nitrogen vacancies ($N3_C$), where the associated defect states around these sites enhanced the activation and dissociation of O_2 molecules. Besides, introducing unsaturated coordination sites can also modulate the electron transfer efficiency of organic semiconductors. In our previous work, Kondo et al.[45] employed acetic acid as a modulator to create missing-linker defects in UiO-66-NH_2, thereby enhancing the linker-to-cluster charge transfer (LCCT) process.

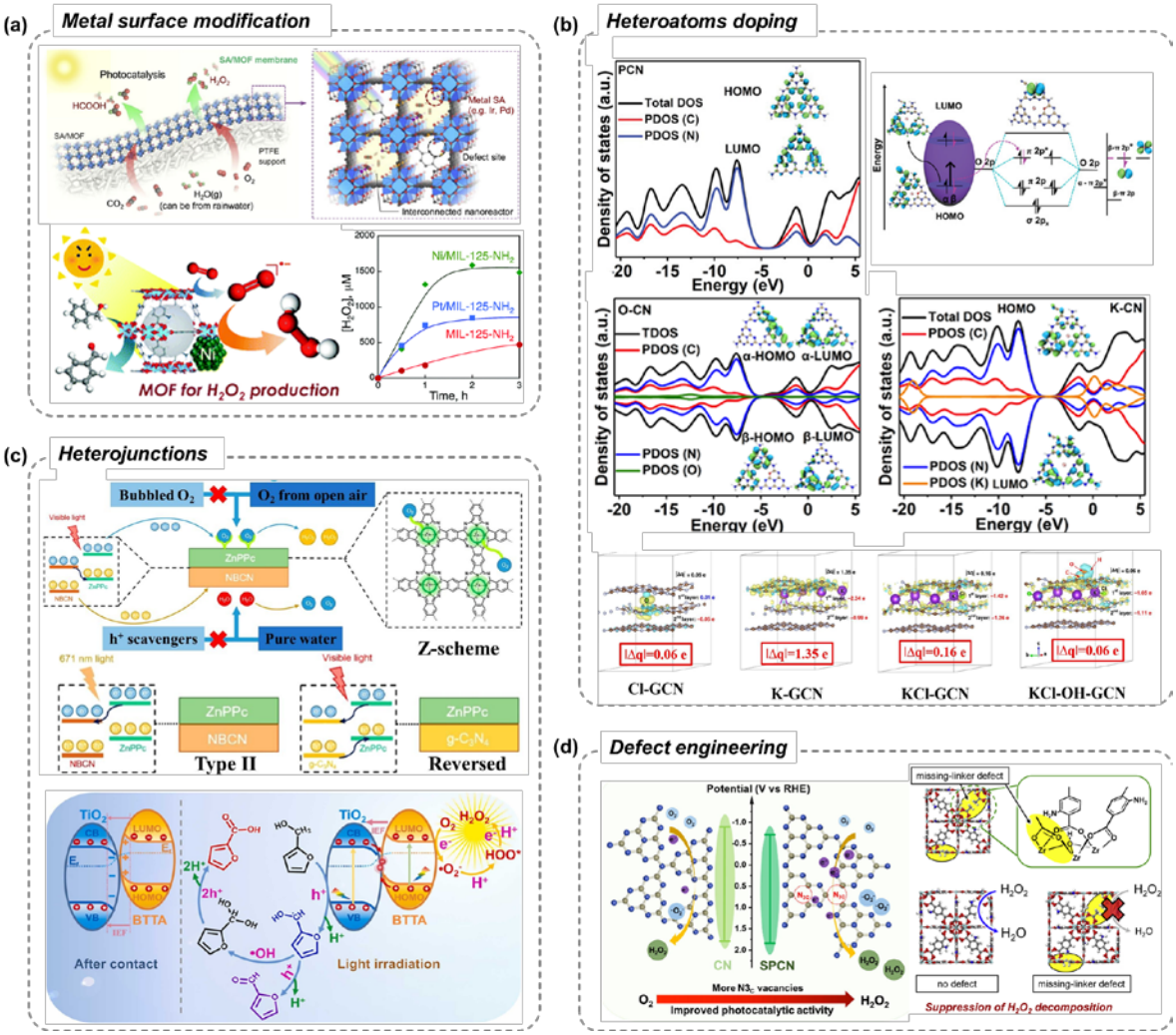

Figure 6. (a) Ir or Pd single atoms-deposited UiO-type MOF membranes and NiO NPs-deposited MIL-125-NH_2;[17,65] (b) Charge distribution of heteroatom-doped g-C_3N_4;[66,68] (c) Schematic diagram of charge transfer mechanisms upon heterojunctions of type II, Z-scheme, and S-scheme;[71,72] (d) Photocatalytic H_2O_2 production over g-C_3N_4 with $N3_C$ vacancies and Zr-MOF containing missing-linker defects.[45,74]

1.1.5 Hydrophobic modification for semiconductors

To apply the above semiconductors into a two-phase system, they should be designed to maintain stably within the organic phase, which suppresses the H_2O_2 decomposition and facilitates the H_2O_2 production in the aqueous phase. Therefore, the optimal hydrophobicity of diverse materials plays a critical role in enhancing the H_2O_2 production efficiency in the biphasic reaction. This was evidenced by the observation that excessive hydrophobicity of catalysts might adversely affect the adsorption and mass transfer of O_2 molecules on their surface in the organic phase.[75,76] Except for inherently hydrophobic materials, some methods of hydrophobic modification were summarized in this section (**Figure 7**), such as perfluroalkyl-fuctionalization,[77,78] alkylation,[42,43,79,80] substitution by fluorine-containing polymer,[81] alkyl-silanization,[82] as well as the construction of missing-linker defect.[45]

As exhibited in **Figure 7a**, our previous work modified Zr-based MOF (Zr-TCPP) with perfluoroalkyl carboxylates with different lengths of alkyl groups, aiming to accelerate the desorption of polar H_2O_2 molecules from the hydrophobic catalyst surface.[77] It was investigated that Zr-TCPP-RF9, owing to the optimized chain length, exhibits a 7.2 times higher activity relative to the pristine hydrophilic Zr-TCPP. Shao et al.[78] developed a superhydrophobic COF photocatalyst (PF-BTTA-COF) by introducing perfluoroalkyl groups through a Schiff-base reaction between unreacted aldehyde sites of BTTA-COF and 1H,1H-undecafluorohexylamine (UFHA).

Besides, Hong et al.[81] synthesized a series of poly(9,9-dioctylfluorene-alt-benzothiadiazole) (PFBT) polymers with fluorine for the hydrophobization of TiO_2 (**Figure 7b**). They found that the hydrophobic polymeric component promotes charge mobility essential for H_2O_2 synthesis and simultaneously suppresses its photodegradation on the catalyst surface through the establishment of a protective repulsion layer.

As for the alkylation strategy, Chen et al.[83] regulated the hydrophobicity of the TiO_2 catalyst by a facile stearic acid modification (**Figure 7c**). The formation of stable ester bonds on the interface promotes O_2 accessibility on the catalyst surface for ORR process. By attaching alkyl chains to the linkers via amide bonds, Kawase et al.[84] modified MIL-125-NH_2 to produce the hydrophobic derivative MIL-125-R7 (**Figure 7d**). However, the one-third decreased

surface area of MIL-125-R7 (560.7 m^2 g^{-1}) compared to that of MIL-125-NH_2 (1498 m^2 g^{-1}) inspired them to use another method, cluster alkylation with octadecylphosphonic acid (OPA). The obtained cluster-alkylated OPA/MIL-125-NH_2 maintained a surface area of 1242 m^2 g^{-1}, due to the unblocked pores, which provide sufficient channels for faster diffusion of $O_2^{\bullet-}$ species.

In addition, an effective hydrophobization of ionic carbon nitride (PHI) was accomplished by Krivtsov et al.[82] through compositing with alkylated silica, yielding the material known as KPHI (**Figure 7e**). They implemented the hydrophobic catalysts into a biphasic system, containing 1-octanol as a lipophilic electron donor for ORR.

Furthermore, Kondo et al.[45] reported that the formation of missing-linker defects in UiO-66-NH_2-X, induced by acetic acid modulation, leads to increased hydrophobicity within the pore environment, which inhibits the H_2O_2 decomposition to H_2O (**Figure 7f**). Specifically, the improved hydrophobicity originates from the structural replacement of hydrophilic 2-aminoterephthalate linkers with hydrophobic acetate groups, which terminate the Zr-oxo nodes in UiO-66-NH_2-X.

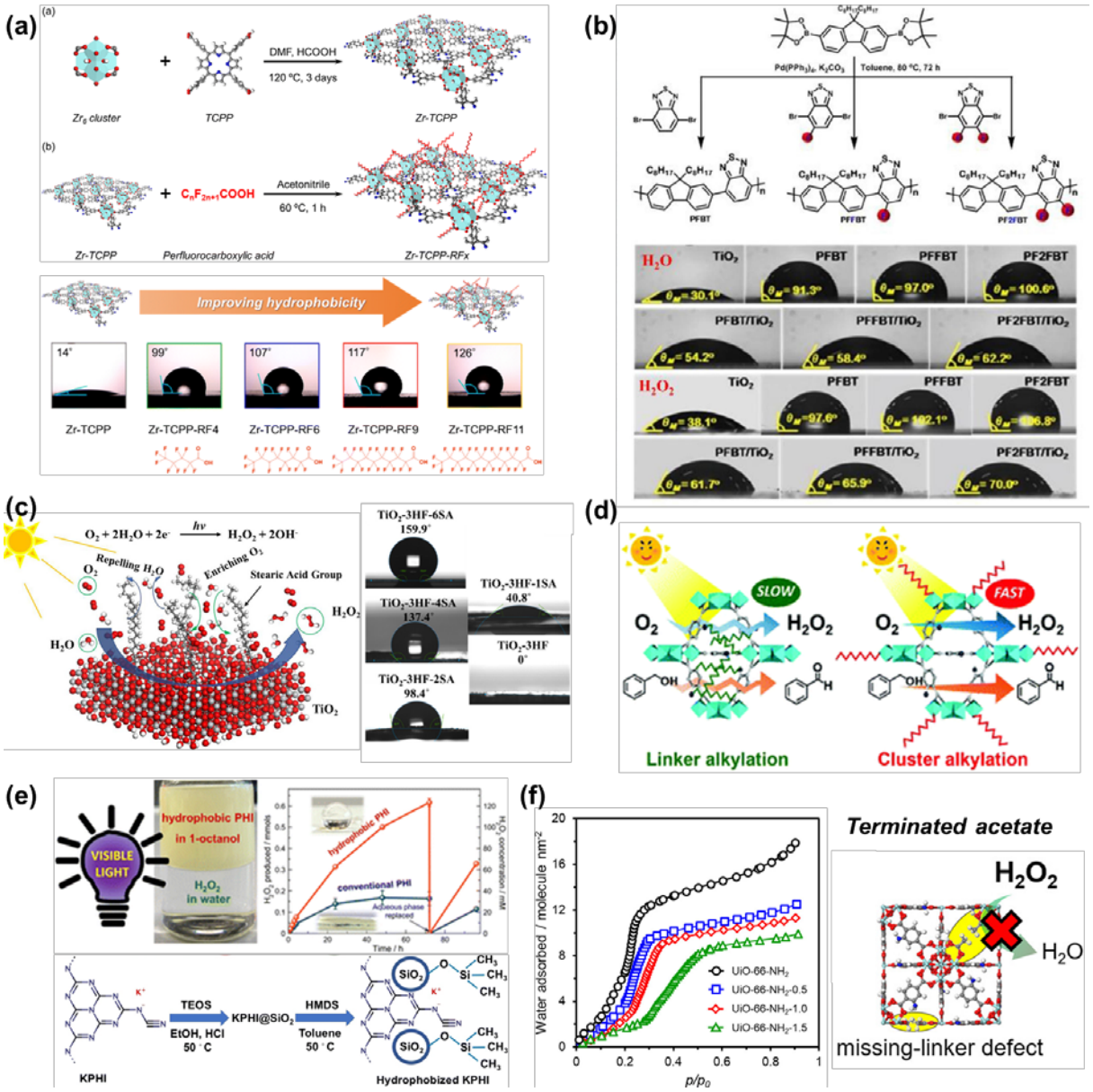

Figure 7. (a) Scheme of the preparation of perfluoroalkyl-functionalized Zr-TCPP-RFx;[77] (b) Hydrophobic modification of TiO_2 with fluorinated polymers;[81] (c) Enhanced hydrophobicity of TiO_2 photocatalyst by a facile stearic acid modification;[83] (d) Linker- and Ti cluster-alkylated hydrophobic MOFs with different mass transfer efficiency;[84] (e) Hydrophobic ionic carbon nitride composite with alkylated silica for photocatalytic H_2O_2 formation in an 1-octanol/water two-phase reaction system;[82] (f) Hydrophobic acetate-terminated UiO-66-NH_2-X with proper missing-linker defects.[45]

1.1.6 Recent advances for photocatalytic ORR in a two-phase system

Until now, there has been a surge in studies focusing on the photocatalytic production of H_2O_2 within the water/oil two-phase system, composed of water and aromatic compounds or aliphatic alcohols. As illustrated in **Scheme 1**, this section summarized various organic/inorganic semiconductors hitherto used in several innovative two-phase reaction systems and their improvement on the H_2O_2 production efficiency.

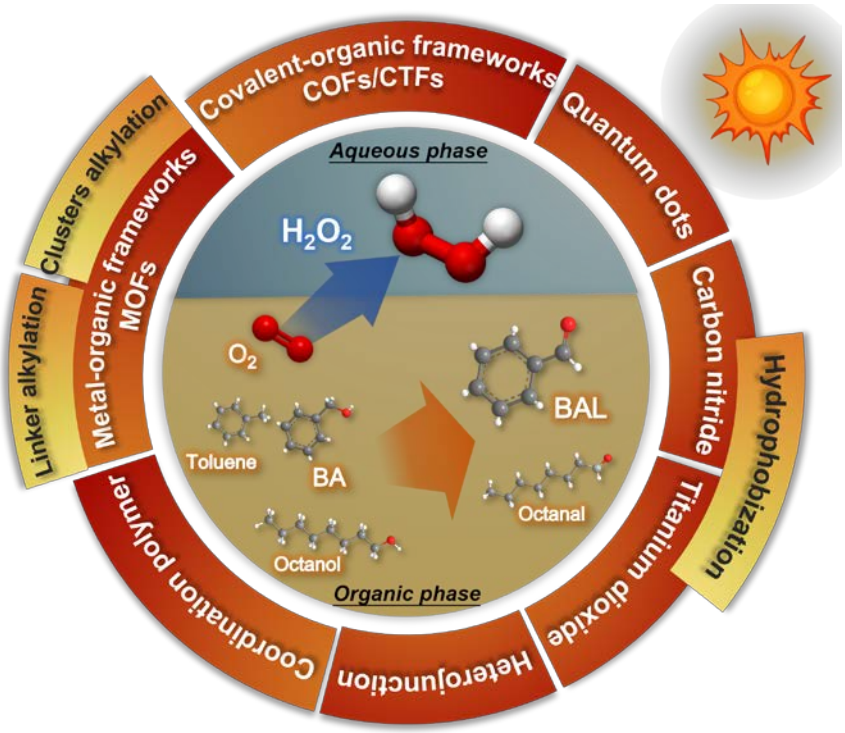

Scheme 1. Applications of inorganic/organic semiconductors in two-phase reaction systems.

1.1.6.1 Benzyl alcohol/water biphase system

As reported, BA as the popular sacrificial agent exhibits more efficient H_2O_2 formation compared to aliphatic alcohols (e.g., methanol, ethanol), owing to the formation of benzyl radicals that are more stable and less likely to undergo side reactions.[85] Using BA as the organic phase of a two-phase reaction system not only retains its effectiveness as a sacrificial agent but also serves to inherently shield the generated H_2O_2 from decomposition by facilitating phase separation.

MOF applications in BA/water phase

MOFs, as a class of porous materials with unique structures, have infinite potentials to create numerous two- or three-dimensional networks with nanoscale-sized pores.[86,87] Our previous work initiated the utilization of hydrophobic MOFs in biphasic photocatalysis. As shown in **Figure 8a**, Isaka et al.[42] carried out post-synthetic modification (PSM) to alkylate the linkers of MIL-125-NH_2, forming the hydrophobic MIL-125-Rn, where n is the number of carbon atoms in the alkyl chain (4 or 7). As expected, MIL-125-NH_2 exists in the aqueous solution of a BA/water two-phase reaction system, while MIL-125-Rn disperses selectively in the BA phase. As a result, MIL-125-R7 exhibits a highly improved H_2O_2 production rate for photocatalytic H_2O_2 synthesis. Moreover, the authors optimized the volume ratio of the H_2O to BA phases to 2:5 (v/v), which demonstrates superior performance compared to ratios of 5:5 and 10:5. Ultimately, the authors attribute the superiority of MIL-125-R7 to the discrepancy in the H_2O_2 decomposition rate. When H_2O_2 and MIL-125-NH_2 exist in one phase, produced H_2O_2 will be photo-reduced into OH^- and •OH, which eventually leads to the stagnation of H_2O_2 production.[88] Therefore, utilization of alkylated MIL-125-Rn in the two-phase system provides a promising thought for suppressing photocatalytic decomposition of H_2O_2, resulting from the partial separation of H_2O_2 and photocatalysts.

In addition, our group further devised an alternative hydrophobic MOF named OPA/MIL-125-NH_2 (**Figure 8b**), where the Ti clusters were alkylated using the OPA molecule.[79] In the case of MIL-125-R7, the introduction of alkyl chains onto the organic linkers results in partial blockage of internal pores, hindering the mass transfer. In contrast, OPA/MIL-125-NH_2 was synthesized through a surface-selective alkylation strategy, where OPA molecules preferentially bind to the exposed $Ti_8O_8(OH)_4$ clusters featuring open coordination sites. This modification is confined to the external surface, thus preserving the intrinsic porosity of the original MIL-125-NH_2 framework. When tested in a biphasic BA/H_2O (5:2) system, OPA/MIL-125-NH_2 exhibited a H_2O_2 productivity of 853 μmol h^{-1} g^{-1} at a catalyst loading of 1 mg mL^{-1}. This performance markedly exceeded that of MIL-125-R7 under the same conditions, ascribed to the unobstructed pore channels in OPA/MIL-125-NH_2. The open

networks facilitate the rapid diffusion of reactants and products, thereby promoting BA oxidation and suppressing the decomposition of the generated H_2O_2.

Based on the advantages of cluster-hydrophobization as mentioned above for Ti-based MOFs, our group subsequently extended the versatility of this approach to Zr-based UiO-66-NH_2, which features excellent structural stability and high porosity.[89–91] Moreover, doping some suitable metal ions into Zr-oxo clusters, serving as electron mediators through the substitution of partial Zr^{4+} ions in Zr-MOFs, is able to enhance the charge separation and mitigate the recombination of photoexcited electrons and holes within the MOF matrix.[92]

Owing to the similar chemical properties between Zr^{4+} and Ti^{4+}, as well as the fact that Ti^{4+} effectively acts as active sites in the photocatalytic reactions,[93,94] our group launched a series of hydrophobic Ti-doped UiO-66-NH_2 catalysts modified with OPA (OPA/$Zr_{100-x}Ti_x$-MOF) as presented in **Figure 8c**.[43] The Ti^{4+}-doping helps suppress the recombination of photoinduced electrons with holes, achieved through the redox reaction of Ti^{4+}/Ti^{3+}. Doped Ti^{4+} ions within clusters capture the photoexcited electrons in the lowest unoccupied molecular orbital (LUMO) of OPA/$Zr_{100-x}Ti_x$-MOF. Subsequently, they are reduced to Ti^{3+} followed by O_2 reduction to produce $O_2^{\bullet-}$ species for H_2O_2 synthesis. Simultaneously, the holes residing in the highest occupied molecular orbital (HOMO) are effectively extinguished through the oxidation of BA. The BA/water two-phase system, which enables the transfer of $O_2^{\bullet-}$ into an aqueous phase separated from the catalysts, also contributes to improving catalytic performance by suppressing H_2O_2 decomposition.

Furthermore, our group conducted research about OPA-modified Fe^{3+}-doped Zr-MOF (OPA/Fe-Zr-MOF) for photocatalytic synthesis of H_2O_2 as illustrated in **Figure 8d**,[80] based on the fact that the electron-donating properties of Fe^{3+} to enhance the metal-to-cluster charge transfer (MCCT).[95] Fe^{3+}-doping endows the UiO-66 Zr-MOF with visible-light responsiveness, as evidenced by UV-vis DRS measurements, and facilitates the generation of electrons that reduce Zr^{4+} species in the clusters to Zr^{3+}. Subsequently, the generated electrons are used for the reduction of adsorbed O_2 to $O_2^{\bullet-}$ species through the redox of Zr^{4+}/Zr^{3+}, while formed Fe^{4+} species from Fe^{3+} are quenched through the oxidation of BA in the two-phase system. In the aqueous phase, for hydrophilic Fe-Zr-MOF, H_2O_2 is produced via the reaction of $O_2^{\bullet-}$ with

protons. Unfortunately, the formed H_2O_2 will be consumed because of the Fenton-like reaction induced by Fe^{3+} ions, in which Fe^{3+} reacts with H_2O_2 to yield superoxide species (•OOH) and hydroxyl radicals (•OH). As for the hydrophobic OPA/Fe-Zr-MOF, the spatial separation of OPA/Fe-Zr-MOF in the BA phase from H_2O_2 in the aqueous phase effectively inhibits the Fenton-like reaction, thereby preventing the consumption of H_2O_2.

In summary, the linker-alkylated MIL-125-Rn, cluster-alkylated OPA/MIL-125-NH_2, OPA-modified Ti-doped UiO-66-NH_2 (OPA/$Zr_{100-x}Ti_x$-MOF), and OPA-modified Fe^{3+}-doped Zr-MOF (OPA/Fe-Zr-MOF) were applied in such BA/water phase. The design of this two-phase system allows for the retention of active $O_2^{\bullet-}$ intermediates, which act as the reactant of disproportionation of $O_2^{\bullet-}$ to H_2O_2 (**Equation 5**).[17] Moreover, higher H_2O_2 concentration was observed under low pH conditions of the aqueous phase. Employing saturated NaCl solution as the aqueous phase led to enhanced H_2O_2 production. This notable surge in activity can be attributed to the strong complexation of $O_2^{\bullet-}$ with Na^+ Lewis acid, resulting in heightened stabilization of $O_2^{\bullet-}$ radicals.[96,97]

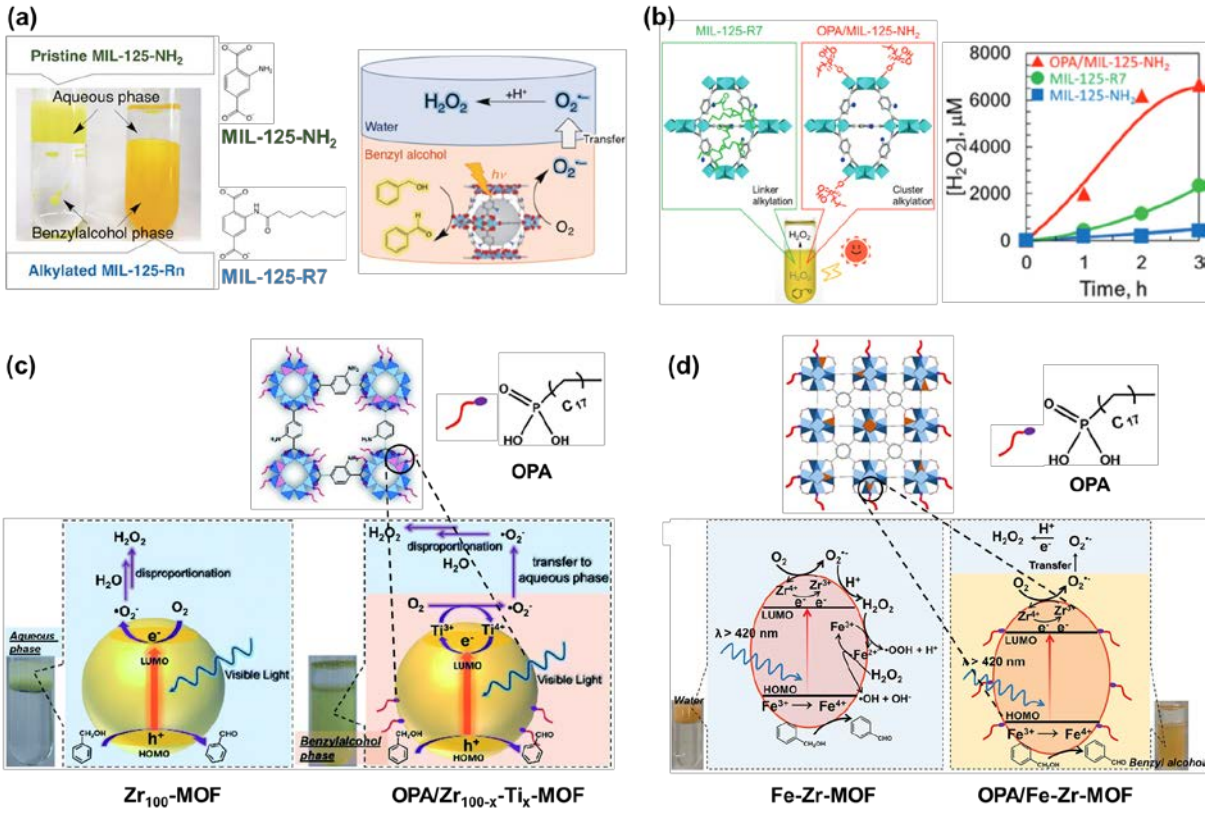

Figure 8. (a) Proposed schematic diagram of photocatalytic H_2O_2 synthesis in the two-phase system over linker-alkylated MIL-125-Rn (n = 4 or 7);[42] (b) Superiority in biphasic photo-catalytic H_2O_2 production over cluster-alkylated MOFs (OPA/MIL-125-NH_2) compared to linker-alkylated MOFs (MIL-125-Rn);[79] Illustrations showing the use of hydrophobic (c) OPA/Zr_{100-x}-Ti_x-MOF[43] and (d) OPA/Fe-Zr-MOF[80] for photocatalytic H_2O_2 production in the water/BA two-phase reaction system.

COF applications in BA/water phase

Besides MOFs, a novel class of metal-free crystalline porous organic polymers, known as COFs, has gained prominence as potential photocatalysts owing to their expansive surface areas, remarkable structural tunability, visible-light harvesting properties, and promising stability.[98–100] To date, a few COFs, such as those based on triphenyl-benzene,[101] triazine,[102] bipyridine,[103] and vinylene-linked triazine,[104] have been explored for their potentials in photocatalytic H_2O_2 production. These COFs exhibit heightened photo-activity for H_2O_2 synthesis, primarily attributed to their exceptionally porous conjugated frameworks coupled

with their capacity for structural customization and designability. Inspired by the design of the biphasic BA/water system as mentioned above, several researchers directed their efforts towards utilizing hydrophobic COFs in the context of photocatalytic H_2O_2 production within a two-phase system.

Zhao et al.[105] developed an imine-based COF (sonoCOF-F2) containing triazine units as shown in **Figure 9a**. Specifically, the triazine unit of sonoCOF-F2, composed of three nitrogen atoms, gave rise to a configuration with both electron-rich and electron-poor sites. This unique arrangement contributes to enhanced charge separation, subsequently resulting in superior photocatalytic activity when compared to the benzene-containing COFs. However, during a long-term stability test exceeding 96 hours in a pure water solvent, the H_2O_2 yield catalyzed by sonoCOF-F2 gradually declines due to the transformation of imine linkages into amide linkages within the COFs, which results in weakened crystallinity and electronic conjugation (**Figure 9b**). Furthermore, the authors observed that the employment of the BA/water system could finely address this problem of imine inactivation. In detail, a higher volume ratio of BA/water phases (9:1) contributes to increased H_2O_2 concentration rate (414.6 mmol h^{-1} g^{-1}), resulting from the higher dispersion of catalysts in the BA phase. Therefore, this two-phase system not only proficiently protects the imine-based COF catalysts from oxidation, caused by photogenerated holes or $O_2^{\bullet-}$ radicals, into inactive amide-linked COFs, but also allows for the spontaneous segregation of the H_2O_2 and BAL products.

In addition to the electron-rich interaction of the triazine moiety, which contributes to the superior catalytic performance in biphasic photosynthesis of H_2O_2, pyrene-based COFs have also been studied. Their stacked π-π conjugated structure leads to a narrower HOMO-LOMO gap, and the pyrene units are regarded as active reduction centers.[106,107] Inspired by the structural features of pyrene, Sun et al.[108] designed four imine-linked COFs with varying degrees of π-conjugation. Among them, Py-Py-COF, incorporating pyrene units, exhibits comparable surface areas and the most active pyrene moieties. However, Py-Py-COF exhibits lower photoactivity under irradiation of $\lambda > 420$ nm in the aqueous phase compared to other pyrene-contained COFs with fewer pyrene units as presented in **Figure 9c**. The authors concluded that the generated H_2O_2 undergoes decomposition on the surface of Py-Py-COF

rather than diffuses into water, as supported by the notably rapid decomposition rate of H_2O_2 observed in **Figure 9d**. Therefore, the closely spaced and abundant pyrene active sites within Py-Py-COF induce undesired H_2O_2 decomposition, a challenge that can be addressed by implementing a two-phase system, as illustrated in **Figure 4e**. Similarly, Py-Da-COF disperses in the BA phase with the concentration of 1 mg mL^{-1}, which yields H_2O_2 with a producing rate of 1242 μmol h^{-1} g^{-1}, two times higher than that observed in the water phase. A more uniform distribution of Py-Da-COF in the organic phase was realized by modifying the water-to-BA ratio to 1:1, thereby increasing the cumulative H_2O_2 output by 37%.

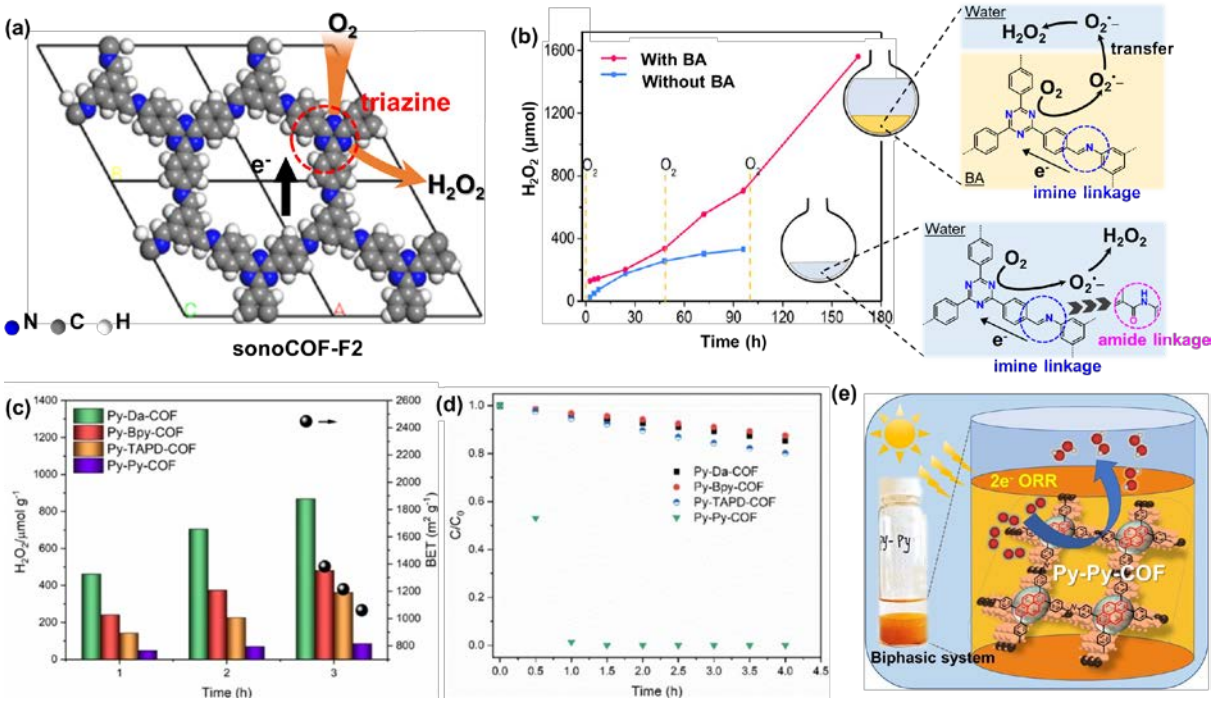

Figure 9. (a) Proposed schematic for the photocatalytic formation of H_2O_2 using the triazine-containing COF (sonoCOF-F2); (b) The H_2O_2 concentration during long-term stability test and reaction mechanism of sonoCOF-F2 for photocatalytic H_2O_2 production in aqueous phase and two-phase systems;[105] (c) Photoactivity and (d) time course of H_2O_2 decomposition on pyrene-based COFs for H_2O_2 production in water under light irradiation; (e) Schematic diagram for photocatalytic H_2O_2 synthesis of Py-Py-COF in a biphasic system.[108]

For the sake of synthesizing COFs with robust structures and linkages, the one-pot multi-component reactions process (MCR) is thought as a facile synthetic approach to achieve the formation of chemically stable COFs.[109] Das et al.[110] reported the one-pot synthesized COF (PMCR-1) with quinoline-linkages and the pending phenyl moieties inside the micropores, and its application in the photocatalytic H_2O_2 production within BA/water system. As illustrated in **Figure 10a**, although PMCR-1 is able to produce high amounts of H_2O_2 in water with the rate of 1445 μmol h^{-1} g^{-1}, the arrangement of BA/water two-phase system brings a marked increase of H_2O_2 production, which reaches 5500 μmol h^{-1} g^{-1} with 5 mg mL^{-1} of PMCR-1 dispersing in the water/BA (volume ratio of 10:1) medium. On one hand, this significant improvement is attributed to the strong π-π interaction between the introduced BA molecules and the pending benzene rings within the pores of PMCR-1 (**Figure 10b**), leading to the efficient hole transfer for BA oxidation. On the other hand, the hydrophobic PMCR-1 remains in the BA phase, separating from the formed H_2O_2 in the aqueous phase, which plays a vital role for the suppression of H_2O_2 decomposition. Furthermore, the authors investigated the versatility of the selective oxidation of benzyl amines and thiols (**Figure 10b**) in two-phase photocatalytic systems comprising water/benzyl amine and water/benzyl thiol. This expanded exploration broadens the scope for designing other novel binary systems in the context of photocatalytic production of H_2O_2 or even other photoexcited reactions.

Besides, Shang et al.[111] reported the application of carboxy-functionalized quinoline-linked COF (COF-COOH) in the BA/water photo-reaction system for H_2O_2 production. The incorporation of Au nanoclusters (Au NCs) within the pores of COF-COOH enhances the yield of H_2O_2. The formation of COF-O-Au bonds optimizes the energy band structure of Au@COF (**Figure 10c**) and accelerates the migration efficiency of photogenerated carriers. **Figure 10d** shows the photocatalytic activity of Au@COF in single- and dual-phase solutions containing different electron donors. Notably, the BA/water biphasic system produced up to 1893 μmol within 1 hour when catalyzed by Au@COF at a concentration of 1 mg mL^{-1}. This corresponds to a production rate of 18933 μmol h^{-1} g^{-1}, far exceeding the rates observed in single-phase systems using aqueous solutions of methanol, ethanol, or isopropanol. This enhanced activity is attributed to the limited catalytic decomposition of H_2O_2 by Au@COF present in the BA

phase, which enables BA molecules to be oxidized quickly by the photoexcited holes. The electrons of COF-COOH are easily transported to Au NCs via the COF-O-Au bridge bonds and participate in the ORR process as illustrated in **Figure 10e**. Moreover, the HOMO potential of BA (-5.590 eV) makes it easier to lose electrons compared to other fatty alcohols and provides abundant protons for H_2O_2 production.[112]

The aforementioned studies primarily focus on the two-phase photosynthesis of H_2O_2 reaction where the photocatalysts are situated in the organic phase. There has been research conducted by Yang et al.[113] according to the weakly hydrophilic acetylene-based COFs at the interface between BA and water. The authors designed COF-TAPB-BPDA, featuring benzene-acetylene frameworks, which exhibits more suitable band structures and stronger driving force to produce H_2O_2 thermodynamically than the corresponding triazine-containing COFs (COF-TAPT-BPDA and COF-TAPP-BPDA) as depicted in **Figure 10f**. COF-TAPB-BPDA exhibits a superior H_2O_2 production rate of 1240 μmol h^{-1} g^{-1} with a concentration of 1 mg mL^{-1} in the two-phase solution (**Figure 10g**). Furthermore, the -OH groups on these COFs impart appropriate hydrophilicity, as evidenced by a water contact angle of approximately 88^o (**Figure 10h**). This moderate hydrophilicity facilitates the efficient mass transfer of H_2O and O_2 molecules from the water phase to the COF surface in the two-phase system, thereby promoting H_2O_2 formation.

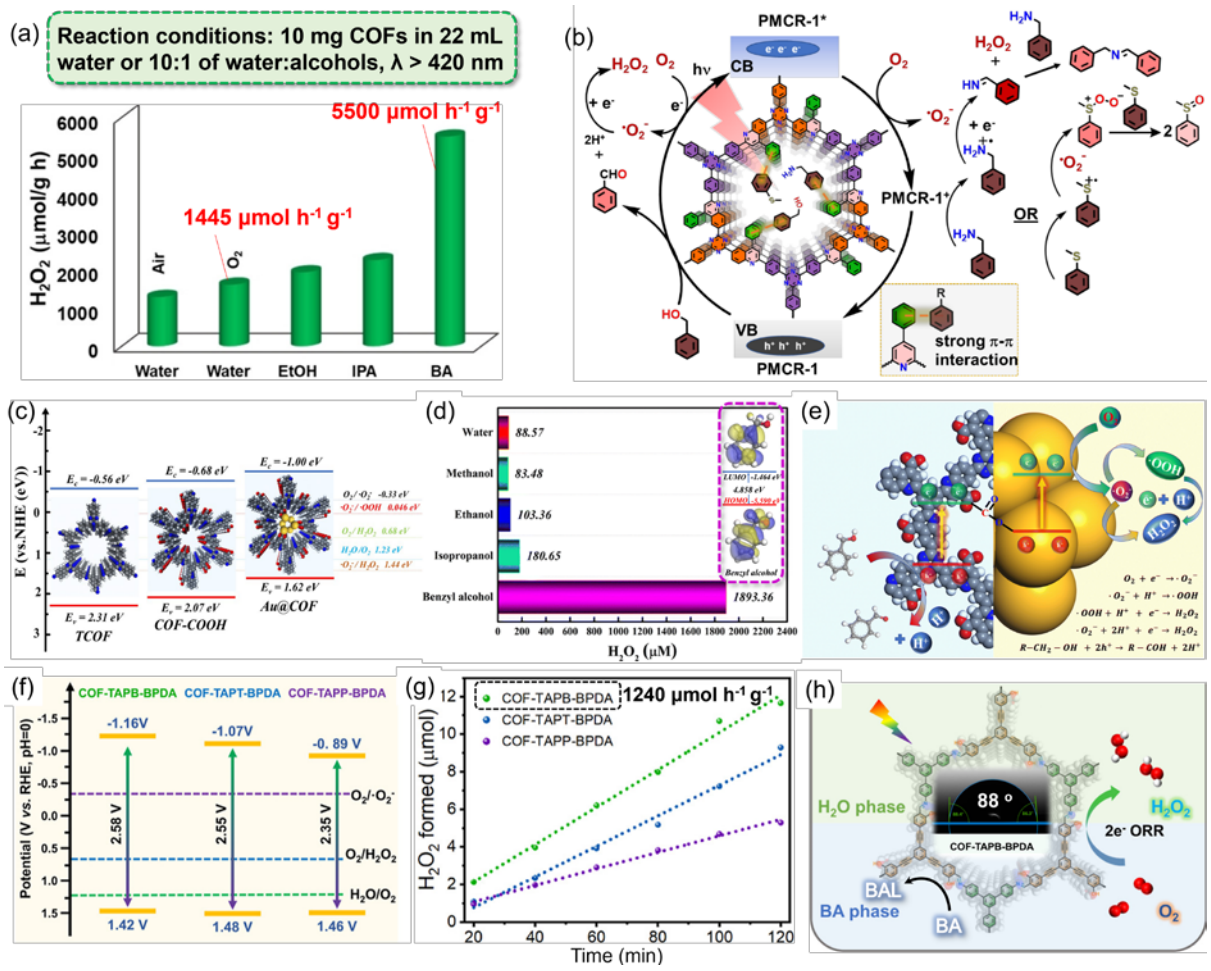

Figure 10. (a) Photocatalytic H_2O_2 production rate using PMCR-1 COF in water or water with different sacrificial agents; (b) Reaction mechanism catalyzed by PMCR-1 with different electron donors;[110] (c) Band structure diagram of TCOF, COF-COOH, and Au@COF; (d) H_2O_2 generation using Au@COF in pure water (pH = 3) with different sacrificial agents under simulated sunlight irradiation, with the insert showing calculated HOMO and LUMO energies of BA; (e) Reaction mechanism of photoinduced H_2O_2 production and photogenerated electrons migration route using Au@COF;[111] (f) Proposed band structure diagrams of covalent benzene-acetylene frameworks and (g) their H_2O_2 formation within a two-phase system; (h) Schematic drawing of photocatalytic H_2O_2 formation in BA/water two-phase system with weakly hydrophilic COF-TAPB-BPDA.[113]

Other semiconductors in BA/water phase

There are still several semiconductor-like compounds employed in such BA/water two-phase systems, with quantum dots (QDs), coordination polymer (CP), and heterojunction summarized in this section.

QDs have emerged as promising photocatalysts for ORR because $O_2^{\bullet-}$ radicals could be generated on the surface of QDs under an aerobic atmosphere when exposed to visible light.[114,115] Ji et al.[116] achieved a remarkable milestone in photocatalytic H_2O_2 production within the BA/water system, reaching a production rate of 61 mmol L^{-1} h^{-1}. This exceptional result was obtained using CdSe-based core/shell QDs as depicted in **Figure 11a**. In the BA phase, the electrons were activated from the CdSe QDs core under visible light and reacted for O_2 reduction on the surface of QDs. However, QDs are suffering from deterioration due to gathering or etching during irradiation, which is a challenge that can be overcome by the epitaxy of CdS. The extended CdS shell serves to eliminate the surface defects of the QD core, consequently promoting the utilization of photogenerated carriers. Unfortunately, since the easy oxidation of the CdS shell, the photostability of CdSe/CdS core-shell QDs remains inadequate. Therefore, the structure of ZnS-covered CdSe/CdS core-shell QDs (CdSe/CdS/ZnS) was eventually elaborated, considering the excellent stability and broad energy level of ZnS. Furthermore, the implementation of a BA/water two-phase system for photoinduced H_2O_2 production, employing CdSe/CdS/ZnS QDs, resulted in an exceptional lifting in H_2O_2 concentration, approximately 630 times higher than that in a single-phase system shown in the embedded chart of **Figure 11a**. Such an improvement serves as explicit evidence of the significant role that a two-phase system plays in the photocatalytic ORR.

Additionally, organometallic CP was also used as photocatalysts for the two-phase H_2O_2 production. As illustrated in **Figure 11b**, Zhu et al.[117] directly synthesized the hydrophobic Ag-based CP (silver phenyl acetylide, PhC_2Ag), rather than via post-hydrophobic modification, dispersing in the organic phase of the BA/water system. During the photocatalytic reaction, the electrons were activated by light irradiation to transfer to the CB of PhC_2Ag, participating in the reduction of O_2 to $O_2^{\bullet-}$ species. Similarly, $O_2^{\bullet-}$ species migrated from the BA phase to the aqueous phase for the indirect 2e-ORR process, inhibiting the over-reduction by $O_2^{\bullet-}$ radicals.

Meanwhile, the photoinduced holes were preferentially quenched through the BA oxidation to BAL. Notably, the authors also explored how varying the volume ratio of BA and water phases, as well as the pH values in the aqueous phase, affected the H_2O_2 production efficiency. A rise in the H_2O_2 yield was achieved as the volume of the aqueous phase decreased. Furthermore, a pH-dependent increase in the H_2O_2 concentration was observed with the highest activity for pH 1, attributed to the reliance of proton-coupled electron transfer processes (**Equations 2, 3 and 5** in **Figure 2**) on the concentration of protons.

Li et al.[118] reported the fabrication of a Co-based heterojunction photocatalyst (denoted as Co_9S_8-$CoZnIn_2S_4$), composed of discrete Co_9S_8 NPs deposited onto Co-based $ZnIn_2S_4$, and its utilization in BA/water system for photoinduced H_2O_2 production. As depicted in **Figure 11c**, in contrast to the above studies, the hydrophilic Co_9S_8-$CoZnIn_2S_4$ existing in the aqueous phase seems to be more advantageous than hydrophobic Co_9S_8 in terms of H_2O_2 production, despite the formed H_2O_2 will be cleaved to •OH radicals. Regarding this contradiction, the authors explain that the synergistic effects of Co-doping and Co_9S_8-$CoZnIn_2S_4$ heterojunction formation, evident in the interfacial lattice match between Co_9S_8 and $CoZnIn_2S_4$, mainly contributing to the photocatalytic performance.

Except for exploring the inherent properties of catalysts, the authors used the abundant seawater resource to establish the present two-phase system with BA solution. They also investigated the influence of various soluble metal cations, including Na^+, Sr^+, K^+, Mg^{2+}, and Ca^{2+}, on the H_2O_2 synthesis. It is evident that a higher concentration of metal cations enhances the H_2O_2 production, attributable to the electron sink effect of Co_9S_8-$CoZnIn_2S_4$ surrounded by metal cations, which facilitates the two-electron reduction pathways of O_2.[119] In such a two-phase system, the photocatalytic reaction mechanism of Co_9S_8 (**Figure 11d**) is similar to that of the MIL-125-NH_2 catalyst mentioned before. In contrast, Co_9S_8-$CoZnIn_2S_4$ facilitates the formation of H_2O_2 through the indirect 2e-ORR in the aqueous phase, and partially produced H_2O_2 is decomposed into •OH radicals, which are transferred into the BA phase and enable the production of BAL (**Figure 11e**). This strategy of heterojunction establishment is expected to provide valuable insights for the systematic design of high-performance catalysts for concurrent photocatalytic reactions.

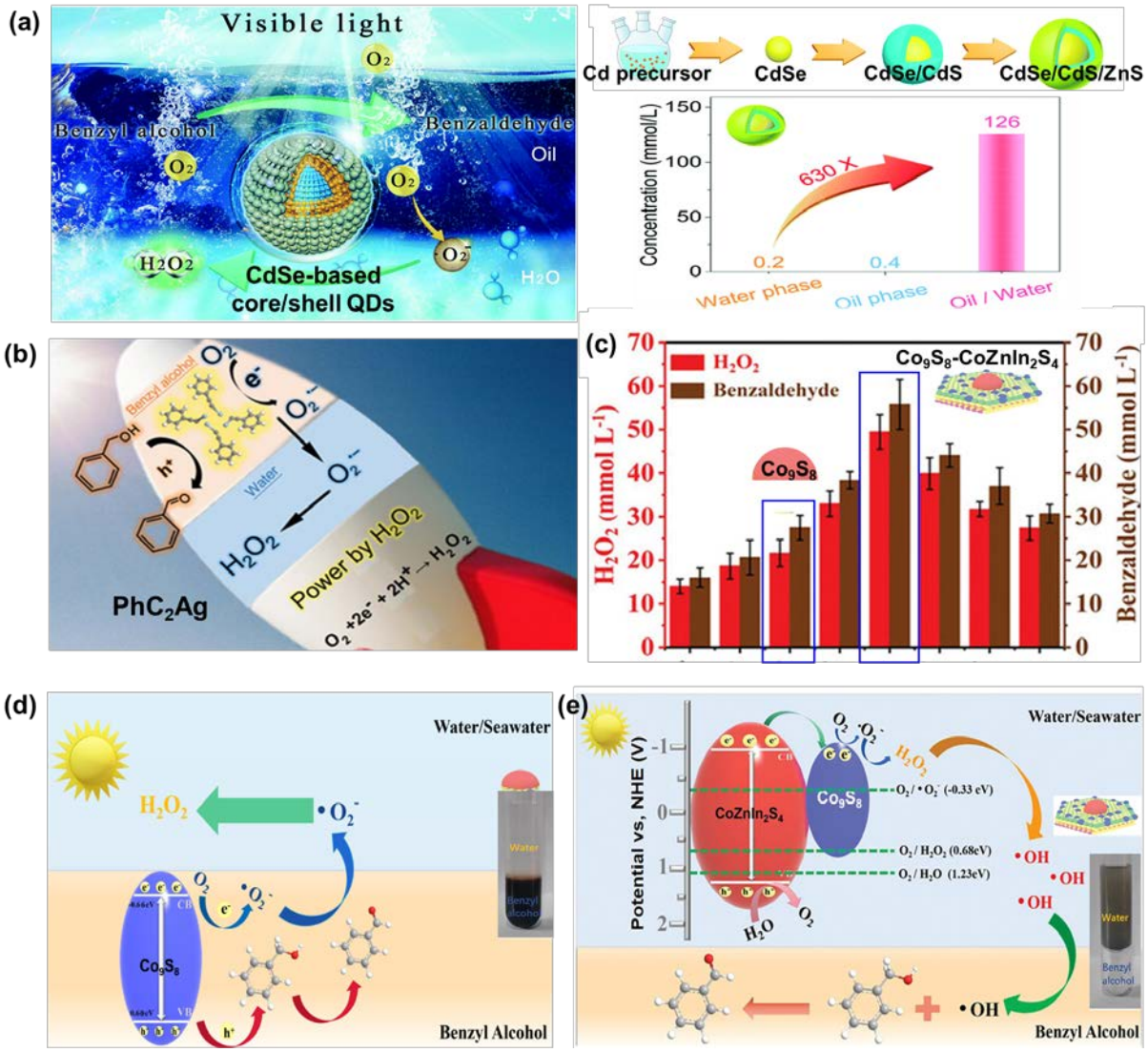

Figure 11. (a) Synthesis process of CdSe/CdS/ZnS and H_2O_2 concentration over CdSe/CdS/ZnS in single and two-phase systems, and proposed schematic diagrams for the photocatalytic co-production of H_2O_2 and BAL in a two-phase system over CdSe-based core/shell quantum dots;[116] (b) Proposed reaction mechanism of the biphasic photosynthesis of H_2O_2 over Ag-based coordination polymer (PhC_2Ag) photocatalysts;[117] (c) H_2O_2 and BAL concentration of Co-based heterojunction materials in two-phase system and proposed mechanisms of (d) hydrophobic Co_9S_8 and (e) hydrophilic Co_9S_8-$CoZnIn_2S_4$ for the biphasic photocatalytic H_2O_2 synthesis.[118]

1.1.6.2 Toluene/water biphase system

Recently, several researchers queried that the source of the summarized high H_2O_2 production rate in the BA/water two-phase system mostly depends on the BAL-induced auto-photocatalytic process of BA molecular for H_2O_2 production, rather than on the photocatalytic activity of heterogeneous photocatalysts.[120–122] As presented in **Scheme 2**, the BAL impurity existing in BA solution could act as a photocatalyst and contribute to the oxidation process from BA and O_2 even under visible light irradiation ($\lambda > 420$ nm).[120] Note, however, the autocatalysis of BA has been demonstrated to have little impact on H_2O_2 concentration in the overall system under visible light illumination,[122,123] as indicated by the monitored BAL and H_2O_2 yields in the blank contrast experiment without any photocatalysts.[120] Furthermore, several unquestioned electron donors, such as toluene and 1-octanol organic solutions, were employed to constitute the dual phases alongside the aqueous phase.

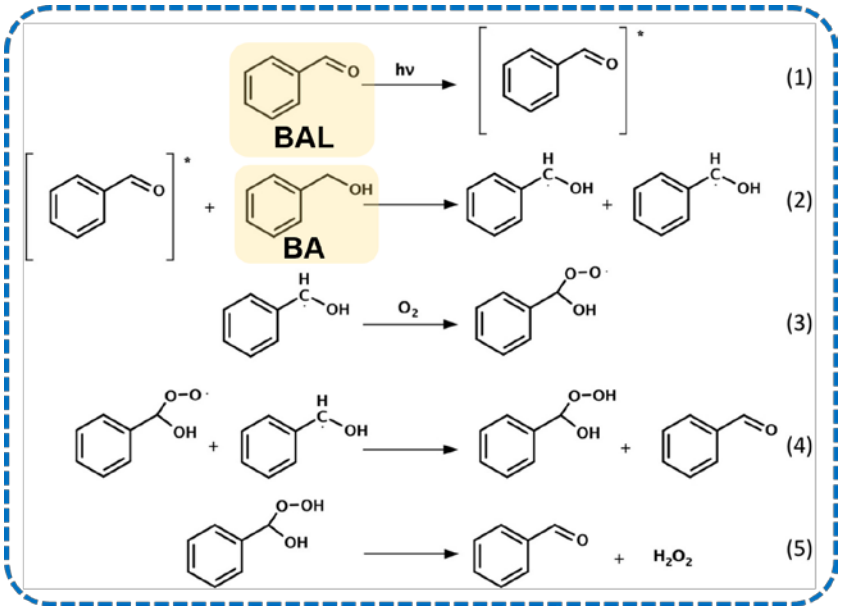

Scheme 2. Proposed reaction mechanism of auto-photocatalytic oxidation process for H_2O_2 production in the BA-BAL system.[120]

As illustrated in **Figure 12a**, the operation of a toluene/water biphasic solution brought an alternative dual-phase solvent system, in which the real performance of photocatalysts could be unambiguously evaluated. Vibbert et al.[124] developed a direct photosensitization of anthraquinone (AQ) for H_2O_2 production upon this biphasic system. The synthesized H_2O_2 was

subsequently accumulated in the aqueous phase with the oxidized product of BAL remaining in the toluene phase, contributing to the on-demand H_2O_2 yield with sustainable solvents.

Inspired by this concept, Kumar et al.[125] constructed a cooperative reaction system of ORR process and toluene oxidation reaction for H_2O_2 production, which are initiated by promising covalent triazine frameworks (CTFs) materials with tunable photophysical properties. As exhibited in **Figure 12b**, the different chemical structures between thiophene-linked CTF-Th and phenyl-linked CTF-Ph result in a diverse yield of H_2O_2 in the organic media including toluene and acetonitrile. This superiority of CTF-Th in H_2O_2 production is attributed to the thiophene donor linkers of CTF-Th, which support the higher interaction of thiophene with both toluene and O_2 molecules, based on the results of DFT binding energy calculations. Moreover, the toluene/water dual-phase setup was employed for the feasibility test and achieved the H_2O_2 yield of 37.8 μmol for 3 h along with a production rate of 630 μmol h^{-1} g^{-1} in the lower layer of the dual-phase system under simulated sunlight irradiation. Although the solar to chemical conversion (SCC) efficiency of CTF-Th is quite low (0.02%), this design of toluene/water dual-phase medium simplifies the separation of toluene oxidization product of BAL and reduction product of H_2O_2, selectively transporting to the aqueous phase, which can produce the cleaner H_2O_2 solution with high purity.

1.1.6.3 Octanol/water biphase system

Except for aromatic alcohols, the long-chain aliphatic alcohols like 1-octanol are also suitable for the construction of a biphasic system for photochemical H_2O_2 formation, which are readily obtained from biomass-derived chemicals.[126–128]

Recently, a kind of well-designed hydrophobic ionic carbon nitride (KPHI) nanoparticles, in the form of PHI and methyl- and alkylsilane-linked silica (**Figure 12c**), was achieved for the first time by Krivtsov et al.[82] and applied in the 1-octanol/water dual-liquid photocatalytic reaction system for producing H_2O_2. As depicted in **Figure 12d**, hydrophilic KPHI and KPHI-Si (silica-modified KPHI) catalysts located in the aqueous layer with 0.5M HCl solution, while hydrophobized KPHI (KPHI-HMDS) dispersed in the 1-octanol organic phase. The H_2O_2

production behavior of hydrophilic materials upon biphasic conditions, involved in a 1-octanol/water ratio of 5:5 (v:v), approached stabilization during 72 h-reaction, with a final concentration of 0.05 mol L^{-1} (**Figure 12e**). This suggests that equilibrium was reached between the H_2O_2 formation and decomposition processes in the aqueous phase. In contrast, the hydrophobic material of KPHI-HMDS exhibits continuously enhanced H_2O_2 concentration without limitation during the long-time illustration process. Benefiting from the separation of KPHI-HMDS and formed H_2O_2, the photo-redox decomposition of H_2O_2 was inhibited and its concentration reached 0.12 mol L^{-1} after reaction for 72 h.

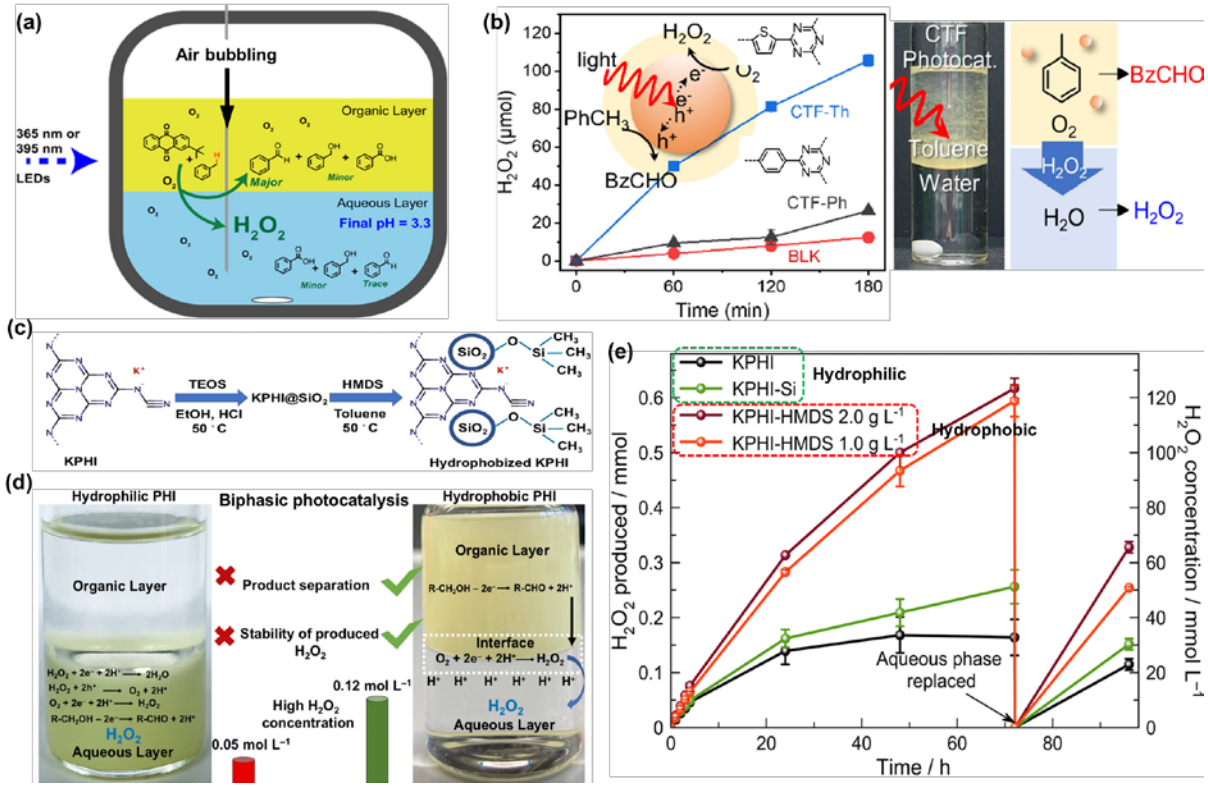

Figure 12. (a) Photochemical H_2O_2 synthesis from anthraquinone in toluene/water biphasic solution under 365 nm LED irradiation;[124] (b) Photocatalytic H_2O_2 production on CTF-Ph and CTF-Th in the single phase (toluene/acetonitrile) under simulated sunlight; Schematic diagram of CTF-Th in the toluene/H_2O dual-phase system;[125] (c) Silylation treatment on hydrophilic potassium poly(heptazine imide) (KPHI) to silica-hydrophobized KPHI material (KPHI-Si); (d) Proposed reaction mechanism of biphasic (1-octanol/H_2O) photosynthesis of H_2O_2 using hydrophilic and hydrophobic PHI and (e) their H_2O_2 production activities under 406 nm LED light excitation.[82]

1.1.6.4 Fluorocarbon/water biphasic system

Besides, Sun et al.[129] developed a special biphasic system comprising a super amphiphobic fluorocarbon (FC) phase and a water phase. For the photocatalyst, a hydrophobic COF, named TTBA, was constructed by condensing (1,3,5-triazine-2,4,6-triyl) tribenzaldehyde (TTB) with (1,3,5-triazine-2,4,6-triyl) trianiline (TTA), both containing triazine-based cores (**Figure 13a**). Notably, perfluoroalkanes, used as the FC phase, are a class of highly non-polar solvents that are immiscible with both water and conventional organic liquids.[130] As illustrated in **Figure 13b**, the superhydrophobic nature of fluorocarbons contributes to the formation of a stable FC-H_2O interface, enabling hydrophobic TTBA to be selectively located at this boundary.

Moreover, this biphasic configuration facilitates the formation of a thin air layer at the interface among the FC phase, the hydrophobic photocatalyst surface, and the aqueous phase. By leveraging the high oxygen solubility of the FC phase and the ultrafast mass transport facilitated by the interfacial gas layer, the system significantly boosts H_2O_2 production. Under visible light irradiation and without the use of sacrificial agents, it achieves a yield of 4.9 mmol g^{-1} h^{-1} (**Figure 13c**). This performance is more than six times greater than that of a conventional O_2/H_2O single-system setup, which yields only 0.8 mmol g^{-1} h^{-1} under comparable conditions.

DFT calculations reveal that the ORR on the TTBA framework proceeds with a remarkably low energy barrier. Consequently, the rapid O_2 diffusion enabled by the FC/H_2O biphasic interface is identified as a key factor in achieving enhanced photocatalytic efficiency for H_2O_2 generation.

1.1.6.5 Continuous trifluorotoluene/water biphasic field system

Photocatalytic synthesis of H_2O_2 offers a promising route toward sustainable and decentralized production. The design of catalysts and reaction systems above shows advantageous H_2O_2 production efficiency. Unfortunately, most investigations remain limited to laboratory-scale batch reactors, which are inherently unsuited for continuous operation. Herein, Shao et al.[78] introduced a biphasic fluidic system enabling both efficient H_2O_2

generation and real-time extraction under continuous flow conditions. As shown in **Figure 13d**, the authors selected a structure-stable BTTA-COF as the photocatalyst, synthesized through a Schiff-base condensation between a tritopic amine monomer (TAPT) and a tetratopic aldehyde precursor (BTDIPA). BTTA-COF was subsequently grafted with perfluoroalkyl chains for superhydrophobicity, forming a PF-BTTA-COF catalyst. In addition, a TFT/H_2O two-phase system, containing water phase and α,α,α-trifluorotoluene (TFT) as oil phase, was constructed as the foundation of a fluid system for H_2O_2 photosynthesis. **Figure 13e** exhibits the selective dispersity of PF-BTTA-COF in TFT solvent rather than in water.

In the TFT/H_2O biphasic fluid system (**Figure 13f**), O_2-saturated organic and aqueous phases containing PF-BTTA-COF are pumped into a T-junction mixer via independently regulated peristaltic pumps. This mixing strategy enabled the formation of discrete and stable oil-water biphasic droplets within transparent microfluidic channels. These droplets are subsequently conveyed into a spiral flow reactor, where they are irradiated by a stationary light source (λ = 455 nm). After the reaction, the biphasic segments are accumulated and fed to a collector in the form of phase-segragation, where H_2O_2 solution is in the upper layer and photocatalyst suspension is in the bottom layer. The H_2O_2 product is extracted in a container for practical applications, whereas the organic solution flows back for subsequent use. During the reaction process, the mechanism of H_2O_2 production and transformation were investigated as presented in **Figure 13g**. H_2O_2 was formed via an indirect 2e-ORR pathway using PF-BTTA-COF and transferred to the oil phase spontaneously due to abundant oil-water interfaces. After the continuous 100 h-reaction for H_2O_2 photosynthesis was carried out, more than 6 L of H_2O_2 solution with a concentration of 5.7 mM was obtained and further employed in wastewater treatment. Furthermore, this novel fluid system achieved a record-high H_2O_2 generation rate of 968 μmol h^{-1}, along with adjustable product concentrations ranging from 2.2 to 38.1 mM.

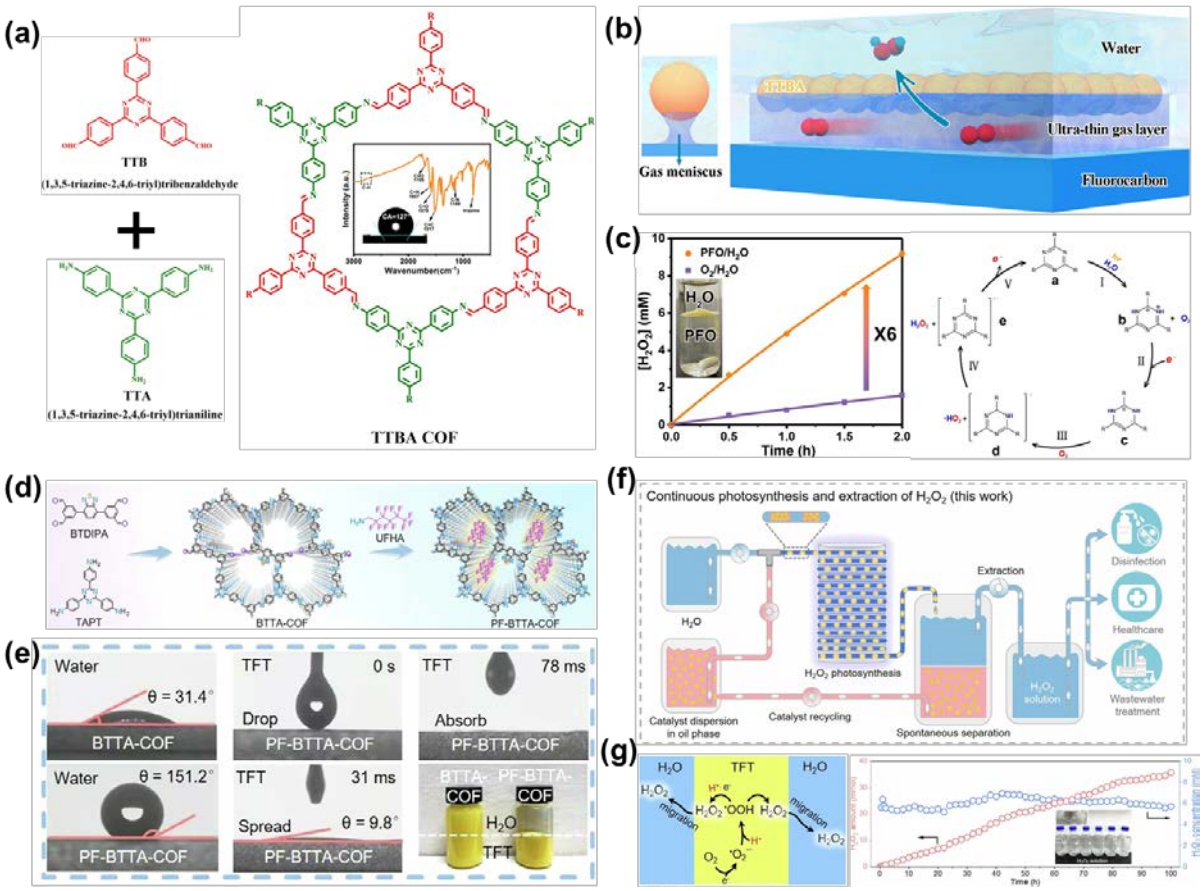

Figure 13. (a) Synthesis of hydrophobic TTBA COF photocatalyst; (b) Schematic diagram of H_2O_2 photosynthesis by the TTBA in the fluorocarbon (FC)/H_2O system; (c) H_2O_2 photosynthesis by the TTBA in the perfluorooctane (PFO)/H_2O and O_2/H_2O systems and schematic mechanism of H_2O_2 photosynthesis over TTBA photocatalyst;[129] (d) Synthesis of hydrophilic BTTA-COF and superhydrophobic PF-BTTA-COF; (e) Water or α,α,α-trifluorotoluene (TFT) contact angle measurements of BTTA-COF and PF-BTTA-COF; (f) Schematic illustration of the biphasic fluid system for continuous H_2O_2 photosynthesis and extraction. The colors yellow, blue, and pink represent the photocatalyst, water phase, and oil phase, respectively; (g) Reaction mechanism of continuous H_2O_2 photosynthesis under TFT/H_2O biphasic system and the 100 h-stability test result.[78]

1.2 Purpose of this thesis

H_2O_2 as a green oxidant is widely utilized in environmental and industrial processes. However, the current H_2O_2 production strategy via the anthraquinone method is energy-intensive and environmentally unfriendly. As a sustainable alternative, photocatalytic H_2O_2 generation, via the two-electron oxygen reduction reaction (2e-ORR) under visible light, offers mild, decentralized production using solar energy and oxygen. Despite significant advances, the efficiency of photocatalytic H_2O_2 production remains insufficient for practical applications due to several intrinsic limitations: low light absorption, inefficient charge carrier separation, and rapid decomposition of H_2O_2 on the catalyst surface.

To address these limitations, this thesis focuses on the rational design and functional engineering of Ti-based semiconductors, including both inorganic (TiO_2) and organic (Ti-MOFs) systems, which represent a highly promising class of photocatalytic materials. Ti-based semiconductors possess several intrinsic advantages for photocatalytic ORR. Structurally, they offer high thermal and chemical stability, are non-toxic, earth-abundant, and exhibit excellent resistance to photo-corrosion. From an electronic perspective, Ti^{4+} centers with empty 3d orbitals provide suitable acceptor states for photogenerated electrons, facilitating efficient charge separation. Additionally, the conduction band of Ti-based materials, typically derived from Ti 3d orbitals, is well-aligned with the reduction potential of O_2 to H_2O_2, making them thermodynamically favorable for 2e-ORR.[131,132]

Thus, Ti-based semiconductors provide a versatile platform for tuning light-harvesting properties, charge carrier dynamics, and surface reaction selectivity toward highly efficient and selective photocatalytic H_2O_2 production. Among them, facet engineering of Ti-based MOFs, MIL-125-NH_2, has been extensively explored to tailor its morphology and expose highly reactive facets such as the {001} facet. However, it is controversial whether the transformation of highly reactive facets will occur through metal incorporation.

Ti-based semiconductors own typically wide bandgap (e.g., 3.2 eV for anatase TiO_2), limited UV-light responsive property, and accelerated H_2O_2 decomposition due to the formation of ≡Ti-OOH complexes. These drawbacks can be overcome by structural modifications such

as molecular functionalization, plasmonic metal decoration, and facet engineering. In addition, this study leverages a two-phase reaction system to spatially separate the photocatalyst from the H_2O_2 product, thereby suppressing decomposition and improving overall efficiency. Moreover, the reaction mechanism of H_2O_2 production and formation of intermediate products (e.g., $O_2^{\bullet-}$ or $^1O_2$ species) over diverse Ti-based semiconductors in a two-phase system still needs to be deeply illustrated.

Regarding the selection of biphasic systems, benzyl alcohol (BA) has been identified as a superior hole scavenger compared to methanol, ethanol, and isopropanol. Its efficient hole-trapping capability facilitates rapid hole consumption and prolongs electron lifetime, thereby promoting the ORR. Moreover, the distinct and stable interface between water and BA enables the spontaneous phase separation of the reduction product (H_2O_2) and the oxidation product (benzaldehyde), contributing to efficient product isolation and system stability.

Overall, in this thesis, several advanced Ti-based inorganic and organic semiconductors were rationally designed and systematically studied for efficient photocatalytic H_2O_2 production in a BA/water biphasic system under visible-light irradiation. By tailoring the materials through the three key strategies, molecular functionalization, plasmonic metal decoration, and facet engineering, their structural and electronic properties were finely tuned from the molecular to the crystallographic level. The resulting insights contribute to a deeper understanding of the structure-activity relationship and offer guiding principles for the development of high-performance, selective, and stable photocatalysts for solar-to-chemical energy conversion.

1.3 Outline of this thesis

This thesis is composed of five chapters.

In Chapter I, recent advances in diverse semiconductors and their applications in photocatalytic ORR for H_2O_2 production are comprehensively reviewed. The chapter begins by introducing the fundamental principles and reaction mechanisms of photocatalytic H_2O_2 generation, with particular emphasis on water/oil biphasic systems. Next, various inorganic and organic semiconductor materials employed for photocatalytic H_2O_2 production are surveyed. Subsequently, key functionalization strategies, including organic molecule grafting, functional group modification, plasmonic metal incorporation, facet engineering, metal surface modification, heteroatoms doping, heterojunction, and defect engineering, are summarized and discussed; and they are shown to significantly improve visible-light harvesting and charge separation efficiency, thereby enhancing overall photocatalytic ORR performance. Finally, hydrophobic surface modification techniques for materials and recent progress in different two-phase systems for photocatalytic ORR are highlighted, demonstrating their important role in suppressing H_2O_2 decomposition. From Chapters II to IV, four kinds of functionalization methods for Ti-based inorganic and organic semiconductors, TiO_2 and MIL-125-NH_2(Ti), are investigated for a BA/water biphasic photocatalytic H_2O_2 production, as shown in **Figure 14**.

In Chapter II, to address the wide bandgap (3.2 eV) and hydrophilic property of TiO_2, organic molecule grafting of 2,3-dihydroxynaphthalene (2,3-DN) and hydrophobization using octadecylphosphonic acid (OPA) are employed on TiO_2 surface. The introduction of 2,3-DN enables TiO_2 visible-light absorption ability via the formation of Ti-O-aromatic carbon (Ti-O-ArC) between 2,3-DN and TiO_2 surface. However, the structural instability of 2,3-DN-modified TiO_2 (DN-TiO_2) leads to its shift from the BA phase to the aqueous phase during light irradiation, causing the deactivation of TiO_2. To address this problem, OPA modification imparts DN-TiO_2 hydrophobicity, allowing the catalyst to stably localize in the BA phase, thereby effectively maintaining its electron-excitation ability and minimizing H_2O_2 decomposition. This study provides a novel strategy for a TiO_2-employed photocatalytic H_2O_2 generation system.

In Chapter III, another visible-light responsive modification, plasmonic metal decoration, is developed on TiO_2 and the biphasic photocatalytic H_2O_2 production system. The introduced Au nanoparticles (NPs), with surface plasmon resonance (SPR) effect, significantly optimize band structure and electronic structure of TiO_2, because hot electrons excited from Au transfer to the TiO_2 conduction band, thereby promoting the ORR process. Furthermore, hydrophobic modification with OPA ensures TiO_2 well dispersion in the organic phase of the BA/water system, effectively suppressing H_2O_2 decomposition. This study highlights the importance of integrating plasmonic metal–semiconductor composites with biphasic reaction strategies to effectively address the inherent limitations of TiO_2-based photocatalysts.

Chapter IV proposes a transformation method of highly reactive facet on Ti-based MOF, MIL-125-NH_2(Ti), via combining facet engineering and electron-acceptor metal surface modification, and their efficient photocatalytic H_2O_2 yield in the two-phase system. The {001} facet, well acknowledged as the reactive facet on MIL-125-NH_2, shows lower reactive compared to the {111} facet after Au metal incorporation, owing to the distinct electron transfer pathways caused by the selective anchoring of Au NPs on {001} and {111} facets. Furthermore, OPA-modified optimal MOF sample (OPA-AuTM(111)) is applied in the BA/water biphasic system, achieving an exceptional H_2O_2 production via a $^1O_2$-mediated direct 2e-ORR pathway. This work demonstrates the overall functionalization of material composition and crystal orientation, achieving the redirection of charge carrier dynamics and providing novel insights into the design of facet-engineered MOF photocatalysts.

Finally, the overall conclusion of the thesis is presented in Chapter V.

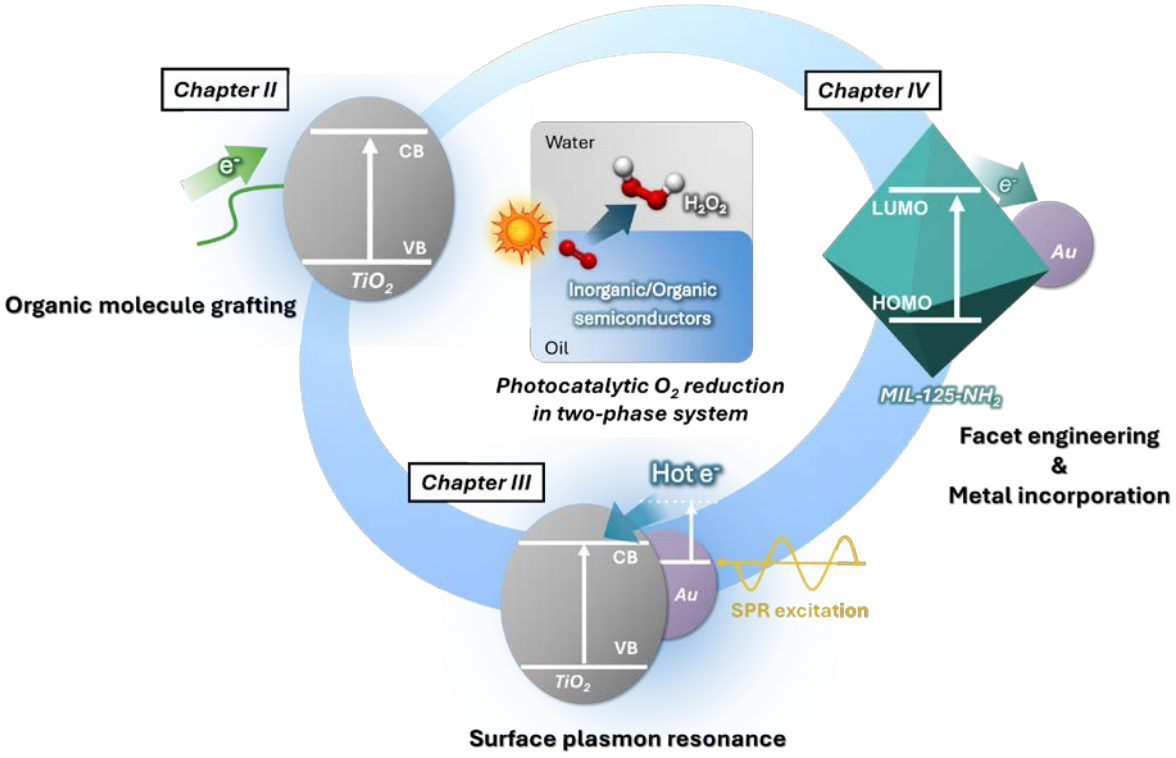

Figure 14. Ti-based inorganic/organic semiconductors developed for efficient photocatalytic H_2O_2 production in a two-phase system.

1.4 References

1 J. M. Campos-Martin, G. Blanco-Brieva and J. L. G. Fierro, *Angew. Chem. Int. Ed.*, 2006, **45**, 6962–6984.

2 W. Zhan, L. Ji, Z. mei Ge, X. Wang and R. tao Li, *Tetrahedron*, 2018, **74**, 1527–1532.

3 M. Ksibi, *Chem. Eng. J.*, 2006, **119**, 161–165.

4 R. N. Gurram, M. Al-Shannag, N. J. Lecher, S. M. Duncan, E. L. Singsaas and M. Alkasrawi, *Bioresour. Technol.*, 2015, **192**, 529–539.

5 B. He, Z. Wang, P. Xiao, T. Chen, J. Yu and L. Zhang, *Adv. Mater.*, 2022, **34**, 1–10.

6 Y. Kondo, K. Hino, Y. Kuwahara, K. Mori, H. Kobayashi and H. Yamashita, *Chem. Commun.*, 2022, **58**, 12345–12348.

7 H. il Kim, Y. Choi, S. Hu, W. Choi and J. H. Kim, *Appl. Catal. B Environ.*, 2018, **229**, 121–129.

8 S. Yang, A. Verdaguer-Casadevall, L. Arnarson, L. Silvioli, V. Čolić, R. Frydendal, J. Rossmeisl, I. Chorkendorff and I. E. L. Stephens, *ACS Catal.*, 2018, **8**, 4064–4081.

9 J. García-Serna, T. Moreno, P. Biasi, M. J. Cocero, J. P. Mikkola and T. O. Salmi, *Green Chem.*, 2014, **16**, 2320–2343.

10 H. Hou, X. Zeng and X. Zhang, *Angew. Chem. Int. Ed.*, 2020, **59**, 17356–17376.

11 Z. Chen, D. Yao, C. Chu and S. Mao, *Chem. Eng. J.*, 2023, **451**, 138489.

12 M. G. Walter, E. L. Warren, J. R. McKone, S. W. Boettcher, Q. Mi, E. A. Santori and N. S. Lewis, *Chem. Rev.*, 2010, **110**, 6446–6473.

13 H. Cheng, J. Cheng, L. Wang and H. Xu, *Chem. Mater.*, 2022, **34**, 4259−4273.

14 X. Zeng, Y. Liu, X. Hu and X. Zhang, *Green Chem.*, 2021, **23**, 1466–1494.

15 J. Tang, T. Zhao, D. Solanki, X. Miao, W. Zhou and S. Hu, *Joule*, 2021, **5**, 1432–1461.

16 W. Hou, Y. Li, S. Ouyang, H. Chen, J. Ye, X. Han and Y. Deng, *Chem. Commun.*, 2019, **55**, 13279–13282.

17 Y. Isaka, Y. Kondo, Y. Kawase, Y. Kuwahara, K. Mori and H. Yamashita, *Chem. Commun.*, 2018, **54**, 9270–9273.

18 Y. Kondo, Y. Kuwahara, K. Mori and H. Yamashita, *Chem*, 2022, **8**, 2924–2938.

19 T. Zhang, W. Schilling, S. U. Khan, H. Y. V. Ching, C. Lu, J. Chen, A. Jaworski, G. Barcaro, S. Monti, K. De Wael, A. Slabon and S. Das, *ACS Catal.*, 2021, **11**, 14087–14101.

20 X. Wu, X. Zhang, S. Zhao, Y. Gong, R. Djellabi, S. Lin and X. Zhao, *Appl. Catal. Gen.*, 2020, **591**, 117271.

21 Y. Shiraishi, S. Kanazawa, D. Tsukamoto, A. Shiro, Y. Sugano and T. Hirai, *ACS Catal.*, 2013, **3**, 2222–2227.

22 L. Zheng, H. Su, J. Zhang, L. S. Walekar, H. Vafaei Molamahmood, B. Zhou, M. Long and Y. H. Hu, *Appl. Catal. B Environ.*, 2018, **239**, 475–484.

23 L. Zheng, J. Zhang, Y. H. Hu and M. Long, *J. Phys. Chem. C*, 2019, **123**, 13693–13701.

24 L. Zheng, X. Yu, M. Long and Q. Li, *Chin. J. Catal.*, 2017, **38**, 2076–2084.

25 K. Fuku, Y. Miyase, Y. Miseki, T. Gunji and K. Sayama, *RSC Adv.*, 2017, **7**, 47619–47623.

26 H. Shi, Y. Li, X. Wang, H. Yu and J. Yu, *Appl. Catal. B Environ.*, 2021, **297**, 120414.

27 H. Shi, Y. Li, K. Wang, S. Li, X. Wang, P. Wang, F. Chen and H. Yu, *Chem. Eng. J.*, 2022, **443**, 136429.

28 Y. Wang, Y. Wang, J. Zhao, M. Chen, X. Huang and Y. Xu, *Appl. Catal. B Environ.*, 2021, **284**, 119691.

29 S. Thakur, T. Kshetri, N. H. Kim and J. H. Lee, *J. Catal.*, 2017, **345**, 78–86.

30 P. Sun, Z. Mo, H. Chen, Y. Song, J. Liu, W. Yin, H. Dai, Z. Chen, H. Li and H. Xu, *Inorg. Chem. Front.*, 2022, **9**, 1701–1707.

31 X. Yu, Z. Wei, Y. Qin, X. Zhang, D. Hao, L. Jing, Y. Liu, H. Dai, J. Deng and Y. Zhu, *Adv. Mater.*, 2025, **37**, 2501494.

32 G. Ren, M. Zhou and H. Wang, *J. Am. Chem. Soc.*, 2024, **146**, 6084–6093.

33 Z. Wei, S. Zhao, W. Li, X. Zhao, C. Chen, D. L. Phillips, Y. Zhu and W. Choi, *ACS Catal.*, 2022, **12**, 11436–11443.

34 S. Zhao, T. Guo, X. Li, T. Xu, B. Yang and X. Zhao, *Appl. Catal. B Environ.*, 2018, **224**, 725–732.

35 Q. Hu, Y. Dong, K. Ma, X. Meng and Y. Ding, *J. Catal.*, 2022, **413**, 321–330.

36 M. Wu, Z. Shan, J. Wang, T. Liu and G. Zhang, *Chem. Eng. J.*, 2023, **454**, 140121.

37 C. Qin, X. Wu, L. Tang, X. Chen, M. Li, Y. Mou, B. Su, S. Wang, C. Feng, J. Liu, X. Yuan, Y. Zhao and H. Wang, *Nat. Commun.*, 2023, **14**, 5238.

38 J. Lim, H. Kim, J. Park, G. H. Moon, J. J. M. Vequizo, A. Yamakata, J. Lee and W. Choi, *Environ. Sci. Technol.*, 2020, **54**, 497–506.

39 Z. Teng, Q. Zhang, H. Yang, K. Kato, W. Yang, Y. R. Lu, S. Liu, C. Wang, A. Yamakata, C. Su, B. Liu and T. Ohno, *Nat. Catal.*, 2021, **4**, 374–384.

40 P. Ren, T. Zhang, N. Jain, H. Y. V. Ching, A. Jaworski, G. Barcaro, S. Monti, J. Silvestre-Albero, V. Celorrio, L. Chouhan, A. Rokicińska, E. Debroye, P. Kuśtrowski, S. Van Doorslaer, S. Van Aert, S. Bals and S. Das, *J. Am. Chem. Soc.*, 2023, **145**, 16584–16596.

41 A. Gopakumar, P. Ren, J. Chen, B. V. Manzolli Rodrigues, H. Y. Vincent Ching, A. Jaworski, S. Van Doorslaer, A. Rokicińska, P. Kuśtrowski, G. Barcaro, S. Monti, A. Slabon and S. Das, *J. Am. Chem. Soc.*, 2022, **144**, 2603–2613.

42 Y. Isaka, Y. Kawase, Y. Asutaka Kuwahara, K. Mori and H. Yamashita, *Angew. Chem. Int. Ed.*, 2019, **131**, 5456–5460.

43 X. Chen, Y. Kuwahara, K. Mori, C. Louis and H. Yamashita, *J. Mater. Chem. A*, 2020, **8**, 1904–1910.

44 Y. Kondo, K. Honda, Y. Kuwahara, K. Mori, H. Kobayashi and H. Yamashita, *ACS Catal.*, 2022, **12**, 14825–14835.

45 Y. Kondo, Y. Kuwahara, K. Mori and H. Yamashita, *J. Phys. Chem. C*, 2021, **125**, 27909–27918.

46 F. Liu, P. Zhou, Y. Hou, H. Tan, Y. Liang, J. Liang, Q. Zhang, S. Guo, M. Tong and J. Ni, *Nat. Commun.*, 2023, **14**, 1–10.

47 W. K. Han, H. S. Lu, J. X. Fu, X. Liu, X. Zhu, X. Yan, J. Zhang, Y. Jiang, H. Dong and Z. G. Gu, *Chem. Eng. J.*, 2022, **449**, 1–43.

48 J. Sun, J. Chakraborty, M. Deng, A. Laemont, X. Feng, Y. Y. Liu and P. Van Der Voort, *J. Mater. Chem. A*, 2023, **11**, 21516–21540.

49 X. Chen, S. Shen, L. Guo and S. S. Mao, *Chem. Rev.*, 2010, **110**, 6503–6570.

50 Q. Wang and K. Domen, *Chem. Rev.*, 2020, **120**, 919–985.

51 Y. Deng, Y. Shi, L. Li, R. Tang, Z. Zhou, S. Xiong, W. Li, J. Liu and Y. Huang, *Appl. Catal. B Environ. Energy*, 2024, **352**, 124043.

52 S. S. Xia, L. Li, C. Bao, J. Wu, C. Li, X. Wang, J. Gao, J. Hu, X. Wang and Z. Chen, *J. Catal.*, 2024, **433**, 115488.

53 X. Chen, Y. Kondo, S. Li, Y. Kuwahara, K. Mori, D. Zhang, C. Louis and H. Yamashita, *J. Mater. Chem. A*, 2021, **9**, 26371–26380.

54 X. Luo, S. Zhou, S. Zhou, X. Zhou, J. Huang, Y. Liu, D. Wang, G. Liu and P. Gu, *Adv. Funct. Mater.*, 2025, **35**, 2415244.

55 L. Yuan, Y. Zou, L. Zhao, C. Zhang, J. Wang, C. Liu, G. Wei and C. Yu, *Appl. Catal. B Environ.*, 2022, **318**, 121859.

56 J. Zhao, S. Xue, R. Ji, B. Li and J. Li, *Chem. Soc. Rev.*, 2021, **50**, 12070–12097.

57 M. Sayed, J. Yu, G. Liu and M. Jaroniec, *Chem. Rev.*, 2022, **122**, 10484–10537.

58 N. Lemcoff, N. B. Nechmad, O. Eivgi, E. Yehezkel, O. Shelonchik, R. S. Phatake, D. Yesodi, A. Vaisman, A. Biswas, N. G. Lemcoff and Y. Weizmann, *Nat. Chem.*, 2023, **15**, 475–482.

59 M. Teranishi, R. Hoshino, S. Naya and H. Tada, *Angew. Chem. Int. Ed.*, 2016, **55**, 12773–12777.

60 S. Li, H. Huang, L. Shao and J. Wang, *ACS Nano*, 2021, **15**, 10759–10768.

61 K. Meng, J. Zhang, B. Cheng, X. Ren, Z. Xia, F. Xu, L. Zhang and J. Yu, *Adv. Mater.*, 2024, **36**, 2406460.

62 X. M. Cheng, Y. Gu, X. Y. Zhang, X. Y. Dao, S. Q. Wang, J. Ma, J. Zhao and W. Y. Sun, *Appl. Catal. B Environ.*, 2021, **298**, 120524.

63 L. Yuan, P. Du, C. Zhang, Y. Xi, Y. Zou, J. Li, Y. Bi, T. Bao, C. Liu and C. Yu, *Appl. Catal. B Environ. Energy*, 2025, **364**, 124855.

64 T. Liu, Z. Pan, K. Kato, J. J. M. Vequizo, R. Yanagi, X. Zheng, W. Yu, A. Yamakata, B. Chen, S. Hu, K. Katayama and C. Chu, *Nat. Commun.*, 2022, **13**, 7783.

65 Y. C. Hao, L. W. Chen, J. Li, Y. Guo, X. Su, M. Shu, Q. Zhang, W. Y. Gao, S. Li, Z. L. Yu, L. Gu, X. Feng, A. X. Yin, R. Si, Y. W. Zhang, B. Wang and C. H. Yan, *Nat. Commun.*, 2021, **12**, 1–11.

66 P. Zhang, D. Sun, A. Cho, S. Weon, S. Lee, J. Lee, J. W. Han, D.-P. Kim and W. Choi, *Nat. Commun.*, 2019, **10**, 940.

67 G. Moon, M. Fujitsuka, S. Kim, T. Majima, X. Wang and W. Choi, *ACS Catal.*, 2017, **7**, 2886–2895.

68 W. Liu, P. Wang, J. Chen, X. Gao, HuinanN. Che, B. Liu and Y. Ao, *Adv. Funct. Mater.*, 2022, **32**, 2205119.

69 J. Low, J. Yu, M. Jaroniec, S. Wageh and A. A. Al-Ghamdi, *Adv. Mater.*, 2017, **29**, 1601694.

70 Z. Chen, D. Yao, C. Chu and S. Mao, *Chem. Eng. J.*, 2023, **451**, 138489.

71 Y. X. Ye, J. Pan, F. Xie, L. Gong, S. Huang, Z. Ke, F. Zhu, J. Xu and G. Ouyang, *Proc. Natl. Acad. Sci.*, 2021, **118**, e2103964118.

72 Y. Yang, J. Liu, M. Gu, B. Cheng, L. Wang and J. Yu, *Appl. Catal. B Environ.*, 2023, **333**, 122780.

73 A. Kumar, P. Raizada, A. Hosseini-Bandegharaei, V. K. Thakur, V. H. Nguyen and P. Singh, *J. Mater. Chem. A*, 2021, **9**, 111–153.

74 W. Miao, Y. Wang, Y. Liu, H. Qin, C. Chu and S. Mao, *Engineering*, 2023, **25**, 214–221.

75 X. Chen, X. Sheng, H. Zhou, Z. Liu, M. Xu and X. Feng, *Small*, 2024, **20**, 2310128.

76 Z. Chen, H. Chen, K. Wang, J. Chen, M. Li, Y. Wang, P. Tsiakaras and S. Song, *ACS Catal.*, 2023, **13**, 6497–6508.

77 Y. Kondo, S. Mizutani, Y. Kuwahara, K. Mori, T. Sekino and H. Yamashita, *J. Mater. Chem. A*, 2025, **13**, 3701–3710.

78 C. Shao, X. Yu, Y. Ji, J. Xu, Y. Yan, Y. Hu, Y. Li, W. Huang and Y. Li, *Nat. Commun.*, 2024, **15**, 8023.

79 Y. Kawase, Y. Isaka, Y. Kuwahara, K. Mori and H. Yamashita, *Chem. Commun.*, 2019, **55**, 6743–6746.

80 X. Chen, Y. Kuwahara, K. Mori, C. Louis and H. Yamashita, *ACS Appl. Energy Mater.*, 2021, **4**, 4823–4830.

81 Y. Hong, Y. Cho, E. M. Go, P. Sharma, H. Cho, B. Lee, S. M. Lee, S. O. Park, M. Ko,

S. K. Kwak, C. Yang and J.-W. Jang, *Chem. Eng. J.*, 2021, **418**, 129346.

82 I. Krivtsov, A. Vazirani, D. Mitoraj, M. M. Elnagar, C. Neumann, A. Turchanin, Y. Patiño, S. Ordóñez, R. Leiter, M. Lindén, U. Kaiser and R. Beranek, *J. Mater. Chem. A*, 2023, **11**, 2314–2325.

83 Z. Chen, H. Chen, K. Wang, J. Chen, M. Li, Y. Wang, P. Tsiakaras and S. Song, *ACS Catal.*, 2023, **13**, 6497–6508.

84 Y. Kawase, Y. Isaka, Y. Kuwahara, K. Mori and H. Yamashita, *Chem. Commun.*, 2019, **55**, 6743–6746.

85 O. Ito and M. Matsuda, *J. Am. Chem. Soc.*, 1982, **104**, 568–572.

86 H. Furukawa, K. E. Cordova, M. O'Keeffe and O. M. Yaghi, *Science*, 2013, **341**, 1230444.

87 S. Kitagawa, R. Kitaura and S. I. Noro, *Angew. Chem. Int. Ed.*, 2004, **43**, 2334–2375.

88 Y. Nosaka and A. Y. Nosaka, *Chem. Rev.*, 2017, **117**, 11302–11336.

89 L. Valenzano, B. Civalleri, S. Chavan, S. Bordiga, M. H. Nilsen, S. Jakobsen, K. P. Lillerud and C. Lamberti, *Chem. Mater.*, 2011, **23**, 1700–1718.

90 J. H. Cavka, S. Jakobsen, U. Olsbye, N. Guillou, C. Lamberti, S. Bordiga and K. P. Lillerud, *J. Am. Chem. Soc.*, 2008, **130**, 13850–13851.

91 Y. Han, M. Liu, K. Li, Q. Sun, W. Zhang, C. Song, G. Zhang, Z. Conrad Zhang and X. Guo, *Inorg. Chem. Front.*, 2017, **4**, 1870–1880.

92 M. A. Syzgantseva, C. P. Ireland, F. M. Ebrahim, B. Smit and O. A. Syzgantseva, *J. Am. Chem. Soc.*, 2019, **141**, 6271–6278.

93 D. Sun, W. Liu, M. Qiu, Y. Zhang and Z. Li, *Chem. Commun.*, 2015, **51**, 2056–2059.

94 A. Santiago Portillo, H. G. Baldoví, M. T. García Fernandez, S. Navalón, P. Atienzar, B. Ferrer, M. Alvaro, H. Garcia and Z. Li, *J. Phys. Chem. C*, 2017, **121**, 7015–7024.

95 C. Xu, Y. Pan, G. Wan, H. Liu, L. Wang, H. Zhou, S. H. Yu and H. L. Jiang, *J. Am. Chem. Soc.*, 2019, **141**, 19110–19117.

96 S. Kato, J. Jung, T. Suenobu and S. Fukuzumi, *Energy Environ. Sci.*, 2013, **6**, 3756.

97 K. Mase, M. Yoneda, Y. Yamada and S. Fukuzumi, *Nat. Commun.*, 2016, **7**, 1–7.

98 K. Geng, T. He, R. Liu, S. Dalapati, K. T. Tan, Z. Li, S. Tao, Y. Gong, Q. Jiang and D.

Jiang, *Chem. Rev.*, 2020, **120**, 8814–8933.

99 Z. Liang, R. Shen, Y. H. Ng, Y. Fu, T. Ma, P. Zhang, Y. Li and X. Li, *Chem Catal.*, 2022, **2**, 2157–2228.

100 H. Wang, H. Wang, Z. Wang, L. Tang, G. Zeng, P. Xu, M. Chen, T. Xiong, C. Zhou, X. Li, D. Huang, Y. Zhu, Z. Wang and J. Tang, *Chem. Soc. Rev.*, 2020, **49**, 4135–4165.

101 L. Li, L. Xu, Z. Hu, J. C. Yu, L. Li, L. Xu, J. C. Yu and Z. Hu, *Adv. Funct. Mater.*, 2021, **31**, 2106120.

102 H. Wang, C. Yang, F. Chen, G. Zheng and Q. Han, *Angew. Chem. Int. Ed.*, 2022, **61**, e202202328.

103 M. Kou, Y. Wang, Y. Xu, L. Ye, Y. Huang, B. Jia, H. Li, J. Ren, Y. Deng, J. Chen, Y. Zhou, K. Lei, L. Wang, W. Liu, H. Huang and T. Ma, *Angew. Chem. Int. Ed.*, 2022, **61**, e202200413.

104 L. Zhai, Z. Xie, C. X. Cui, X. Yang, Q. Xu, X. Ke, M. Liu, L. B. Qu, X. Chen and L. Mi, *Chem. Mater.*, 2022, **34**, 5232–5240.

105 W. Zhao, P. Yan, B. Li, M. Bahri, L. Liu, X. Zhou, R. Clowes, N. D. Browning, Y. Wu, J. W. Ward and A. I. Cooper, *J. Am. Chem. Soc.*, 2022, **144**, 9902–9909.

106 F. P. Kinik, A. Ortega-Guerrero, D. Ongari, C. P. Ireland and B. Smit, *Chem. Soc. Rev.*, 2021, **50**, 3143–3177.

107 G. Cheng, T. Hasell, A. Trewin, D. J. Adams and A. I. Cooper, *Angew. Chem. Int. Ed.*, 2012, **51**, 12727–12731.

108 J. Sun, H. Sekhar Jena, C. Krishnaraj, K. Singh Rawat, S. Abednatanzi, J. Chakraborty, A. Laemont, W. Liu, H. Chen, Y. Liu, K. Leus, H. Vrielinck, V. Van Speybroeck and P. Van Der Voort, *Angew. Chem. Int. Ed.*, 2023, **62**, 1–9.

109 P. Das, G. Chakraborty, J. Roeser, S. Vogl, J. Rabeah and A. Thomas, *J. Am. Chem. Soc.*, 2023, **145**, 31.

110 P. Das, J. Roeser and A. Thomas, *Angew. Chem. Int. Ed.*, 2020, **59**, 6984–7006.

111 Q. Shang, Y. Liu, J. Ai, Y. Yan, X. Yang, D. Wang and G. Liao, *J. Mater. Chem. A*, 2023, **11**, 21109–21122.

112 J. Zhang, L. Zheng, F. Wang, C. Chen, H. Wu, S. A. K. Leghari and M. Long, *Appl.*

Catal. B Environ., 2020, **269**, 118770.

113 T. Yang, Y. Chen, Y. Wang, X. Peng and A. Kong, *ACS Appl. Mater. Interfaces*, 2022, **15**, 8075.

114 Y. Nosaka and A. Y. Nosaka, *Chem. Rev.*, 2017, **117**, 11302–11336.

115 Z. Hu, S. Liu, H. Qin, J. Zhou and X. Peng, *J. Am. Chem. Soc.*, 2020, **142**, 4254–4264.

116 W. Ji, Z. Xu, S. Zhang, Y. Li, Z. Bao, Z. Zhao, L. Xie, X. Zhong, Z. Wei and J. Wang, *Catal. Sci. Technol.*, 2022, **12**, 2865–2871.

117 P. Zhu, Y. Ma, J. Li, Y. Jin, H. Cai, C. Xu, M. Huang and N. Ming chen, *Ind. Eng. Chem. Res.*, 2023, **62**, 982–990.

118 L. Li, X. Huo, S. Chen, Q. Luo, W. Wang, Y. Wang and N. Wang, *Small*, 2023, 19, 2301865.

119 Q. Wu, J. Cao, X. Wang, Y. Liu, Y. Zhao, H. Wang, Y. Liu, H. Huang, F. Liao, M. Shao and Z. Kang, *Nat. Commun.* 2021, **12**, 483.

120 I. Krivtsov, A. Vazirani, D. Mitoraj and R. Beranek, *ChemCatChem*, 2023, **15**, e202201215.

121 B. C. Moon, B. Bayarkhuu, K. A. I. Zhang, D. K. Lee and J. Byun, *Energy Environ. Sci.*, 2022, **15**, 5082–5092.

122 M. J. Pavan, H. Fridman, G. Segalovich, A. I. Shames, N. G. Lemcoff and T. Mokari, *ChemCatChem*, 2018, **10**, 2541–2545.

123 R. Arcas, E. Peris, E. Mas-Marzá and F. Fabregat-Santiago, *Sustain. Energy Fuels*, 2021, **5**, 956–962.

124 H. B. Vibbert, C. Bendel, J. R. Norton and A. J. Moment, *ACS Sustain. Chem. Eng.*, 2022, **10**, 11106–11116.

125 S. Kumar, B. Bayarkhuu, H. Ahn, H. Cho and J. Byun, *Nano Trends*, 2023, **4**, 100023.

126 T. Ishida, Y. Ogihara, H. Ohashi, T. Akita, T. Honma, H. Oji and M. Haruta, *ChemSusChem*, 2012, **5**, 2243–2248.

127 G. Marques, J. C. del Río and A. Gutiérrez, *Bioresour. Technol.*, 2010, **101**, 260–267.

128 V. C. Corberán, M. E. González-Pérez, S. Martínez-González and A. Gómez-Avilés, *Appl. Catal. Gen.*, 2014, **474**, 211–223.

129 M. Sun, M. Murugananthan, Z. Zhou, Y. Shen, Y. Zhang and Y. Zhang, *Chem. Eng. J.*, 2024, **486**, 150245.

130 V. H. Dalvi and P. J. Rossky, *Proc. Natl. Acad. Sci.*, 2010, **107**, 13603–13607.

131 Y. Yamamoto, S. Kasamatsu and O. Sugino, *J. Phys. Chem. C*, 2019, **123**, 19486–19492.

132 R. Shwetharani, M. Sakar, C. A. N. Fernando, V. Binas and R. Geetha Balakrishna, *Catal. Sci. Technol.*, 2019, **9**, 12–46.

Chapter II

Hydrophobic TiO_2 Modified by Visible-light Responsive Organic Molecules as an Efficient Photocatalyst for Promoting H_2O_2 Production in a Two-Phase System

2.1 Introduction

Ever since its initial synthesis by Thenard in 1818, hydrogen peroxide (H_2O_2) has attracted much attention from researchers and has been recognized as one of the "100 most valuable chemicals worldwide".[1] H_2O_2 has been widely utilized in diverse fields, such as organic synthesis,[2] wastewater treatment, disinfection,[3] bleaching,[4] and fuel cells.[5] Oxidation of anthraquinone method, being the prevailing approach for industrial H_2O_2 production, involves a complex industrial process that demands a substantial energy input.[1] Moreover, the waste generated from the oxidation process greatly exacerbates the burden on environmental safety.[6] In order to moderate the reaction conditions and alleviate pollution, researchers have developed a direct synthesis method using hydrogen (H_2) and oxygen (O_2) as an alternative route for H_2O_2 production.[7] However, the risk of explosion of the H_2/O_2 mixture gas cannot be avoided even though precise control of its ratio, which limited the large-scale industrial applications of this reaction process. Consequently, there is a pressing requirement for an environmentally sustainable and operationally secure approach to produce H_2O_2.

More recently, the discovery of photocatalytic synthesis of H_2O_2 (**Equations 1-3**) has broken the bottleneck of H_2O_2 chemistry.[8] The entire reaction process relies solely on readily available resources such as earth-abundant water, oxygen, and renewable sunlight as energy supply, and has no pollution emission throughout the entire process. Therefore, the photocatalytic synthesis of H_2O_2 shows wide application prospects and a fair amount of research focus on photocatalysts, such as TiO_2,[9,10] g-C_3N_4,[11,12] $BiVO_4$,[13] CdS,[14,15] and MOFs[16,17] materials, which produce photogenerated electrons for O_2 reduction contributing to H_2O_2 production.

$$O_2 + 2e^- + 2H^+ \rightarrow H_2O_2 \quad (1)$$

$$O_2 + e^- \rightarrow O_2^{\cdot -} \quad (2)$$

$$O_2^{\cdot -} + e^- + 2H^+ \rightarrow H_2O_2 \quad (3)$$

In recent years, TiO_2 photocatalysts have been widely investigated due to their notable benefits, such as high chemical stability and cost-effectiveness.[18] While emerging materials

with engineered nanostructures exhibit a wider range of light absorption and higher absorption efficiency,[19,20] TiO_2-based photocatalysts remain prominent candidates considering practical application factors.[21] Nonetheless, there are two major challenges in the system of TiO_2 photocatalytic H_2O_2 production. First, TiO_2 with a broadband energy structure (3.2 eV) can only attain the UV light spectrum response, which exhibits low efficiency for light utilization;[22] second, the synthesized H_2O_2 will combine with hydroxyl groups on the surface of TiO_2 forming peroxide complexes (≡Ti-OOH), which causes the H_2O_2 decomposition.[23] Therefore, continuous efforts are in demand on the surface modification of TiO_2 to enhance its sensitivity to visible light and inhibit the H_2O_2 photodecomposition.

The doping of TiO_2 with noble metals,[24] transition metals,[25] nitrogen atoms,[26] and nonmetallic quantum dots[9] has been reported to effectively enhance the photocatalytic activity under visible light radiation. The addition of sensitizing substances such as organic dyes[25] and humic acids[18] can form a strong coupling interaction with TiO_2, which broadens the spectral absorption range of TiO_2. In addition, the surface modification of TiO_2 using colorless aromatic compounds has been reported to contribute to the performance of photocatalytic reaction, which is attributed to the direct electron transfer from the aromatic ligands to the conduction band of TiO_2 when exposed to visible light radiation.[27–29] Kamegawa et al.[30] compared the effects of several kinds of naphthol with different contents and positions of phenolic hydroxyl groups on the photocatalytic reaction activity of TiO_2. They found that 2,3-dihydroxynaphthalene (2,3-DN) with adjacent hydroxyl groups formed surface complexes with TiO_2, which exhibited strong visible light absorption and superior photocatalytic activity.

Economically, it is more preferred that O_2 reduction reaction (ORR) to H_2O_2 coupling with an oxidative synthesis of high value-added chemicals.[16] But the separation process of organic products and H_2O_2 present in a single phase requires a large amount of energy and presents a great technical challenge. Therefore, in the present study, a benzyl alcohol (BA)/water two-phase system has been adopted in photocatalytic H_2O_2 production, which enables the spontaneous separation of the products benzaldehyde (BAL) (**Equation 4**) and H_2O_2.[31]

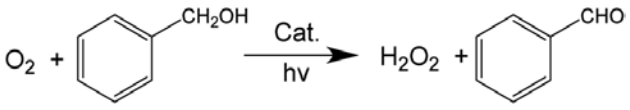

(4)

Herein, we report 2,3-DN and octadecylphosphonic acid (OPA) co-modified TiO_2 material applied for photosynthesis H_2O_2 production in a BA/water two-phase system (**Scheme 1**). 2,3-DN modification renders TiO_2 visible photosensitivity, but it is unstable in this system. Then the effect of OPA on the stability of the co-modified TiO_2 catalysts was investigated. Furthermore, the addition of OPA imparts TiO_2 hydrophobic properties and enables it to exist stably in the BA phase with high dispersion. In this two-phase system, O_2 molecule is reduced by photo-generated electrons of hydrophobic TiO_2 in the organic phase. The reactive peroxide radicals $O_2^{\bullet-}$ formed are transferred to the aqueous phase, which contributes to a superior H_2O_2 production because of the inhibition of the secondary H_2O_2 decomposition.[16]

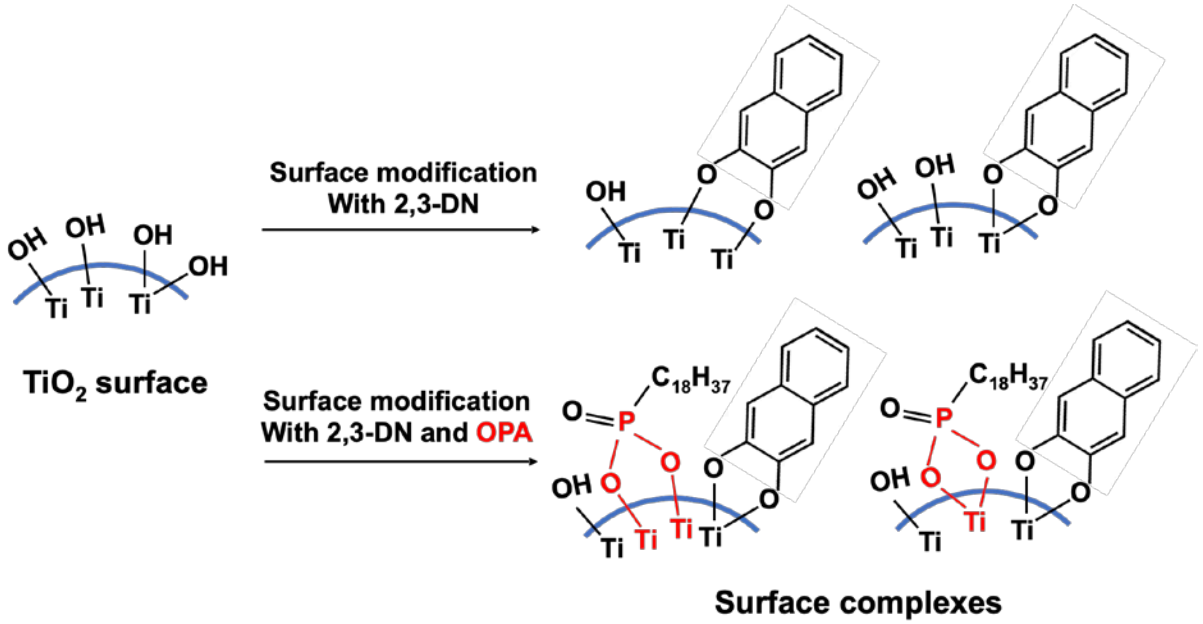

Scheme 1. Schematic illustration of surface modification on TiO_2 material with 2,3-DN and OPA.

2.2 Experimental

2.2.1 Materials

TiO_2 used in this study (JRC-TIO-8, anatase) was obtained from the Catalysis Society of Japan. Octadecylphosphonic acid (OPA, > 98%), 2,3-dihydroxynaphthalene (2,3-DN, > 98%), and oxo[5,10,15,20-tetra(4-pyridyl)porphinato]titanium(IV) ($[TiO(tpypH_4)]^{4+}$) (Ti-TPyP reagent) were purchased from Tokyo Chemistry Industry Co., Ltd. Hydrogen peroxide (30%), benzyl alcohol (BA, > 97%), ethanol (C_2H_5OH, > 99%), perchloric acid ($HClO_4$, 60%), and hydrochloric acid (HCl, 16.9%) were provided by Nacalai Tesque. All chemicals were purchased and used without any additional purification.

2.2.2 Synthesis of DN-TiO_2

For the surface treatment of TiO_2 using 2,3-DN, 100 mg of TiO_2 was dispersed in an ethanol solution of 2,3-DN (100 mL, 20 mM). Following 24 hours of stirring at room temperature, the obtained suspension was centrifuged, and the excess 2,3-DN was removed by washing with ethanol for six times. Then the sample was dried for 12 h at 80 ^oC, and was denoted as DN-TiO_2.

2.2.3 Synthesis of DNxOPA4-TiO_2 (x = 1, 1.5, and 2)

Briefly, specific amounts of 2,3-DN and OPA were dissolved in 100 mL of ethanol containing TiO_2 powder, with the concentration of ethanol solution of 10 mM and 40 mM, respectively. After stirring, washing, and drying under the same conditions as mentioned in **Section 2.2.2**, the sample was named as DN1OPA4-TiO_2.

DN1.5OPA4-TiO_2 and DN2OPA4-TiO_2 were prepared according to the same procedure as DN1OPA4-TiO_2 but the concentration of ethanol solution of 2,3-DN was 15 mM for DN1.5OPA4-TiO_2 and 20 mM for DN2OPA4-TiO_2.

2.2.4 Synthesis of DN2OPAy-TiO_2 (y = 1, 2, and 4)

DN2OPAy-TiO_2 catalysts were prepared using a similar method as mentioned in **Section 2.2.3** but with the addition of varying amounts of 2,3-DN and OPA. The concentration of 2,3-DN ethanol solution remains 20 mM, but that of OPA ethanol solution was 10, 20 and 40 mM for DN2OPAy-TiO_2 (y = 1, 2, and 4), respectively.

2.2.5 Synthesis of OPA-TiO_2

The preparation method of OPA-TiO_2 was similar to that mentioned in **Section 2.2.3** except for the addition of 2,3-DN. OPA-modified TiO_2 was denoted as OPA-TiO_2.

2.2.6 Characterization

X-ray diffraction (XRD) analysis (Rigaku Ultima IV) with Cu Kα radiation (λ = 1.5405 Å) was conducted to examine the crystal structures of prepared samples. The specific surface area and pore distributions were carried out using Nitrogen physisorption measurements equipped with a BELSORP-max system (Microtrac BEL Corp., Inc.). Prior to the test, the samples were pretreated under a vacuum at 100 ^oC for 4 hours to remove the moisture and surface impurities. Ultraviolet-visible diffuse reflectance spectra (UV-vis DRS, Shimadzu UV-2450) were employed for the optical absorption capacity of photocatalysts, with $BaSO_4$ serving as the reference and absorption spectra analyzed using Kubelka–Munk function. TG-DTA analysis (Rigaku Thermo Plus EVO II) was performed under an airflow at 800 ^oC via a ramp of 2.0 $^oC\ min^{-1}$. Using an ESCA-3400 instrument from Shimadzu, X-ray photoelectron spectroscopy (XPS) was carried out to explore the electrons states. XPS results were calibrated using the C 1s at 284.6 eV. Fourier transform infrared spectroscopy (FT-IR) was conducted by a JASCO FTIR-6100 instrument by analyzing the plates formed from the catalysts and KBr mixture with a mass ratio of 1:100.

2.2.7 Photocatalytic H_2O_2 production

In a typical procedure for the two-phase photocatalytic reaction system, photocatalysts (5 mg), distilled water (2 mL), and BA (5 mL) were added in a reaction tube with a volume of 30 mL. The reactor was sealed and subjected to sonication for about 5 minutes to ensure the proper dispersion of the photocatalyst. Subsequently, the mixture was bubbled with O_2 at a flow rate of 20 mL min^{-1} for 30 min, at the same time being stirred magnetically without light. The reaction tube was then positioned under irradiation of a 500W Xe-lamp (Sanei Electric XEF-501S) through a 450 nm cut-off glass filter, with the lamp located with 5 cm away from the tube. Throughout the reaction conducted at 25 ^oC and ambient pressure, the mixture was continuously stirred magnetically. At hourly intervals, an aliquot of 20 μL was withdrawn from the aqueous solution for subsequent analysis.

2.2.8 Stability test

10 mg of modified TiO_2 was dispersed into a two-phase system containing 10 mL of BA and 4.0 mL of water. After bubbling the mixture with O_2 for 30 minutes at a rate of 20 mL min^{-1} in the absence of light, the mixture was then subjected to irradiation under visible light ($\lambda > 450$ nm). During the reaction for 8 h, the quantification of produced H_2O_2 was detected every 1 h.

2.2.9 Detection of produced H_2O_2

The H_2O_2 concentration was detected by a $[TiO(tpypH_4)]^{4+}$ complex titration method. A solution of aqueous HCl (50 mM, 100 mL) containing 3.4 mg of the $[TiO(tpypH_4)]^{4+}$ complex was prepared and served as the Ti-TPyP reagent. The sample solution was diluted 100-fold with distilled water, then the diluted solution (250 μL) was mixed with $HClO_4$ aqueous solution (4.8 M, 250 μL) and the Ti-TPyP solution (250 μL). After a brief interval, the mixture was further diluted to a final volume of 2.5 mL using purified water. The absorbance of this solution at a wavelength of 434 nm (designated as A_S) was measured employing a Shimadzu UV-2600

UV-Vis spectroscope. The absorbance of a blank solution, consisting of distilled water (250 μL) in place of the sample solution, was recorded as A_B. Then the amount of H_2O_2 was obtained based on ΔA_{434} (calculated by $\Delta A_{434} = A_B - A_S$) and the volume of the solution, following established procedures described in the literature.[32]

2.2.10 Detection of produced benzaldehyde

The amount of benzaldehyde (BAL) produced was quantified by gas chromatography (Shimadzu GC-2014) equipped with a flame ionization detector (FID) and an autosampler (Shimadzu AOC-20i). In the GC system, the injected samples were vaporized and separated as they passed through the column (TC-1) with the carrier gas N_2 and subsequently detected by the detector. The temperature of column, injector, and detector was set at 80 °C, 250 °C, and 250 °C, respectively. The solution used for GC analysis consisted of a mixture of 250 μL of reaction solution, 77 μL of acetonitrile solution containing 1 mg of biphenyl (internal standard), and 173 μL of acetonitrile. The concentration of BAL was determined by calculating the ratio of the peak areas of BAL to biphenyl and referencing the standard linear calibration curve.

2.2.11 Calculation process of CB and VB potentials

The potential of VB related to standard electrode (NHE, pH=0) can be calculated using the following **Equation 5**,[33]

$$E_{VB} = \varphi + E_{XPS\_VB} - 4.44 \qquad (5)$$

where E_{VB} is the potential of VB related to standard hydrogen electrode (vs NHE, pH=0), φ is electron work function of the XPS analyzer (4.50 eV), and E_{XPS_VB} is the value of XPS valence band spectra of samples.

The potential of CB is determined from the **Equation 6**,

$$E_{CB} = E_{VB} - E_g \qquad (6)$$

where E_{CB} is the potential of CB related to standard hydrogen electrode (vs NHE, pH=0), and

E_g is the bandgap energy of samples estimated by Tauc plots.

2.2.12 Calculation of the apparent quantum efficiency by a LED lamp

According to the literature,[34] the apparent quantum efficiency (AQE) can be calculated from **Equation 7**,

$$AQE = \frac{2 \times n_{H_2O_2} \times N_A}{N} \qquad (7)$$

where $n_{H_2O_2}$ is the number of H_2O_2 molecules produced, N_A is Avogadro number (6.02×10^{23}) and N represents the number of incident photons, which can be calculated from **Equation 8**,

$$N = \frac{light\ intensity(W\ cm^{-2}) \times illumination\ area(cm^2)}{\frac{hc}{\lambda}} \qquad (8)$$

where h is plank constant (6.626×10^{-34} J·s = 4.136×10^{-15} eV·s), c is the speed of light (3.0×10^8 m s^{-1}), λ is the wavelength of light (365, 405, and 450 nm). The illuminated area is 1 cm^2, and the light intensity is 100 mW cm^{-2}.

2.3 Results and discussion

2.3.1 Characterization results

Powder X-ray diffraction (XRD) patterns of 2,3-DN and OPA modified samples were shown in **Figures 1a and 1b**. The characteristic diffraction peak at 25.4° was assigned to (101) facet of anatase TiO_2.[35] 2,3-DN and OPA modification makes no novel peak displayed on TiO_2 material but with a weakened peak intensity of TiO_2(101), which implies reduced crystallinity and lattice expansion of TiO_2 due to the addition of 2,3-DN and OPA.

The N_2-physisorption isotherms of synthesized catalysts are presented in **Figure 2**. All samples show type IV adsorption isotherms with a rapid increase of adsorption volume at extremely low p/p_0, which indicates that all samples exhibit the typical mesoporous structures with a small part of micropores. Based on the non-porous properties of commercial TiO_2, the adsorption of N_2 is due to the space interface among the TiO_2 nanoparticles.[36] **Table 1** shows the structural properties of obtained samples, from which it is found that both specific surface area and pore volumes decreased apparently with the amount of OPA or 2,3-DN addition increases. This change demonstrates the successful connection of OPA and 2,3-DN on the surface of TiO_2, which is consistent with XRD results.[17]

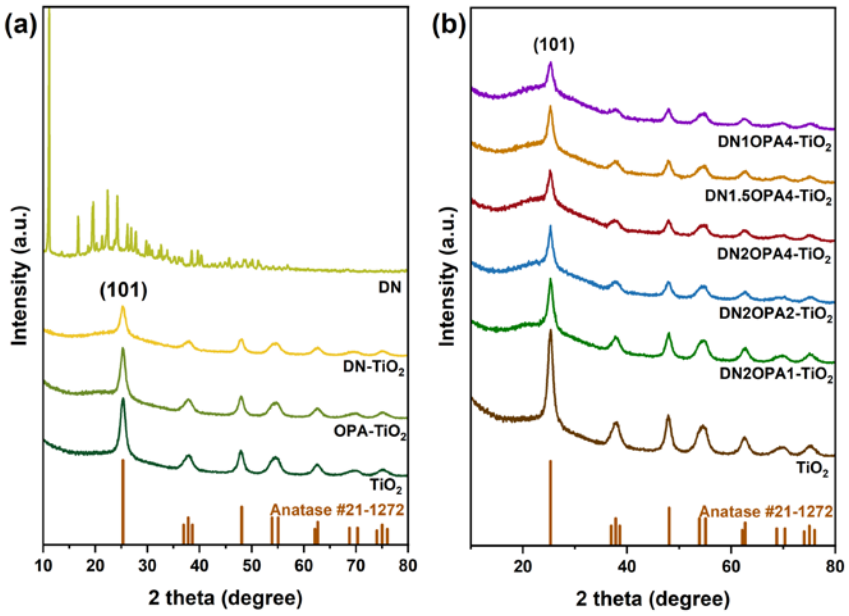

Figure 1. XRD patterns of (a) TiO_2, DN-TiO_2, OPA-TiO_2 and (b) 2,3-DN and OPA co-modified TiO_2 samples.

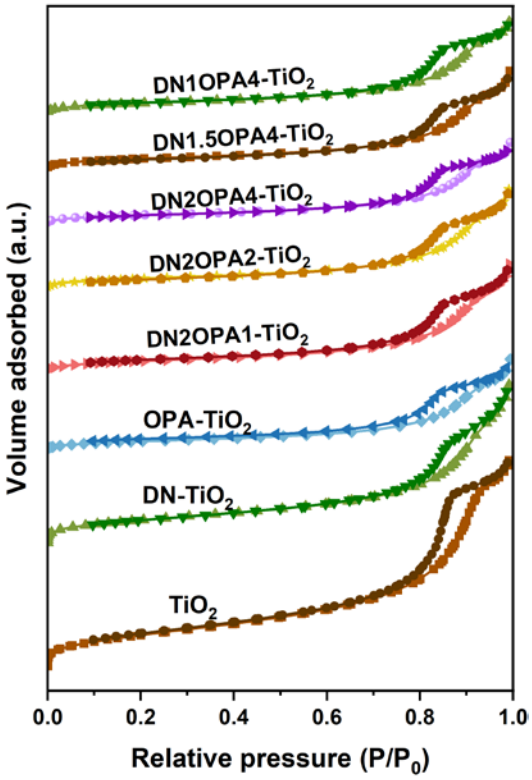

Figure 2. N_2-adsorption/desorption isotherms of 2,3-DN and OPA modified TiO_2 materials.

Table 1. Structural properties of TiO_2, 2,3-DN and OPA modified TiO_2 catalysts.

Samples	S_{BET} (m^2 g^{-1})[a]	D_p (nm)[b]	V_p (cm^3 g^{-1})[c]
DN1OPA4-TiO_2	72.6	0.93	0.33
DN1.5OPA4-TiO_2	73.0	0.91	0.34
DN2OPA4-TiO_2	61.4	0.96	0.28
DN2OPA2-TiO_2	74.6	0.91	0.38
DN2OPA1-TiO_2	80.3	0.91	0.38
OPA-TiO_2	64.8	1.18	0.31
DN-TiO_2	193.1	0.56	0.58
TiO_2	285.5	0.59	0.77

[a] Surface area (S_{BET}) determined using the BET method.

[b] Average pore diameter (D_p) calculated using the Saito Foley (SF) method.

[c] Total pore volume (V_p) reported at a relative pressure of $p/p_0 = 0.99$.

The UV-vis DRS was employed to evaluate the optical absorption properties of photocatalysts. As depicted in **Figures 3a and 3b**, OPA-TiO_2 appears a little visible light harvesting compared to TiO_2, whereas DN-TiO_2 shows significant visible-light-sensitive properties. In addition, all OPA and 2,3-DN co-modified catalysts could be light-responsive above 450 nm of wavelength, which indicates that the electrons of these samples could be activated more easily than that of TiO_2 and they are suitable for photocatalytic production of H_2O_2 induced by visible light.[33]

XPS measurement (**Figure 4**) was conducted to determine the electronic states of modified TiO_2. The peaks observed at approximately 465.1 eV and 459.4 eV in **Figures 4a and 4b** correspond to the Ti $2p_{1/2}$ and Ti $2p_{3/2}$ energy levels, respectively.[37] The addition of OPA apparently weakens the peak intensities of Ti 2p spectrum, which is attributed to the surface fabrication of TiO_2 with OPA leading to degraded signals.[17] Combined with the XPS P 2p spectra in **Figure 4c**, the appearance of P 2p peak at 133.4 eV on TiO_2 materials confirms the successful modification with OPA. Moreover, compared to TiO_2, the binding energy of Ti 2p in DNxOPA4-TiO_2 samples all show the negative shifts of about 0.4 eV (**Figure 4a**). The similar shifts for DN2OPAy-TiO_2 catalysts are also found with the amount of OPA increasing (**Figure 4b**), which illustrates the interaction between OPA, 2,3-DN and TiO_2 owing to the formation of Ti-O-P and Ti-O-aromatic carbon (Ti-O-ArC) ligands as shown in **Scheme 1**, respectively.[30,38] The photo-generated electrons of OPA and 2,3-DN are able to transfer to Ti through the ligands, which act as electron-donators during the photocatalytic reaction.[30,39]

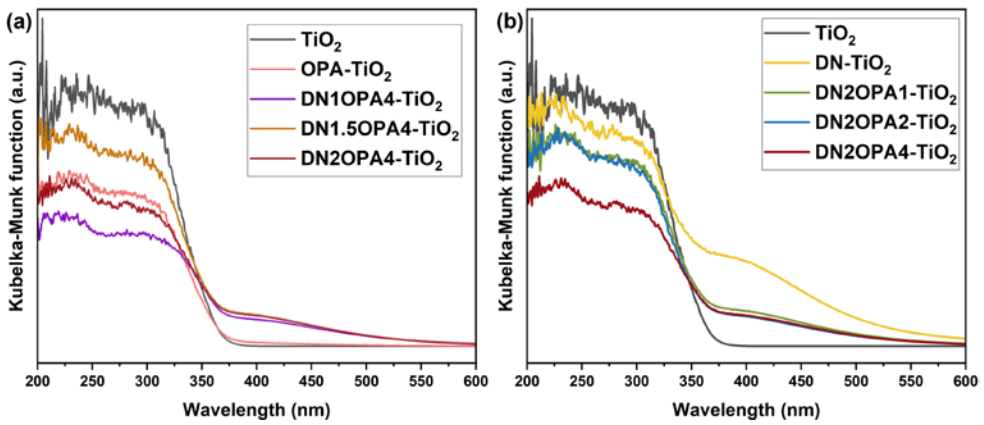

Figure 3. UV-vis DRS of (a) DNxOPA4-TiO_2 (x = 0, 1, 1.5, and 2) and (b) DN2OPAy-TiO_2 (y = 0, 1, 2, and 4) samples.

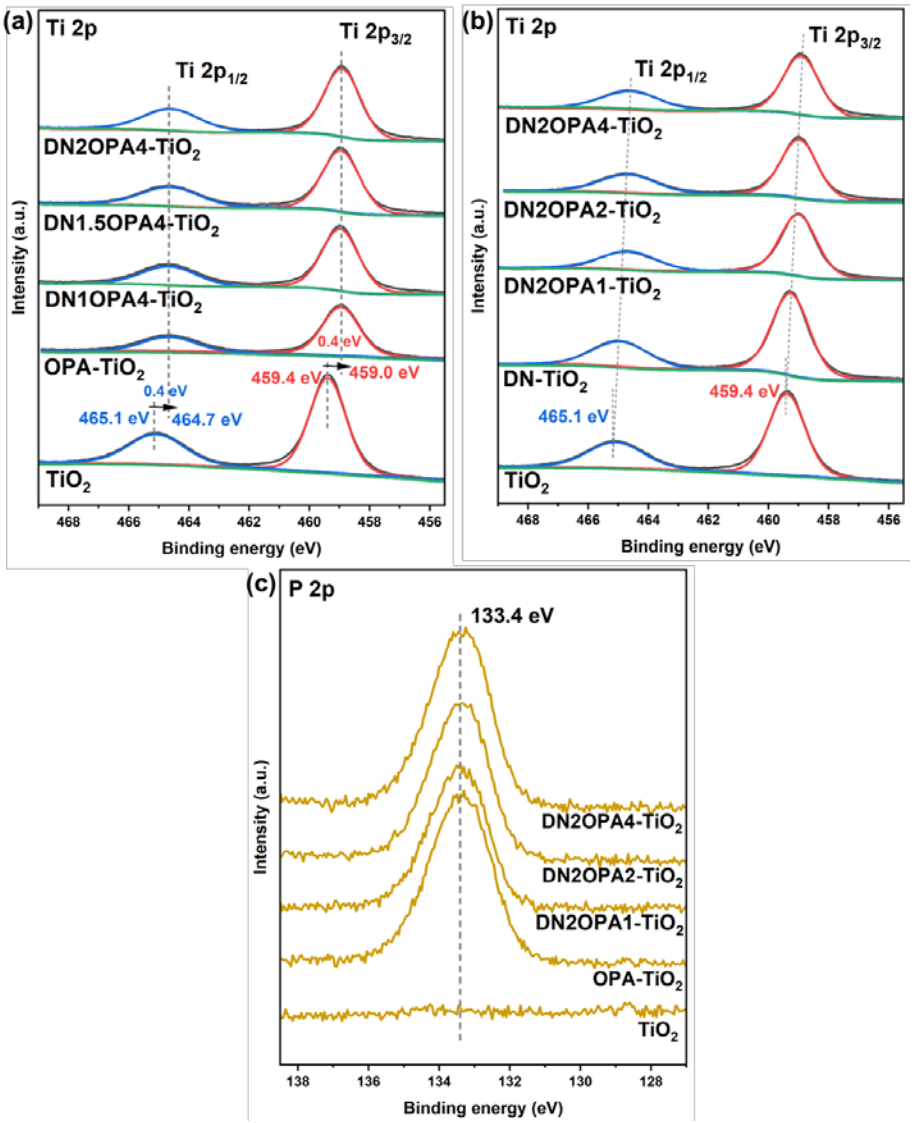

Figure 4. XPS Ti 2p spectra of (a) DNxOPA4-TiO_2 (x = 0, 1, 1.5, and 2) and (b) DN2OPAy-TiO_2 (y = 0, 1, 2, and 4) samples. (c) P 2p spectra of DN2OPAy-TiO_2 (y = 0, 1, 2, and 4) samples.

The grafting of 2,3-DN and OPA on TiO_2 could also be declared in FTIR results (**Figure 5**). The absorption bands at 2920-2850 cm^{-1} and 1470 cm^{-1} in pure OPA are due to the presence of n-octyl groups (-$C_{18}H_{37}$), showing the stretching vibrations of -CH_2- and bending band of C-H, respectively.[38] As observed in **Figure 5b**, the intensities of -CH_2- peaks become stronger with increasing the content of OPA in DN2OPAy-TiO_2 samples, which is consistent with the results obtained from the TG analysis (**Figure 6 and Table 2**). The peaks at 950 cm^{-1} and between 1080-1000 cm^{-1} are characteristic of the stretching vibration of P-OH and P-O, respectively.[38] Compared to pure OPA, the peak of P-OH disappears, and the sharp peaks of P-O become broader in OPA-modified TiO_2, implying the formation of Ti-O-P bonds between

OPA and TiO_2.

For 2,3-DN modified catalysts, the characteristic peaks of phenolic groups C-OH at 1300-1150 cm^{-1} and stretching vibrations of aromatic ring C-C/C=C at 1500-1360 cm^{-1} are weakened compared with free 2,3-DN.[39] However, the existence of phenolic groups in DNxOPA4-TiO_2 and DN2OPAy-TiO_2 suggests that the surface complexes of Ti-O-ArC were formed by the dehydration reaction as illustrated in **Scheme 1**.[30] The above analysis of XPS and FTIR provides solid evidence for the coordination of 2,3-DN and OPA on the surface of TiO_2 in 2,3-DN and OPA co-modified TiO_2 materials.

As presented in **Figure 7**, the hydrophobicity of modified TiO_2 samples was evaluated by measuring the water contact angles (WCA). The original TiO_2 is hydrophilic given by the WCA of nearly 0°. Although the WCA of DN-TiO_2 is 10° (< 90°), it can also disperse in the BA phase during the reaction as shown in the inert digital photo of **Figure 7b**. By contrast, the addition of OPA significantly achieves higher WCA exceeding 140° of DN2OPAy-TiO_2 as seen in **Figures 7c-7h**, which reveals that OPA modification is efficient to endow TiO_2 with hydrophobic nature.

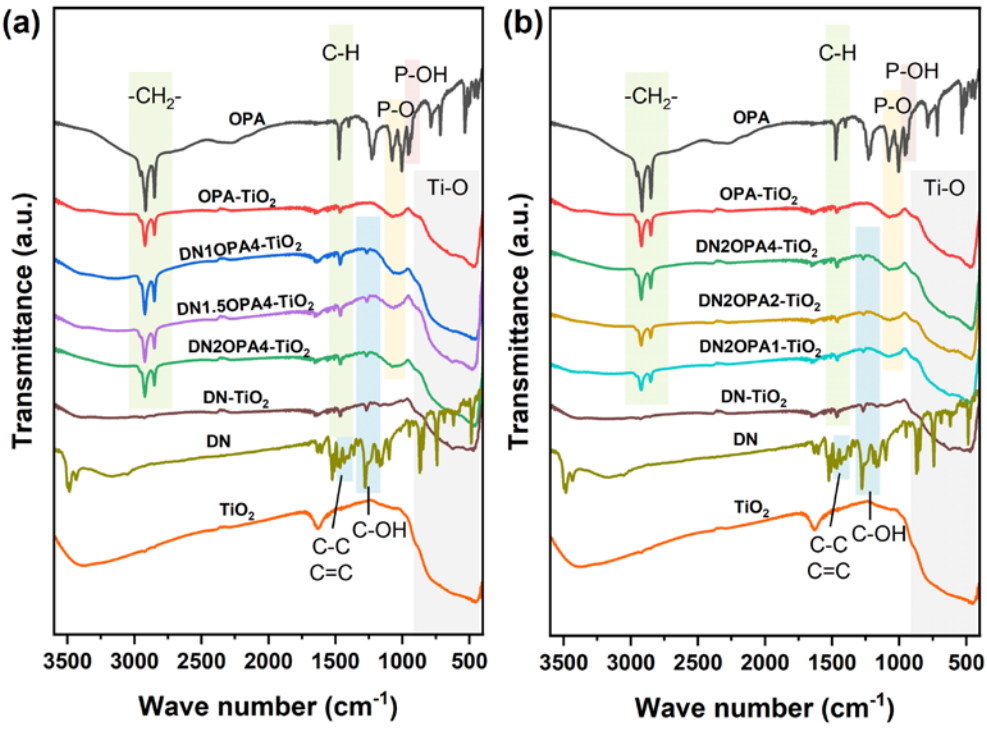

Figure 5. FTIR spectra of (a) DNxOPA4-TiO_2 (x = 0, 1, 1.5, and 2) and (b) DN2OPAy-TiO_2 (y = 0, 1, 2, and 4) samples.

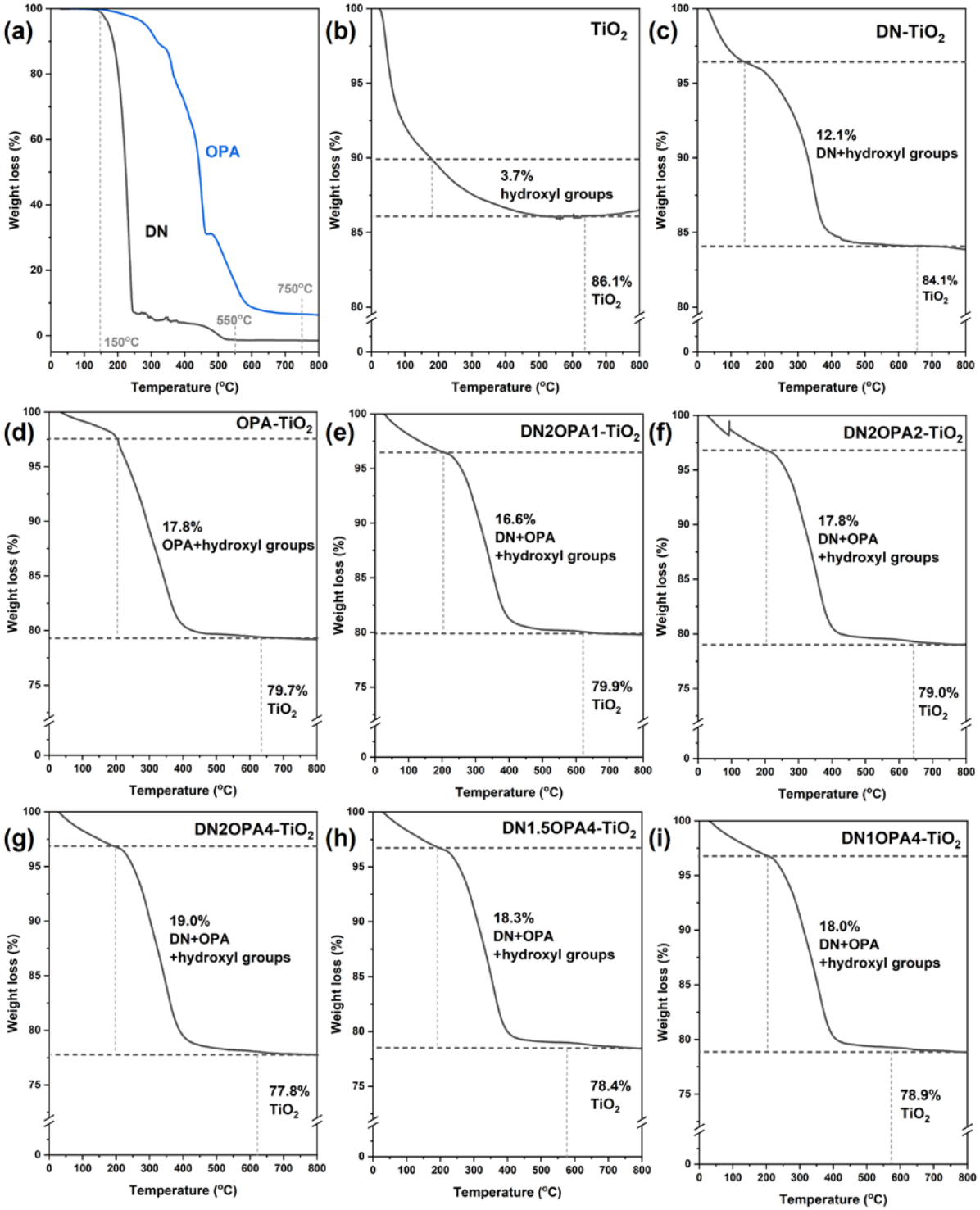

Figure 6. TG profiles of (a) 2,3-DN and OPA, (b) TiO_2, (c) DN-TiO_2, (d) OPA-TiO_2, (e) DN2OPA1-TiO_2, (f) DN2OPA2-TiO_2, (g) DN2OPA4-TiO_2, (h) DN1.5OPA4-TiO_2 and (i) DN1OPA4-TiO_2.

Calculation of the relative contents of 2,3-DN and OPA in DNxOPA4-TiO_2 (x=0, 1, 1.5 and 2) and DN2OPAy-TiO_2 (y=0, 1, 2 and 4) samples:

TG measurements were conducted to estimate the relative amounts of 2,3-DN and OPA grafted on the TiO_2 surface in DNxOPA4-TiO_2 and DN2OPAy-TiO_2 (**Figure 6**).

The first weight loss up to 200 ^oC in every sample is attributed to the removal of residual organic groups and water absorbed on the surface of samples. For TiO_2 (**Figure 6b**), the weight loss above 200 ^oC is due to the elimination of hydroxyl groups with content of 4.1% [3.7%/(3.7%+86.1%)], in which the weight of residual TiO_2 is 86.1 %.

For DN-TiO_2 (**Figure 6c**), the weight loss of removing 2,3-DN and hydroxyl groups accounts for 12.5% [12.1%/(12.1%+84.1%)]. So the amount of 2,3-DN upon DN-TiO_2 is 8.4% [12.5%-4.1%]. According to the similar method, the amount of OPA in OPA-TiO_2 obtained (**Figure 6d**) is 14.1% [17.8%/(17.8%+79.7%)-4.1%].

For the co-modified catalysts, we assumed that the actual amounts of 2,3-DN and OPA in DN2OPA4-TiO_2 were in accordance with the mass ratio when added separately, because of the similar concentration of 2,3-DN or OPA solution of ethanol during the preparation experiments. Therefore, for DN2OPA4-TiO_2 (**Figure 6g**), the amount ratio of 2,3-DN and OPA is 0.6 (8.4%/14.1%). Combined with the total amount of 2,3-DN, OPA and hydroxyl groups is 19.6% [19.0%/(19.0%+77.8%)], the amount of 2,3-DN upon DN2OPA4-TiO_2 can be easily calculated as 5.8% [(19.6%-4.1%)*(0.6/1.6)] and that of OPA is 9.7% [19.6%-4.1%-5.8%].

For DN2OPAy-TiO_2 (y=1 and 2) catalysts, the amount of 2,3-DN is regarded as same as DN2OPA4-TiO_2, so the amount of OPA of DN2OPA1-TiO_2 (**Figure 6e**) is 7.3% [16.6%/(16.6%+79.9%)-5.8%-4.1%], and that of DN2OPA2-TiO_2 (**Figure 6f**) is 8.5% [17.8%/(17.8%+79.0%)-5.8%-4.1%]. Likewise, the amount of OPA is regarded as same as DN2OPA4-TiO_2 for DNxOPA4-TiO_2 (x=1 and 1.5). Then the amount of 2,3-DN in DN1OPA4-TiO_2 (**Figure 6i**) is 4.6% [17.8%/(17.8%+78.9%)-9.7%-4.1%] and that in DN1.5OPA4-TiO_2 (**Figure 6h**) is 5.1% [18.3%/(18.3%+78.4%)-9.7%-4.1%].

The calculated results were summarized as shown in **Table 2**.

Table 2. Relative contents of 2,3-DN and OPA in modified TiO_2 catalysts.

Catalysts	Relative content of 2,3-DN /%	Relative content of OPA /%
DN-TiO_2	8.4	--
OPA-TiO_2	--	14.1
DN2OPA1-TiO_2	5.8	7.3
DN2OPA2-TiO_2	5.8	8.5
DN2OPA4-TiO_2	5.8	9.7
DN1.5OPA4-TiO_2	5.1	9.7
DN1OPA4-TiO_2	4.6	9.7

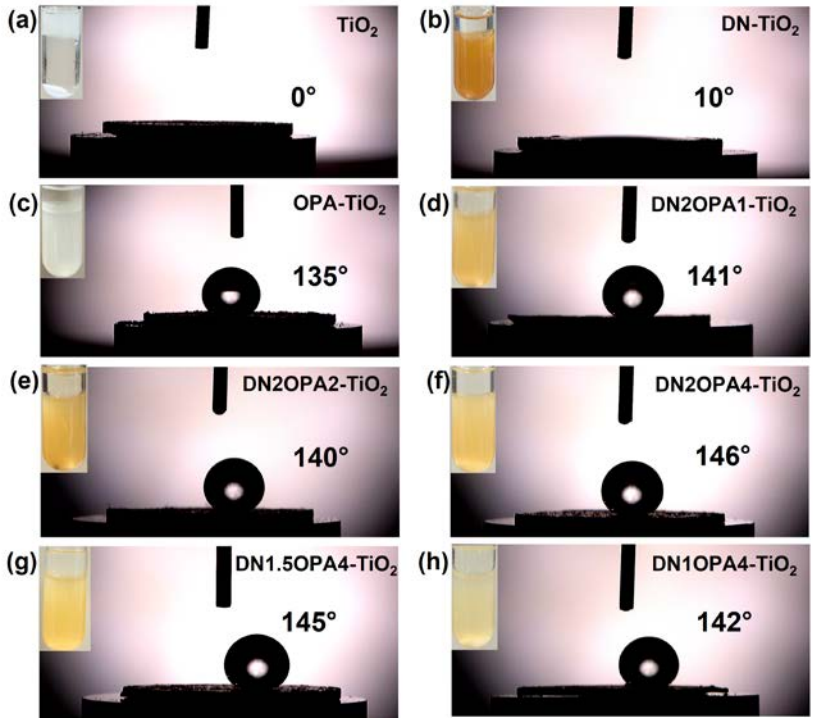

Figure 7. Water contact angles of (a) TiO_2, (b) DN-TiO_2, (c) OPA-TiO_2, (d) DN2OPA1-TiO_2, (e) DN2OPA2-TiO_2, (f) DN2OPA4-TiO_2, (g) DN1.5OPA4-TiO_2 and (h) DN1OPA4-TiO_2. (Sample preparation: The tablets of samples were prepared by pressing powders of about 20 mg at 5 MPa for 10 s. Then 20 μL of water droplet was dropped on the tablets of samples.)

2.3.2 Photocatalytic activity evaluation

Photocatalytic H_2O_2 production was conducted in a two-phase setup under photoirradiation ($\lambda > 450$ nm). Original TiO_2 was dispersed in the water phase while hydrophobically modified TiO_2 materials were present in the BA phase, as depicted in the digital photos of **Figure 7**. During the reaction, H_2O_2 produced was transferred to the aqueous solution, whereas BAL, the oxidation product of BA, remained in the organic phase.

The effect of 2,3-DN modification on TiO_2:

The concentration of H_2O_2 produced for DNxOPA4-TiO_2 catalysts was collected at a certain period of time and shown in **Figures 8a and 8b**. OPA-TiO_2 shows a little activity under visible-light irradiation, while 2,3-DN-doping promotes the activity of H_2O_2 production significantly and the H_2O_2 concentration exhibits a volcanic curve with the amount of 2,3-DN increases. It implies that 2,3-DN makes it much easier for the catalysts to generate more electrons under visible light for O_2 reduction than TiO_2 and OPA-TiO_2 catalysts, which is due to the visible light absorption property as confirmed by the UV-vis DRS results.[28–30]

Specifically, the H_2O_2 concentration over DNxOPA4-TiO_2 samples decreased after reacting for 4 h. Apart from the decomposition of H_2O_2 by TiO_2, it can be judged from the digital photos of the catalysts before and after reaction (**Figure 8d**) that the grafted 2,3-DN is easy to be detached during the reaction, which reduces the absorption of visible light and leads to a decrease in H_2O_2 production.

However, when the content of OPA increases to 9.7% in DN2OPA4-TiO_2, the activities either in H_2O_2 or in BAL production decrease obviously compared to other 2,3-DN-modified TiO_2 catalysts as present in **Figures 8b and 8c**. This is due to fewer active sites exposed for H_2O_2 production, which is resulted from the smaller specific surface area and pore volume of DN2OPA4-TiO_2. Similarly, the smaller surface area and pore volume of DNxOPA4-TiO_2 catalysts suppress the mass transfer of BAL,[17] as evidenced by the results of pore structure analysis as shown in **Table 1** and provided a lower concentration of BAL (**Figure 8c**).

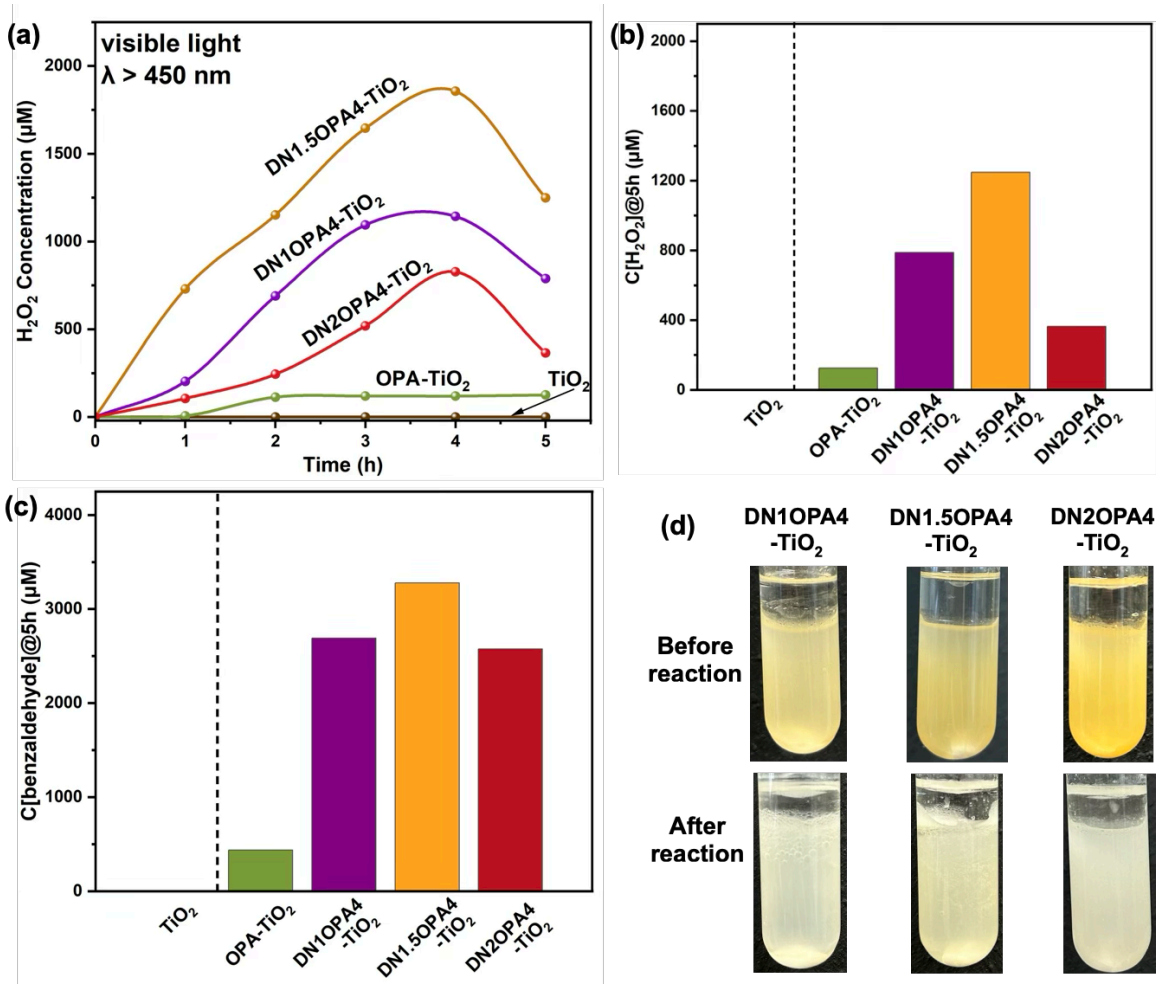

Figure 8. (a, b) Activity test for H_2O_2 production and (c) BAL production in the two-phase system composed of BA (5 mL) and water (2 mL) under photoirradiation (λ > 450 nm) using DNxOPA4-TiO_2 (x = 0, 1, 1.5, and 2) samples; (d) The digital photos of DNxOPA4-TiO_2 before and after reaction.

The effect of OPA modification on TiO_2:

To explore the influence of OPA grafting on the H_2O_2 production reaction using DN2OPAy-TiO_2 catalysts, the concentration of H_2O_2 was monitored throughout the reaction (**Figures 9a and 9b**). DN-TiO_2 shows much higher activity in H_2O_2 production than TiO_2 under visible light, which indicates that 2,3-DN modification endows TiO_2 with a much stronger capacity for visible light absorption as mentioned before. However, DN-TiO_2 was deactivated rapidly after 2 h of reaction, which is attributed to the instability of Ti-O-ArC ligands between 2,3-DN and TiO_2 during the reaction process.

After grafting OPA, DN2OPA1-TiO_2 could continue to produce H_2O_2 for 3 h, although the activity was a little lower than that of DN-TiO_2, and the highest point of the activity was shifted back. It illustrates that the effect of OPA addition on the stability of the catalyst. With the amount of OPA added increases, DN2OPA2-TiO_2 showed a continuous increase in activity even for 5 h, reflecting the better catalytic activity and stability of OPA-modified catalysts. OPA grafting imparts the hydrophobic property in the 2,3-DN and OPA co-modified TiO_2, as well as enhances the stability of catalysts and makes it active under visible light irradiation.

As presented in **Figures 9b and 9c**, DN2OPA2-TiO_2 displays higher activity in H_2O_2 production than other DN2OPAy-TiO_2 catalysts without deactivation for 5 h of reaction, which illustrates that modification with relative contents of 5.8% for 2,3-DN and 8.5% for OPA is optimal for TiO_2. According to similar results of H_2O_2 production as DNxOPA4-TiO_2 (**Figure 8a**), DN2OPA4-TiO_2 showed the lower activity performance, which is attributed to the limited availability of exposed active sites caused by the smallest surface area and pore volumes. Besides, compared to the continuous H_2O_2 production over DN2OPA2-TiO_2 in an O_2-saturated solution, H_2O_2 production was not detected in the absence of oxygen (**Figure 10a**). It is evident that H_2O_2 was photocatalytically generated via O_2 reduction over the modified TiO_2 materials. In addition, the apparent quantum efficiency (AQE) was calculated with different incident light wavelengths, containing 365, 405, and 450 nm. As shown in **Figure 10b**, the AQE for H_2O_2 production at 450 nm reached 0.22%.

Furthermore, a correlation is observed between the decrease of BAL concentration and the increase in OPA content in DN2OPAy-TiO_2 catalysts. It can also be explained by the impact of the catalysts' pore volumes on the mass transfer of BAL, as evidenced by the declining trend in surface area and pore volumes as summarized in **Table 1**.

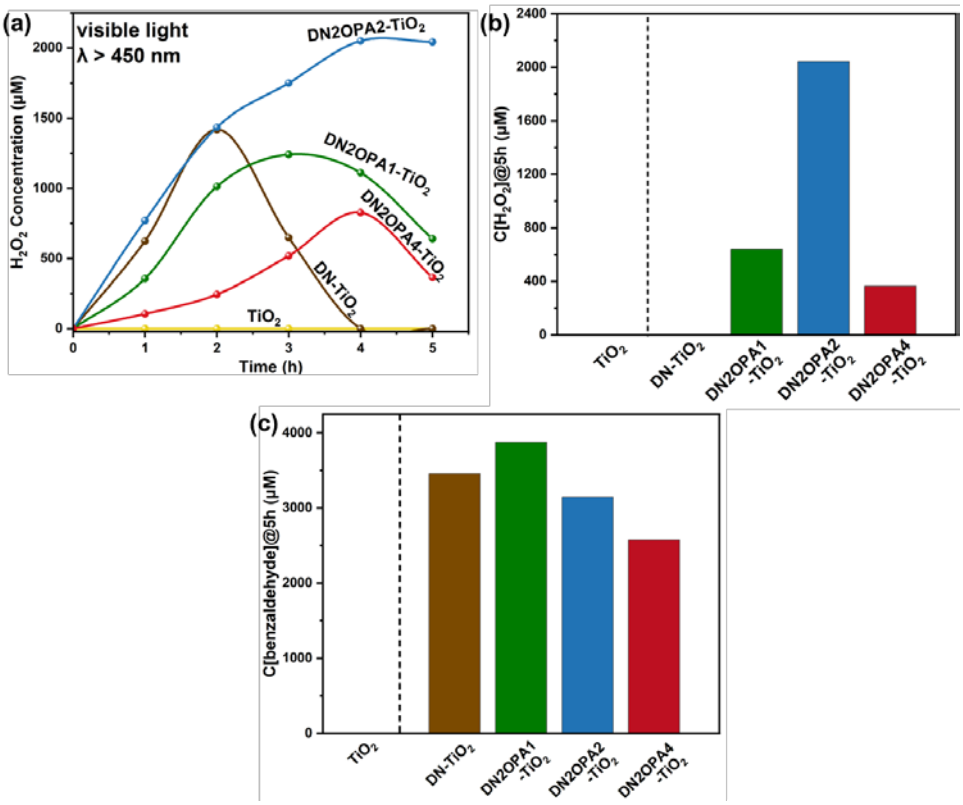

Figure 9. (a, b) Activity test for H_2O_2 production and (c) BAL production in the two-phase system composed of BA (5 mL) and water (2 mL) under photoirradiation (λ > 450 nm) using DN2OPAy-TiO_2 (y = 0, 1, 2, and 4) samples.

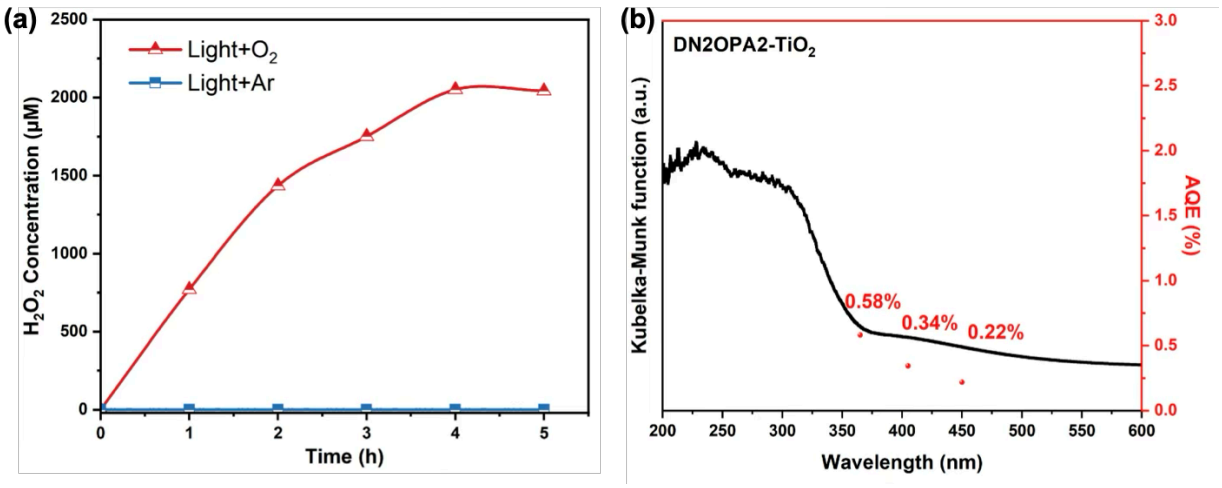

Figure 10. (a) Time courses of H_2O_2 production using DN2OPA2-TiO_2 in various reaction conditions. (b) Apparent quantum efficiency (AQE) obtained with different incident light wavelengths (365, 405, and 450 nm) versus UV-vis spectra of DN2OPA2-TiO_2. (5 mg catalyst dispersed in 5 mL BA and 2 mL water with irradiation for 1 h)

2.3.3 Stability test of DN-TiO_2 and DN2OPA2-TiO_2

The results of the stability test for 8 h were displayed in **Figure 11a**. DN2OPA2-TiO_2 still retains increasing H_2O_2 production during the 8 h-reaction, while DN-TiO_2 exhibits decreased activity after 4 h. This is attributed to the enhanced stability of the hydrophobic TiO_2 structure in the organic phase, achieved through the fabrication of OPA, which is verified by the UV-vis DRS and FTIR characterizations of used catalysts.

As presented in **Figure 12a**, the used DN2OPA2-TiO_2 has a stronger capacity for visible light absorption compared with DN-TiO_2 used. Combined with FTIR results (**Figure 12b**), the decrease in the visible light response is ascribed to the fracture of surface complexes Ti-O-ArC and the formation of phenolic groups C-OH, resulting in the re-emerging peaks of phenolic groups at 1300-1150 cm^{-1}.[30] The FTIR spectra of DN2OPA2-TiO_2 before and after the reaction manifests that the peaks at 2920-2850 cm^{-1} representing -CH_2- groups of OPA are still retained (**Figure 12c**), confirming its retained hydrophobicity.

Usually, decomposition of H_2O_2 occurs during the photocatalytic H_2O_2 production reaction using TiO_2 material, causing reduced H_2O_2.[18,40] This phenomenon could be inhibited by separating the TiO_2 catalysts from produced H_2O_2. Therefore, a H_2O_2 decomposition test was performed in the two-phase system (**Figure 11b**). DN2OPA2-TiO_2 exhibits higher H_2O_2 concentration and tends to be stable during the test in the dark, while the H_2O_2 concentration in which DN-TiO_2 exists continuously declines. This demonstrates that hydrophobic TiO_2 modified by OPA in the organic phase does suppress the decomposition of H_2O_2, thereby maintaining the higher H_2O_2 production. Although 2,3-DN and OPA-modified TiO_2 shows moderately advantageous activity compared with other typical TiO_2-based materials as summarized in **Table 3**, the use of TiO_2 for two-phase photocatalytic synthesis of H_2O_2 provides a novel perspective for the modification of semiconductors.

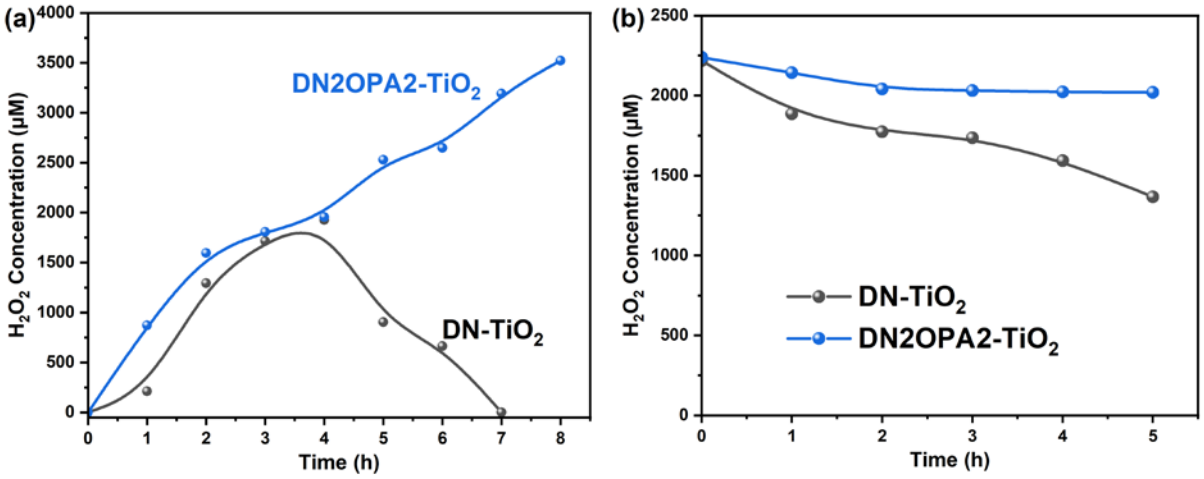

Figure 11. (a) Stability test for H_2O_2 production and (b) H_2O_2 decomposition using DN-TiO_2 and DN2OPA4-TiO_2 samples. (Conditions of H_2O_2 decomposition test: 5 mg of catalysts in the two-phase system composed of BA (5 mL) and water (2 mL) in the dark.)

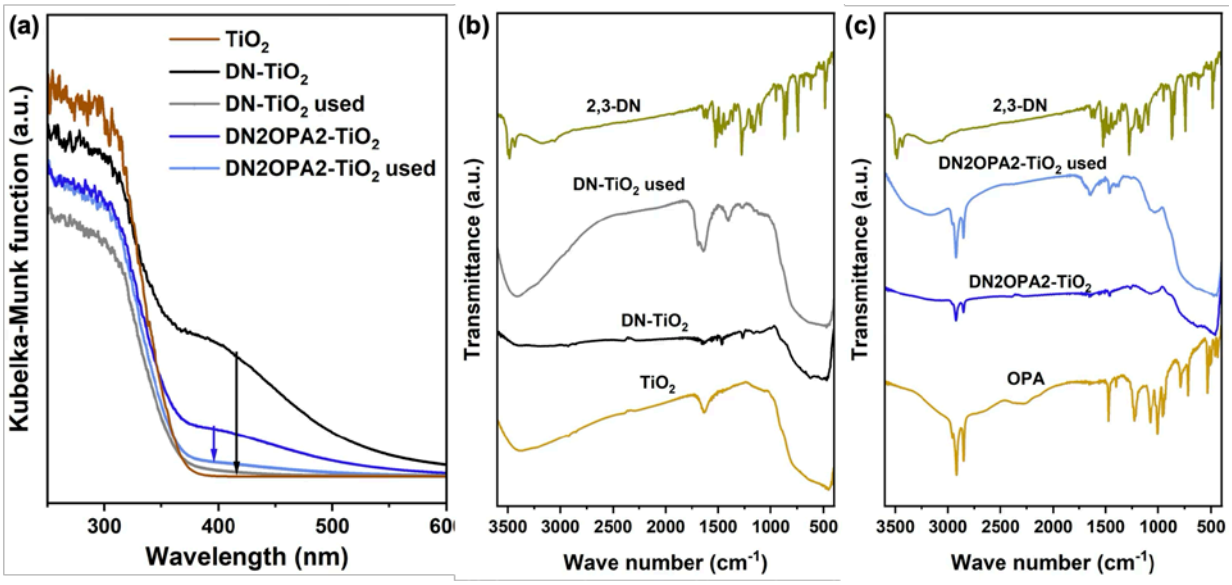

Figure 12. (a) UV-vis DRS of DN-TiO_2 and DN2OPA2-TiO_2 before and after reaction. FTIR spectra of (b) DN-TiO_2 and (c) DN2OPA2-TiO_2 before and after reaction.

Table 3. Activity comparison with other reported TiO_2-based photocatalysts for H_2O_2 production.

Catalysts	Reaction condition	Irradiated wavelength (nm)	H_2O_2 production ($\mu mol\ h^{-1}\ g^{-1}$)	Reference
SN-GQD/ TiO_2	2-propanol/water (3:47, pH=3.0)	≥ 420	110	Zheng et al.[9]
Nf-SNG /TiO_2	2-propanol/water (3:47, pH=3.0)	≥ 420	135	Zheng et al.[21]
TiO_2/In_2S_3	Ethanol/water (1:9)	≥ 365	752	Yang et al.[41]
B-doped g-C_3N_4/TiO_2	Ethanol/water (1:19)	≥ 400	917	Behera et al.[42]
DNOPA-TiO_2	Benzyl alcohol/water (5:2, two-phase)	≥ 450	205	This work

2.3.4 Proposed reaction mechanism of photocatalytic H_2O_2 production over modified TiO_2

To explore the electron transfer process and proposed reaction mechanism, the bandgap energies and valence band level of modified TiO_2 were obtained by UV-vis DRS characterization and XPS valence band diagram, respectively (**Figure 13**). The corresponding band structures of TiO_2, DN-TiO_2 and DN2OPA2-TiO_2, calculated from the results of Tauc plots and XPS valence band spectra.

As shown in **Figures 13a**, a narrower bandgap was observed in the spectra of DN-TiO_2 and DN2OPA2-TiO_2, which contributes to the extended light-responsive range, on the basis of UV-vis DRS results (**Figure 3**). Besides, the energy levels structure (**Figure 13c**) of DN-TiO_2 and DN2OPA2-TiO_2 clearly show a negative shift in both VB and CB band positions compared to TiO_2. Therefore, the higher activity of modified TiO_2 may benefit from the well-tuned band structure, in which 2,3-DN provides more electrons for driving the activation of the $O_2^{\bullet-}$

superoxide radical.[43]

In addition, the lowest conductive band of these catalysts (-0.80 V vs NHE), shown in **Figure 13c**, is more negative than the redox potential of the single-electron O_2 reduction (-0.33 V vs NHE), whereas the highest valence band (2.18 V vs NHE) is more positive than the redox potential of BA oxidation (1.98 V vs NHE). These results suggest that the production of H_2O_2 by O_2 reduction and the BA oxidation are thermodynamically favorable with TiO_2 and the modified TiO_2 materials.

Combined with the referred literature,[44] it can be seen that during the reaction process with DN-TiO_2, the photogenerated electrons transfer from the π-π bond of 2,3-DN to Ti. Along with the valence change from Ti^{4+} to Ti^{3+}, the electrons are transferred to O_2 for ORR reaction, whereas BA molecules react with positively charged holes (h^+) to produce BAL.

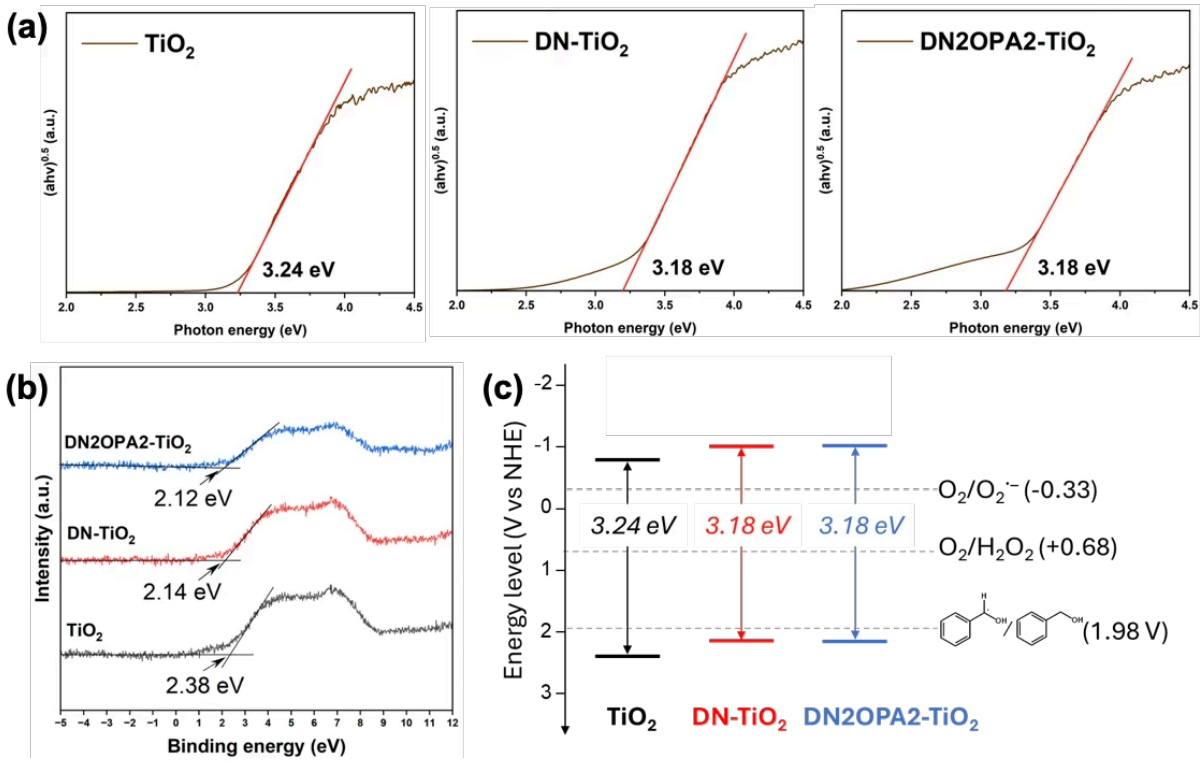

Figure 13. (a) The estimated band gap energies determined from the $(ahv)^{0.5}$ versus photon-energy plot, (b) XPS valence band spectra, and (c) estimated energy levels of TiO_2, DN-TiO_2, and DN2OPA2-TiO_2.

2.4 Conclusions

A series of 2,3-DN and OPA co-modified TiO_2 materials with unique hydrophobic properties was synthesized and utilized for photocatalytic H_2O_2 production in a two-phase system. The addition of 2,3-DN promotes the formation of charge-transfer complexes connected with the surface of TiO_2, which enables TiO_2 to absorb visible light and provides electrons for O_2 reduction reaction (ORR). OPA-modification imparts TiO_2 stable and hydrophobic property allowing it to exist in the organic phase, which inhibits the H_2O_2 decomposition. As a result, the co-modified DN2OPA2-TiO_2 exhibited higher activity and stability for H_2O_2 production (205 μmol g^{-1} h^{-1}) over an 8-hour reaction under visible light ($\lambda >$ 450 nm). This study broadened the scope of hydrophobic TiO_2 material applications in the realm of photocatalytic H_2O_2 production.

2.5 References

1 J. M. Campos-Martin, G. Blanco-Brieva and J. L. G. Fierro, *Angew. Chem. Int. Ed.*, 2006, **45**, 6962–6984.

2 W. Zhan, L. Ji, Z. mei Ge, X. Wang and R. tao Li, *Tetrahedron*, 2018, **74**, 1527–1532.

3 M. Ksibi, *Chem. Eng. J.*, 2006, **119**, 161–165.

4 R. N. Gurram, M. Al-Shannag, N. J. Lecher, S. M. Duncan, E. L. Singsaas and M. Alkasrawi, *Bioresour. Technol.*, 2015, **192**, 529–539.

5 K. Mase, M. Yoneda, Y. Yamada and S. Fukuzumi, *Nat. Commun. 2016 71*, 2016, **7**, 1–7.

6 S. Yang, A. Verdaguer-Casadevall, L. Arnarson, L. Silvioli, V. Čolić, R. Frydendal, J. Rossmeisl, I. Chorkendorff and I. E. L. Stephens, *ACS Catal.*, 2018, **8**, 4064–4081.

7 J. García-Serna, T. Moreno, P. Biasi, M. J. Cocero, J. P. Mikkola and T. O. Salmi, *Green Chem.*, 2014, **16**, 2320–2343.

8 H. Hou, X. Zeng and X. Zhang, *Angew. Chem. Int. Ed.*, 2020, **59**, 17356–17376.

9 L. Zheng, H. Su, J. Zhang, L. S. Walekar, H. Vafaei Molamahmood, B. Zhou, M. Long and Y. H. Hu, *Appl. Catal. B Environ.*, 2018, **239**, 475–484.

10 V. Smeets, L. Ben Mustapha, J. Schnee, E. M. Gaigneaux and D. P. Debecker, *Mol. Catal.*, 2018, **452**, 123–128.

11 J. Lim, H. Kim, J. Park, G. H. Moon, J. J. M. Vequizo, A. Yamakata, J. Lee and W. Choi, *Environ. Sci. Technol.*, 2020, **54**, 497–506.

12 Z. Teng, Q. Zhang, H. Yang, K. Kato, W. Yang, Y.-R. Lu, S. Liu, C. Wang, A. Yamakata, C. Su, B. Liu and T. Ohno, *Nat. Catal.*, 2021, **4**, 374–384.

13 K. Fuku, Y. Miyase, Y. Miseki, T. Gunji and K. Sayama, *RSC Adv.*, 2017, **7**, 47619–47623.

14 S. Thakur, T. Kshetri, N. H. Kim and J. H. Lee, *J. Catal.*, 2017, **345**, 78–86.

15 P. Sun, Z. Mo, H. Chen, Y. Song, J. Liu, W. Yin, H. Dai, Z. Chen, H. Li and H. Xu, *Inorg. Chem. Front.*, 2022, **9**, 1701–1707.

16 Y. Isaka, Y. Kawase, Y. Asutaka Kuwahara, K. Mori and H. Yamashita, *Angew. Chem.*

Int. Ed., 2019, **131**, 5456–5460.

17 X. Chen, Y. Kuwahara, K. Mori, C. Louis and H. Yamashita, *J. Mater. Chem. A*, 2020, **8**, 1904–1910.

18 L. Zheng, X. Yu, M. Long and Q. Li, *Chin. J. Catal.*, 2017, **38**, 2076–2084.

19 Z. Mo, G. Wu, P. Yan, X. Zhu, J. Qian, Y. Lei, L. Xu, H. Xu and H. Li, *Mater. Today Chem.*, 2022, **25**, 100956.

20 Z. Mo, Z. Miao, P. Yan, P. Sun, G. Wu, X. Zhu, C. Ding, Q. Zhu, Y. Lei and H. Xu, *J. Colloid Interface Sci.*, 2023, **645**, 525–532.

21 L. Zheng, J. Zhang, Y. H. Hu and M. Long, *J. Phys. Chem. C*, 2019, **123**, 13693–13701.

22 S. T. T. Le, W. Khanitchaidecha and A. Nakaruk, *Bull. Mater. Sci.*, 2016, **39**, 569–572.

23 H. Sheng, H. Ji, W. Ma, C. Chen and J. Zhao, *Angew. Chem. Int. Ed.*, 2013, **52**, 9686–9690.

24 J. Wan, W. Chen, C. Jia, L. Zheng, J. Dong, X. Zheng, Y. Wang, W. Yan, C. Chen, Q. Peng, D. Wang, Y. Li, J. W. Wan, W. X. Chen, C. Chen, Q. Peng, D. S. Wang, Y. D. Li, C. Y. Jia, L. R. Zheng, J. C. Dong, X. S. Zheng, W. S. Yan and Y. Wang, *Adv. Mater.*, 2018, **30**, 1705369.

25 J. Bae, H.-J. Jeon, S.-H. Cho, Y. Cho, S.-E. Lee and T.-O. Kim, *Appl. Surf. Sci.*, 2023, **621**, 156823.

26 Q. Hu, Y. Liu, W. Li, Y. Wang, W. Liao, H. Zou, J. Li and X. Huang, *Chem. Eng. J.*, 2023, **451**, 138670.

27 Y. Yamamoto, M. Fukui, A. Tanaka, K. Hashimoto and H. Kominami, *Catal. Sci. Technol.*, 2019, **9**, 966–973.

28 M. Fukui, Y. Omori, S. ya Kitagawa, A. Tanaka, K. Hashimoto and H. Kominami, *J. Catal.*, 2019, **374**, 36–42.

29 S. K. Parayil, H. S. Kibombo and R. T. Koodali, *Catal. Today*, 2013, **199**, 8–14.

30 T. Kamegawa, H. Seto, S. Matsuura and H. Yamashita, *ACS Appl. Mater. Interfaces*, 2012, **4**, 6635–6639.

31 X. Chen, Y. Kuwahara, K. Mori, C. Louis and H. Yamashita, *ACS Appl. Energy Mater.*, 2021, **4**, 4823–4830.

32 C. Matsubara, N. Kawamoto and K. Takamura, *Analyst*, 1992, **117**, 1781–1784.

33 Y. Kondo, K. Honda, Y. Kuwahara, K. Mori, H. Kobayashi and H. Yamashita, *ACS Catal.*, 2022, **12**, 14825–14835.

34 Y. Zhao, Y. Liu, J. Cao, H. Wang, M. Shao, H. Huang, Y. Liu, Z. Kang, X. Jin, X. Fan, J. Tian, R. Cheng, M. Li and L. Zhang, *Appl. Catal. B Environ.*, 2020, **278**, 1–7.

35 J. Y. Hwang, G. Moon, B. Kim, T. Tachikawa, T. Majima, S. Hong, K. Cho, W. Kim and W. Choi, *Appl. Catal. B Environ.*, 2021, **286**, 119905.

36 D. R. Eddy, M. D. Permana, L. K. Sakti, G. A. N. Sheha, Solihudin, S. Hidayat, T. Takei, N. Kumada and I. Rahayu, *Nanomaterials*, 2023, **13**, 704.

37 P. Krishnan, M. Liu, P. A. Itty, Z. Liu, V. Rheinheimer, M. H. Zhang, P. J. M. Monteiro and L. E. Yu, *Sci. Rep.* 2017, **7**, 1–11.

38 M. Kobayashi, H. Saito, B. Boury, K. Matsukawa and Y. Sugahara, *Appl. Organomet. Chem.*, 2013, **27**, 673–677.

39 T. D. Savi, I. A. Jankovi, Z. V. Saponji, M. I. Comor, D. San, Z. Veljkovi, S. Zana, D. Zari and J. M. Nedeljkovi, *Nanoscale*, 2012, **4**, 1612–1619.

40 Y. Shiraishi, S. Kanazawa, D. Tsukamoto, A. Shiro, Y. Sugano and T. Hirai, *ACS Catal.*, 2013, **3**, 2222–2227.

41 Y. Yang, B. Cheng, J. Yu, L. Wang and W. Ho, *Nano Res.*, 2023, **16**, 4506–4514.

42 A. Behera, P. Babu and K. Parida, *Inorg. Chem. Front.*, 2021, **8**, 1489–1499.

43 K. Li, W. Zhou, X. Li, Q. Li, S. A. C. Carabineiro, S. Zhang, J. Fan and K. Lv, *J. Hazard. Mater.*, 2023, **442**, 130040.

44 H. Nishikiori, K. Todoroki, R. A. Setiawan, K. Teshima, T. Fujii, H. Satozono and N. Queiroz, *Langmuir*, 2015, **31**, 964–969.

Chapter III

Photosynthesis of Hydrogen Peroxide in a Two-Phase System by Hydrophobic Au Nanoparticle-Deposited Plasmonic TiO_2 Catalysts

3.1 Introduction

In contemporary industrial contexts, hydrogen peroxide (H_2O_2) assumes a pivotal role, notably in applications such as disinfection,[1] pulp bleaching,[2] and its prospective deployment as a clean energy vector in fuel cell technology.[3] Currently, the industrial synthesis of H_2O_2 relies upon the anthraquinone method predominantly, which is characterized by a two-step process, involving the hydrogenation of anthraquinone with H_2 and oxidation with O_2, an energetically demanding process.[4] This has spurred contemporary research endeavors aimed at exploring alternative methodologies to streamline and optimize H_2O_2 synthesis. Notably, the investigation into a one-step synthesis of H_2O_2 has gained traction. This involves the direct reaction of H_2 with O_2, often facilitated by Pd-based catalysts.[5,6] While this approach manifests quantitative H_2O_2 production, it introduces challenges related to the safe handling of potentially explosive mixtures of H_2 and O_2 gases.

The quest for more sustainable and efficient H_2O_2 production methods inspires another process with cleaner and environmentally friendly practices, photocatalytic H_2O_2 production.[7] This approach harnesses the catalytic potential of semiconductors,[8–11] metal-,[12,13] or nonmetal-organic compounds[14,15] under light irradiation to facilitate the direct synthesis of H_2O_2 from water and O_2, which is noteworthy for its green and selective characteristics and offers a promising alternative to conventional methods. The photogeneration of H_2O_2 is composed of O_2 reduction reaction (ORR) and water oxidation reaction (WOR) processes, which is induced by the photogenerated electrons (e^-) and holes (h^+), respectively, from semiconductors after irradiation. Specific reaction pathways of ORR (**Equations 1-3**) and WOR (**Equations 4-6**) are shown as follows.

Direct 2e-ORR pathway: $O_2 + 2e^- + 2H^+ \rightarrow H_2O_2$ (1)

Indirect 2e-ORR pathway: $O_2 + e^- \rightarrow O_2^{\cdot -}$ (2)

$O_2^{\cdot -} + e^- + 2H^+ \rightarrow H_2O_2$ (3)

Direct 2e-WOR pathway: $2H_2O + 2h^+ \rightarrow H_2O_2 + 2H^+$ (4)

Indirect 2e-WOR pathway: $H_2O + h^+ \rightarrow 2 \cdot OH + H^+$ (5)

$\cdot OH + \cdot OH \rightarrow H_2O_2$ (6)

In 2019, our group presented photocatalytic H_2O_2 synthesis using hydrophobic MOFs in a two-phase system containing benzyl alcohol (BA) and water phases.[12] The proposal of such a two-phase system is based on economical consideration, including the combination of ORR for H_2O_2 synthesis with the oxidation process for other valuable chemicals, such as BA oxidation for benzaldehyde (BAL) production. However, single-phase requires lots of energy and consumption in the demand of product separation, whereas the BA/water phase system supports the in-situ formation of BAL and H_2O_2 upon organic and aqueous phases, respectively.[16] Therefore, H_2O_2 forms via disproportionation of superoxide radicals ($O_2^{\bullet-}$) (**Equation 7**) and the WOR pathways could be replaced by BA oxidation process (**Equation 8**) in such a two-phase system.

$$2O_2^{\cdot-} + 2H^+ \rightarrow H_2O_2 + O_2 \qquad (7)$$

$$R - CH_2OH + 2h^+ \rightarrow R - CHO + 2H^+ \qquad (8)$$

Titanium dioxide (TiO_2), recognized as one of the most ubiquitous semiconductors, shows competitive and prominent properties owing to its excellent chemical durability and cost-effectiveness for large-scale applications.[17,18] Although the inherent limitation of a broad bandgap (~3.2 eV), which hampers electron activation without ultraviolet (UV) light irradiation,[19] the plasmon-induced metallic deposition[20,21] enables TiO_2 to exhibit improved charge transfer efficiency and considerable photocatalytic activity under visible light. Notably, Saito et al.[22] prepared the gold-nanoparticle-deposited TiO_2 material (AuNP/TiO_2) using a chemical bath deposition method and investigated the surface plasmon resonance (SPR) excitation of plasmonic metallic Au, which extends the absorption range into the visible light spectrum. In this process, photoexcited electrons transfer from the Fermi energy level of Au to the conduction band (CB) of TiO_2 and actively participate in the reduction process, leaving hot holes within Au NPs available for oxidation reactions.[22]

However, the photodecomposition of generated H_2O_2 is prone to occur in the single-phase reaction system, and the peroxide complexes (≡Ti-OOH) is formed due to the absorption of H_2O_2 molecules on the TiO_2 surface.[23] Herein, based on previous results obtained by our group on the stabilizing effect of octadecylphosphonic acid (OPA) on TiO_2 in organic phases,[13,24] we

propose the utilization of hydrophobic and plasmonic OPA-grafted xAu/TiO_2 materials with varying Au contents (x=0.5, 1, 1.5, and 2) in photocatalytic H_2O_2 production in a BA/water two-phase system. We aim to explore the reaction mechanism of SPR-induced TiO_2 in the two-phase system, which is advantageous to electron separation efficiency and the inhibition of secondary H_2O_2 decomposition.

3.2 Experimental

3.2.1 Materials

The anatase TiO_2 employed in this study was procured from the Catalysis Society of Japan (JRC-TIO-8, ST-01). Octadecylphosphonic acid (OPA, > 98%) and oxo[5,10,15,20-tetra(4-pyridyl)porphinato]titanium(IV) ($[TiO(tpypH_4)]^{4+}$) (Ti-TPyP reagent) were supported from Tokyo Chemistry Industry Co., Ltd. Hydrogen tetrachloroaurate(III) tetrahydrate ($HAuCl_4$ $4H_2O$, > 99.0%), hydrogen peroxide (30%), benzyl alcohol (BA, > 97%), methanol (CH_3OH, > 99%), ethanol (C_2H_5OH, > 99%), acetonitrile (CH_3CN, > 99%), perchloric acid ($HClO_4$, 60%), and hydrochloric acid (HCl, 16.9%) were supplied by Nacalai Tesque. No additional purification is perfomed on all the above chemicals before utilization.

3.2.2 Preparation of xAu/TiO_2 (x = 0.5, 1, 1.5, and 2)

A series of TiO_2 catalysts with Au NPs loading were prepared using photocatalytic deposition and photoreduction methods. In this process, 250 mg of TiO_2 was dispersed in a methanol/deionized water solution with a volume ratio of 3:20 (mL/mL), containing a specific amount of $HAuCl_4$ precursor. The resulting suspension was placed into a 50 mL Pyrex tube, which was stirred and bubbled with argon gas for 30 min to remove O_2. After being irradiated for 15 min under UV light (Xe lamp, 300 W), the specimens were centrifugated, washed with water, and dried for 12 h at 80 ^oC. Subsequently, the dried sample was denoted as xAu/TiO_2 (x = 0.5, 1, 1.5, and 2), where x represents the weight percentage of Au in the xAu/TiO_2 catalysts.

3.2.3 Preparation of OPA-xAu/TiO_2

Briefly, a 20 mM of OPA ethanol solution (100 mL) serves as the impregnating solution, undergoing ultrasonication for 20 min to prepare a uniform solution. Then, 120 mg of xAu/TiO_2 powder was dissolved in the obtained solution, followed by stirring at room temperature for 24 h. After washing with ethanol and drying for 12 h at 80 ^oC, the dried powder was collected and designated as OPA-xAu/TiO_2.

3.2.4 Preparation of OPA-TiO_2

The preparation method for OPA-modified TiO_2 closely resembled that detailed in **Section 3.2.3**, with the only deviation being the substitution of xAu/TiO_2 with TiO_2. The resulting sample is named as OPA-TiO_2.

3.2.5 Characterization

Ultraviolet-visible diffuse reflectance spectra (UV-vis DRS) was measured using Shimadzu UV-2450 equippment, with $BaSO_4$ powder employed as the reference. Obtained data was analyzed by Kubelka–Munk function. X-ray diffraction (XRD) analysis was equipped with a Rigaku Ultima IV diffractometer with Cu Kα radiation (λ = 1.5405 Å). Shimadzu ESCA-3400 instrument was carried out to explore electronic states for X-ray photoelectron spectroscopy (XPS) characterization, and the obtained data was analyzed through charge correction using C 1s at 284.6 eV. Fourier transform infrared spectroscopy (FT-IR) (JASCO FTIR-6100) was conducted by scanning the tablets composed of samples and KBr mixture. Photoluminescence (PL) emission spectra were obtained in the air at room temperature using a spectrofluorometer (Fluorolog-3, Horiba), with an excitation wavelength of 550 nm.

3.2.6 Electrochemical measurements

Transient photocurrent experiments were carried out using the HS-5000 electrochemical measurement system. In a conventional Pyrex three-electrode cell, containing a prepared electrode as the working electrode, a platinum wire as a counter electrode, and an Ag/AgCl reference electrode. The electrochemical workstation was employed to capture and record the current density signal. The cell was filled with the Na_2SO_4 solution of 0.5 M when it was working. Before the measurements, the solution comprising 5 mg of samples in the mixture of water (0.5 mL), ethanol (1.5 mL), and 5% Nafion solution (100 μL) should be prepared. Then the working electrode was obtained by coating 40 μL of the prepared solution onto the FTO conductive glass.

3.2.7 Photocatalytic H_2O_2 production

A 30 mL quartz vessel contains photocatalysts (5 mg), deionized water (2 mL), and BA (5

mL) with sealed rubber plug compose the two-phase reaction setup. The reactor was ultrasonically treated for about 5 min to achieve a uniform suspension. Before light irradiation, the mixture was bubbled with O_2 at a flow rate of 20 mL min^{-1} for 30 min in the dark. Subsequently, the reactor was exposed to the illumination of a Xenon lamp (Sanei Electric XEF-501S, 500 W) through a 420 nm cut-off glass filter, maintaining a distance of 5 cm between the lamp and reactor. The reaction was conducted at ambient temperature and pressure, a 20 μL aliquot was withdrawn from the aqueous phase every 1 h interval for subsequent analysis.

For the single-phase system, 5 mg of photocatalysts was uniformly dispersed into the reaction solution composed of 3 mL of CH_3CN and 2 mL of BA or 5 mL of CH_3CN without BA. Following procedures were the same as mentioned for the two-phase system.

3.2.8 H_2O_2 decomposition test

5 mg of 1.5Au/TiO_2 or 5 mg of OPA-1.5Au/TiO_2 were added to the two-phase solution system in a Pyrex reaction vessel (30 mL). The composition of the solution was referred as **Section 3.2.7**. The solution was sealed using a rubber septum and stirred under the dark at ambient temperature and pressure.

3.2.9 Recycling test

The Pyrex tube of 50 mL was employed as the reactor, containing a dispersion of OPA-2Au/TiO_2 (10 mg), BA (10 mL), and water (4 mL). After bubbling with O_2, the reaction and detection processes shown in Section 2.4 were followed up for the first cycle. After 3 h-reaction ended, the reacted suspension was transferred into a centrifugated tube and washed and centrifugated using ethanol to remove the remained BA. The collected catalysts were dried in a vacuum and prepared for the next cycle.

3.2.10 Detection of H_2O_2 and BAL products

The H_2O_2 concentration was detected by a $[TiO(tpypH_4)]^{4+}$ complex titration method. A solution of aqueous HCl (50 mM, 100 mL) containing 3.4 mg of the $[TiO(tpypH_4)]^{4+}$ complex was prepared and served as the Ti-TPyP reagent. The sample solution was diluted 100-fold

with distilled water, then the diluted solution (250 μL) was mixed with $HClO_4$ aqueous solution (4.8 M, 250 μL) and the Ti-TPyP solution (250 μL). After a brief interval, the mixture was further diluted to a final volume of 2.5 mL using purified water. The absorbance of this solution at a wavelength of 434 nm (designated as A_S) was measured employing a Shimadzu UV-2600 UV-Vis spectroscope. The absorbance of a blank solution, consisting of distilled water (250 μL) in place of the sample solution, was recorded as A_B. Then the amount of H_2O_2 was obtained based on ΔA_{434} (calculated by $\Delta A_{434} = A_B - A_S$) and the volume of the solution, following established procedures described in the literature.[25]

The amount of benzaldehyde (BAL) produced was quantified by gas chromatography (Shimadzu GC-2014) equipped with a flame ionization detector (FID) and an autosampler (Shimadzu AOC-20i). In the GC system, the injected samples were vaporized and separated as they passed through the column (TC-1) with the carrier gas N_2 and subsequently detected by the detector. The temperature of column, injector, and detector was set at 80 °C, 250 °C, and 250 °C, respectively. The solution used for GC analysis consisted of a mixture of 250 μL of reaction solution, 77 μL of acetonitrile solution containing 1 mg of biphenyl (internal standard), and 173 μL of acetonitrile. The concentration of BAL was determined by calculating the ratio of the peak areas of BAL to biphenyl and referencing the standard linear calibration curve.

3.2.11 CB and VB energy levels of TiO_2 catalysts

The determination of the valence band (VB) energy level relative to the standard hydrogen electrode (NHE, pH=0) (E_{VB}) can be computed using **Equation 9**,[26] where φ represents the electron work function of the XPS analyzer (4.50 eV), and E_{XPS_VB} represents the values derived from XPS valence band spectra of the samples. Subsequently, the potential of CB (E_{CB}) is ascertained through **Equation 10**, where E_g denotes the bandgap energy of the samples, estimated by Tauc plots from UV-vis results.

$$E_{VB} = \varphi + E_{XPS\_VB} - 4.44 \quad (9)$$

$$E_{CB} = E_{VB} - E_g \quad (10)$$

3.3 Results and discussion

3.3.1 Characterization results

To obtain the optical absorbance properties of Au-deposited TiO_2 samples, the UV-vis DRS was employed (**Figures 1a and 1b**). It can be concluded that the loading of Au NPs strengthens the absorbance intensity of TiO_2, especially in the region of visible light. Furthermore, xAu/TiO_2 samples exhibit an optical absorption peak at approximately 550 nm, corresponding to the SPR band of Au NPs.[22] Notably, the intensity of this peak is directly proportional to the content of Au loading. Compared to pure TiO_2, OPA-modification enables TiO_2 a little response to visible light between 400-550 nm, although pure OPA exhibits little optical absorption across the entire spectrum range (**Figure 2**). The introduction of OPA did not clearly change the light absorption profiles of xAu/TiO_2 materials, which indicates a more pronounced optimization of semiconductor light absorption by plasmonic Au metals.

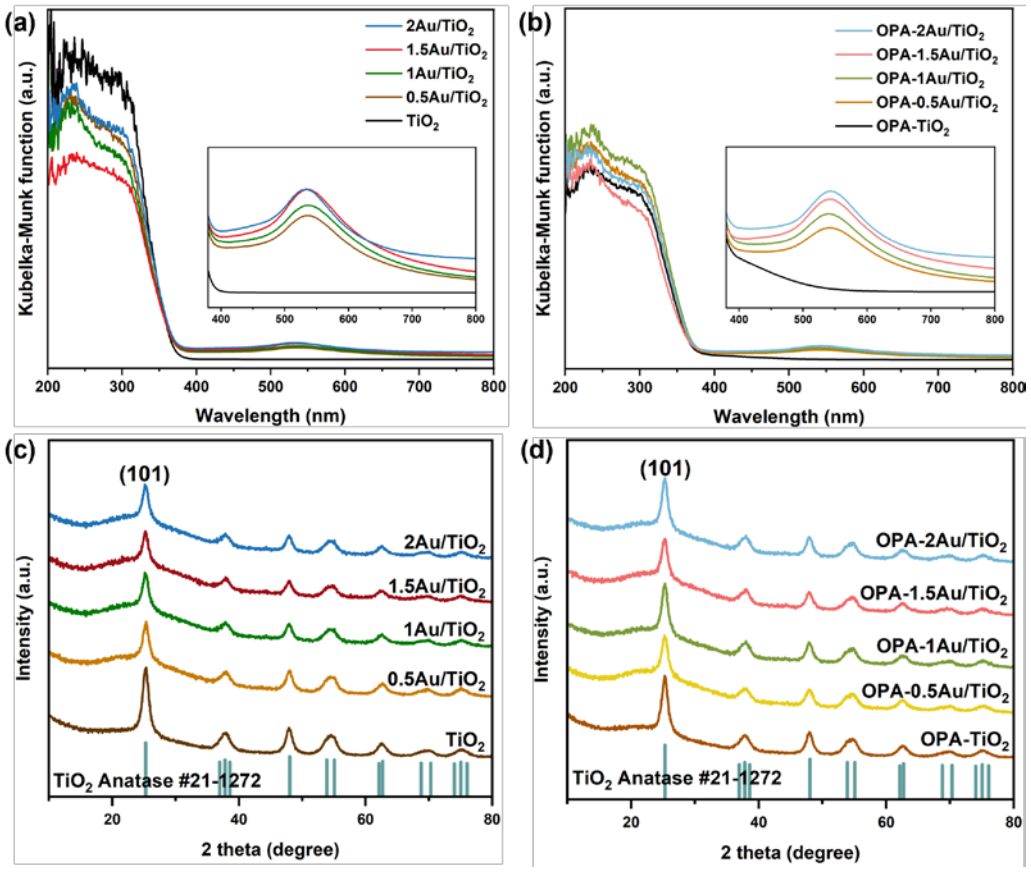

Figure 1. UV-vis DRS spectra of (a) xAu/TiO_2 and (b) OPA-xAu/TiO_2 samples; XRD patterns of (c) xAu/TiO_2 and (d) OPA-xAu/TiO_2 samples (x = 0, 0.5, 1, 1.5, and 2).

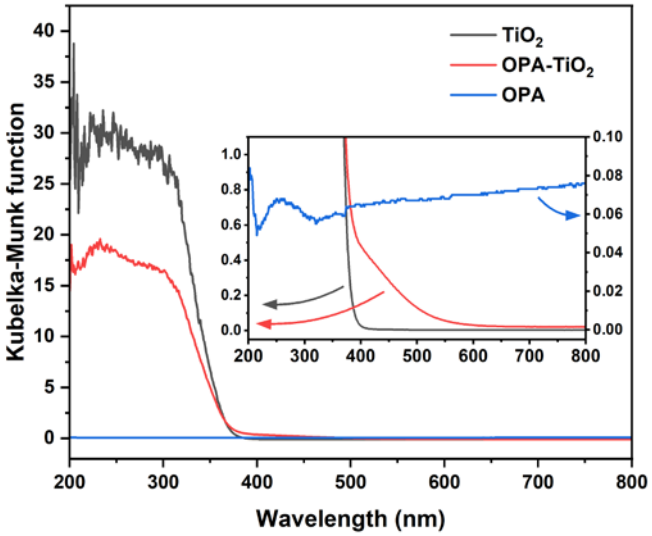

Figure 2. UV-vis DRS spectra of TiO_2, OPA, and OPA-TiO_2 samples, with an enlarged spectral insert for detailed observation.

Figures 1c and 1d display the XRD patterns of Au-deposited TiO_2 and those after OPA grafting. As for both xAu/TiO_2 and OPA-xAu/TiO_2 samples, only the diffraction peaks of TiO_2 were found, specifically positioned at 25.4° corresponding to the anatase TiO_2 (101) facet.[27] No diffraction peaks of Au were observed, suggesting that the particle size of Au NPs is small and beyond the detection range of the XRD diffractometer.

In addition, the Au NPs deposition and OPA grafting could also be determined by FTIR results (**Figure 3**). The absorption peaks at 3409 cm^{-1} and 1623 cm^{-1} belong to the Ti-OH stretching and H-O-H bending vibrations, respectively, which results from the H_2O absorbed on the sample surface.[28] The broad band of 483 cm^{-1} is attributed to the stretching vibration of Ti-O-Ti,[29] which becomes weakened after Au NPs deposition, accompanied by the appearance of the peak observed at 820 cm^{-1} owing to the Au-O band vibration.[30] This phenomenon proves the successful bonding through the Ti-O-Au bonds between Au NPs and the TiO_2 surface. As observed in **Figure 3b**, the OPA-grafting introduces characteristic features to OPA-xAu/TiO_2, including the stretching vibration band of -CH_2- (2920-2850 cm^{-1}) and the bending vibration band of C-H (1470 cm^{-1}). These bands originated from the n-octyl groups (-$C_{18}H_{37}$) of grafted OPA molecules.[31] Moreover, the stretching vibration peaks of P-OH at 950 cm^{-1} vanish, and the broadened band of P-O at 1080-1000 cm^{-1} is observed to be less pronounced compared to the sharper one in the pure OPA profile, which implies the formation of Ti-O-P bonds.[31]

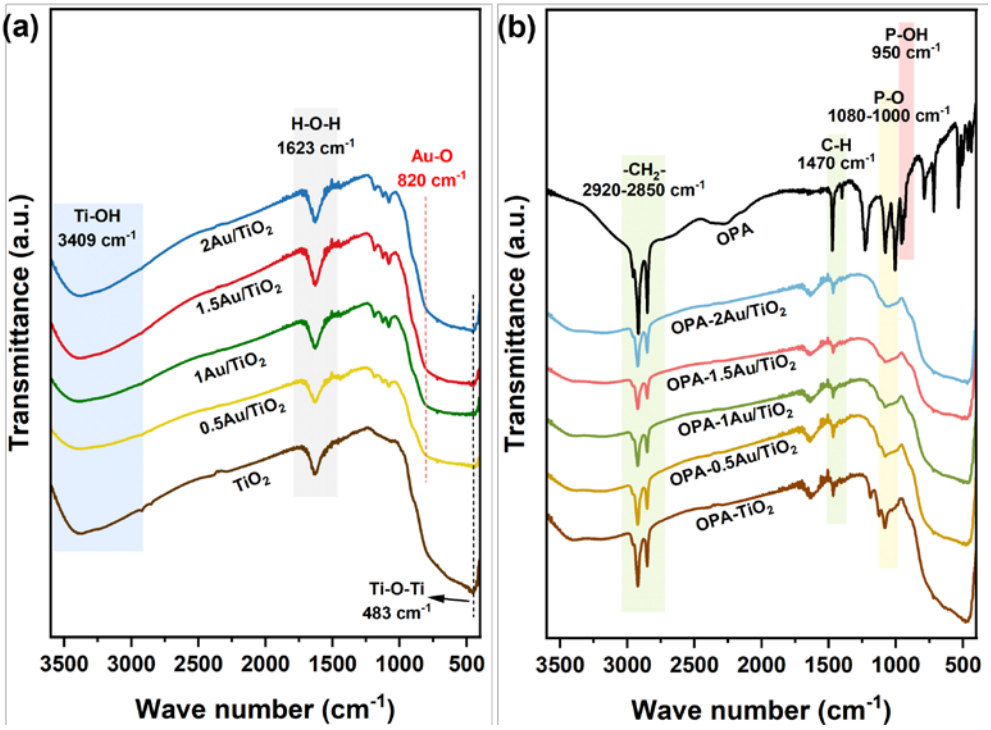

Figure 3. FTIR spectra of (a) xAu/TiO_2 and (b) OPA-xAu/TiO_2 (x = 0, 0.5, 1, 1.5, and 2).

To investigate the interaction between plasmon-induced metallic Au, OPA modification and the TiO_2 samples, XPS measurement was conducted (**Figure 4**). **Figure 4a** illustrates the peaks in the Au 4f spectra of xAu/TiO_2 catalysts, corresponding to the Au $4f_{5/2}$ and Au $4f_{7/2}$ energy states at 86.7 eV and 83.1 eV, respectively.[32] The intensity of the Au 4f peaks is observed to increase as the amount of Au deposited increases, which roughly reflects that the actual amount of metallic Au in xAu/TiO_2 is close to the theoretical value.

The peaks evident at approximately 465.0 eV and 459.3 eV in **Figure 4b** are attributed to the Ti $2p_{1/2}$ and Ti $2p_{3/2}$ energy levels, respectively.[33] Notably, the Ti $2p_{3/2}$ peaks of Au-deposited TiO_2 exhibit a negative shift of 0.6 eV compared to the pure TiO_2. This shift indicates that the deposited Au NPs contribute to a higher electronic density in TiO_2, attributed to the formation of Ti-O-Au bonds identified from FTIR results. The electron transfer from metallic Au NPs to the surface of TiO_2, resulting from the SPR property of Au metal, makes xAu/TiO_2 materials show a strong visible-light response, which is consistent with the UV-vis DRS profiles.

Moreover, OPA addition diminishes the peak intensities observed in the Ti 2p spectrum depicted in **Figure 4d**. This reduction is ascribed to the deterioration in signals owing to the surface modification of TiO_2 with OPA.[13] Combined with the appearence of P 2p peaks at 133.3

eV of OPA-grafted TiO_2 samples (**Figure 4e**), the successful OPA fabrication could be confirmed. Furthermore, as depicted in **Figure 4d**, the Ti 2p binding energy of OPA-modified TiO_2 exhibits a negative shift of 0.4 eV, which illustrates the interaction between OPA and TiO_2 elucidated by the presence of Ti-O-P ligands, as corroborated by our previous studies.[24] However, there appears a slight positive shift of OPA-1.5Au/TiO_2 compared to 1.5Au/TiO_2 sample in **Figure 4f**. This is due to the fact that the grafted OPA molecules cover parts of the surface deposited Au NPs. Therefore, the electron-donating ability of plasmonic Au NPs seems superior to grafted OPA groups, which exhibits stronger optical absorption as reflected in the UV-vis DRS results.

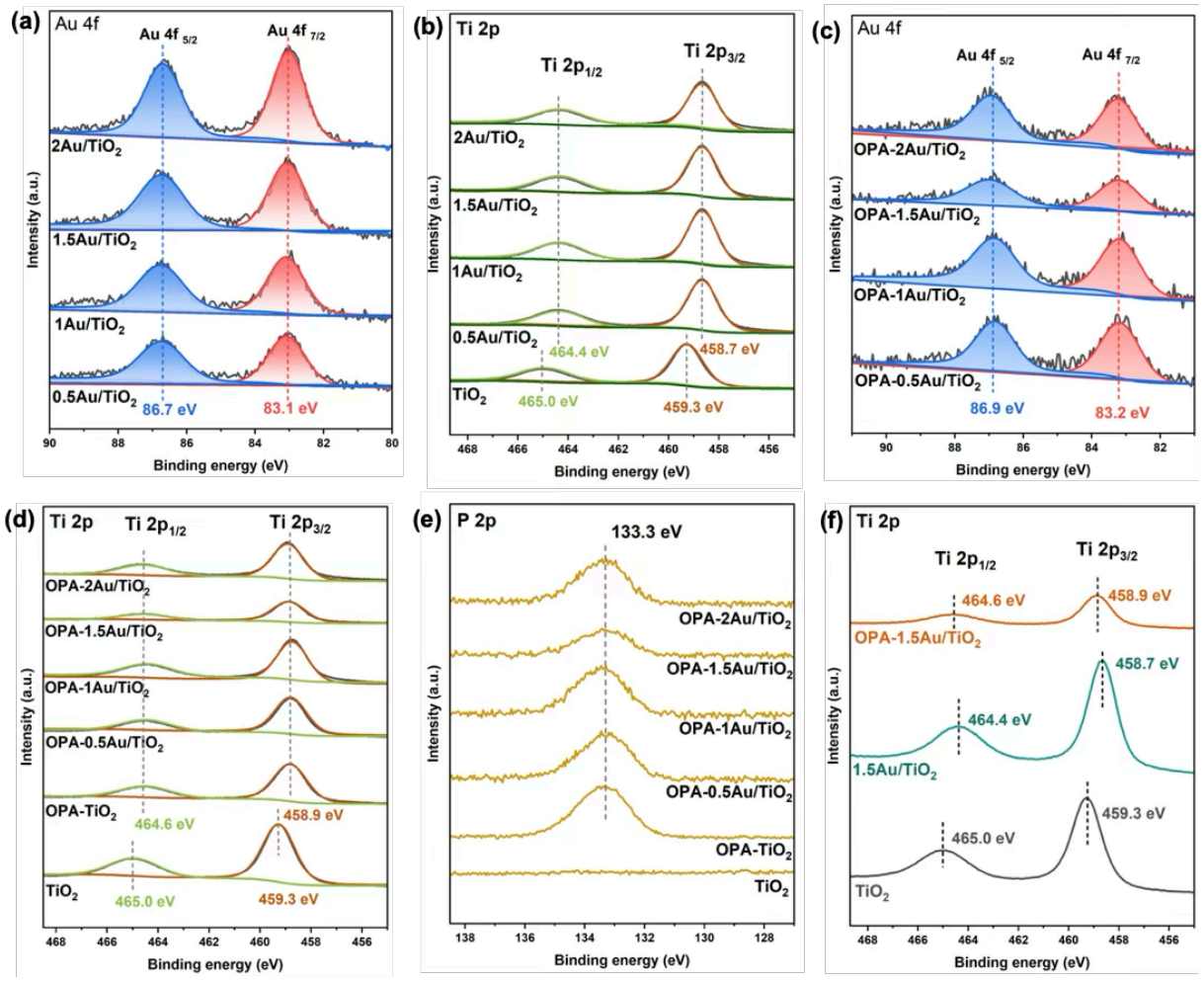

Figure 4. XPS Au 4f, Ti 2p, and P 2p spectra of (a, b) xAu/TiO_2 and (c, d, e) OPA-xAu/TiO_2 (x = 0, 0.5, 1, 1.5, and 2); (f) XPS Ti 2p spectra of TiO_2, 1.5Au/TiO_2, and OPA-1.5Au/TiO_2 catalysts.

Apart from the slight electron-donating property of OPA to TiO_2, the OPA-modified catalysts exhibit noteworthy hydrophobicity, as confirmed by water contact angle (WCA) experiments shown in **Figure 5**. While the original TiO_2 is super-hydrophilic with a WCA of 0^o, both OPA-TiO_2 and OPA-2Au/TiO_2 materials show hydrophobic properties. This characteristic allows OPA-xAu/TiO_2 to disperse in the BA phase during the reaction period, as seen in the digital photos in **Figure 6**.

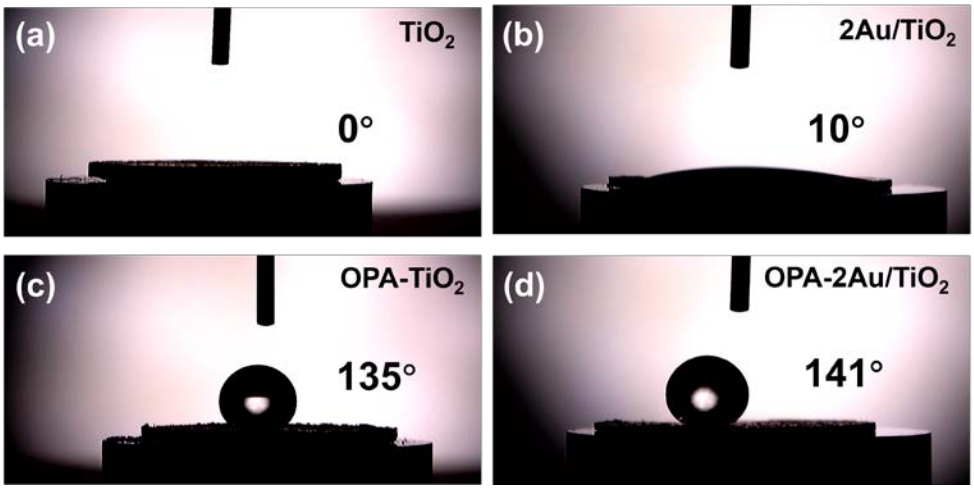

Figure 5. Water contact angle measurements of (a) TiO_2, (b) 2Au/TiO_2, (c) OPA-TiO_2, and (d) OPA-2Au/TiO_2.

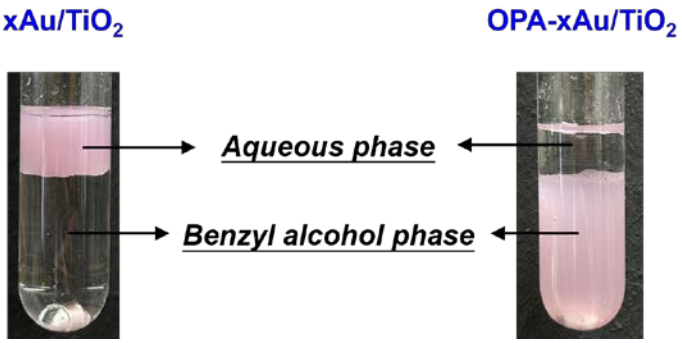

Figure 6. The digital photos of reactors with xAu/TiO_2 and OPA-xAu/TiO_2 catalysts (x=0.5, 1, 1.5, and 2).

3.3.2 Photocatalytic activity evaluation

An evaluation test of photocatalytic H_2O_2 production was conducted in a two-phase setup

composed of water and BA phases under visible light irradiation. The time course of produced H_2O_2 concentration was posted in **Figure 7**. As we know, the electrons in the VB of original TiO_2 cannot be activated due to the broad bandgap of TiO_2, showing nearly no photocatalytic activity under visible light.[34] As depicted in **Figure 7a**, only OPA-grafting makes OPA-TiO_2 have a little activity under visible light, which is attributed to the slight electron-donating property of OPA as mentioned above. However, OPA-xAu/TiO_2 catalysts exhibit significant enhancement of H_2O_2 production. With the content of deposited Au NPs increasing, the H_2O_2 concentration in the aqueous phase rises up during the reaction, in which OPA-1.5Au/TiO_2 shows the continuously increased H_2O_2 concentration even after reacting for 5 h. This obtained activity of photocatalytic H_2O_2 synthesis was induced by the SPR effect of the loaded Au NPs.[32]

Additionally, it is observed that OPA-2Au/TiO_2 sample shows a rapid increase of H_2O_2 concentration but decreases after 3 h, exhibiting lower H_2O_2 concentration after 6 h-reaction than OPA-1.5Au/TiO_2 (**Figure 7b**). We speculated that this phenomenon is attributed to the high activity of OPA-2Au/TiO_2 in the initial stage of the reaction, leading to rapid oxygen consumption.

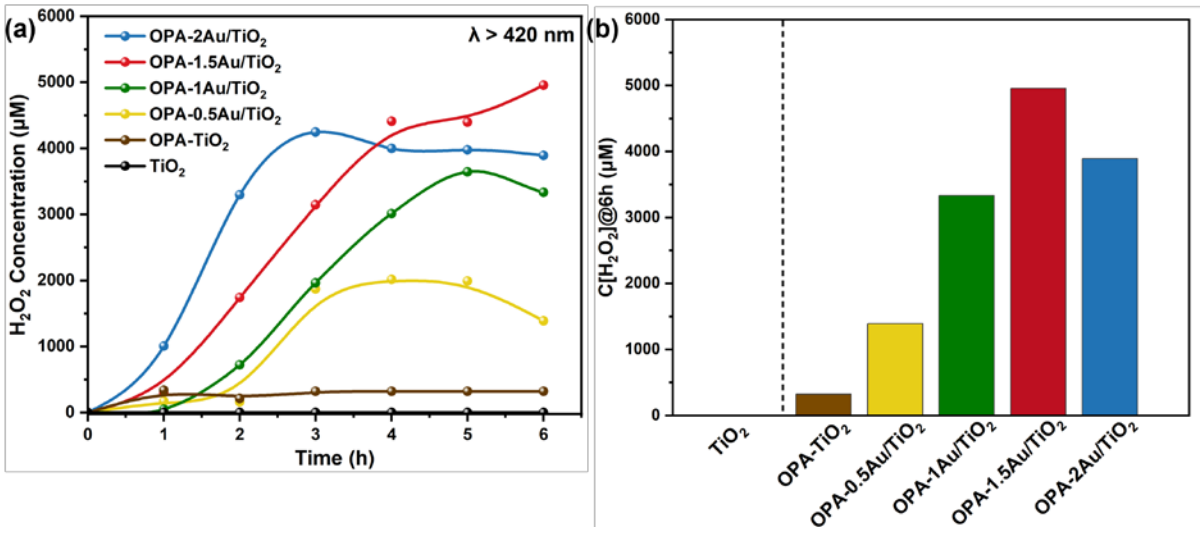

Figure 7. (a) Activity performance of H_2O_2 production with TiO_2 and OPA-xAu/TiO_2 photocatalysts (x = 0, 0.5, 1, 1.5, and 2) in the BA/water two-phase system (BA: water = 5 mL: 2 mL) under $\lambda > 420$ nm irradiation; (b) The produced H_2O_2 concentration in the aqueous phase after reaction for 6 h.

To substantiate this hypothesis, a comparative experiment between OPA-1.5Au/TiO_2 and OPA-2Au/TiO_2 samples was conducted under continuous input of oxygen. As shown in **Figure 8a**, the results confirmed that OPA-2Au/TiO_2 indeed exhibits higher activity when maintained in an O_2-saturated atmosphere during the reaction, which validates our conjecture. Additionally, the OPA-0.5Au/TiO_2 and OPA-1Au/TiO_2 samples displayed decreased activities after 3 h, owing to the constraint in electron transfer from limited Au NPs contents to TiO_2.[30] Moreover, the recycling test of OPA-2Au/TiO_2 was conducted and shown in **Figure 8b**.

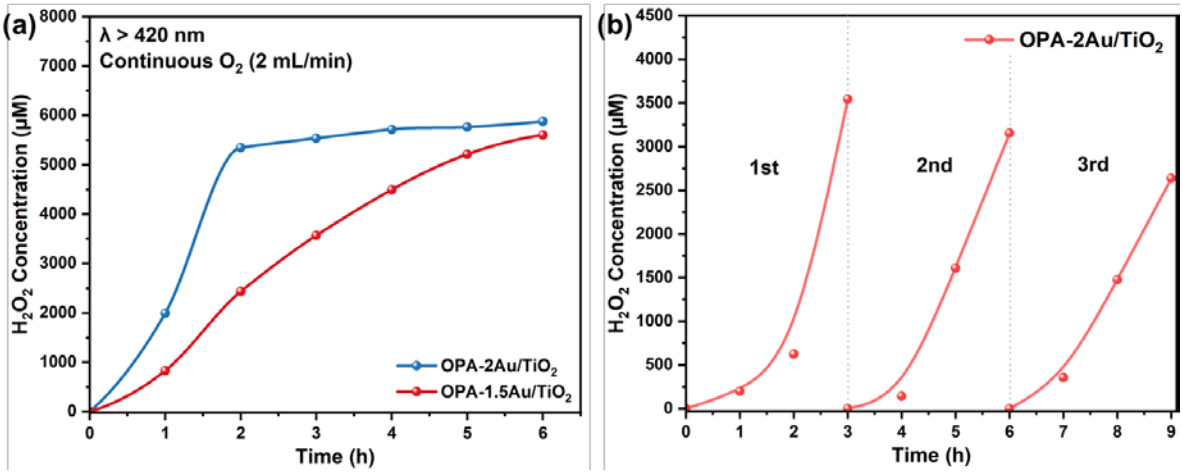

Figure 8. (a) Comparison of H_2O_2 production using OPA-1.5Au/TiO_2 and OPA-2Au/TiO_2 materials when continuous O_2 supplying with the flowrate of 2 mL min^{-1} under visible light irradiation ($\lambda > 420$ nm); (b) Recycling test of OPA-2Au/TiO_2 in the two-phase reaction system.

3.3.3 Effect of the BA/water two-phase reaction system

The BA/water reaction system is displayed in **Figure 6**. xAu/TiO_2 featuring hydrophilic dispersed in the aqueous phase, whereas OPA-xAu/TiO_2 materials are present in the BA phase. As present in **Figure 9**, the 1.5Au/TiO_2 sample exhibited similar activity as the OPA-modified sample in the first hour of the reaction but underwent a substantial decline in H_2O_2 concentration thereafter. This stands in contrast to the OPA-1.5Au/TiO_2 catalyst. Combined with the results of H_2O_2 decomposition test in **Figure 9b**, we can infer that the decreased activity of 1.5Au/TiO_2 results from the H_2O_2 decomposition, which stems from the absorption of produced H_2O_2 on the surface of the 1.5Au/TiO_2 sample.[24]

Except for providing an organic shield for the hydrophobic catalysts, BA solution also serves as the sacrificial agent to capture the photoexcited holes of photocatalysts.[12] Furthermore, the generated BAL, the oxidation product of BA, has also been evaluated using OPA-1.5Au/TiO_2 as shown in **Figure 9c**. In the ORR process involving BA as the sacrificial agent, the theoretical molar ratio of H_2O_2 to BAL is 1:1 based on the stoichiometric reaction pathway (**Equation 11**).[35] The nearly equivalent concentrations of the products observed in **Figure 9c** imply that H_2O_2 rarely decomposed in such a two-phase system, which is dominated by the OPA-modified catalysts.

$$O_2 + R - CH_2OH \xrightarrow[hv]{cat.} H_2O_2 + R - CHO \qquad (11)$$

Therefore, the design of the two-phase setup facilitates the separation of produced H_2O_2 from the TiO_2 surface without forming ≡Ti-OOH complexes, which exerts a significant effect on inhibiting the disproportionation of H_2O_2. As summarized in **Table 1**, the utilization of hydrophobic Au-deposited TiO_2 in a two-phase system for photocatalytic H_2O_2 production seems advantageous compared to other reported TiO_2 materials, providing a kind of strategy and method for the modification of plasmon-induced photocatalysts.

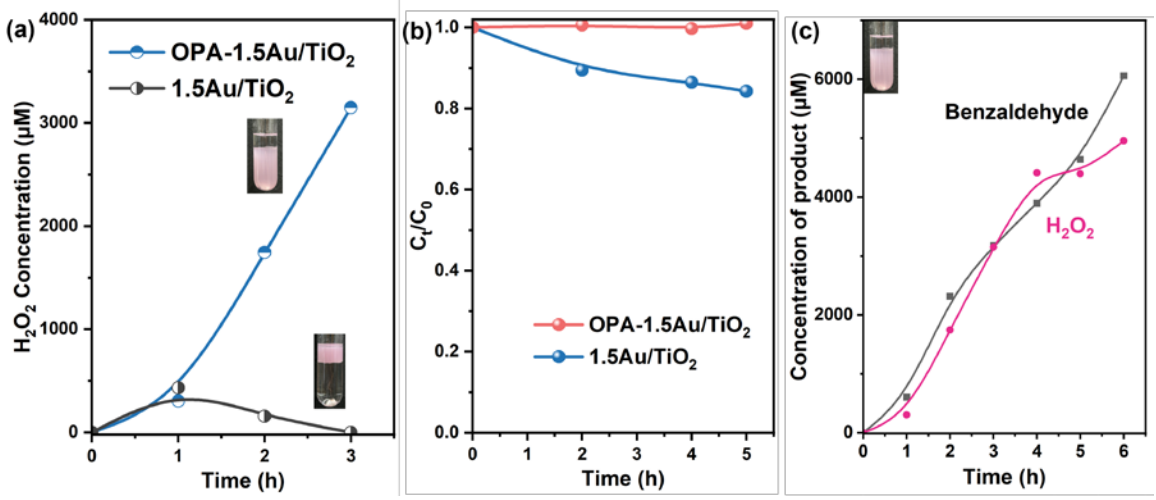

Figure 9. (a) Activity test under visible light irradiation (λ > 420 nm) and (b) H_2O_2 decomposition test in the dark employing 1.5Au/TiO_2 and OPA-1.5Au/TiO_2 photocatalysts in the two-phase system. (c) Photocatalytic products of benzaldehyde (BAL) and H_2O_2 in a two-phase system using OPA-1.5Au/TiO_2 sample.

Table 1. Activity comparison with other reported TiO_2-based photocatalysts for H_2O_2 production.

Catalysts	Reaction condition	Irradiated wavelength (nm)	H_2O_2 production ($\mu mol\ h^{-1}\ g^{-1}$)	Reference
SN-GQD/ TiO_2	2-propanol/water (3:47, pH=3.0)	> 420	110	Zheng et al.[8]
Nf-SNG /TiO_2	2-propanol/water (3:47, pH=3.0)	> 420	135	Zheng et al.[18]
TiO_2/In_2S_3	Ethanol/water (1:9)	> 365	752	Yang et al.[36]
B-doped g-C_3N_4/TiO_2	Ethanol/water (1:19)	> 400	917	Behera et al.[37]
DNOPA-TiO_2	Benzyl alcohol/water (5:2, two-phase)	> 450	205	Zhao et al.[24]
OPA-2Au/TiO_2	Benzyl alcohol/water (5:2, two-phase)	> 420	567	This work

3.3.4 Proposed reaction mechanism for photocatalytic H_2O_2 production

The measurement of transient photocurrent density was carried out to evaluate the charge transfer capacity of xAu/TiO_2. As shown in **Figure 10a**, the photocurrent density of xAu/TiO_2 is correlated to the amount of Au NPs on the TiO_2 surface, which confirms that the plasmon-induced ORR process contributes to the photogenerated electron transfer from plasmonic Au atoms to TiO_2.[32] And OPA-2Au/TiO_2 performs higher H_2O_2 production under the O_2 flowing conditions.

The PL emission spectra (**Figure 10b**) provides insights into the charge separation efficiency of xAu/TiO_2. When the metallic Au is exposed under light irradiation with a wavelength of 550 nm, hot electrons of Au metals is photoexcited and a portion of them transfers to the CB of TiO_2. Spontaneously, the remaining hot electrons are unstable and are

susceptible to recombination with the hot holes, emitting fluorescence in this process.[22,38] As the amount of Au increases, the PL intensity of 2Au/TiO_2 becomes lower compared to other Au-deposited TiO_2, demonstrating that more hot electrons transfer to CB of TiO_2 to produce $O_2^{\bullet-}$ species via ORR pathway. The recombination process of the photoinduced hot e^--h^+ pairs is suppressed owing to the increase in SPR effect of Au NPs.[26]

Moreover, the bandgap energies of TiO_2 and Au/TiO_2 were calculated to be 3.23 eV and 3.12 eV, respectively, as determined from UV-vis DRS spectra (**Figure 10c**). And the CB energy levels, based on the XPS-VB spectra of TiO_2, Au/TiO_2, and OPA-Au/TiO_2, are illustrated in **Figure 10d**. Subsequently, the energy band structure of these catalysts, as presented in **Figure 10e**, was obtained through the calculation process detailed in **Section 3.2.11**. The reduction in bandgap energy of Au/TiO_2 is attributable to the SPR effect of the plasmonic metallic Au, facilitating the activation and transfer of hot carriers to the CB of TiO_2.[38] In addition, the CB energy level of Au/TiO_2 is more negative compared to the redox potential of the 2e-ORR to $O_2^{\bullet-}$ radicals (-0.33 V vs NHE), which suggests that plasmonic Au

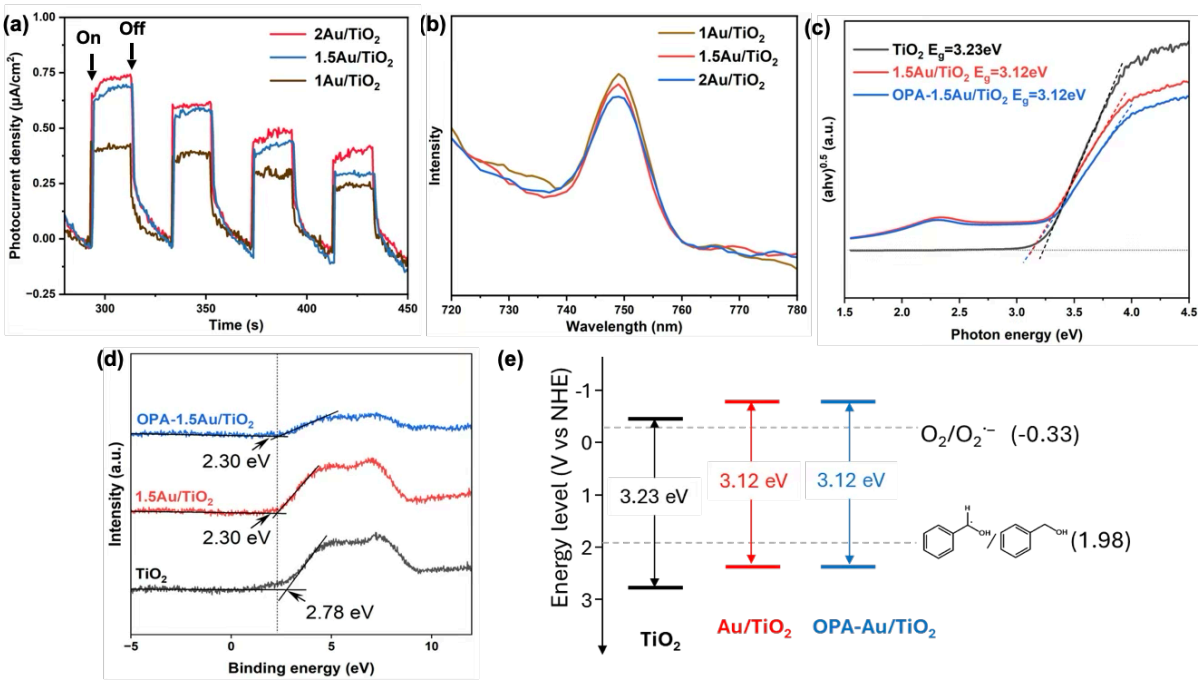

Figure 10. (a) Photocurrent density measurement and (b) PL emission spectra of xAu/TiO_2 samples (x = 1, 1.5, and 2); (c) Band gap energies obtained from UV-vis DRS results, (d) XPS valence band spectra, and (e) band structure of TiO_2, Au/TiO_2, and OPA-Au/TiO_2.

NPs provide more hot electrons to TiO_2 resulting in the generation of abundant $O_2^{\bullet-}$ species via indirect 2e-ORR pathway,[39] and enhanced photocatalytic ORR performance.[30,38] Furthermore, compared to the redox potential of BA oxidation to BAL (1.98 V vs NHE), the more positive energy level in the VB of Au/TiO_2 (2.36 V vs NHE) demonstrates that the BA oxidation reaction is also favorable for the Au-deposited TiO_2 catalysts.

However, it is noted that the OPA modification has a limited effect on the band structure of the TiO_2 material. The significance of OPA fabrication becomes evident in enabling the presence of Au/TiO_2 in the organic phase of the two-phase system. Therefore, the proposed reaction mechanism of OPA-hydrophobized Au/TiO_2 for H_2O_2 production in a two-phase system is depicted in **Figure 11**.

In such a BA/water two-phase reaction system, when the Au-deposited TiO_2 catalyst, existing in the aqueous phase, is irradiated under visible light, hot electrons of Au NPs are excited owing to the SPR effect. These SPR-excited electrons transfer to the CB of TiO_2, contributing to the O_2 reduction reaction for H_2O_2 formation, while leaving hot holes in the Au NPs. Simultaneously, dissolved BA molecules participate in the oxidation process for BAL product. However, the generated H_2O_2 is absorbed on the surface of Au/TiO_2, forming peroxide complexes (≡Ti-OOH), leading to the disproportionation of H_2O_2 and limited activity performance.

To mitigate H_2O_2 decomposition, the hydrophobic organic molecule OPA is introduced to Au/TiO_2, resulting in OPA-Au/TiO_2, which can exist in the BA organic phase. The synthesized $O_2^{\bullet-}$ radicals, possessing hydrophilic properties, are prone to transfer into the aqueous phase and undergo the disproportionation reaction to produce H_2O_2 with the participation of protons (H^+) (**Equation 7**).[26,40] And at the interface between the aqueous and organic phases, $O_2^{\bullet-}$ species were reduced to H_2O_2 by single-electron ORR pathway (**Equation 3**).[41] Spontaneously, BA molecules react with hot holes on the surface of Au NPs, contributing to BAL production in the organic phase. The separation of produced H_2O_2 from photocatalysts in the two-phase system suppresses the decomposition of formed H_2O_2, leading to a significant enhancement in the photocatalytic H_2O_2 production rate.

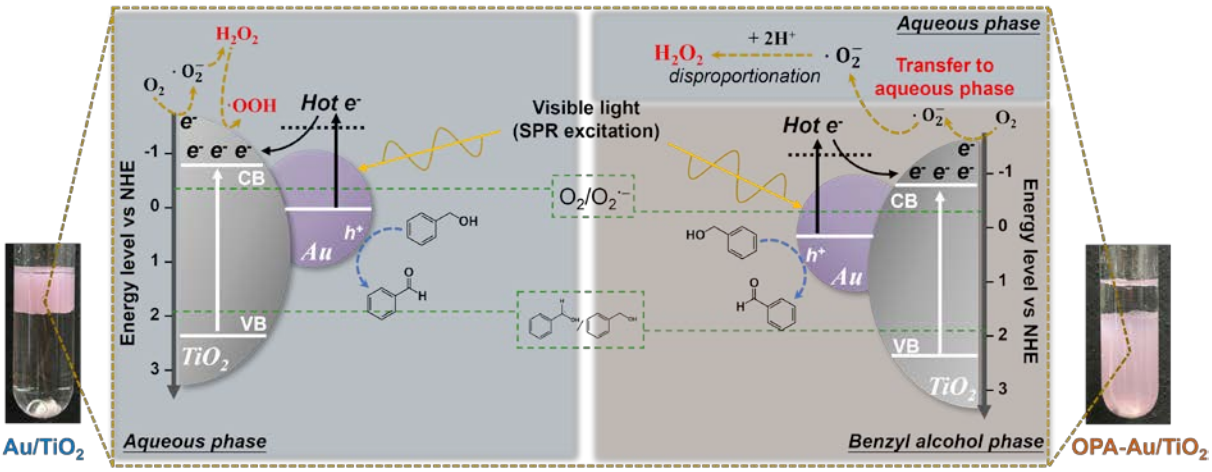

Figure 11. Schematic diagram of the proposed reaction mechanism for photocatalytic H_2O_2 production in BA/water two-phase system using Au/TiO_2 and OPA-Au/TiO_2 catalysts.

3.4 Conclusion

The OPA-modified plasmonic Au-deposited TiO_2 material featuring hydrophobic properties was investigated and applied in a two-phase photocatalytic H_2O_2 production process under visible light irradiation. Based on the results of UV-vis DRS, PL, and XPS spectra, the impact of metallic Au with plasmon resonance on photocatalytic H_2O_2 production was emphasized and elucidated. Specifically, a narrowed bandgap of Au/TiO_2 was observed, enhancing electron transfer to the conductive band of TiO_2 and improving the photocatalytic performance of the O_2 reduction reaction (ORR). However, produced H_2O_2 is inclined to decompose due to the direct contact with TiO_2-based catalysts. This challenge was addressed by introducing a two-phase reaction system, which allows Au/TiO_2 modified by OPA present in the benzyl alcohol (BA) phase, separated from H_2O_2 in the aqueous phase. Consequently, the H_2O_2 decomposition has been efficiently suppressed in such a two-phase system, and OPA-Au/TiO_2 demonstrated enhanced activity in H_2O_2 production (567 $\mu mol\ g^{-1}\ h^{-1}$) under $\lambda > 420$ nm irradiation.

3.5 References

1 M. Ksibi, *Chem. Eng. J.*, 2006, **119**, 161–165.

2 R. N. Gurram, M. Al-Shannag, N. J. Lecher, S. M. Duncan, E. L. Singsaas and M. Alkasrawi, *Bioresour. Technol.*, 2015, **192**, 529–539.

3 K. Mase, M. Yoneda, Y. Yamada and S. Fukuzumi, *Nat. Commun.*, 2016, **7**, 1–7.

4 J. M. Campos-Martin, G. Blanco-Brieva and J. L. G. Fierro, *Angew. Chem. Int. Ed.*, 2006, **45**, 6962–6984.

5 J. K. Edwards, B. Solsona, E. N. N, A. F. Carley, A. A. Herzing, C. J. Kiely and G. J. Hutchings, *Science*, 2009, **323**, 1037–1041.

6 Q. Liu, J. C. Bauer, R. E. Schaak and J. H. Lunsford, *Angew. Chem. Int. Ed.*, 2008, **47**, 6221–6224.

7 H. Hou, X. Zeng and X. Zhang, *Angew. Chem. Int. Ed.*, 2020, **59**, 17356–17376.

8 L. Zheng, H. Su, J. Zhang, L. S. Walekar, H. Vafaei Molamahmood, B. Zhou, M. Long and Y. H. Hu, *Appl. Catal. B Environ.*, 2018, **239**, 475–484.

9 V. Smeets, L. Ben Mustapha, J. Schnee, E. M. Gaigneaux and D. P. Debecker, *Mol. Catal.*, 2018, **452**, 123–128.

10 J. Lim, H. Kim, J. Park, G. H. Moon, J. J. M. Vequizo, A. Yamakata, J. Lee and W. Choi, *Environ. Sci. Technol.*, 2020, **54**, 497–506.

11 S. Thakur, T. Kshetri, N. H. Kim and J. H. Lee, *J. Catal.*, 2017, **345**, 78–86.

12 Y. Isaka, Y. Kawase, Y. Asutaka Kuwahara, K. Mori and H. Yamashita, *Angew. Chem. Int. Ed.*, 2019, **131**, 5456–5460.

13 X. Chen, Y. Kuwahara, K. Mori, C. Louis and H. Yamashita, *J. Mater. Chem. A*, 2020, **8**, 1904–1910.

14 F. Liu, P. Zhou, Y. Hou, H. Tan, Y. Liang, J. Liang, Q. Zhang, S. Guo, M. Tong and J. Ni, *Nat. Commun.*, 2023, **14**, 1–10.

15 Q. Shang, Y. Liu, J. Ai, Y. Yan, X. Yang, D. Wang and G. Liao, *J. Mater. Chem. A*, 2023, **11**, 21109–21122.

16 X. Chen, Y. Kuwahara, K. Mori, C. Louis and H. Yamashita, *ACS Appl. Energy Mater.*,

2021, **4**, 4823–4830.

17 L. Zheng, X. Yu, M. Long and Q. Li, *Chin. J. Catal.*, 2017, **38**, 2076–2084.

18 L. Zheng, J. Zhang, Y. H. Hu and M. Long, *J. Phys. Chem. C*, 2019, **123**, 13693–13701.

19 S. T. T. Le, W. Khanitchaidecha and A. Nakaruk, *Bull. Mater. Sci.*, 2016, **39**, 569–572.

20 J. Wan, W. Chen, C. Jia, L. Zheng, J. Dong, X. Zheng, Y. Wang, W. Yan, C. Chen, Q. Peng, D. Wang, Y. Li, J. W. Wan, W. X. Chen, C. Chen, Q. Peng, D. S. Wang, Y. D. Li, C. Y. Jia, L. R. Zheng, J. C. Dong, X. S. Zheng, W. S. Yan and Y. Wang, *Adv. Mater.*, 2018, **30**, 1705369.

21 T. Kamegawa, H. Seto, S. Matsuura and H. Yamashita, *ACS Appl. Mater. Interfaces*, 2012, **4**, 6635–6639.

22 H. Saito and Y. Nosaka, *J. Phys. Chem. C*, 2014, **118**, 15656–15663.

23 H. Sheng, H. Ji, W. Ma, C. Chen and J. Zhao, *Angew. Chem. Int. Ed.*, 2013, **52**, 9686–9690.

24 Y. Zhao, Y. Kondo, Y. Kuwahara, K. Mori and H. Yamashita, *Catal. Today*, 2024, **425**, 114350.

25 C. Matsubara, N. Kawamoto and K. Takamura, *Analyst*, 1992, **117**, 1781–1784.

26 Y. Kondo, K. Honda, Y. Kuwahara, K. Mori, H. Kobayashi and H. Yamashita, *ACS Catal.*, 2022, **12**, 14825–14835.

27 J. Y. Hwang, G. Moon, B. Kim, T. Tachikawa, T. Majima, S. Hong, K. Cho, W. Kim and W. Choi, *Appl. Catal. B Environ.*, 2021, **286**, 119905.

28 M. Teranishi, R. Hoshino, S. Naya and H. Tada, *Angew. Chem. Int. Ed.*, 2016, **55**, 12773–12777.

29 S. Rajkumar, M. R. Venkatraman, K. Suguna, P. Karuppasamy, M. S. Pandian and P. Ramasamy, *J. Mater. Sci. Mater. Electron.*, 2022, **33**, 4965–4973.

30 S. Samanta, S. Martha and K. Parida, *ChemCatChem*, 2014, **6**, 1453–1462.

31 M. Kobayashi, H. Saito, B. Boury, K. Matsukawa and Y. Sugahara, *Appl. Organomet. Chem.*, 2013, **27**, 673–677.

32 B. Zeng, S. Wang, Y. Gao, G. Li, W. Tian, J. Meeprasert, H. Li, H. Xie, F. Fan, R. Li, C. Li, B. Zeng, S. Wang, Y. Gao, H. Li, H. Xie, F. Fan, R. Li, C. Li, G. Li, J. Meeprasert

and W. Tian, *Adv. Funct. Mater.*, 2021, **31**, 2005688.

33 P. Krishnan, M. Liu, P. A. Itty, Z. Liu, V. Rheinheimer, M. H. Zhang, P. J. M. Monteiro and L. E. Yu, *Sci. Rep.* 2017, **7**, 1–11.

34 D. R. Eddy, M. D. Permana, L. K. Sakti, G. A. N. Sheha, Solihudin, S. Hidayat, T. Takei, N. Kumada and I. Rahayu, *Nanomaterials*, 2023, **13**, 704.

35 X. Chen, Y. Kuwahara, K. Mori, C. Louis and H. Yamashita, *J. Mater. Chem. A*, 2021, **9**, 2815–2821.

36 Y. Yang, B. Cheng, J. Yu, L. Wang and W. Ho, *Nano Res.*, 2023, **16**, 4506–4514.

37 A. Behera, P. Babu and K. Parida, *Inorg. Chem. Front.*, 2021, **8**, 1489–1499.

38 K. Suzuki, X. Li, T. Toda, F. Nagasawa and K. Murakoshi, *ACS Energy Lett.*, 2021, **6**, 4374–4382.

39 C. Wang, X. Zhang and Y. Liu, *Appl. Surf. Sci.*, 2015, **358**, 28–45.

40 S. Kato, J. Jung, T. Suenobu and S. Fukuzumi, *Energy Environ. Sci.*, 2013, **6**, 3756.

41 I. Krivtsov, A. Vazirani, D. Mitoraj, M. M. Elnagar, C. Neumann, A. Turchanin, Y. Patiño, S. Ordóñez, R. Leiter, M. Lindén, U. Kaiser and R. Beranek, *J. Mater. Chem. A*, 2023, **11**, 2314–2325.

Chapter IV

Highly Reactive Facet Modulation of Ti-based MOFs by Selective Anchoring of Au Metal for Efficient Photocatalytic H_2O_2 Production

4.1 Introduction

Photocatalytic production of hydrogen peroxide (H_2O_2) via artificial photosynthesis is a promising green chemistry strategy. H_2O_2 is widely utilized in disinfection, water treatment, and as an oxidizing agent in various industries.[1–3] However, traditional methods like the anthraquinone process are energy-intensive and environmentally unfriendly.[4,5] In contrast, photocatalytic systems harness sunlight as a renewable energy source, utilizing water and oxygen under mild conditions.[6] This approach eliminates the need for hazardous intermediates, reduces energy requirements, and minimizes carbon emissions. Additionally, the decentralized and scalable nature of photocatalytic systems enables on-site H_2O_2 generation, offering potential benefits for remote or resource-limited regions.

Metal-organic frameworks (MOFs), characterized by their high surface area, tunable porosity, and versatile chemical functionalities, have emerged as promising photocatalysts.[7] Their structural versatility allows precise engineering of active sites and light-harvesting capabilities.[8,9] For instance, coupling MOFs with semiconductors (e.g., TiO_2, g-C_3N_4, V_2O_5, SnO_2)[10–12] or noble metal nanoparticles (NPs)[13–15] improves charge separation via heterojunction formation or plasmonic effects. Surface functionalization of MOFs through the introduction of specific organic linkers or metal nodes provides tailored active sites, enhancing adsorption of reactant molecules and redox catalytic selectivity.[9,16]

In recent years, facet engineering of MOFs has emerged as a crucial strategy to improve light harvesting and charge dynamics.[17] By fine-tuning factors such as precursors, solvents, and the solution pH, MOFs with various morphologies and specific exposed crystal facets can be synthesized. The exposure of specific crystal facets has been successfully achieved in the synthesis of MIL-125-NH_2,[18–20] ZIF-8,[14,15,21] MOF-5,[17] HKUST-1,[22,23] etc. The distinct atomic arrangements on different crystal facets allow MOFs to expose highly reactive facets, which are characterized by higher densities of active sites and higher surface energy.[24,25] For instance, Guo et al.[26] first predicted via density functional theory (DFT) calculations that the {110} facet of MIL-125-NH_2(Ti) exhibits more Ti-oxo clusters and higher surface energy (1.18 J m^{-2}) than {001} (0.71 J m^{-2}) and {111} (0.51 J m^{-2}) facets.[26] Synthesis techniques that prioritize the

exposure of {110} facets or combinations of facets, such as {001}/{111} and {110}/{111}, have led to notable advancements in photocatalytic applications like hydrogen evolution, CO_2 reduction, and H_2O_2 production.[27–30]

However, there is ongoing debate regarding whether single- or mixed-crystal facet MOFs offer higher photocatalytic reaction efficiency. For instance, studies have investigated the effects of MIL-125-NH_2 with exposed {001}, {111}, and mixed {001}/{111} crystal facets on photocatalytic performance. Liu et al.[30] reported that the {001} facet exhibits superior oxygen reduction capabilities due to abundant Ti-O coordination sites. Conversely, Zheng et al.[25] and Wang et al.[28] proposed that the co-exposure of {001} and {111} facets could form a Z-scheme heterojunction structure suppressing the charge recombination for dual-channel H_2O_2 production. Cheng et al.,[29] however, suggested that the {111} facet has a higher Ti concentration, which promotes the ligand-to-metal nodes charge transfer (LMCT) effect in MIL-125-NH_2, resulting in better charge separation efficiency. These conflicting findings undoubtedly created considerable ambiguity to related researchers in the field.

In addition, metal incorporation is also a common strategy to improve charge separation efficiency.[31–33] However, prior studies suggest metal modification typically enhances charge separation uniformly, without altering their original activity trend. For example, Cheng et al.[19] demonstrated that for MIL-125-NH_2 exposing {001}, {110}, and {111} facets, the CO_2 photoreduction performance followed the trend {111} > {110} > {001}. The addition of Ag NPs significantly increased CO and CH_4 yields for all three catalysts, yet the overall activity sequence remained unchanged. In contrast, our study reveals facet-dependent metal binding can reshape electronic structures and redefine facet reactivity. The facet-dependent metal interactions may play a more complex role in photocatalytic performance than previously understood.

Herein, we synthesized amine-functionalized MIL-125-NH_2-type MOFs with precisely exposed {001}, {111}, and hybrid {001}/{111} facets. The {111} facet, although less reactive and with poor charge separation, can be activated via selective Au NPs decoration using a simple one-pot hydrothermal strategy. DFT and characterization results suggest that Au preferentially binds -NH_2 groups on the {111} facet, whereas Au interacts with TiOx clusters

on the {001} facet. This study seeks to explore a straightforward strategy for modulating the highly reactive facets of MOFs and to examine how this modulation affects electron-hole separation efficiency, which acts as a critical parameter governing the photocatalytic activity of facet-engineered MOFs.

To overcome H_2O_2 decomposition commonly observed in single-phase evaluation systems, our group applied a water/benzyl alcohol (BA) dual-phase system for efficient H_2O_2 production. This setup, previously developed by our group,[34] is effective in enhancing H_2O_2 stability and yield. When combined with Au-modified highly reactive {111} facet, it achieves an impressive cumulative concentration of nearly 6000 μmol L^{-1} within 3 h of reaction. Quenching experiments and ESR measurements identified singlet oxygen ($^1O_2$) as a key intermediate product, indicating a direct two-electron oxygen reduction reaction (2e-ORR) pathway for efficient H_2O_2 synthesis. These findings highlight the potential of the dual-phase approach in optimizing photocatalytic H_2O_2 production and provide valuable insights for future advancements in this field.

4.2 Experimental

4.2.1 Materials

Titanium(IV) isopropoxide (TTIP, 97%), 2-aminoterephthalic acid (H_2NBDC, 99%), and potassium bromate ($KBrO_3$) were obtained from Sigma-Aldrich. Octadecylphosphonic acid (OPA, > 98%), 2,2,6,6-tetramethylpiperidine (TEMP, > 98.0%), 5,5-dimethyl-1-pyrroline N-oxide (DMPO, > 97%), and oxo[5,10,15,20-tetra(4-pyridyl)porphinato]titanium(IV) ($[TiO(tpypH_4)]^{4+}$, Ti-TPyP reagent) were supported from Tokyo Chemistry Industry Co., Ltd. Hydrogen tetrachloroaurate(III) tetrahydrate ($HAuCl_4$ $4H_2O$, > 99.0%), tetra-n-butyl titanate monomer (TBOT, > 95.0%), sodium chloride (NaCl, > 99.5%), triethanolamine (TEOA, 98%), p-benzoquinone (p-BQ), L-tryptophan (L-tryp, > 99.0%), sodium azide (NaN_3, 98%), hydrogen peroxide (30%), acetic acid (99.0%), benzyl alcohol (BA, 97%), methanol (99.8%), ethanol (99%), N,N-dimethylformamide (DMF, 99.5%) acetonitrile (99%), perchloric acid ($HClO_4$, 60%), and hydrochloric acid (HCl, 16.9%) were supplied by Nacalai Tesque. All the chemicals and gases used were of analytical grade and were used as received without further purification.

4.2.2 Synthesis of TM(001), TM(001/111), and TM(111)

The synthesis methods of Ti-based MIL-125-NH_2 MOFs with various exposed facets were adapted and further refined based on the protocol reported by Cheng et al.[35] Typically, 1.086 g of H_2NBDC ligand was dissolved in a mixed organic solvent of DMF and methanol (14 mL:6 mL). The solution was subjected to repeated ultrasonication and stirring at 600 rpm to ensure uniform dispersion of H_2NBDC until it exhibited a slightly gel-like appearance. The stirring speed was then increased to 900 rpm, and 0.68 mL (2 mmol) of the TBOT precursor slowly added dropwise to the ligand solution. The mixture was alternately stirred and ultrasonicated for 2 h until it reached a honey-like consistency. Subsequently, the resulting mixture was sealed into a Teflon-lined steel autoclave and heated in an oven at 150 ^oC for 24 h. After cooling to room temperature, the obtained precipitate was centrifuged and washed twice each with DMF,

methanol, and ethanol, respectively, then dried overnight at 80 ^{o}C to yield the TM (001) sample with exposed {001} crystal facets.

For the {111} facet-exposed MOF TM(111), 0.56 g of H_2NBDC was dissolved in a DMF/methanol mixed solvent with a volume ratio of 18:2. After stirring for 5 min, 1.06 mL of acetic acid was added into the suspension. Following a similar process of ultrasonication and stirring as described above, 0.6 mL (2 mmol) of TTIP, instead of TBOT, was dropwise added. The Ti precursor was effectively coordinated with the ligand through high-speed stirring and ultrasonication. The TM(111) material was synthesized using the same hydrothermal and purification method as that employed for the TM(001) sample.

The synthesis route for the mixed-facet-exposed TM(001/111) sample was similar to that of TM(111), with the exception that 1.08 g of H_2NBDC was dissolved in a mixed solvent of DMF and methanol at a volume of 16.4:3.6.

4.2.3 Synthesis of AuTM(001), AuTM(001/111), and AuTM(111)

A one-pot method was employed to prepare Au NPs-anchored MOF catalysts. Initially, a methanol solution of $HAuCl_4$ $4H_2O$ with a concentration of 20.8 mg mL^{-1} was prepared, referred to as the Au precursor solution. The synthesis followed a procedure similar to that used for synthesizing the pure MOFs TM(001), TM(001/111), and TM(111), with the only difference being the addition of the Au precursor. Specifically, after the Ti precursor was introduced and a uniform substrate was formed, 0.4 mL of the Au precursor solution was added dropwise under continuous stirring. The mixture was stirred continuously for an additional hour and subsequently transferred to an autoclave for hydrothermal synthesis. Following washing and drying, the resulting samples AuTM(001), AuTM(001/111), and AuTM(111) were obtained.
To facilitate readers in referencing the synthesis method, the specific amounts of each raw materials used for MOF synthesis are presented in **Table 1**.

Table 1. Detailed composition of precursors for the one-pot hydrothermal synthesis of Ti-MOFs and Au-anchored MOFs.

Catalyst	H_2NBDC /g	Ti precursor /mL	DMF /mL	MeOH /mL	Acetic acid /mL	$HAuCl_4 \cdot 4H_2O$ /mmol
TM(001)	1.086	TBOT, 0.68	14	6	--	--
TM(001/111)	1.08	TTIP, 0.6	16.4	3.6	--	--
TM(111)	0.56	TTIP, 0.6	18	2	1.06	--
AuTM(001)	1.086	TBOT, 0.68	14	6	--	0.02
AuTM(001/111)	1.08	TTIP, 0.6	16.4	3.6	--	0.02
AuTM(111)	0.56	TTIP, 0.6	18	2	1.06	0.02

4.2.4 Synthesis of OPA-AuTM(111)

Hydrophobic modification of AuTM(111) was achieved by treating 40 mg of the hydrophilic AuTM(111) with 100 mL of an OPA ethanol solution (20 mM). The mixture was stirred at room temperature for 24 hours, after which the precipitate was thoroughly washed with ethanol and centrifuged three times to eliminate excess OPA. The final product was then dried overnight at 80 ^{o}C in an oven and labeled as OPA-AuTM(111).

4.2.5 Characterization

The light absorption capacity was characterized by ultraviolet-visible diffuse reflectance spectra (UV-vis DRS), which was obtained from Shimadzu UV-2450 integrating sphere spectrophotometer with $BaSO_4$ serving as the reference solid. The crystal structure of the MOF materials was obtained using an X-ray diffractometer (XRD, Rigaku Ultima IV, Cu Kα radiation with wavelength of 1.5405 Å). N_2-physisorption data was obtained at -196 ^{o}C using BELSORP-max instrument (MicrotracBEL Corp., Inc.). Before testing, the samples were

pretreated under vacuum at 150 ^{o}C for 4 h to remove moisture and residual DMF from the pore channels of MOF samples. X-ray photoelectron spectroscopy (XPS, Shimadzu ESCA-3400) was performed using a monochromatic Mg Kα excitation source (1253.6 eV). And the data obtained was charge corrected using C 1s at 284.8 eV. Fourier transform infrared spectroscopy (FT-IR, JASCO FTIR-6100) was conducted to confirm the chemical environment. Each tablet sample was made by mixing 0.5 mg of powder sample and 50 mg of KBr. Photoluminescence (PL) emission spectra was obtained in the air at room temperature using a spectrofluorometer (Fluorolog-3, Horiba), with excitation wavelength of 374 nm. Field emission scanning electron microscope (FE-SEM, SU9000), produced by Hitachi High-Tech Corporation, Tokyo, Japan, was observed using the accelerating voltage of 20 kV. FE-SEM was equipped with an energy-dispersive X-ray spectrometer (EDS, EMAX Evaluation X-Max, HORIBA, Ltd., Kyoto, Japan). High-angle annular dark-field scanning transmission electron microscopy (HAADF-STEM) was conducted for observing the distribution of elements in samples. HAADF-STEM images were obtained from Talos 200S, Thermo Fisher Scientific Inc., equipped with a probe (Fischione Model 3000) and an EDS (Super X). Inductively coupled plasma optical emission spectrometry (ICP-OES, Perkin Elmer Optima 8300) was carried out for the detection of the Au amount of Au-anchored TiMOFs. The apparatus centers on two independent cooled segmented-array charge-coupled device (SCD) detectors for UV and visible light regions. Electron spin resonance (ESR) measurements were conducted on a JEOL RESONANCE JES-TE200 spectrometer. For the ESR spectra of superoxide radicals (O_2·−) during the reaction, the O_2-saturated reaction solution, containing DMPO (50 mM) with catalyst dispersed (2 g L^{-1}), was added into a Pyrex reaction vessel (30 mL) and then subjected to analysis at room temperature under dark and visible-light irradiation ($\lambda > 420$ nm). For the measurement of singlet oxygen ($^1O_2$), the preparation of samples was similar except adding TEMP as the trapping agent instead of DMPO. For the detection of Ti^{3+} signal, the catalyst (2 g L^{-1}) was dispersed in the reaction solution. The formed mixed solution was added into the ESR tube and bubbled with pure Ar for 10 min, which was frozen at -196 ^{o}C and measured under dark and after visible-light irradiation.

4.2.6 Photoelectrochemical measurements

Transient photocurrent measurement, Mott-Schottky plots, and electrochemical impedance spectroscopy (EIS) experiments were conducted in a standard Pyrex three-electrode cell setup on a HS-5000 electrochemical measurement system. The setup included a prepared catalyst-coated FTO working electrode (1×1.5 cm^2), a platinum wire serving as the counter electrode, and an Ag/AgCl reference electrode. The electrochemical workstation was used to capture and record the current density signal. For the preparation of the working electrode, a sample solution was prepared by dispersing 2 mg of the sample in a mixture containing 1 mL of methanol, and 20 μL of 5% Nafion solution. Subsequently, 40 μL of this solution was uniformly coated onto an FTO conductive glass substrate to fabricate the working electrode. In the photocurrent experiment, a 500W Xenon lamp (Sanei Electric XEF-501S) equipped with a 420 nm cut-off glass filter worked as the light source, and the cell was filled with a 0.5 M Na_2SO_4 solution as the electrolyte. EIS measurements were carried out in a frequency range from 100 kHz to 10 mHz with an amplitude of 10 mV at the initial voltage of 0 V with 0.5 M Na_2SO_4 solution as the electrolyte. Mott-Schottky plots were fulfilled in the potential range from -0.8 V to 1.0 V (vs. Ag/AgCl) at a potential step of 0.05 V and frequencies of 1260, 2000 and 5000 Hz with 0.5 M Na_2SO_4 solution as the electrolyte. The observed positive slope in the C^{-2} plot as a function of applied potential reflects the characteristic behavior of n-type semiconductors. The flat band potential (E_{FB}) was obtained by the equation 1. And the LUMO potential ($LUMO_{M-S}$) was 0.2 V more negative than E_{FB}.[36]

$$E_{FB} = E(Ag/AgCl) + 0.197\ V \qquad (1)$$

4.2.7 Calculation process of the HOMO and LUMO potentials of MOFs

High-resolution XPS spectra of the F 1s region were recorded to analyze the valence band potential for each sample, with charge correction referenced to the C-C sp^3 peak at 284.8 eV. The HOMO potential relative to the standard electrode (NHE, pH = 0) (E_{HOMO}) was determined using **Equation 2**, where φ is the electron work function of the XPS analyzer (4.50 eV), and

E_{XPS_VB} is obtained from the XPS valence band spectra of the samples.[37] Subsequently, the LUMO potential (E_{LUMO}) is ascertained using **Equation 3**, where E_g the gap energy between LUMO and HOMO potentials, is derived from Tauc plots $(ahv)^2$ based on UV-vis measurements.[38]

$$E_{HOMO} = \varphi + E_{XPS\_VB} - 4.44 \quad (2)$$

$$E_{LUMO} = E_{HOMO} - E_g \quad (3)$$

4.2.8 Photocatalytic H_2O_2 production

The photocatalytic reaction was conducted in a thermostatic reaction system as shown in **Figure 1**. Prior to the reaction, the catalysts were vacuum-dried overnight and activated at 150 ^oC for 8 h remove residual DMF from the MOF pore channels.

Evaluation of the catalytic efficiency for H_2O_2 production was conducted using a conventional single-phase reaction apparatus. For the experiment, 5 mg of activated photocatalyst was uniformly dispersed into the reaction solution composed of 4 mL of acetonitrile and 1 mL of TEOA within a 30 mL quartz reaction vessel sealed by a rubber septum. The suspension was sonicated for approximately 10 min to ensure uniform dispersion. Before initiating light irradiation, the mixture was bubbled with O_2 at a flow rate of 40 mL min^{-1} for 30 min in the dark. The O_2-saturated suspension was then exposed to the illumination from the side with a Xe lamp (500 W, Sanei Electric XEF-501S, 100 mW cm^{-2}) through a 420 nm glass filter ($\lambda > 420$ nm). During the reaction period conducted at 20 ^oC, 20 μL aliquots were collected from the aqueous phase at 1-hour intervals for subsequent analysis. The AuTM(111) catalyst used in the single-phase system for H_2O_2 production is denoted as AuTM(111)_S.

For the dual-phase system, a layered solvent consisting of 2 mL of water and 5 mL of BA was designed. 5 mg of hydrophilic AuTM(111) was dispersed in the aqueous phase for the reaction, whereas 5 mg of hydrophobic OPA-AuTM(111) was in the BA phase. All other procedures followed those described above for the single-phase system. AuTM(111) and OPA-AuTM(111) catalysts used in the dual-phase system are named as AuTM(111)_D and OPA-AuTM(111)_D, respectively.

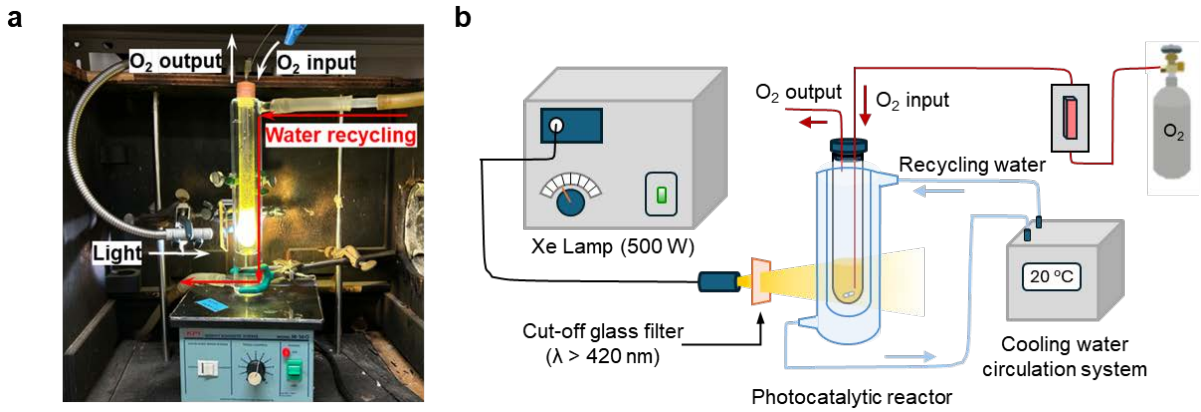

Figure 1. (a) The photograph and (b) schematic illustration of the thermostatic photocatalytic reaction system in operation.

4.2.9 H_2O_2 decomposition test

To investigate the impact of crystal facets on H_2O_2 decomposition, a 30 mL Pyrex reaction vessel was employed as the reactor. The vessel contained a mixture comprising photocatalyst (5 mg), TEOA (1 mL), acetonitrile (4 mL), and H_2O_2 solution (4 mM). After sealed using a rubber septum, the suspension was ultrasonicated for 10 min and stirred in the dark for 3 h under ambient temperature and pressure. At regular intervals of one hour, aliquots of the aqueous phase were collected to determine the concentration of H_2O_2.

4.2.10 Recycling test

After activation, 5 mg of OPA-AuTM(111) was introduced into a BA/water two-phase system and subjected to O_2 bubbling. The reaction and analysis procedures outlined in the **Section 4.2.8** were then carried out for the first cycle. Upon completion of the 3-hour reaction, the mixture was transferred to a centrifuge tube, thoroughly washed with ethanol to remove residual BA, and centrifuged. The catalysts separated were vacuum-dried and stored for subsequent cycles. For the realistic recycling test, a saturated NaCl solution (26.5%) was the aqueous phase in place of water, while all other conditions remained unchanged.

4.2.11 Stability test

5 mg of activated OPA-AuTM(111) was dispersed in the NaCl solution (26.5%)-contained biphasic system for 8 h of stability test. After bubbling with O_2 at a flow rate of 40 mL min^{-1} for 30 min in the dark, the reaction was conducted with the continuous O_2 input (3 mL min^{-1}). The further reaction and analysis processes are similar as those outlined in **Section 4.2.8.**

4.2.12 Quantification of produced H_2O_2

The quantification of H_2O_2 production was performed through spectroscopic titration using an acidic solution of the $[TiO(tpypH_4)]^{4+}$ complex, as described in previous literature.[39] For the preparation of the Ti-TpyP reagent, 3.4 mg of the complex was dissolved in 100 mL of 50 mM HCl aqueous solution. The sample solution collected was diluted with purified water to achieve an appropriate concentration for analysis. For the titration, 0.25 mL of the diluted sample solution was sufficiently mixed with 0.25 mL of 4.8 M $HClO_4$ aqueous solution and 0.25 mL of the Ti-TPyP solution. The mixture was stand for 5 minutes, during which a monoperoxo complex with H_2O_2 formed from $[TiO(tpypH_4)]^{4+}$, as follows:

$$[TiO(tpypH_4)]^{4+} + H_2O_2 \rightarrow [TiO_2(tpypH_4)]^{4+} + H_2O \qquad (4)$$

Subsequently, the mixture was diluted to a total volume of 2.5 mL with purified water. The absorbance of this solution at λ = 433 nm (A_S) was recorded using a Shimadzu UV-2600 UV-vis spectrophotometer. A blank solution also needed to be prepared by replacing the sample solution (0.25 mL) with an equivalent volume of purified water, and its absorbance was defined as A_B. The difference in absorbance (ΔA_{433}) was calculated using the equation of $\Delta A_{433} = A_B - A_S$. Based on ΔA_{433} and the volume of the solution, the amount of H_2O_2 was determined using the standard linear calibration curve presented in **Figure 2**.

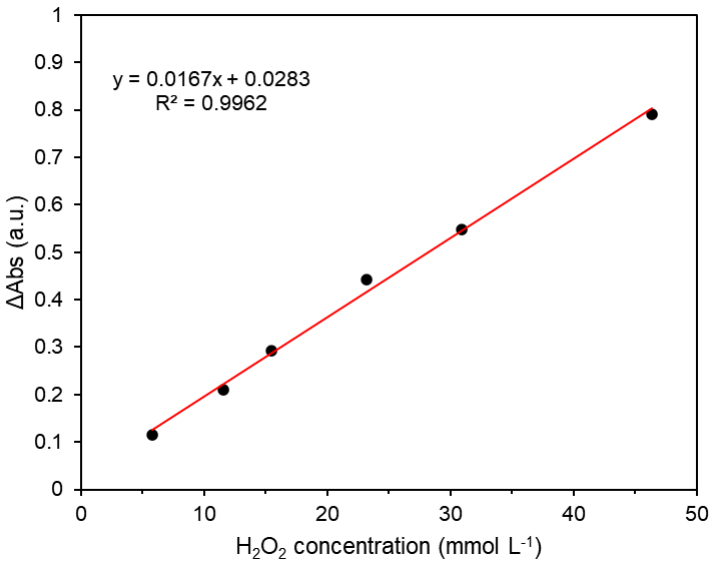

Figure 2. The linear fitting formula of standard H_2O_2 concentration.

4.2.13 Detection of benzaldehyde product

The amount of benzaldehyde (BAL) produced was quantified by gas chromatography (Shimadzu GC-2014) equipped with a flame ionization detector (FID) and an autosampler (Shimadzu AOC-20i). In the GC system, the injected samples were vaporized and separated as they passed through the column (TC-1) with the carrier gas N_2 and subsequently detected by the detector. The temperature of column, injector, and detector was set at 80 ^oC, 250 ^oC, and 250 ^oC, respectively. The solution used for GC analysis consisted of a mixture of 250 μL of reaction solution, 77 μL of acetonitrile solution containing 1 mg of biphenyl (internal standard), and 173 μL of acetonitrile. The concentration of BAL was determined by calculating the ratio of the peak areas of BAL to biphenyl and referencing the standard linear calibration curve presented in **Figure 3**.

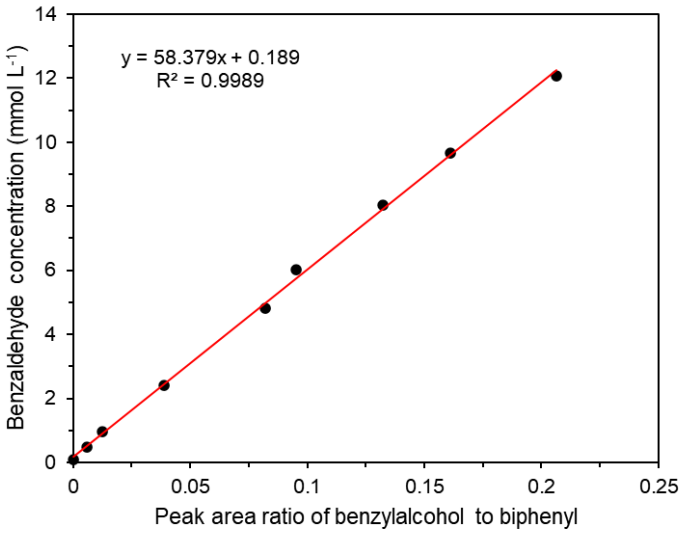

Figure 3. The linear fitting formula of standard concentration of BAL.

4.2.14 DFT calculations

All density functional theory (DFT) calculations were performed with the DMol^3 program in the Materials Studio 17.2 software package. The generalized gradient approximation (GGA) exchange-correlation functional proposed by Perdew, Burke and Ernzerh (PBE) was combined with the double numerical basis set plus polarization functions (DNP).[40] The slab model was employed for the calculation of adsorption energy of Au cluster and the average Mulliken atomic charges, The N and H atoms were allowed to relax during geometry optimizations, while C and Ti atoms were fixed at the corresponding bulk position. The slab was separated by a vacuum space with a height of 20 Å.

4.3 Results and discussion

4.3.1 Characterization of reactive {001} facet

MOFs with varying exposed facets display unique morphologies. As depicted in **Figure 4a**, the selective facet exposure on MIL-125-NH_2 was achieved by turning the Ti precursor, the solvent ratio of DMF to methanol, and the use of acetic acid during hydrothermal synthesis.[35]

Field emission scanning electron microscopy (FE-SEM) imaging (**Figure 4b**) reveals that TM(001), TM(001/111), and TM(111) exhibit disk-shaped plates, truncated bipyramidal shapes, and octahedral structures, respectively.[20,35] X-ray diffraction (XRD) patterns as shown in **Figure 4d** demonstrate the crystallographic phases of the synthesized materials. The diffraction profiles of all samples align well with the calculated patterns for MIL-125-NH_2, generated using the VESTA software (**Figure 4c**), verifying the successful synthesis of phase-pure MOFs.

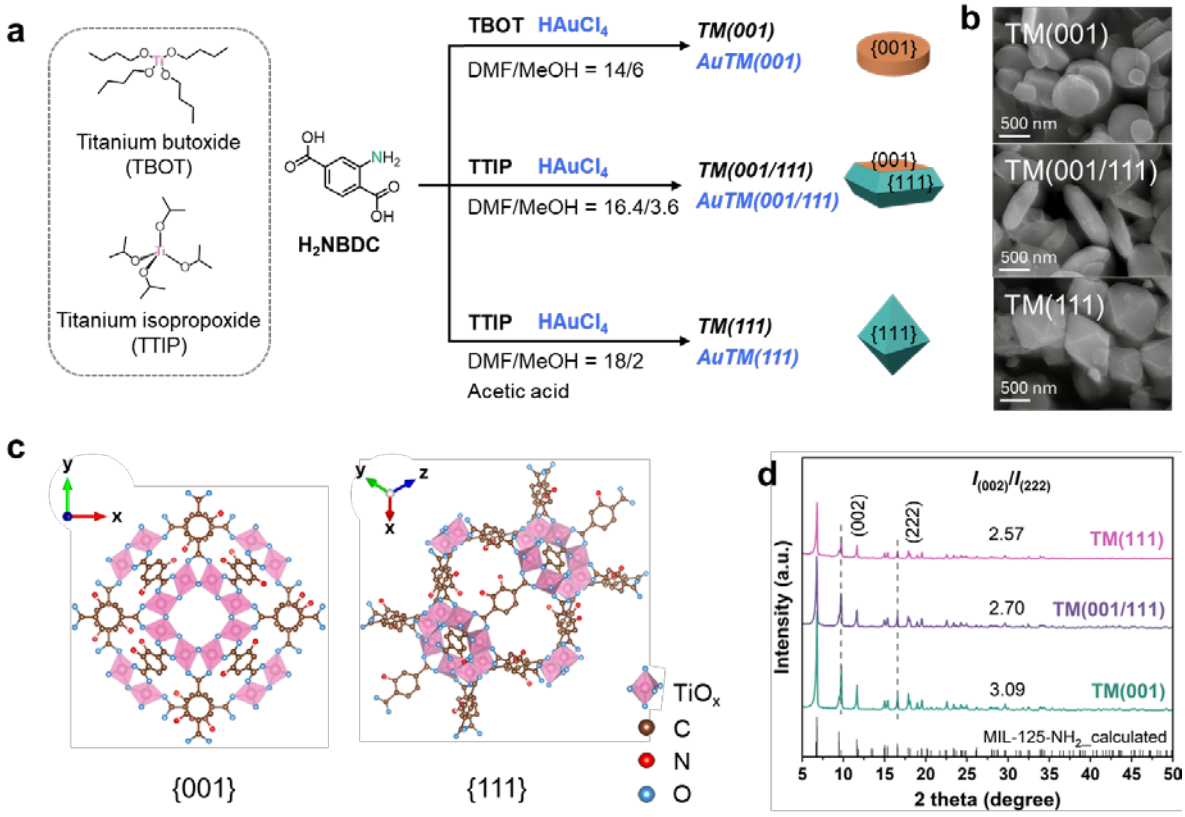

Figure 4. (a) Schematic illustration for the preparation of MOF and Au-anchored MOFs with different exposed facets; (b) FE-SEM images, (c) structural models, and (d) XRD patterns of as-synthesized MOF catalysts.

Notably, the diffraction intensities of the (002) and (222) planes exhibit an inverse correlation as the exposure of the {111} facet increases. To further quantify the facet exposure, the intensity ratio of the {001} to {111} facet, represented as $I_{(002)}/I_{(222)}$, was analyzed.[19] A higher $I_{(002)}/I_{(222)}$ value was observed for the TM(001) sample. These results collectively confirm the successful synthesis of MIL-125-NH_2 with controlled facet exposure.

As we all know, the efficiency of facet-dependent photocatalytic reactions is primarily determined by three crucial factors: light absorption, charge separation, and surface catalysis.[10,41] To evaluate optical properties and band structures, ultraviolet-visible diffraction spectra (UV-vis DRS) and corresponding Tauc plots were conducted (**Figure 5a**). A red shift in the absorption edge was observed with an increasing proportion of {111} crystal facets. This shift was accompanied by a narrower gap between the highest occupied molecular orbital (HOMO) and lowest unoccupied molecular orbital (LUMO), suggesting that the {111} facets play a significant role in enhancing light-harvesting efficiency. It was also evidenced by the fact that predominant exposure of the {001} facet was inherently less effective in harnessing light.[30]

For MIL-125-NH_2, the insertion of -NH_2 groups into ligands substantially enhances light absorption and the LMCT effect.[13,42] Thus, the high-resolution X-ray photoelectron spectroscopy (XPS) spectra for N 1s (**Figure 5b**) reveals that higher exposure of {111} facets exhibit a greater potential for electron generation, as evidenced by the noticeable negative shift of the -NH-$^{+}$ peak.[28] However, steady-state photoluminescence (PL) spectra (**Figure 5c**) indicate that TM(001) exhibits a reduced peak intensity, suggesting longer lifetimes of photogenerated electrons and superior charge separation efficiency on the {001} facets than those on {111} facets. This observation is further supported by the higher photocurrent density of TM(001) observed in photoelectrochemical measurements (**Figure 5d**).

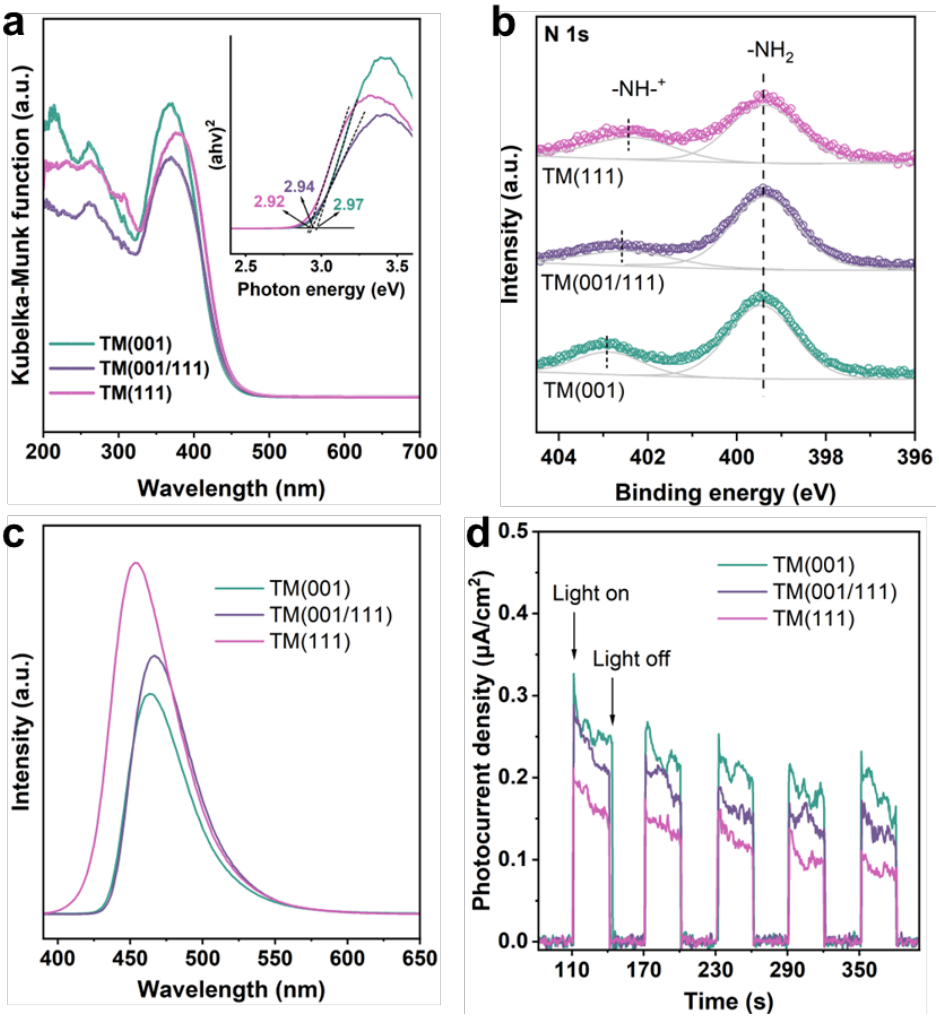

Figure 5. (a) UV-vis DRS with corresponding Tauc plots inserted, (b) high-resolution XPS spectra of N 1s, (c) PL spectra excited at 374 nm, and (d) photocurrent transient response of TM(facet) series MOFs.

Surface catalysis, the third factor, is primarily influenced by the availability of active sites.[43,44] Ti^{4+} species on the surface of MOFs act as active sites in the photocatalytic ORR, playing a role in electron transfer through the redox cycle of Ti^{4+}/Ti^{3+}.[45,46] First, N_2 adsorption-desorption analysis (**Figure 6 and Table 2**) indicates comparable specific surface areas across the three TM(facet) samples. Moreover, particle size analysis of MOFs (**Figure 7**) revealed an increasing trend in average diameter, following the order of TM(001)< TM(001/111)< TM(111). It is widely studied that smaller MOF particles are beneficial for the exposure of TiOx clusters, acting as electron acceptors, which facilitates O_2 capture by Ti-O reactive sites and the ORR process.[47] Furthermore, thanks to the smaller particle size, the {001} facet offers a shorter

electron transfer path, facilitating the rapid reduction of Ti^{4+} to Ti^{3+}. This enhanced charge transport capability is believed as the rate-determining step (RDS) influencing catalytic performances in facet-dependent photocatalytic processes.[30]

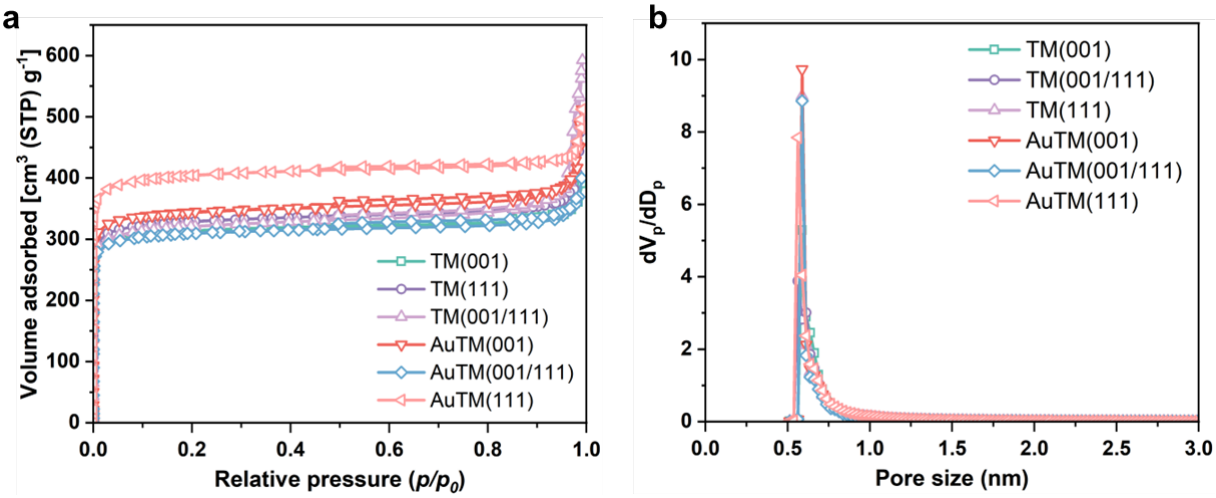

Figure 6. (a) N_2 adsorption-desorption isotherms and (b) pore distributions of TM(001), TM(001/111), TM(111), AuTM(001), AuTM(001/111), and AuTM(111) catalysts.

Table 2. BET specific surface areas and total pore volumes of the catalysts.

Catalyst	S_{BET}[a] /m^2 g^{-1}	S_{micro}[b] /m^2 g^{-1}	Pore volume[b] /cm^3 g^{-1}	Pore size[c] /nm
TM(001)	1233	1641	0.49	0.59
TM(001/111)	1255	1636	0.48	0.56
TM(111)	1291	1716	0.51	0.59
AuTM(001)	1369	1789	0.53	0.59
AuTM(001/111)	1212	1610	0.48	0.59
AuTM(111)	1590	2117	0.63	0.56

[a] Total specific surface area (S_{BET}) was determined by the BET method;

[b] Micropore specific surface area (S_{micro}) and pore volume analyzed by t-plot method at $p/p_0 < 0.05$;

[c] Micropore size calculated by SF method at $p/p_0 < 0.05$.

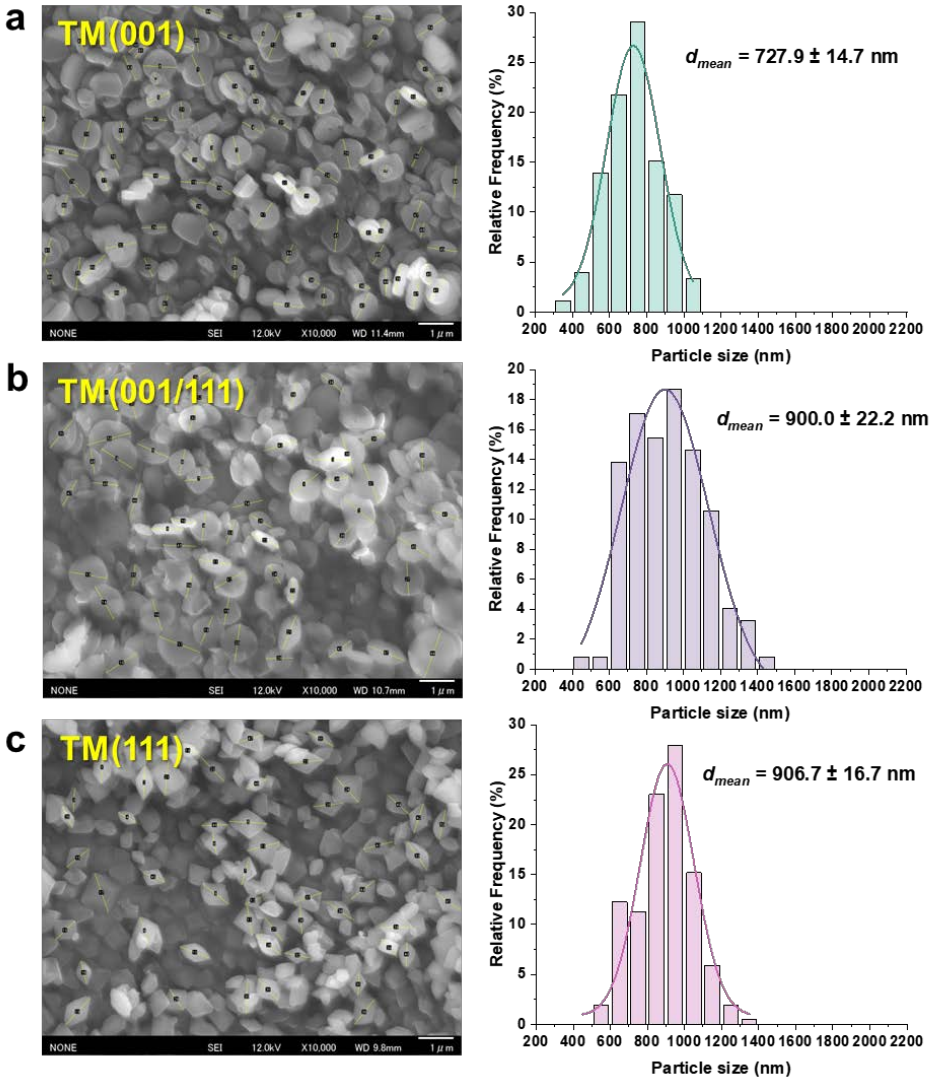

Figure 7. Particle size distribution of (a) TM(001), (b) TM(001/111), and (c) TM(111).

To confirm this hypothesis, we conducted a performance evaluation of the three MOFs in photocatalytic ORR for H_2O_2 production. As shown in **Figure 8a**, regardless of whether TEOA or BA was used as a sacrificial agent to consume photogenerated holes, {001} facets demonstrated more favorable for H_2O_2 production. Reasonably, compared to {111} facets, {001} facets on MIL-125-NH_2 are identified as the reactive facet for photocatalytic ORR. **Figure 8b** provides an apparent depiction of the interplay between light absorption capability and charge separation efficiency on ORR performance. Notably, TM(001), despite having the broadest HOMO-LUMO gap and the weakest light absorption capability, exhibited the highest charge separation efficiency and H_2O_2 production. This finding underscores the predominant status of charge separation efficiency in the facet-dependent photocatalytic ORR process.[30]

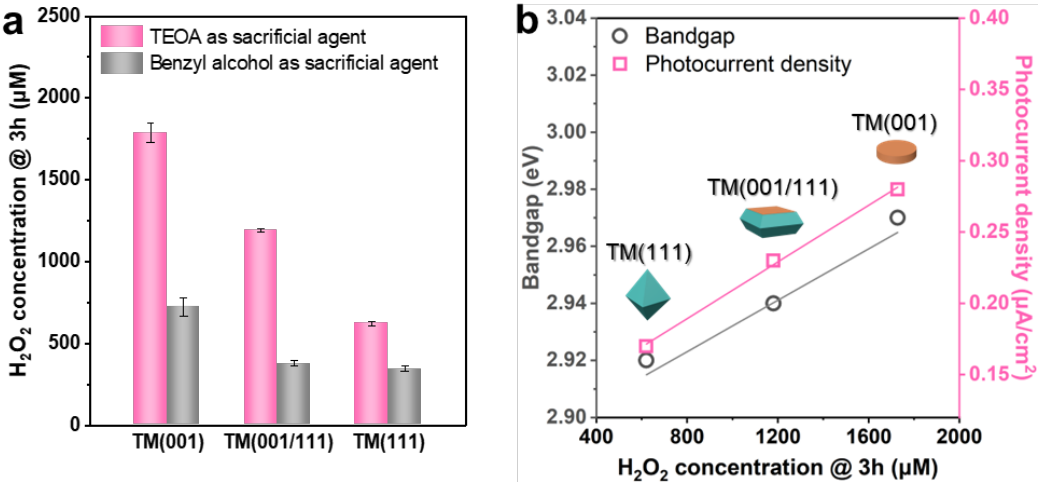

Figure 8. (a) H_2O_2 production after 3 h-reaction on TM(facet) in the single-phase system using TEOA or BA as the sacrificial agent (Reaction conditions: acetonitrile, 4 mL; TEOA or BA, 1 mL); (b) The relative diagram of HOMO-LUMO gap, photocurrent density, and H_2O_2 concentration accumulated after 3 h-reaction using TM(facet) series catalysts.

4.3.2 Construction of emerging highly reactive {111} facet

The {111} facet, despite being a less reactive surface, exhibits an inherent advantage in visible-light absorption.[29] To work from this property, efforts in research must be redirected towards addressing its limitation in electron-hole separation efficiency. The aim is to engineer a novel emerging highly reactive facet that synergistically combines exceptional light-harvesting ability with superior electron transfer capacity.[19]

Building on this promising concept, we utilized a one-pot hydrothermal method to incorporate Au NPs into MOFs with distinct facet exposures, forming the AuTM(facet) series of Au-anchored MOFs. According to the FE-SEM images (**Figure 9**), it is observed that selective facet exposure, characteristic morphology, and particle size trends of AuTM(facet) are well maintained after Au incorporation. XRD patterns (**Figure 10**) further verify that all three MOF samples preserved their original crystal structures, with the appearance of a minor peak at 38.2°, indicative of the presence of Au NPs in MOFs.[48] High-angle annular dark-field scanning transmission electron microscopy (HAADF-STEM) imaging (**Figure 11**) with EDS-mapping reveals that the Au NPs distribute uniformly on MOFs. Inductively coupled plasma optical emission spectrometry (ICP-OES) analysis quantified the Au loadings as 0.36, 0.47,

and 0.48 wt% for AuTM(001), AuTM(001/111), and AuTM(111), respectively. Due to the low loading amount and small particle size of Au NPs, directly observing their distribution on specific facets was challenging, even with high-resolution electron microscopy.

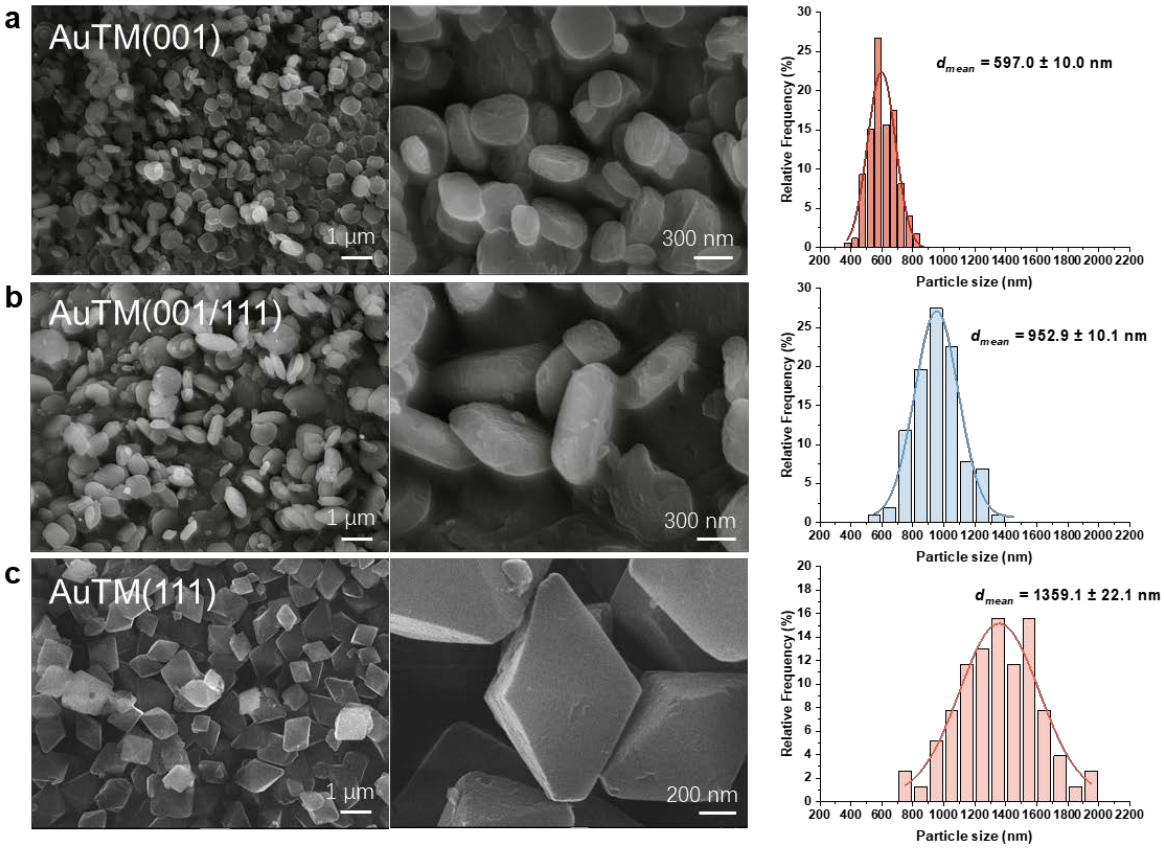

Figure 9. FE-SEM images and the particle size distribution of (a) AuTM(001), (b) AuTM(001/111), and (c) AuTM(111) samples.

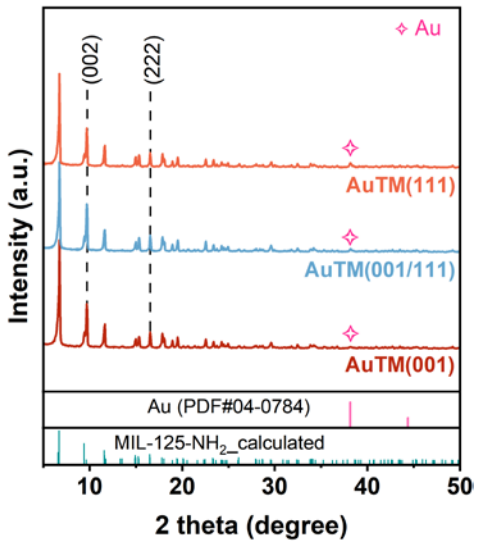

Figure 10. XRD patterns of Au-anchored MOFs.

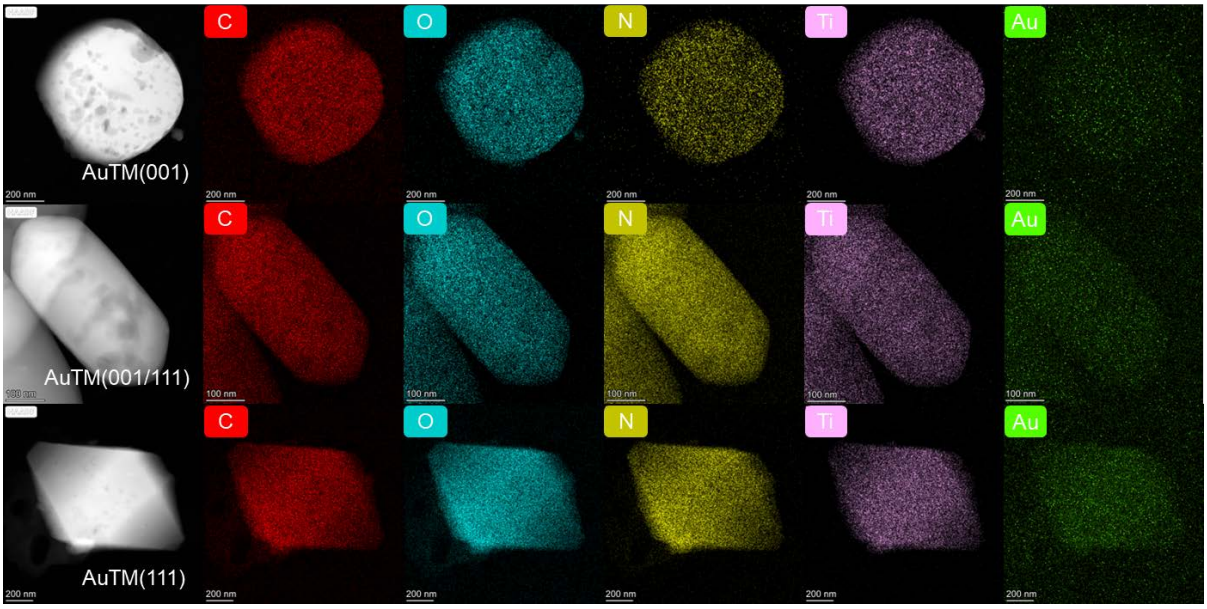

Figure 11. HAADF-STEM images and corresponding EDS-mapping results for C, O, N, Ti, and Au elements of AuTM(001), AuTM(001/111), and AuTM(111) samples.

To elucidate the facet-dependent coordination behavior of Au NPs in AuTM(facet) samples, XPS, Fourier transform infrared spectroscopy (FT-IR), and DFT calculations were employed. As shown in **Figure 12a**, the peak at 284.8 eV in the XPS C 1s spectra, corresponding to extraneous contaminant carbon, was used for charge correction of other elements. Upon introducing Au NPs, the N 1s spectra (**Figure 12b**) of AuTM(111) exhibits a 0.3 eV positive shift in the -NH-$^{+}$ peak compared to bare TM(111), whereas no shift was observed for AuTM(001). Meanwhile, the Au peaks in AuTM(111) appear at slightly lower binding energies than in AuTM(001) (**Figure 12c**), consistent with higher electron density on the Au of AuTM(111). In the Ti 2p spectra (**Figure 12d**). Au-incorporation on TM(111) induces 0.3 eV positive shifts in Ti $2p_{1/2}$ and Ti $2p_{3/2}$ peaks (from 464.3/458.6 eV to 464.6/458.9 eV), which is larger than those observed in AuTM(001/111) (+0.2 eV) and AuTM(001) (+0.1 eV). This suggests that stronger Au-NH_2 interactions of AuTM(111), redirecting that electrons would typically flow to Ti^{4+} toward Au. Moreover, in AuTM(001), Ti 2p peaks exhibit +0.1 eV shift, while no shift is observed in the N 1s peak of AuTM(001) after Au incorporation. Combined with the negative shift in Au 4f peaks, it is concluded that Au NPs in AuTM(001) preferentially localize near TiOx clusters rather than -NH_2 groups.[49]

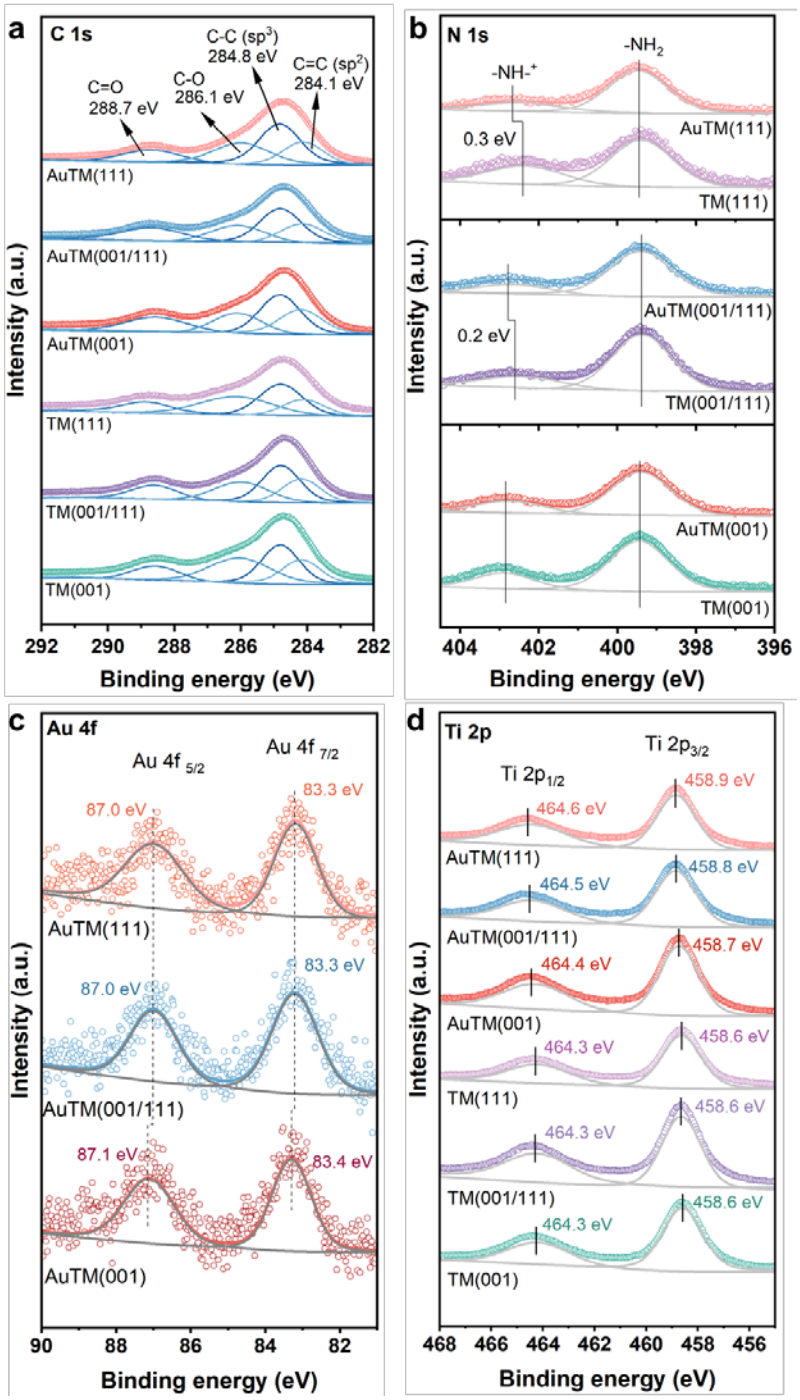

Figure 12. High-resolution XPS spectra of (a) C 1s, (b) N 1s, (c) Au 4f, and (d) Ti 2p of as-synthesized Ti-MOFs and Au-anchored MOF samples.

FTIR analysis provides additional confirmation (**Figure 13**). The peaks at around 1060 cm^{-1} can be ascribed to the rocking vibration of $-NH_2$ groups. And the peaks at 773 cm^{-1} represent the characteristic Ti-O vibration. For TM(111), the $-NH_2$ rocking vibration at 1063 cm^{-1} redshifts to 1048 cm^{-1} after Au decoration,[50] with increased intensity at higher Au loadings,

while the Ti-O vibration at 773 cm^{-1} remains unchanged.[51,52] DFT calculations were conducted using Au13 cluster models adsorbed on different facets (**Figure 14a**). The calculated adsorption energies (E_{ad}), summarized in **Figure 14b**, indicate that more favorable configurations are Au13-TiOx in AuTM(001) and Au13-NH_2 in AuTM(111), as they exhibit higher E_{ad} values compared to other models.

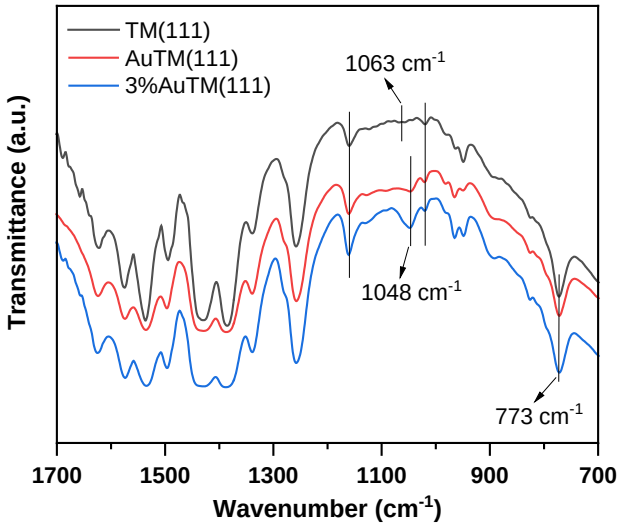

Figure 13. FT-IR spectra of TM(111), AuTM(111) (Au loading: 0.5wt%) and 3%AuTM(111) (Au loading: 3 wt%).

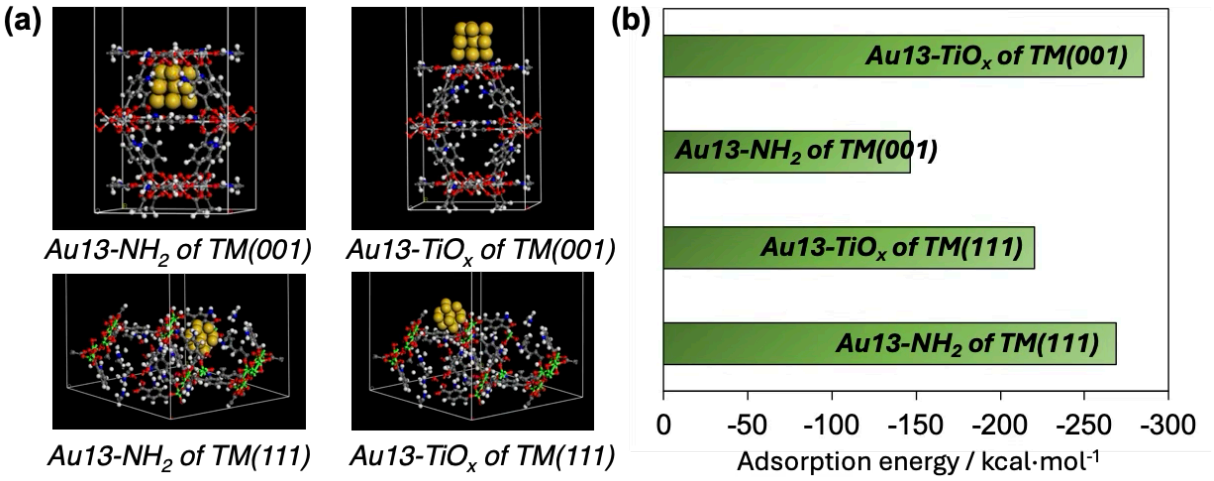

Figure 14. (a) The structural models of Au13 cluster adsorbed on -NH_2 group or TiOx clusters on TM(001) or TM(111). (b) Adsorption energies of Au13 cluster on MOFs (E_{ad}), defined by the following equation of E_{ad} = E(Au13+MOF) − E(MOF) − E(Au13).

Honestly, this selective distribution can also be explained by the underlying principles of the one-pot thermal synthesis. Literatures report that for synthesizing TM(001), the use of a highly polar solvent (DMF: MeOH = 14:6) and fast-dissolving TBOT precursor promotes the preferential formation of $Ti_8O_8(OH)_4$ clusters, which tend to adsorb $AuCl_4^-$ ions and subsequently reduce them in situ upon heating. In contrast, the synthesis of TM(111) involves a low-polarity solvent (DMF: MeOH = 18:2) and a slow-dissolving TTIP precursor, allowing $AuCl_4^-$ ions to preferentially interact with the -NH_2 groups on the ligand.[48,49] This ultimately results in the facet-selective distribution of Au. Therefore, it is theoretically and experimentally concluded that Au NPs bind to -NH_2 groups on {111} facet and to TiOx clusters on {001} facet.

As illustrated in the schematic diagram in **Figure 15**, the distribution of Au NPs differs significantly between the {001} and {111} facets of MIL-125-NH_2, leading to distinct pathways for photogenerated electron transportation. Upon light irradiation, electrons are excited from the ligands and transferred to Ti-oxo clusters via the LMCT effect of MOFs.[13] On the Au-anchored {001} facet, electrons continuously flow toward the Au NPs localized near Ti atoms, depleting electron density on Ti. In contrast, on the {111} facet, electrons preferentially transfer directly to the Au NPs positioned near -NH_2 groups, facilitated by Au-NH_2 interactions. This facet-dependent electron transfer mechanism endows AuTM(111) with superior electron transfer efficiency, which has been identified as a decisive factor influencing photocatalytic performance.[30]

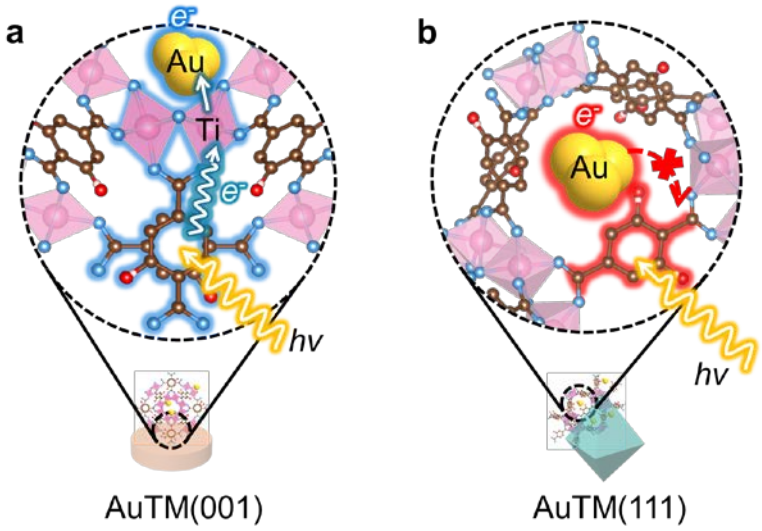

Figure 15. Schematic illustrations of electron transfer pathway on the surface of (a) AuTM(001) and (b) AuTM(111) samples.

Au incorporation on MOFs, formed as AuTM(facet), induced notable changes in the band structure of MOFs with distinct facet exposures. As revealed by the UV-vis DRS spectra (**Figure 16a**), the AuTM(facet) series still exhibit consistent light absorption behavior across the TM(facet) samples, AuTM(111)> AuTM(001/111)> AuTM(001). Analysis of the Tauc plots (**Figures 16b**) demonstrates a narrowing of the HOMO-LUMO gap (E_g) for AuTM(facet) compared to TM(facet), indicative of a reduced electronic transition barrier upon Au modification.[53] Furthermore, the Mott-Schottky (M-S) measurements (**Figure 17**) provide flat band potentials for all six samples, enabling the estimation of their LUMO potentials ($LUMO_{M-S}$). It is obvious that Au incorporation renders MOFs a positive shift of flat band potentials.

The HOMO and LUMO potentials were calculated using the UV-vis DRS-derived E_g and $LUMO_{M-S}$, and further confirmed by XPS valence band spectra (**Figure 18a**), with results summarized in **Table 3**. The good agreement between calculated and experimental values validates the reliability of the data. As visualized in **Figure 18b**, {111} facet exposure facilitates band structure optimization, while Au incorporation shifts the bands to more negative potentials. Specifically, the LUMO potential of AuTM(111) (-0.44 V vs. NHE) was more negative than the reduction potential of O_2 to H_2O_2 (0.68 V vs. NHE), indicating its immense potential for optimizing the photocatalytic ORR.[6]

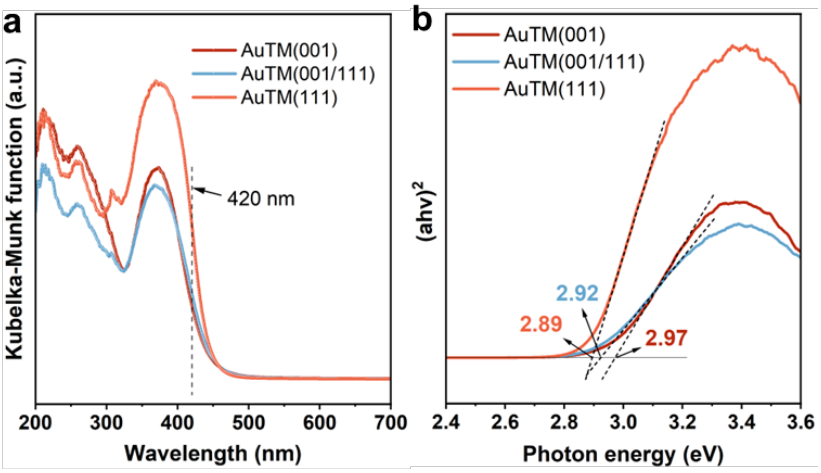

Figure 16. (a) UV-vis DRS spectra and (b) Tauc plots of Au-anchored MOF samples; (c) Comparison of HOMO-LUMO gaps between as-synthesized MOFs TM(facet) and Au-anchored MOFs AuTM(facet).

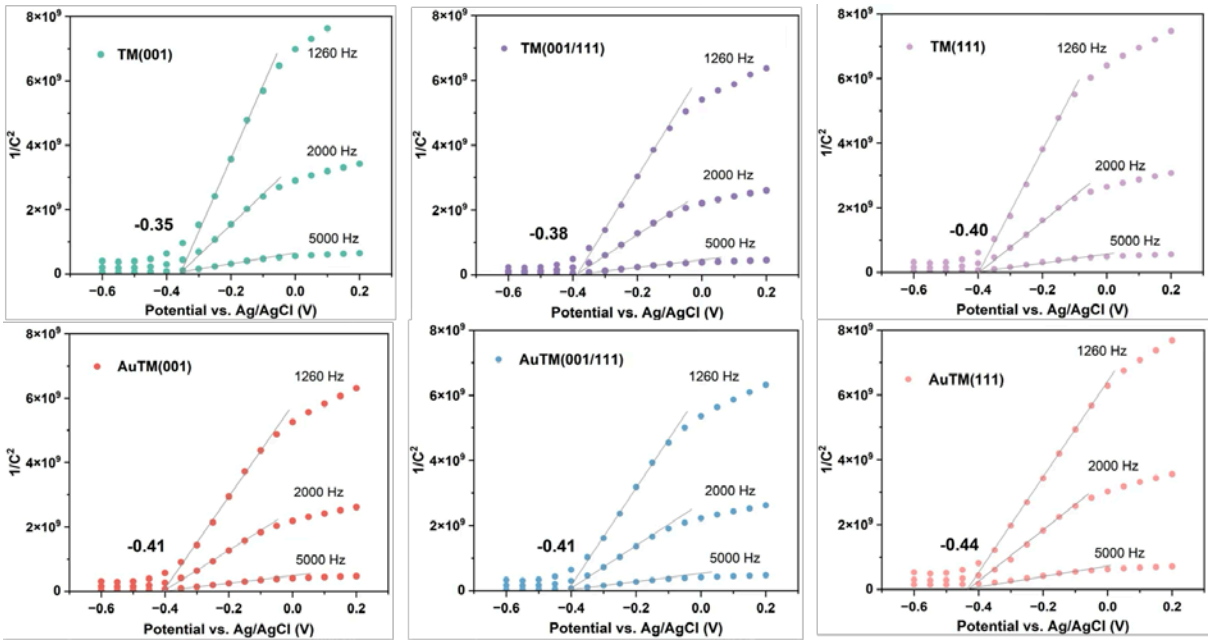

Figure 17. Mott-Schottky plots for pure MOFs and Au-anchored MOFs materials at frequencies of 1260, 2000 and 5000 Hz.

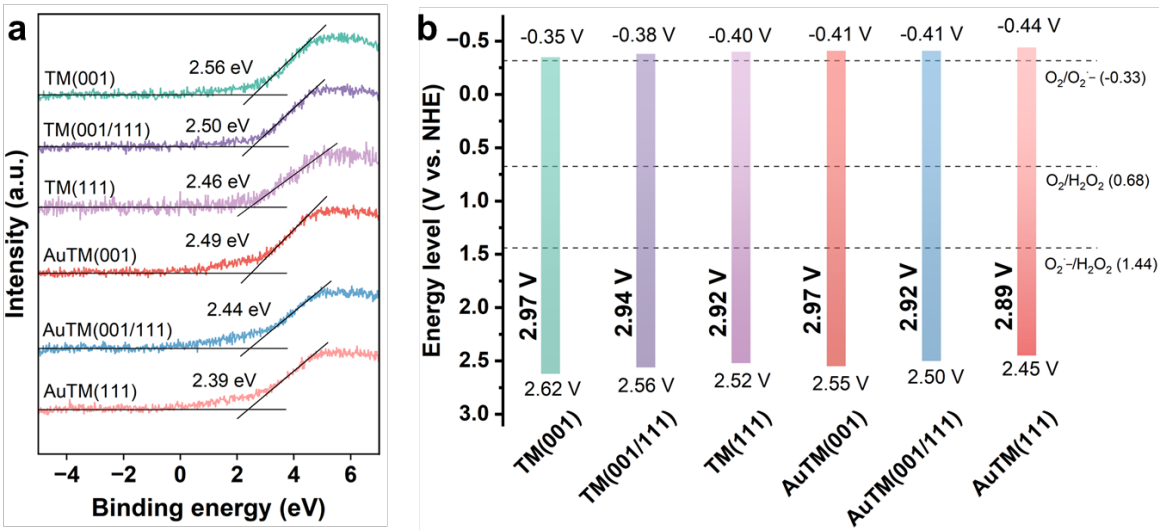

Figure 18. (a) XPS valence band spectra and (b) energy level schematic of pure MOFs and Au-anchored MOFs catalysts.

Table 3. Summary of energy level potentials of Ti-based MOFs and Au-anchored MOFs.

Catalyst	E_g[a] /eV	$HOMO_{XPS}$[b] /V	$LUMO_{M\text{-}S}$[c] /V	$HOMO_{cal}$[d] /V	$LUMO_{cal}$[e] /V
TM(001)	2.97	2.62	-0.35	2.62	-0.35
TM(001/111)	2.94	2.56	-0.38	2.56	-0.38
TM(111)	2.92	2.52	-0.40	2.52	-0.40
AuTM(001)	2.97	2.55	-0.41	2.56	-0.42
AuTM(001/111)	2.92	2.50	-0.41	2.51	-0.42
AuTM(111)	2.89	2.45	-0.44	2.45	-0.44

[a] Obtained from Tauc plots based on UV-vis results;

[b] Observed using XPS valence band spectra;

[c] Derived from Mott-Schottky plots;

[d] Calculated using the equation $HOMO_{cal} = LUMO_{M\text{-}S} + E_g$;

[e] Calculated using the equation $LUMO_{cal} = HOMO_{XPS} – E_g$.

The impact of Au on charge separation efficiency was also investigated. As shown in the PL spectra (**Figure 19a**), Au modification substantially reduced the fluorescence intensities, reflecting improved suppression of electron-hole recombination.[54] Notably, the difference between TM(111) and AuTM(111) is more pronounced than that between TM(001) and AuTM(001), highlighting a stronger impact of Au on the improvement of charge separation efficiency, especially on the {111} facet. DFT-calculated average Mulliken charges (**Figure 20**) further revealed that N atoms in Au–NH_2 groups of AuTM(111) exhibited a less negative charge (−0.63) than in TM(111) (−0.87), indicating electron transfer from N atoms to Au. {111} facet-located Au acts as an efficient electron acceptor, directly capturing photogenerated electrons from ligands, thereby suppressing recombination more effectively than {001} facet-located Au. These findings further support that Au incorporation effectively alters the electronic structure of the {111} facet, modifying the local charge distribution.

Consequently, Au modification transforms the {111} facet from a less reactive facet into an emerging highly reactive facet, which owns inherent light absorption and superior charge separation efficiency, simultaneously. Remarkably, AuTM(111) outperforms the conventional highly reactive {001} facet, as evidenced by its higher photocurrent density (**Figure 19b**) and lower impedance (**Figure 19c**) than AuTM(001). These results underscore the unique advantages of the AuTM(111) material, paving the way for its efficient photocatalytic ORR.

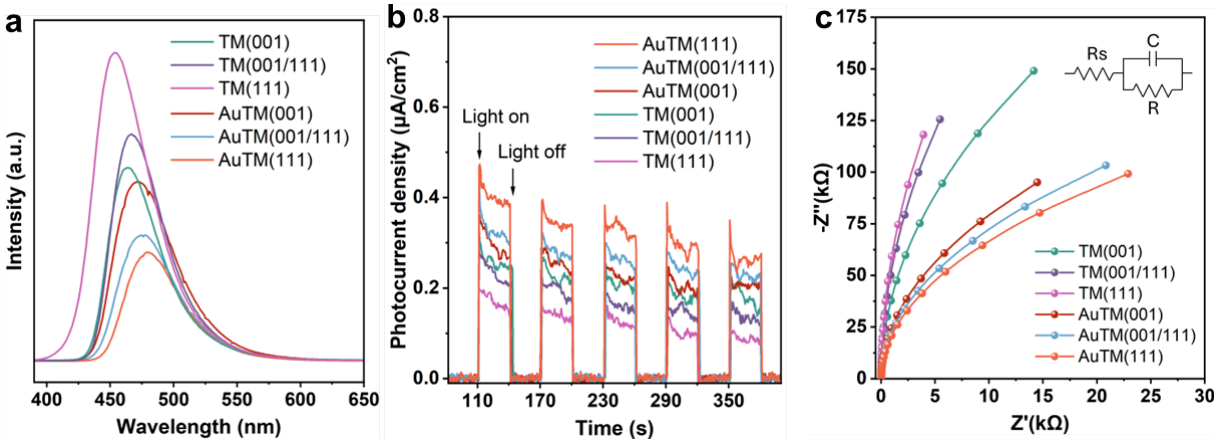

Figure 19. (a) PL spectra excited at 374 nm, (b) photocurrent transient density, and (c) EIS results of TM(facet) and AuTM(facet) samples.

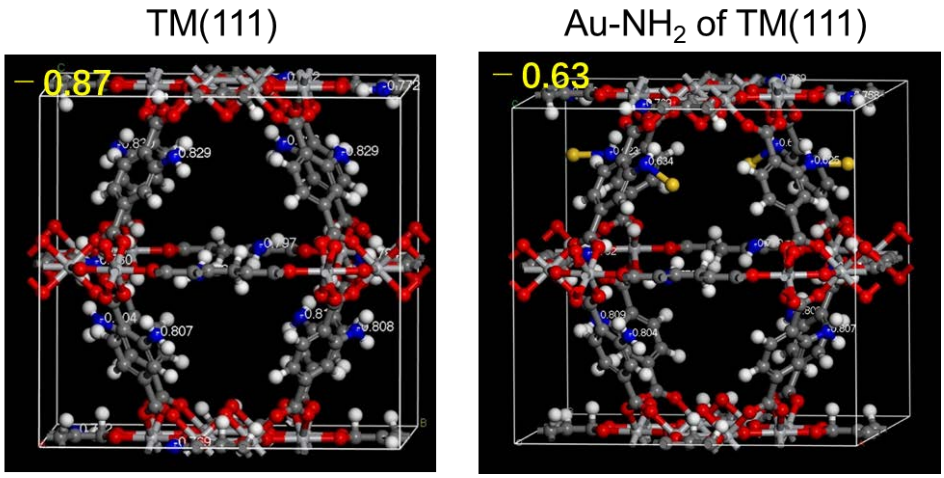

Figure 20. Mulliken atomic charge of N atoms in TM(111) and AuTM(111).

4.3.3 Effect of Au NPs selective anchoring on photocatalytic H_2O_2 production

The photocatalytic H_2O_2 production performance of AuTM(facet) samples was systematically evaluated, with results presented in **Figure 21a**. Surprisingly, the catalytic activity of AuTM(facet) exhibits a positive correlation with the increased exposure of the {111} facet, in stark contrast to the trend observed for TM(facet). After 3 h of reaction, AuTM(001) displays only marginal improvement compared to TM(001), while AuTM(111) achieved the H_2O_2 concentration of 3221 μmol L^{-1}, five times higher than TM(111). This pronounced enhancement is attributed to the selective anchoring of Au NPs near -NH_2 groups on the {111} facet, leading to superior charge separation efficiency, coupled with the intrinsic light-harvesting advantage of the {111} facet.[20,29] Moreover, H_2O_2 decomposition tests (**Figure 21b**) reveal that the exposure of {111} facet effectively suppresses H_2O_2 decomposition, further contributing to the superior H_2O_2 productivity on AuTM(111).

To elucidate the underlying reaction mechanism, the photocatalytic performance of AuTM(111) was further examined under varying light and atmospheric conditions, as well as through quenching experiments. As shown in **Figure 21c**, negligible H_2O_2 was detected in the absence of either light or oxygen. The introduction of light and air modestly increases H_2O_2 concentration, but it remains obviously lower than under light and O_2-saturated conditions. Therefore, H_2O_2 is generated via the reduction of O_2 under light irradiation, specifically through the two-electron oxygen reduction reaction (2e-ORR).

The 2e-ORR can proceed via two distinct pathways, the direct or indirect pathway, with singlet O_2 species ($^1O_2$) and superoxide species ($O_2^{\bullet-}$) acting as intermediates, respectively.[33,55] The detailed mechanisms are as follows:

Direct 2e-ORR pathway: $^1O_2 + 2e^- + 2H^+ \rightarrow H_2O_2$ (5)

Indirect 2e-ORR pathway: $O_2 + e^- \rightarrow O_2^{\cdot-}$ (6)

$O_2^{\cdot-} + e^- + 2H^+ \rightarrow H_2O_2$ (7)

To identify the dominant pathway, quenching experiments were conducted using scavengers for electrons ($KBrO_3$), $O_2^{\bullet-}$ (p-BQ), and $^1O_2$ species (L-tryp).[56] As shown in **Figure 21d**, the addition of an $O_2^{\bullet-}$ scavenger significantly reduced H_2O_2 production for both TM(111)

and AuTM(111), indicating the involvement of $O_2^{\bullet-}$ intermediates. However, upon introducing a $^1O_2$ scavenger, H_2O_2 production remained nearly unchanged for TM(111) but decreased markedly for AuTM(111). This suggests that $O_2^{\bullet-}$ serves as the primary intermediate in the TM(111) system, while $^1O_2$ intermediate dominates in the AuTM(111) system. Furthermore, the in-situ ESR measurement supported this conclusion (**Figure 22**), where comparable DMPO-$O_2^{\bullet-}$ signals were detected for both samples, and a stronger TEMP-$^1O_2$ adduct was observed in AuTM(111). Therefore, TM(111) follows an indirect 2e-ORR pathway mediated via $O_2^{\bullet-}$ radicals (**Equations 6-7**), while Au incorporation on MOFs promotes a direct, $^1O_2$-mediated 2e-ORR pathway (**Equation 5**).

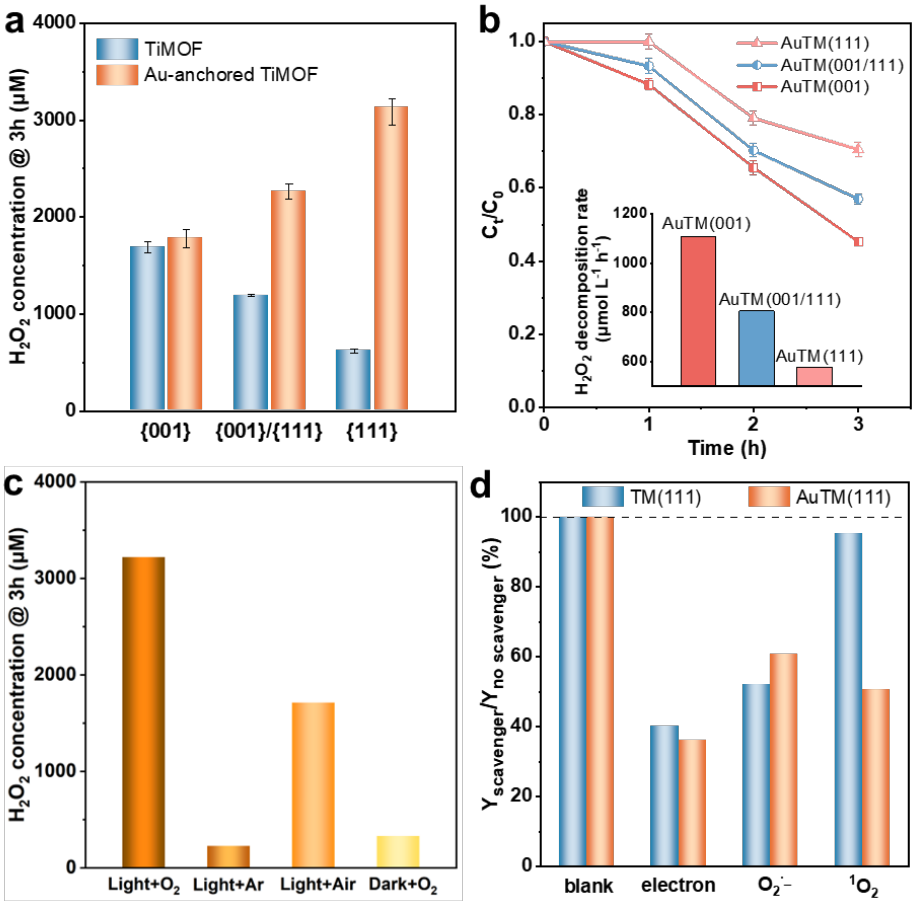

Figure 21. (a) Single-phase H_2O_2 production using TEOA as the sacrificial agent of as-synthesized samples under $\lambda > 420$ nm irradiation; (b) H_2O_2 decomposition test employing AuTM(facet) catalysts in the single-phase system; (c) Single-phase H_2O_2 accumulation using AuTM(111) under various conditions; (d) Contributions of different active species to 3 h-reaction of single-phase photosynthesis of H_2O_2 (each scavenger's concentration: 50 mM).

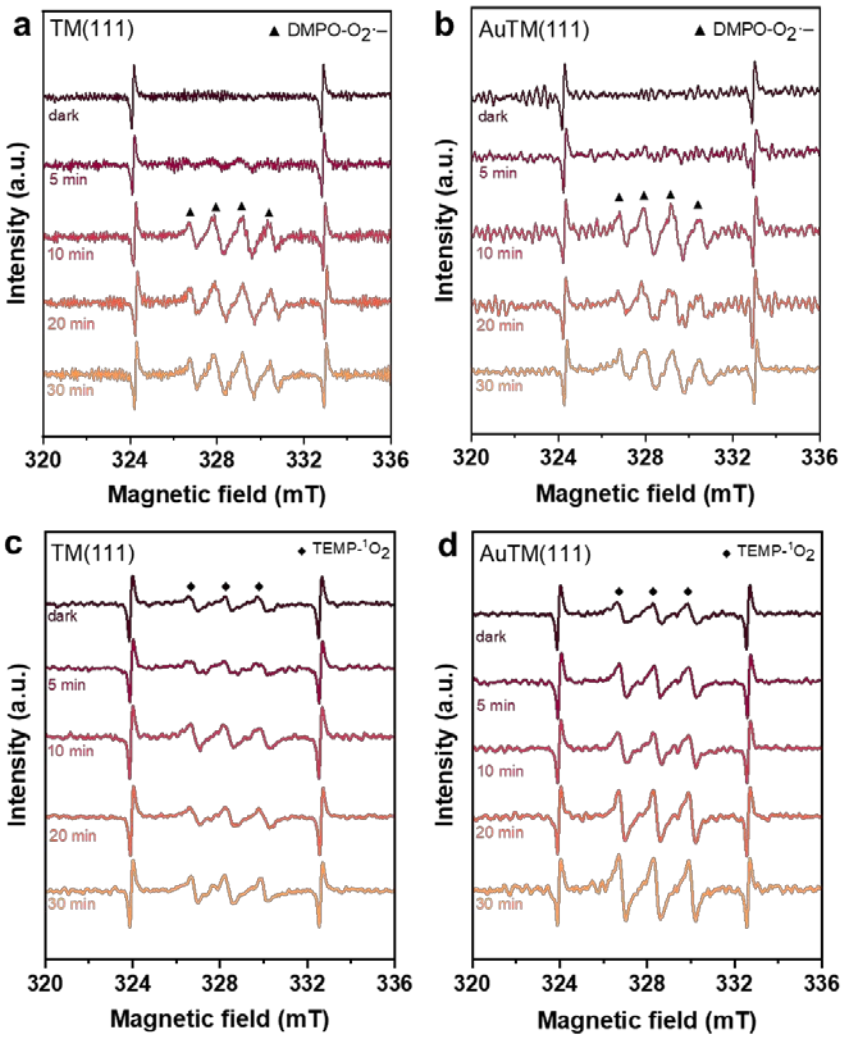

Figure 22. In-situ ESR spectrum of (a,b) DMPO-$O_2^{\cdot-}$ and (c,d) TEMP-$^1O_2$ signals in suspensions containing acetonitrile, TEOA, DMPO or TEMP, and catalyst of TM(111) or AuTM(111) under dark and visible-light irradiation for 30 min.

Based on the above comprehensive characterization and activity evaluation, a schematic illustration of potential photocatalytic ORR mechanisms is presented in **Figure 23.** For pristine MOFs without Au, photoexcited electrons transfer from the ligands to Ti-oxo clusters via the LMCT effect, driving the ORR via the Ti^{4+}/Ti^{3+} cycle. This was confirmed by the colorimetric experiment in **Figure 24**, where the solution turned blue under light in an inert atmosphere and reverted to its original color upon O_2 introduction. Despite its strong light absorption, the {111} facet suffers from significant electron-hole recombination, limiting its ORR efficiency, defined as the less reactive facet compared to the {001} facet.

Upon Au incorporation, the electron transfer pathways diverge depending on the exposed facet, as supported by ESR spectra (**Figure 25**). On the {001} facet, Au-TiOx interactions enhance the original LMCT pathway, as evidenced by a stronger Ti^{3+} signal. In contrast, on the {111} facet, Au-NH_2 interactions lead to a diminished Ti^{3+} signal, indicating a new electron transfer route where photoexcited electrons are directly transferred to Au rather than TiOx. This redirection likely results from the spatial proximity of Au to NH_2 groups and the superior conductivity of Au.[57] The newly established highly reactive {111} facet (**Figure 23d**), therefore, simultaneously offers strong light absorption, efficient charge separation, and superior charge transport. These synergistic properties contribute to significantly enhanced ORR activity and H_2O_2 productivity of AuTM(111).

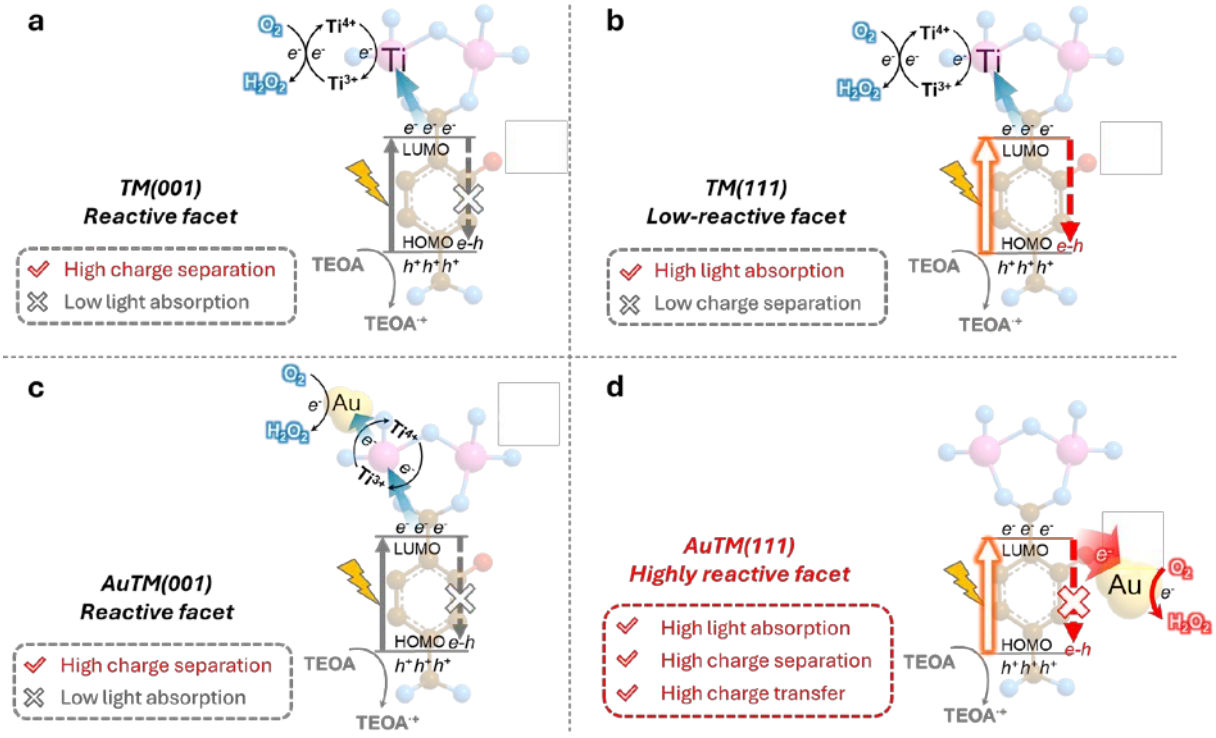

Figure 23. Schematic illustration of possible mechanisms of photocatalytic H_2O_2 synthesis process on (a) TM(001), (b) TM(111), (c) AuTM(001), and (d) AuTM(111).

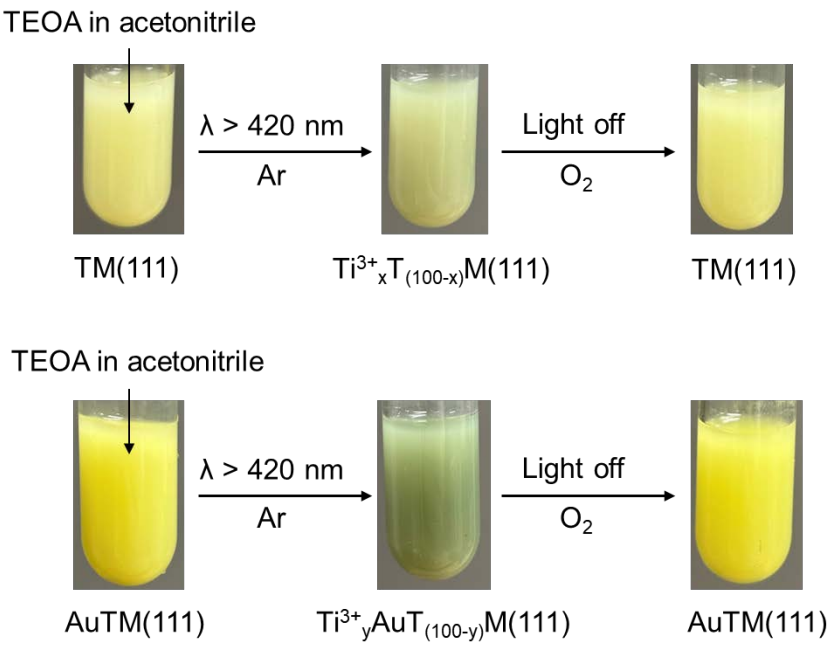

Figure 24. Photos of TM(111) and AuTM(111) samples under different conditions: (left) fresh TM(111) or AuTM(111) in the acetonitrile solution of TEOA (20 vol%), (middle) under Ar atmosphere and visible-light irradiation, (right) after cutting down the light and introducing O_2. The color changes at each step occur after 10 minutes.

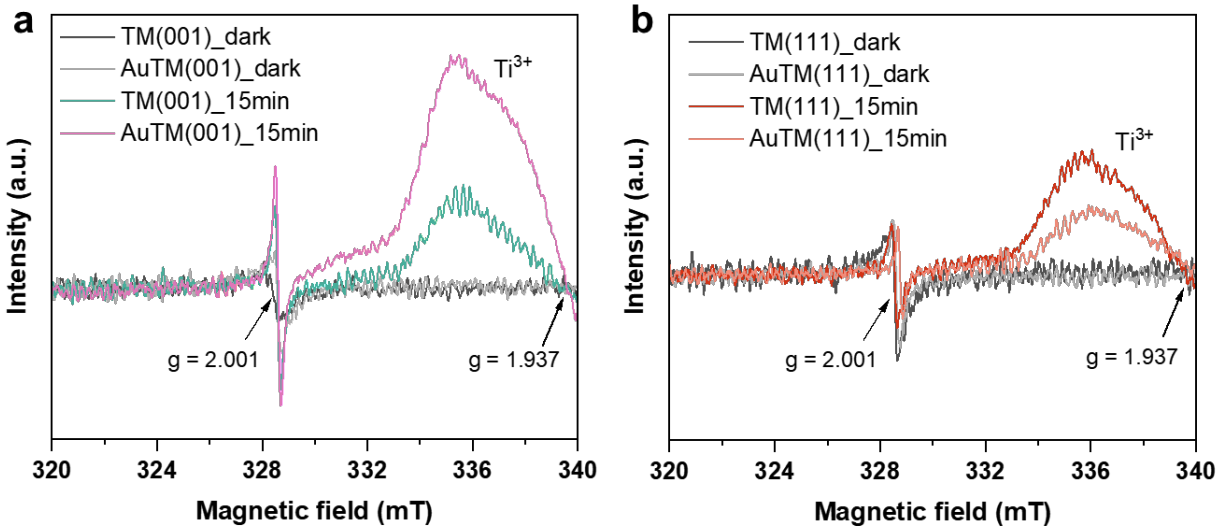

Figure 25. ESR spectra of (a) TM(001), AuTM(001) and (b) TM(111), and AuTM(111) in a frozen acetonitrile solution containing TEOA at -196 ^{o}C under Ar atmosphere under dark and visible-light conditions.

4.3.4 Photocatalytic H_2O_2 production in a dual-phase system over AuTM(111)

Although the optimized AuTM(111) demonstrated remarkable H_2O_2 production, it still exhibited a high H_2O_2 decomposition rate of about 600 μmol L^{-1} h^{-1} as shown in **Figure 21b**. This is attributed to the single-phase reaction system, where H_2O_2 readily interacts with the Ti-based MOF catalysts, forming Ti-OOH complexes that induce H_2O_2 decomposition.[55,58] To address this challenge, we employed a BA/water dual-phase reaction system, which enables spontaneous separation of H_2O_2 produced from catalysts.[34,46] Additionally, BA serves as a sacrificial agent, trapping photogenerated holes. The reaction in this biphasic system proceeds as follows:[59]

$$O_2 + C_6H_5CH_2OH \xrightarrow[hv]{cat.} H_2O_2 + C_6H_5CHO \qquad (8)$$

Figure 26a exhibits the dispersion situation of AuTM(111) in the dual-phase system. The hydrophilic -NH_2 groups allow AuTM(111) to exist in the aqueous phase (denoted as AuTM(111)_D), whereas OPA-modified AuTM(111) with hydrophobic long alkyl chains distributes in the BA phase (denoted as OPA-AuTM(111)_D). Blank experiments (**Figure 26b**) confirm that the benzaldehyde (BAL) self-catalytic reaction, reported to be able to generate

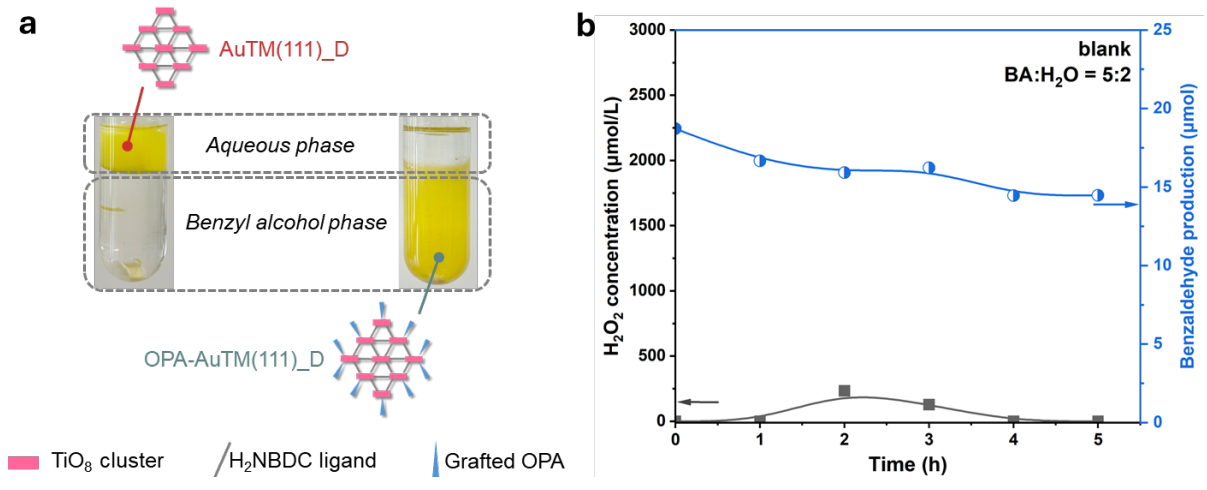

Figure 26. (a) Digital photos of the dual-phase system (water/BA) containing hydrophilic AuTM(111) (left) in the aqueous phase and hydrophobic OPA-AuTM(111) (right) in the BA phase; (b) Products of H_2O_2 and BAL in a BA/water (5:2 mL:mL) dual-phase system without a catalyst during 5 h of visible light irradiation.

large amounts of H_2O_2,[60,61] does not contribute to H_2O_2 production in this system, as H_2O_2 is scarcely detected in the absence of the catalyst. Therefore, the H_2O_2 detected in this system originates exclusively from the catalyst under illumination.

Based on the evaluation results as depicted in **Figure 27a**, AuTM(111)_D hardly exhibits H_2O_2 production over 3 h, with nearly 60% decomposition, due to the structural instability of Ti-based MOF in water.[62] In contrast, OPA-AuTM(111)_D achieves a remarkable H_2O_2 concentration of nearly 6000 μmol L^{-1} without decomposition being detected in the H_2O_2 decomposition test, much higher than 3221 μmol L^{-1} obtained in the single-phase system using the AuTM(111) (AuTM(111)_S). An excellent H_2O_2 production rate of 2160 μmol g^{-1} h^{-1} was obtained as well, surpassing various reported MOF-based catalysts as summarized in **Table 4**. This superiority in performance is attributed to the synergistic effect of the optimized highly reactive {111} facet and the protection for produced H_2O_2 by the dual-phase reaction system.

To elucidate the reaction mechanism, we conducted trapping experiments for $^1O_2$ in both solvent phases (**Figure 27b**). Without NaN_3 scavenging $^1O_2$, H_2O_2 mainly accumulates in the aqueous phase. Adding NaN_3 to the aqueous phase slightly reduces H_2O_2 production, whereas adding it to the BA phase stops H_2O_2 production. This indicates that $^1O_2$ species form exclusively in the BA phase and are subsequently reduced by photogenerated electrons on the catalyst surface to form H_2O_2 (**Equation 5**), which spontaneously migrates to the aqueous phase owing to its hydrophilicity.

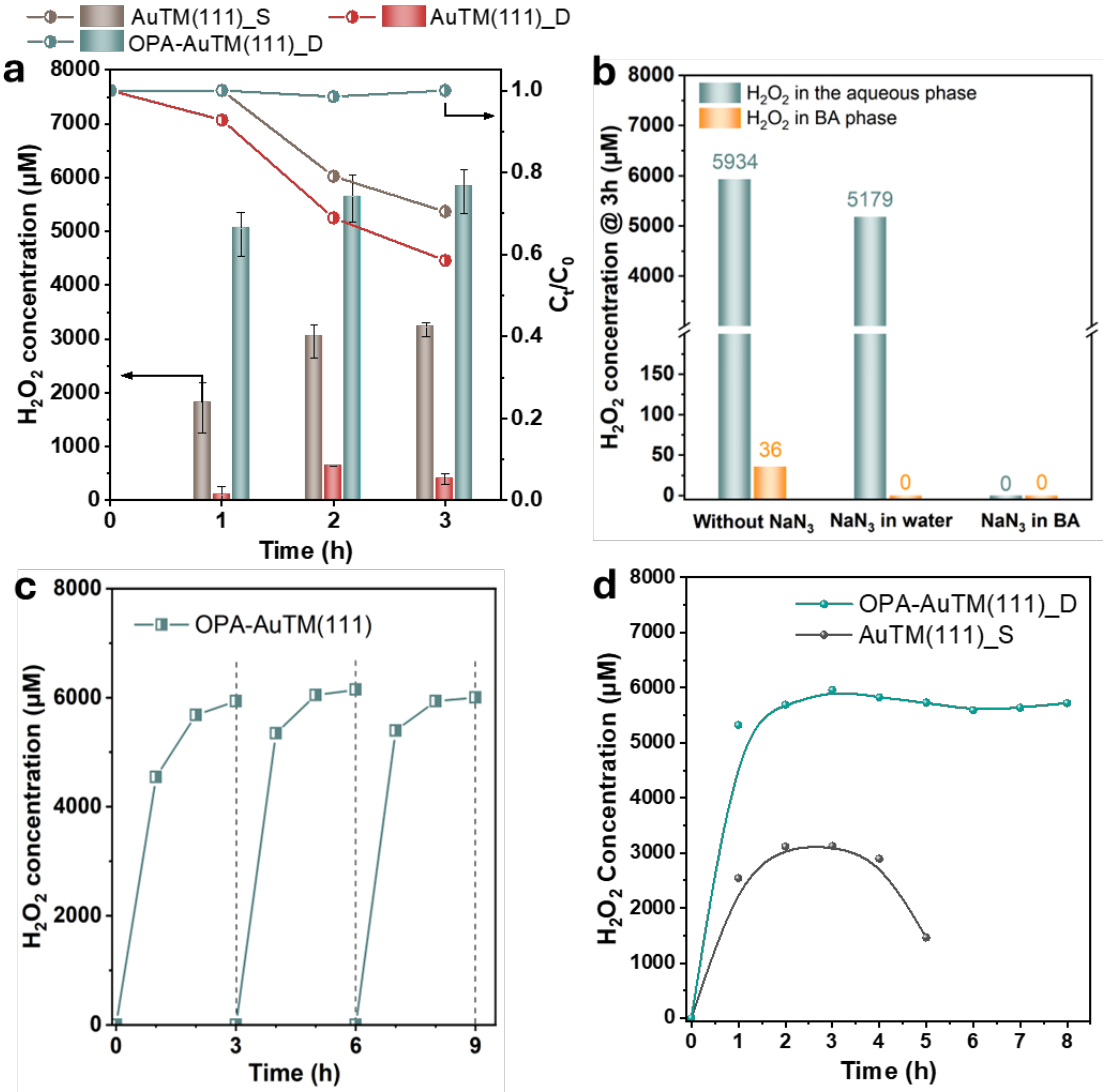

Figure 27. (a) Time courses of H_2O_2 production and decomposition on AuTM(111)_S, AuTM(111)_D, and OPA-AuTM(111)_D samples in single-phase (acetonitrile: TEOA = 4:1) and dual-phase (BA: water = 5:2) reaction systems; (b) Quenching test of OPA-AuTM(111)_D in the dual-phase system using NaN_3 (50 mM) as the scavenger of $^1O_2$; (c) The recycling test of photocatalytic H_2O_2 evolution on OPA-AuTM(111) in the dual-phase system; (d) Stability test of OPA-AuTM(111)_D and AuTM(111)_S in the dual-phase and single-phase system, respectively.

Table 4. Summary of reported photocatalytic H_2O_2 production over MOF materials.

Catalysts	Reaction condition (mL : mL)	Irradiated wavelength (nm)	H_2O_2 production ($\mu mol\ h^{-1}\ g^{-1}$)	Reference
OPA-AuTM(111)	Benzyl alcohol/water (5:2)	> 420	2160	This work
AuTM(111)	Acetonitrile/TEOA (4:1)	> 420	1524	This work
OPA/MIL-125-NH_2	Benzyl alcohol/water (5:2)	> 420	853	Kawase et al.[46]
MIL-125-R7	Benzyl alcohol/water (5:2)	> 420	306	Isaka et al.[34]
NiO/MIL-125-NH_2	Acetonitrile/benzyl alcohol (4:1)	> 420	1124	Isaka et al.[55]
MIL-125-NH_2@ZnS-3	Acetonitrile/benzyl alcohol (4:1)	> 420	1473	Liu et al.[63]
Al-MIL-101-NH_2	Acetonitrile/benzyl alcohol (4:1)	> 420	295	Kondo et al.[64]
UiO-66-NH_2-1.0	Acetonitrile/benzyl alcohol (4:1)	> 350	364	Kondo et al.[16]
Pd_1/A-aUiO	Water/isopropanol (4:1), membrane reactor	> 420	10400	Hao et al.[65]
MIL-111/001	Water	> 420	917	Zheng et al.[25]
Al-TCPP4-TBAPy6	Water	> 420	127	Kondo et al.[66]

Besides, BA is typically thought to be oxidized to BAL by photogenerated holes.[67] As exhibited in **Figure 28a**, the yield ratio of BAL to H_2O_2 is lower than the theoretical value of 1. The excess H_2O_2 formation is speculated via the direct oxidation of BA by $^1O_2$, owing to its strong oxidative property.[68] The quenching experiments (**Figure 28b**) support this conjecture: adding EDTA-2Na (hole scavenger) reduces BAL formation, while NaN_3 completely inhibits BAL formation. Therefore, it is concluded that BAL in this system is produced via two pathways: BA oxidation by photogenerated holes (**Equation 9**) and direct BA oxidation by $^1O_2$ (**Equation 10**). Correspondingly, H_2O_2 is formed via two pathways: reduction of $^1O_2$ by photogenerated electrons (**Equation 5**) and direct oxidation of BA by $^1O_2$ (**Equation 10**).

$$C_6H_5CH_2OH + 2h^+ \rightarrow C_6H_5CHO + 2H^+ \quad (9)$$

$$^1O_2 + C_6H_5CH_2OH \rightarrow H_2O_2 + C_6H_5CHO \quad (10)$$

The proposed reaction mechanisms of AuTM(111) and OPA-AuTM(111) in single- and dual-phase systems were illustrated in **Figure 29**. In both systems, $^1O_2$ is generated through energy transfer between ground-state O_2 and MOF ligands,[66] followed by reduction to H_2O_2 by photogenerated electrons. Distinctly, the single-phase system accelerates H_2O_2 decomposition due to its direct contact with MOFs. In the dual-phase system, hydrophilic AuTM(111) faces similar challenges, compounded by the hydrolysis of Ti-based MOFs in water.[62] However, hydrophobic modification stabilizes OPA-AuTM(111) in the organic phase, avoiding the hydrolysis. The generated H_2O_2 spontaneously migrates to the aqueous phase, effectively preventing its decomposition. Moreover, the direct oxidation of BA by $^1O_2$ further enhances H_2O_2 production.

Notably, the introduction of the dual-phase system enabled H_2O_2 production to level off after 2 h, attributed to the equilibrium established between the decomposition and production of H_2O_2.[1,69] Although the two-phase system effectively inhibits H_2O_2 decomposition via isolating it from the catalyst, its decomposition still occurs induced by photogenerated electrons under continuous light irradiation.[70] Another reason for the decomposition is the insufficient supply of protons in the aqueous phase.[71] Previous studies have demonstrated that an appropriately acidic environment promotes more stable and sustainable production of H_2O_2.[34]

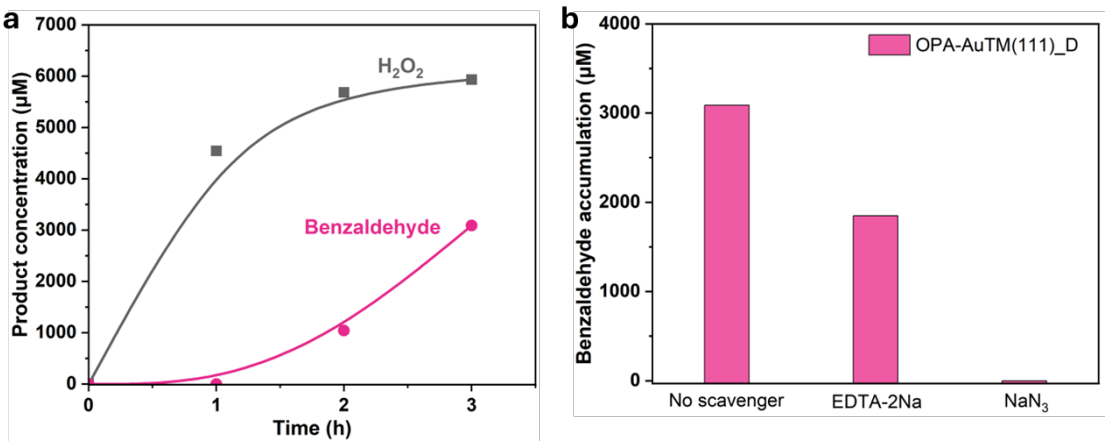

Figure 28. (a) Production distribution of H_2O_2 and BAL during 3h-reaction in the dual-phase system; (b) Quenching test of OPA-AuTM(111)_D in the dual-phase system, containing EDTA-2Na and NaN_3 as scavengers in BA phase with the concentration of 50 mM to consume holes and $^1O_2$ active species during the photocatalytic reaction, respectively.

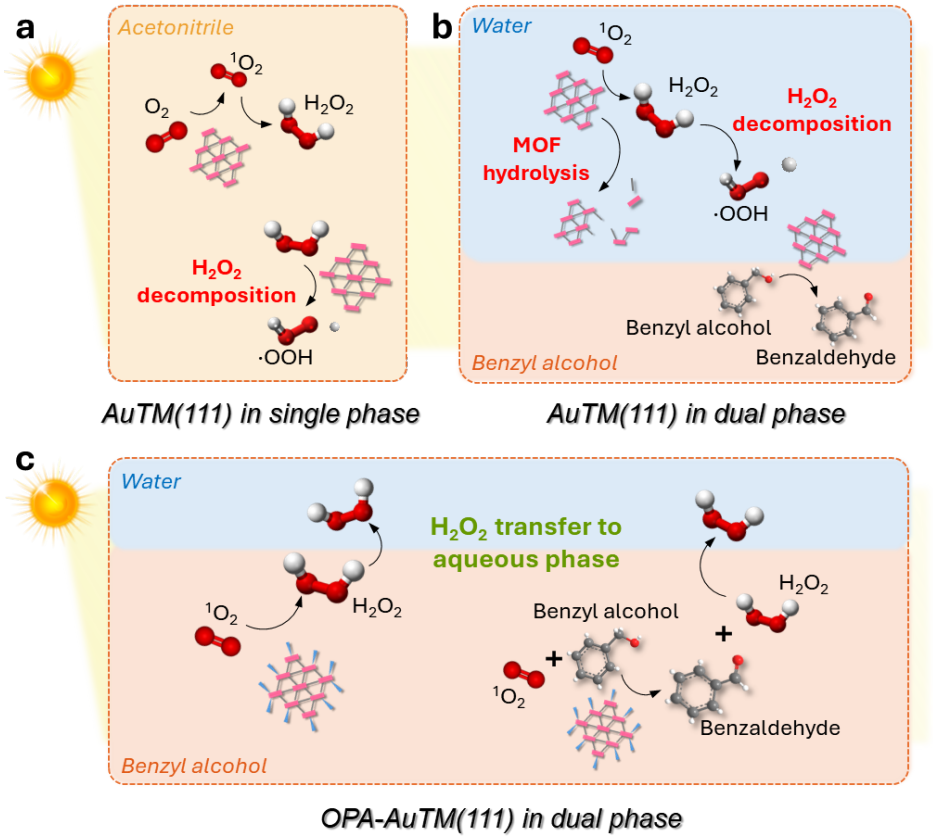

Figure 29. Schematic diagram of proposed reaction mechanism for photoexcited H_2O_2 production in the (a) single-phase and (b, c) dual-phase system using AuTM(111) and OPA-AuTM(111) catalysts.

Additionally, recyclability and long-term stability tests of OPA-AuTM(111) were conducted in H_2O/BA (**Figure 27c**) and saturated NaCl solution/BA dual-phase systems (**Figure 27d**) to simulate realistic conditions. Notably, OPA-AuTM(111)_D performed excellent stability and recyclability under dual-phase conditions, while AuTM(111)_S began to deactivate after 3 h-reaction. As depicted in the XRD, SEM and FT-IR results for used samples (**Figures 30-32**), their crystal structure, morphology, and chemical integrity were well preserved. This demonstrates that the biphasic system effectively maintains the structural integrity and catalytic activity of OPA-AuTM(111), underscoring its potential for sustainable photocatalytic applications.

In summary, this work focuses on the facet-dependent selective anchoring of metal nanoparticles on MOFs, which induces directional control over electron flow and transport kinetics. This phenomenon is experimentally validated in the photocatalytic H_2O_2 production reaction, where the altered electron migration leads to a shift in the reactivity of exposed MOF crystal facets. Such a materials-oriented strategy for tuning charge distribution and surface properties may offer inspiration for the rational design of electrocatalysts with enhanced activity and selectivity.[72] In addition, the biphasic reaction system designed here effectively promotes the selective separation of H_2O_2 from the catalytic interface and suppresses its decomposition. This system-level approach may also provide conceptual guidance for optimizing reaction media in electrocatalytic and photo-electrocatalytic systems.[73]

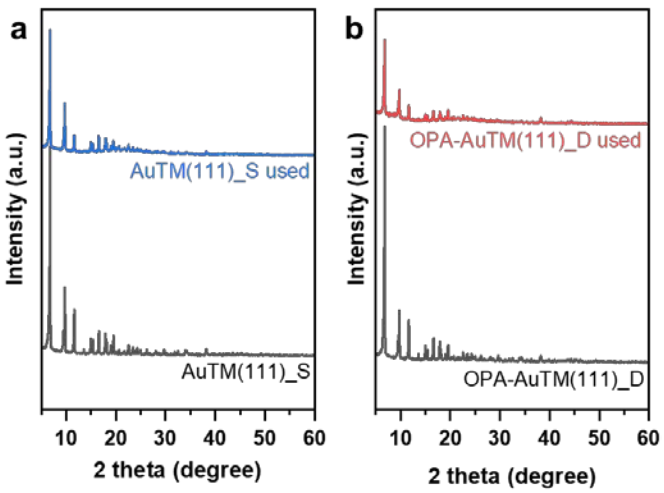

Figure 30. XRD results of (a) AuTM(111) and (b) OPA-AuTM(111) before and after long-term reaction.

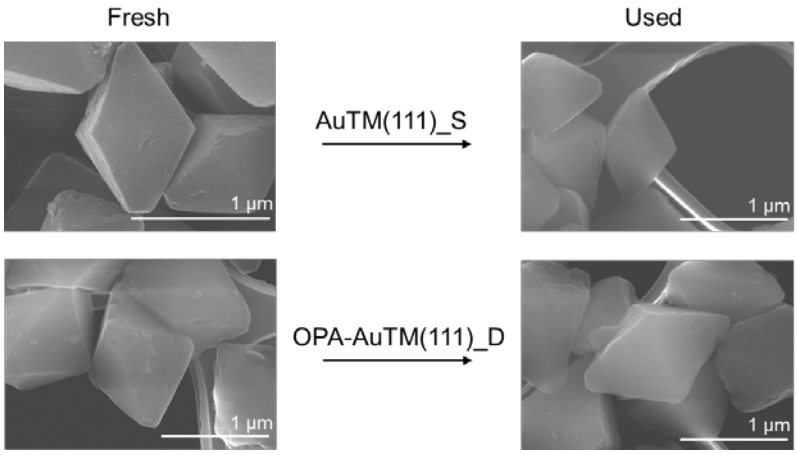

Figure 31. High-resolution FE-SEM images of fresh and used catalysts.

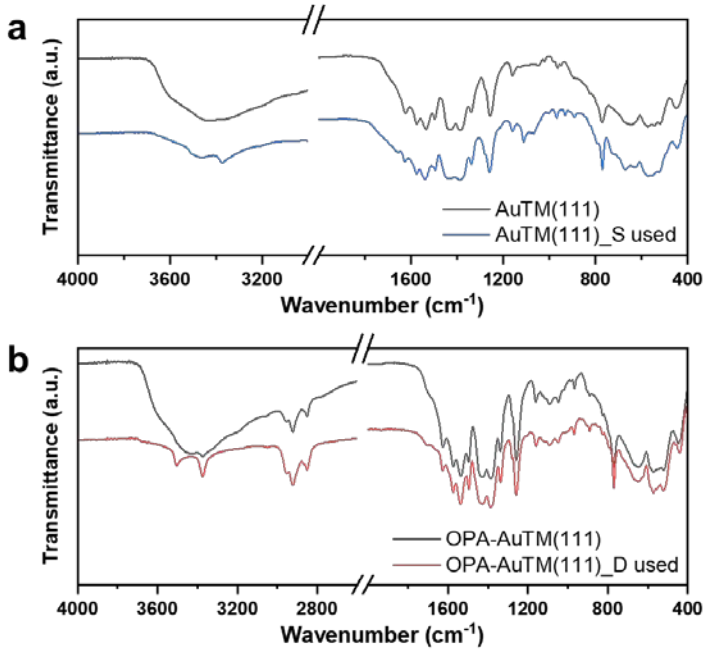

Figure 32. FT-IR spectra of (a) AuTM(111) and (b) OPA-AuTM(111) before and after long-term reaction.

4.4 Conclusion

Here, we present a thorough transformation from less reactive {111} facet to highly reactive {111} facet of MIL-125-NH_2-type MOF, achieved by a simple Au metal incorporation method. This transformation is attributed to the distinct electron transfer pathways after Au anchoring on {001} and {111} facets. Exposure of the {111} facet facilitates rapid separation and migration of photogenerated electrons from ligands to Au NPs, attributed to higher conductivity of Au and shorter electron transfer pathways than that from ligands to Ti clusters occurring on the {001} facet. Moreover, hydrophobically modified AuTM(111) was applied in a BA/water dual-phase reaction system, where spontaneous separation of H_2O_2 from the catalyst effectively suppressed its decomposition. This system achieved an exceptional H_2O_2 production rate of 2160 μmol g^{-1} h^{-1} under $\lambda > 420$ nm irradiation. Beyond the $^1O_2$-mediated oxygen reduction reaction, the direct oxidation of BA by $^1O_2$ further contributed to the increased H_2O_2 yield. The utilization of a dual-phase system provides a practical strategy for facet-engineered MOFs. We have successfully realized the transformation of less-to-highly reactive facets for the model MIL-125-NH_2-type MOFs. The less-reactive {111} facet, despite its limited charge separation efficiency, exhibits strong light absorption capabilities that can be effectively harnessed and transformed into a highly reactive facet through simple metal incorporation. These findings offer valuable insights into the further research of facet engineering for MOF catalysts and provide strategies to the reactor design in electrocatalysis or photoelectrochemical fields.

4.5 References

1 Z. Deng, S. J. Choi, G. Li and X. Wang, *Chem. Soc. Rev.*, 2024, **53**, 8137–8181.

2 T. Wang, F. Ye, S. Wu, S. Chen, H. Yu and X. Quan, *ACS EST Eng.*, 2021, **1**, 1122–1130.

3 L. Qiao, J. Bai, T. Luo, J. Li, Y. Zhang, L. Xia, T. Zhou, Q. Xu and B. Zhou, *Appl. Catal. B Environ.*, 2018, **238**, 491–497.

4 Y. Liu, X. Wang, Y. Zhao, Q. Wu, H. Nie, H. Si, H. Huang, Y. Liu, M. Shao and Z. Kang, *Nano Res.*, 2022, **15**, 4000–4007.

5 A. E. Thorarinsdottir, Daniel P Erdosy, C. Costentin, Jarad A Mason and D. G. Nocera, *Nat. Catal.*, 2023, 425–434.

6 Y. Zhao, Y. Kondo, Y. Kuwahara, K. Mori and H. Yamashita, *Appl. Catal. B Environ. Energy*, 2024, **351**, 123945.

7 H. G. Jin, P. C. Zhao, Y. Qian, J. D. Xiao, Z. S. Chao and H. L. Jiang, *Chem. Soc. Rev.*, 2024, **53**, 9378–9418.

8 X. Chen, Y. Kondo, Y. Kuwahara, K. Mori, C. Louis and H. Yamashita, *Phys. Chem. Chem. Phys.*, 2020, **22**, 14404–14414.

9 Y. Kondo, Y. Kuwahara, K. Mori and H. Yamashita, *Chem*, 2022, **8**, 2924–2938.

10 S. Bai, L. Wang, Z. Li and Y. Xiong, *Adv. Sci.*, 2017, **4**, 1600216.

11 C. Zhang, C. Xie, Y. Gao, X. Tao, C. Ding, F. Fan and H. L. Jiang, *Angew. Chem. Int. Ed.*, 2022, **61**, e202204108.

12 J. Sui, H. Liu, S. Hu, K. Sun, G. Wan, H. Zhou, X. Zheng and H. Jiang, *Adv. Mater.*, 2022, **34**, 2109203.

13 Y. Kondo, K. Honda, Y. Kuwahara, K. Mori, H. Kobayashi and H. Yamashita, *ACS Catal.*, 2022, **12**, 14825–14835.

14 Y. Chen, S. Ji, Y. Wang, J. Dong, W. Chen, Z. Li, R. Shen, L. Zheng, Z. Zhuang, D. Wang and Y. Li, *Angew. Chem. Int. Ed.*, 2017, **56**, 6937–6941.

15 H. Zhang, S. Hwang, M. Wang, Z. Feng, S. Karakalos, L. Luo, Z. Qiao, X. Xie, C. Wang, D. Su, Y. Shao and G. Wu, *J. Am. Chem. Soc.*, 2017, **139**, 14143–14149.

16 Y. Kondo, Y. Kuwahara, K. Mori and H. Yamashita, *J. Phys. Chem. C*, 2021, **125**, 27909–27918.

17 K. Suresh, A. P. Kalenak, A. Sotuyo and A. J. Matzger, *Chem. – Eur. J.*, 2022, **28**, e202200334.

18 L. Yuan, P. Du, C. Zhang, Y. Xi, Y. Zou, J. Li, Y. Bi, T. Bao, C. Liu and C. Yu, *Appl. Catal. B Environ. Energy*, 2025, **364**, 124855.

19 X. M. Cheng, P. Wang, S. Q. Wang, J. Zhao and W. Y. Sun, *ACS Appl. Mater. Interfaces*, 2022, **14**, 32350–32359.

20 X. Y. Ji, Y. Y. Wang, Y. Li, K. Sun, M. Yu and J. Tao, *Nano Res.*, 2022, **15**, 6045–6053.

21 M. Gao, L. Li, Z. Sun, J. Li and H. Jiang, *Angew. Chem. Int. Ed.*, 2022, **61**, e202211216.

22 Z. Li, S. Li, M. Zhu, Q. Liu, Y. Zhang, Y. Wang, L. Wu and X. Jiang, *Langmuir*, 2024, **40**, 25518–25528.

23 Z. Wang, L. Ge, D. Feng, Z. Jiang, H. Wang, M. Li, R. Lin and Z. Zhu, *Cryst. Growth Des.*, 2021, **21**, 926–934.

24 Q. Li, J. Li, H. Bai and F. Li, *Chin. J. Catal.*, 2024, **58**, 86–104.

25 Y. Zheng, H. Zhou, B. Zhou, J. Mao and Y. Zhao, *Catal. Sci. Technol.*, 2022, **12**, 969–975.

26 F. Guo, J. H. Guo, P. Wang, Y. S. Kang, Y. Liu, J. Zhao and W. Y. Sun, *Chem. Sci.*, 2019, **10**, 4834–4838.

27 J. Qiu, D. Dai and J. Yao, *Coord. Chem. Rev.*, 2024, **501**, 215597.

28 J. Wang, J. Yao, L. Yin, B. Wang, X. Liu, L. Yuan, C. Zhang, T. Bao, C. Liu and X. Hu, *Chem. Eng. J.*, 2024, **497**, 154836.

29 X. M. Cheng, X. Y. Dao, S. Q. Wang, J. Zhao and W. Y. Sun, *ACS Catal.*, 2021, **11**, 650-658.

30 L. Liu, S. Du, Y. Xiao, X. Guo, S. Jin, G. Shao and F. Zhang, *Appl. Catal. B Environ.*, 2023, **338**, 123094.

31 M. Kou, Y. Wang, Y. Xu, L. Ye, Y. Huang, B. Jia, H. Li, J. Ren, Y. Deng, J. Chen, Y. Zhou, K. Lei, L. Wang, W. Liu, H. Huang and T. Ma, *Angew. Chem. Int. Ed.*, 2022, **61**, e202200413.

32 L. Wang, J. Zhang, Y. Zhang, H. Yu, Y. Qu and J. Yu, *Small*, 2022, **18**, 2104561.

33 L. Ding, Z. Pan and Q. Wang, *Chin. Chem. Lett.*, 2024, 110125.

34 Y. Isaka, Y. Kawase, Y. Asutaka Kuwahara, K. Mori and H. Yamashita, *Angew. Chem. Int. Ed.*, 2019, **131**, 5456–5460.

35 X. M. Cheng, Y. Gu, X. Y. Zhang, X. Y. Dao, S. Q. Wang, J. Ma, J. Zhao and W. Y. Sun, *Appl. Catal. B Environ.*, 2021, **298**, 120524.

36 H. Chen, Q. Zhou, J. Hai, M. Zhu and F. Zhang, *J. Mater. Chem. A*, 2024, **12**, 10745–10754.

37 M. Sun, X. Wang, Y. Li, H. Pan, M. Murugananthan, Y. Han, J. Wu, M. Zhang, Y. Zhang and Z. Kang, *ACS Catal.*, 2022, **12**, 2138–2149.

38 A. U. Haq, M. Buerkle, S. Askari, C. Rocks, C. Ni, V. Švrček, P. Maguire, J. T. S. Irvine and D. Mariotti, *J. Phys. Chem. Lett.*, 2020, **11**, 1721–1728.

39 C. Matsubara, N. Kawamoto and K. Takamura, *Analyst*, 1992, **117**, 1781–1784.

40 D. Vanderbilt, *Phys. Rev. B*, 1990, **41**, 7892–7895.

41 Q. Wang and K. Domen, *Chem. Rev.*, 2020, **120**, 919–985.

42 Y. Fu, D. Sun, Y. Chen, R. Huang, Z. Ding, X. Fu and Z. Li, *Angew. Chem. Int. Ed.*, 2012, **51**, 3364–3367.

43 X. Wu, H. Zhang, S. Xie and Y. Wang, *Chem Catal.*, 2023, **3**, 100437.

44 X. Zhang, Z. Li, T. Liu, M. Li, C. Zeng, H. Matsumoto and H. Han, *Chin. J. Catal.*, 2022, **43**, 2223–2230.

45 M. Dan-Hardi, C. Serre, T. Frot, L. Rozes, G. Maurin, C. Sanchez and G. Férey, *J. Am. Chem. Soc.*, 2009, **131**, 10857–10859.

46 Y. Kawase, Y. Isaka, Y. Kuwahara, K. Mori and H. Yamashita, *Chem. Commun.*, 2019, **55**, 6743–6746.

47 E. N. Musa, A. K. Yadav, M. Srichareonkul, D. Thampetraruk, E. Frechette, H. C. Thiele and K. C. Stylianou, *ACS Appl. Mater. Interfaces*, 2024, **16**, 70675–70684.

48 X. Li, H. Jiang, C. Ma, Z. Zhu, X. Song, H. Wang, P. Huo and X. Li, *Appl. Catal. B Environ.*, 2021, **283**, 119638.

49 L. Shen, M. Luo, L. Huang, P. Feng and L. Wu, *Inorg. Chem.*, 2015, **54**, 1191–1193.

50 S. Liu, Y. Wang, K. F. Lyu, X. Lan and T. Wang, *Nat. Synth.*, 2024, **3**, 1158–1167.

51 J. Zhu, P.-Z. Li, W. Guo, Y. Zhao and R. Zou, *Coord. Chem. Rev.*, 2018, **359**, 80–101.

52 M. A. Baluk, A. Pieczyńska, M. Kroczewska, J. Łuczak, K. Matus, K. Nikiforow and A. Zaleska-Medynska, *Chem. Eng. J.*, 2024, **492**, 152313.

53 C. C. Cheng, T. Y. Lin, Y. C. Ting, S. H. Lin, Y. Choi and S. Y. Lu, *Nano Energy*, 2023, **112**, 108450.

54 X. Zhang, H. Su, P. Cui, Y. Cao, Z. Teng, Q. Zhang, Y. Wang, Y. Feng, R. Feng, J. Hou, X. Zhou, P. Ma, H. Hu, K. Wang, C. Wang, L. Gan, Y. Zhao, Q. Liu, T. Zhang and K. Zheng, *Nat. Commun.*, 2023, **14**, 7115.

55 Y. Isaka, Y. Kondo, Y. Kawase, Y. Kuwahara, K. Mori and H. Yamashita, *Chem. Commun.*, 2018, **54**, 9270–9273.

56 P. P. Ly, D. V. Nguyen, T. A. Luu, N. Q. Hung, P. T. Hue, N. T. N. Hue, M. T. Pham, T. D. T. Ung, D. D. Bich, P. D. M. Phan, N. H. Anh, H. P. Toan, D. P. Bui, V. A. Dao, S. H. Hur and H. T. Vuong, *Adv. Sustain. Syst.*, 2024, **8**, 2300470.

57 D. Sun, W. Liu, Y. Fu, Z. Fang, F. Sun, X. Fu, Y. Zhang and Z. Li, *Chem. – Eur. J.*, 2014, **20**, 4780–4788.

58 J. S. Kang, S. D. Sohn and H. J. Shin, *J. Phys. Chem. C*, 2020, **124**, 11930–11934.

59 Y. Zhao, Y. Kondo, Y. Kuwahara, K. Mori and H. Yamashita, *Catal. Today*, 2024, **425**, 114350.

60 I. Krivtsov, A. Vazirani, D. Mitoraj and R. Beranek, *ChemCatChem*, 2023, **15**, e202201215.

61 B. C. Moon, B. Bayarkhuu, K. A. I. Zhang, D. K. Lee and J. Byun, *Energy Environ. Sci.*, 2022, **15**, 5082–5092.

62 M. E. Aguirre, R. I. Naveira, P. M. Botta, T. A. Altieri, A. Wolosiuk and M. S. Churio, *New J. Chem.*, 2021, **45**, 10277–10286.

63 C. Liu, T. Bao, L. Yuan, C. Zhang, J. Wang, J. Wan and C. Yu, *Adv. Funct. Mater.*, 2022, **32**, 2111404.

64 Y. Kondo, K. Hino, Y. Kuwahara, K. Mori, H. Kobayashi and H. Yamashita, *Chem. Commun.*, 2022, **58**, 12345–12348.

65 Y. C. Hao, L. W. Chen, J. Li, Y. Guo, X. Su, M. Shu, Q. Zhang, W. Y. Gao, S. Li, Z. L. Yu, L. Gu, X. Feng, A. X. Yin, R. Si, Y. W. Zhang, B. Wang and C. H. Yan, *Nat. Commun.*, 2021, **12**, 1–11.

66 Y. Kondo, K. Hino, Y. Kuwahara, K. Mori and H. Yamashita, *J. Mater. Chem. A*, 2023, **11**, 9530–9537.

67 X. Chen, Y. Kuwahara, K. Mori, C. Louis and H. Yamashita, *J. Mater. Chem. A*, 2021, **9**, 2815–2821.

68 Y. Nosaka and A. Y. Nosaka, *Chem. Rev.*, 2017, **117**, 11302–11336.

69 S. Yang, A. Verdaguer-Casadevall, L. Arnarson, L. Silvioli, V. Čolić, R. Frydendal, J. Rossmeisl, I. Chorkendorff and I. E. L. Stephens, *ACS Catal.*, 2018, **8**, 4064–4081.

70 Y. Y. Tang, X. Luo, R. Q. Xia, J. Luo, S. K. Peng, Z. N. Liu, Q. Gao, M. Xie, R. J. Wei, G. H. Ning and D. Li, *Angew. Chem. Int. Ed.*, 2024, **63**, e202408186.

71 N. Wang, S. Ma, P. Zuo, J. Duan and B. Hou, *Adv. Sci.*, 2021, **8**, 2100076.

72 Y. Zhang, Y. Lin, T. Duan and L. Song, *Mater. Today*, 2021, **48**, 115–134.

73 Y. Wen, T. Zhang, J. Wang, Z. Pan, T. Wang, H. Yamashita, X. Qian and Y. Zhao, *Angew. Chem. Int. Ed.*, 2022, **61**, e202205972.

Chapter V

General Conclusions

In the present thesis, three classes of advanced Ti-based inorganic and organic semiconductors were systematically developed for efficient photocatalytic H_2O_2 production in a benzyl alcohol (BA)/water two-phase system under visible-light irradiation. Centered on the overarching goal of achieving efficient separation and utilization of photogenerated charge carriers, this work systematically employed three complementary material design strategies: molecular functionalization, plasmonic metal decoration, and facet engineering. By progressively enhancing the light absorption, charge separation, and interfacial catalytic properties of TiO_2 and Ti-MOF systems, this work reveals how deliberate structural modifications at the molecular, nanoscale, and crystallographic levels can translate into markedly improved photocatalytic performance.

In Chapter II, a series of 2,3-dihydroxynaphthalene (2,3-DN) and octadecylphosphonic acid (OPA) co-modified TiO_2 catalysts were synthesized (**Figure 1**), exhibiting extended visible-light absorption and unique hydrophobic properties. The introduction of 2,3-DN facilitates the formation of charge-transfer complexes on the TiO_2 surface, enabling visible-light-driven electron generation, which contributes to the enhanced oxygen reduction reaction (ORR). Meanwhile, OPA modification imparts TiO_2 hydrophobicity, allowing the catalyst to

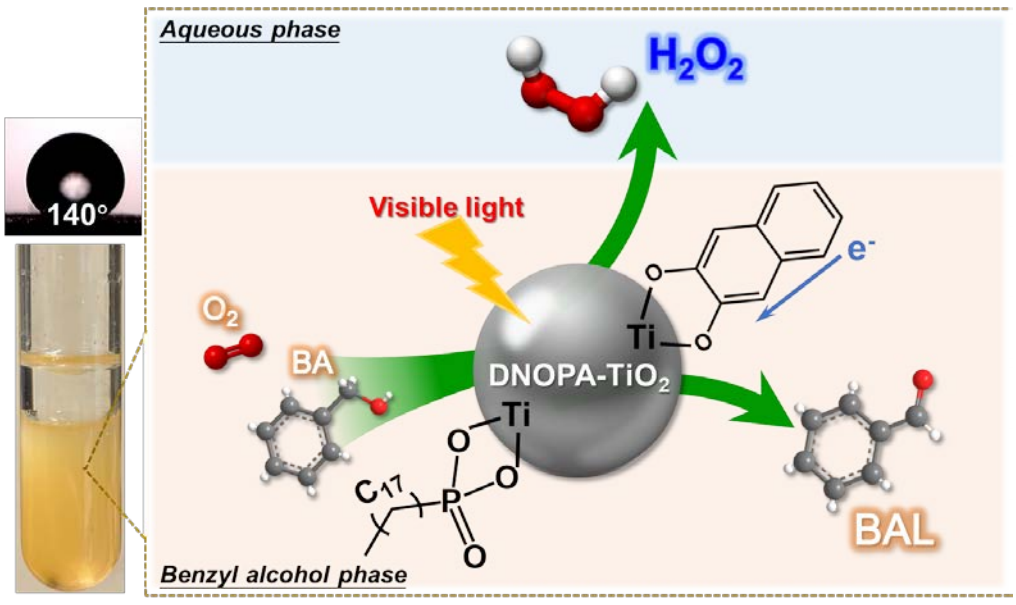

Figure 1. Development of organic-molecule-modified DNOPA-TiO_2 with visible-light response for H_2O_2 photosynthesis in a two-phase system.

localize in the organic phase of a two-phase system, thereby effectively minimizing H_2O_2 decomposition. As a result, the co-modified DN2OPA2-TiO_2 catalyst achieves a notable H_2O_2 concentration of 3522 μmol L^{-1} over 8 h under visible-light irradiation (λ > 450 nm), with a H_2O_2 production rate of 205 μmol g^{-1} h^{-1}, following the indirect 2e-ORR pathway. This work highlights the potential of combining organic molecular modification with hydrophobic surface engineering to broaden TiO_2-based material applications in photocatalytic H_2O_2 synthesis.

In Chapter III, OPA-modified, plasmonic AuNPs-decorated TiO_2 catalysts were developed for the two-phase photocatalytic H_2O_2 production system (**Figure 2**). The deposited Au NPs introduce the surface plasmon resonance (SPR) effect, significantly boosting visible-light absorption and enabling hot electrons transfer to the TiO_2 conduction band, thereby promoting the ORR process. UV-vis DRS, PL, and XPS analyses confirmed the narrowed bandgap and improved charge separation in the Au/TiO_2 composite. Furthermore, hydrophobic modification with OPA helps the catalyst to be well-dispersed in the BA phase, effectively suppressing H_2O_2 decomposition. This system achieved an impressive H_2O_2 production rate of 567 μmol g^{-1} h^{-1} under visible-light irradiation (λ > 420 nm). Collectively, this study underscores the critical role of combining plasmonic metal-semiconductor composite with phase management strategies to overcome the intrinsic limitations of TiO_2-related photocatalysts.

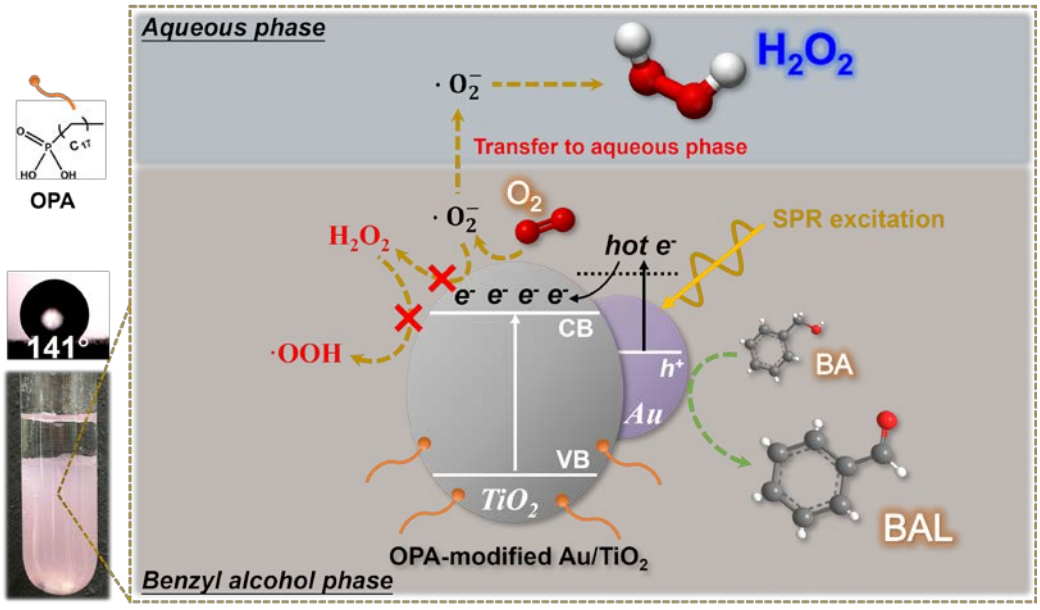

Figure 2. Boosting H_2O_2 photosynthesis from Au nanoparticles-fabricated TiO_2 with surface plasmon resonance effect.

In Chapter IV, a facet engineering strategy was applied to MIL-125-NH_2-type MOFs, successfully transforming the original reactive {001} facet to the highly reactive {111} facet through the selective Au incorporation method (**Figure 3**). This approach exploits the distinct electron transfer pathways determined by the crystallographic orientation of the exposed facets. Specifically, the selective anchoring of Au NPs near the -NH_2 groups of the organic ligands on AuTM(111) facilitates rapid charge separation and efficient migration of photogenerated electrons from the ligands to the Au NPs. This enhanced electron transfer on AuTM(111) is attributed to the superior conductivity of Au and shorter transfer distance, compared to the longer electron migration route from ligands to Au NPs located near Ti clusters on AuTM(001). When combined with OPA modification and applied in the BA/water biphasic system, the optimized system achieves an exceptional H_2O_2 production rate of 2160 μmol g^{-1} h^{-1} under visible-light irradiation (λ > 420 nm). H_2O_2 was formed via both the direct 2e-ORR pathway mediated by the singlet oxygen ($^1O_2$) and the direct oxidation of BA by $^1O_2$. This work further demonstrates the overall functionalization of material composition and crystal orientation, achieving the redirection of charge carrier dynamics and providing novel insights into the design of facet-engineered MOF photocatalysts.

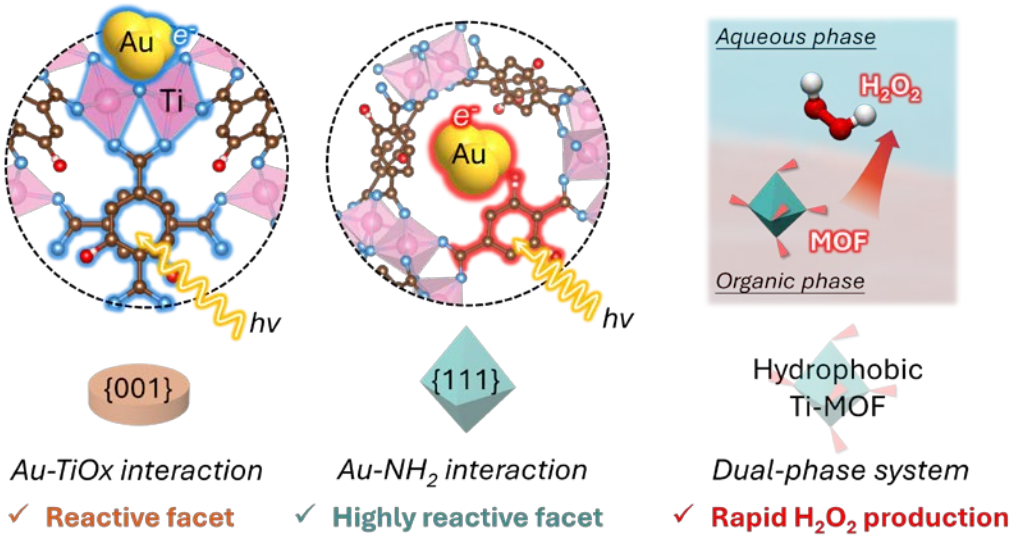

Figure 3. Highly reactive facet modulation of Ti-MOFs by selective anchoring of Au metal for efficient photocatalytic H_2O_2 production.

In summary, this thesis systematically investigated material designs for improving the separation and utilization of photogenerated electrons to enhance photocatalytic ORR in biphasic systems. Chapters II and III focus on Ti-based inorganic semiconductors (TiO_2) modified through surface molecular functionalization and plasmonic metal decoration, respectively, to achieve visible-light responsiveness and hydrophobicity of TiO_2. Chapter IV extended this strategy to Ti-based organic semiconductors (MIL-125-NH_2 MOFs), using facet engineering to optimize electron transfer pathways on MOFs through selective metal anchoring. Overall, these approaches result in materials with strong visible-light adsorption, finely tuned electronic and band structure, high charge separation efficiency, and optimized charge carrier dynamics, enabling highly reactive, stable, and efficient H_2O_2 generation with minimal decomposition. Furthermore, the two-phase system provides an effective platform for spatially separating catalysts from decomposable products, enhancing both catalytic performance and product stability.

To conclude, while this thesis has advanced the design of inorganic/organic Ti-based photocatalysts for efficient H_2O_2 production in biphasic systems, several avenues remain for future exploration: (1) Enhancing O_2 mass transport via catalyst design and triphasic interfaces. Efficient O_2 delivery remains a key bottleneck in photocatalytic H_2O_2 production, especially in organic solvents. To address this, designing catalysts should incorporate hierarchical porosity and solid-gas-liquid triphasic interface (e.g., gas-diffusion electrodes) to maximize O_2 solubility and diffusion at the catalytic sites. (2) Integration of two-phase systems into continuous-flow reactors. Building on the superior H_2O_2 production and stability demonstrated in a batch two-phase system, it is worth focusing on transitioning these findings into continuous-flow reactors, which is essential for scaling up photocatalytic H_2O_2 production. Continuous-flow systems offer enhanced control over reaction parameters, improved mass transfer, and consistent product quality. (3) Development of tandem and synergistic reaction pathways. Expanding the functionality of photocatalytic systems beyond single-step reactions can lead to more versatile applications. Integrating H_2O_2 generation with subsequent oxidation reactions, such as the selective oxidation of organic substrates, can create efficient one-pot processes and produce more high value-added chemicals. For instance, coupling H_2O_2

production with the oxidation of furfuryl alcohol to furoic acid demonstrates the potential of tandem photocatalytic systems. The author hopes that these findings and the above perspectives could contribute to the rational design of next-generation materials in the broader context of solar-to-chemical energy conversion.

List of Publications

(1) **Yifan Zhao**, Hao Ge, Yoshifumi Kondo, Zhenpeng Guo, Yasutaka Kuwahara, Kohsuke Mori, Tohru Sekino, Zhenfeng Bian, Hiromi Yamashita*
"Highly reactive facet modulation of Ti-based MOFs by selective anchoring of Au metal for photocatalytic H_2O_2 production"
ACS Catalysis, **2025**, 15(13), 11313–11325.

(2) **Yifan Zhao**, Yoshifumi Kondo, Yasutaka Kuwahara, Kohsuke Mori, Hiromi Yamashita*
"Two-phase reaction system for efficient photocatalytic production of hydrogen peroxide"
Applied Catalysis B: Environmental and Energy, **2024**, 351, 123945.

(3) **Yifan Zhao**, Hao Ge, Yoshifumi Kondo, Yasutaka Kuwahara, Kohsuke Mori, Hiromi Yamashita*
"Photosynthesis of hydrogen peroxide in a two-phase system by hydrophobic Au nanoparticle-deposited plasmonic TiO_2 catalysts"
Catalysis Today, **2024**, 431, 114558.

(4) **Yifan Zhao**, Yoshifumi Kondo, Yasutaka Kuwahara, Kohsuke Mori, Hiromi Yamashita*
"Hydrophobic and visible-light responsive TiO_2 as an efficient photocatalyst for promoting hydrogen peroxide production in a two-phase system"
Catalysis Today, **2024**, 425, 114350.

(5) Sumiyyah Sabar,* Afiqah M. Jamil, **Yifan Zhao**, Enis Nadia Md Yusof, Raphaël Schneider, Abdul Rahman Mohamed, Yasutaka Kuwahara, Kohsuke Mori, Hiromi Yamashita*
"Construction of Fe_3O_4/ZnO heterostructure photocatalyst derived from Fe-doped ZIF-8 for enhanced photocatalytic degradation of tetracycline and hydrogen peroxide production"
New Journal of Chemistry, **2025**, 49, 8267–8278.

<Related work>

(6) **Yifan Zhao**, Wensi Li, Mooeez Ur Rehman, Shengping Wang, Guobing Li,* Yan Xu*
"Roles of N on the N-doped Ru/AC catalyst in hydrogenation of phthalate esters"
Research on Chemical Intermediates, **2022**, 48, 2987-3006.

(7) Dan Guo, Maoshuai Li, Yao Lu, **Yifan Zhao**, Mianjing Li, Yujun Zhao, Shengping Wang,* Xinbin Ma*
"Enhanced thermocatalytic stability by coupling nickel step sites with nitrogen heteroatoms for dry reforming of methane"
ACS Catalysis, **2022**, 12 (1), 316-330.

(8) Yao Lu, Dan Guo, **Yifan Zhao**, Yujun Zhao, Shengping Wang,* Xinbin Ma
"Enhanced performance of xNi@yMo-HSS catalysts for DRM reaction via the formation of a novel SiMoOx species"
Applied Catalysis B: Environmental, **2021**, 291, 120075.

(9) Yao Lu, Dan Guo, **Yifan Zhao**, Perseverence S. Moyo, Yujun Zhao, Shengping Wang,* Xinbin Ma
"Enhanced catalytic performance of Nix-V@HSS catalysts for the DRM reaction: The study of interfacial effects on Ni-VOx structure with a unique yolk-shell structure"
Journal of Catalysis, **2021**, 396, 65–80.

(10) Yao Lu, Li Kang, Dan Guo, **Yifan Zhao**, Yujun Zhao, Shengping Wang,* and Xinbin Ma
"Double-site doping of a V promoter on Ni_x-V-MgAl catalysts for the DRM reaction: simultaneous effect on CH_4 and CO_2 activation"
ACS Catalysis, **2021**, 11 (14), 8749-8765.

(11) Yao Lu, Dan Guo, **Yifan Zhao**, Perseverence S. Moyo, Yujun Zhao, Shengping Wang,* Xinbin Ma
"Confined high dispersion of Ni nanoparticles derived from nickel phyllosilicate structure in silicalite-2 shell for dry reforming of methane with enhanced performance"
Microporous and Mesoporous Materials, **2021**, 313, 110842.

(12) Yongzhe Ruan, **Yifan Zhao**, Yao Lu, Dan Guo, Yujun Zhao, Shengping Wang,* Xinbin Ma

"Mesoporous $LaAl_{0.25}Ni_{0.75}O_3$ perovskite catalyst using SBA-15 as templating agent for methane dry reforming"

*Microporous and Mesoporous Material*s, **2020**, 303, 110278.

(13) Dan Guo, Yao Lu, Yongzhe Ruan, **Yifan Zhao**, Yujun Zhao, Shengping Wang,* Xinbin Ma

"Effects of extrinsic defects originating from the interfacial reaction of CeO_2-x-nickel silicate on catalytic performance in methane dry reforming"

Applied Catalysis B: Environmental, **2020**, 277, 119278.

Acknowledgement

Throughout the writing of this dissertation, I have received a great deal of support and assistance.

I would first like to express my deepest gratitude to my supervisor, Professor Kohsuke Mori (Division of Materials and Manufacturing Science, Graduate School of Engineering, The University of Osaka) for his professional suggestions on my dissertation and his help with theoretical calculations. I really enjoyed the time we spent on academic discussion. I also express my deepest gratitude to Professor Hiromi Yamashita. His invaluable guidance, unwavering support, and insightful advice have been instrumental not only in my research field but also in shaping my future career path. I consider myself truly fortunate to be his final doctoral student, and I would like to take this opportunity to sincerely wish him a joyful and fulfilling retirement. Thanks to Professor Yamashita's constant support, I have been able to participate in numerous domestic and international conferences, complete my doctoral program efficiently, and successfully secure my next position. Moreover, his optimistic mindset, open and supportive atmosphere, and approachable personality have left a lifelong impact on me. Additionally, many thanks to him for giving me opportunities to collaborate with many distinguished professors. Sincere thanks are extended to Professor Tohru Sekino (The Institute of Scientific and Industrial Research, The University of Osaka) and Professor Yuichiro Koizumi (Division of Materials and Manufacturing Science, Graduate School of Engineering, The University of Osaka), who act as the examiners of the dissertation, for their valuable and constructive suggestions. I am also grateful to Associate Professor Yasutaka Kuwahara (Division of Materials and Manufacturing Science, Graduate School of Engineering, The University of Osaka) for his careful revisions and attention to detail in my manuscript and for acting as the examiner of the dissertation.

Special thanks to Assistant Professor Yoshifumi Kondo (The Institute of Scientific and Industrial Research, The University of Osaka) for his expertise in theoretical calculations and valuable insights. I also thank Dr. Hao Ge for his guidance on research direction and characterization techniques. I truly enjoyed the discussions and collaborations with these professors and colleagues.

I am also deeply grateful to my master's supervisors, Professor Shengping Wang (School of Chemical Engineering and Technology, Tianjin University) and Professor Yujun Zhao (School of Chemical Engineering and Technology, Tianjin University), for the academic training and guidance they provided during my earlier studies, which equipped me with the experience and resilience to tackle challenges throughout my doctoral research. I would like to express my heartfelt thanks to Professor Haijun Chen (College of Electronic Information and Optical Engineering, Nankai University), who recommended me for the doctoral program at The University of Osaka. Without his recommendation, I would not have had such an incredible journey or the opportunity to work alongside such outstanding researchers.

Thanks must be made to Mr. Tetsutaro Ohmichi, Ms. Natsuko Hirozawa, Dr. Hao Ge, Dr. Kaining Li, Dr. Yoshifumi Kondo, Ms. Yan Fang, Dr. Caiyun Xu, Dr. Hyojin Kim, Mr. Tianhan Shen, Mr. Yoshiki Nakahara, Dr. Kazuki Shun, Dr. Naoki Hashimoto, Mr. Mikihiro Sakurai, Ms. Shiori Mizutani and all members in Yamashita Lab and Mori Lab. Thank you for all the wonderful time we shared.

Especially, many thanks to my husband, Mr. Gaopeng Li, for accompanying me through the challenges of studying abroad and for creating the beautiful memories that belong to the two of us.

Last but not least, I want to thank my parents Ms. Jianli Wang and Mr. Yulin Zhao, and my sister Ms. Yilu Zhao for their constant support, trust, and love throughout my life.

Yifan ZHAO

June, 2025